



ROMA TRE UNIVERSITY

Department of Mathematics and Physics
Doctoral School in Physics
XXIX Cycle

PhD Thesis in Physics

Development of a Certified Reference Material
and determination of Nuclear Data
for NORM analysis

By:
Luciano Sperandio
Rome, Italy – 2016

Tutor
Prof. Wolfango Plastino

Coordinator
Prof. Roberto Raimondi

Contents

Introduction	1
Chapter 1 NORM and MetroNORM project	3
1.1 Ionizing radiation and radioactivity	3
1.2 The radioactive decay law	3
1.3 Types of decays	5
1.4 Radioactive decay	10
1.4.1 Secular equilibrium.....	11
1.5 Radioactivity in nature.....	12
1.5.1 Terrestrial origin	14
1.6 What is NORM	18
1.7 Hazards to human health and environment.....	18
1.8 The MetroNORM project	19
1.9 Goal of the project	20
Chapter 2 Experimental methods	21
2.1 Scanning electron microscopy	21
2.2 Gamma-ray spectrometry	24
2.3 Gamma-ray spectrometry at INMRI.....	25
2.4 Detector calibration.....	27
2.4.1 Standard source for detector calibration	28
2.4.2 Energy calibration.....	37
2.4.3 Experimental efficiency calibration.....	40
2.4.4 Measurement apparatus	46

2.4.5 Detector characterization.....	50
2.5 Efficiency transfer	51
2.6 Calibration procedure	57
2.7 Activity concentration determination.....	58
2.8 Emission probability determination	60
2.9 Uncertainty evaluation	61
2.10 Determination of characteristic limits	68
2.11 Power moderate mean	69
Chapter 3 Reference Materials	73
3.1 Preliminary evaluation of the candidate reference materials	74
3.1.1 Sample preparations	74
3.1.2 Chemical characterization	81
3.1.3 Homogeneity measurements	84
3.1.4 INMRI activity measurements	87
3.1.5 Partner activity measurement	102
3.2 Final evaluation of the Ionex resin Certified Reference Material	104
3.2.1 Certified Reference Material preparation.....	104
3.2.2 Homogeneity measurement.....	106
3.2.3 INMRI activity measurement.....	108
3.2.4 Certified Reference Material activity characterization	111
3.3 Development and validation of a reference activity measurement method	116
Chapter 4 Determination of nuclear data.....	121
4.1 International contest of nuclear data	121
4.2 Actual nuclear data available	123
4.3 Source preparation for nuclear data measurement	132
4.4 Emission intensity measurement at INMRI	134
4.5 Emission intensity measurements from the international partners.....	139
4.6 Final measurements of the emission intensities	146
Conclusion	163

Appendix167

Bibliography179

List of figures

Figure 1.1. The activity is shown to decay exponentially with respect to time [9].	4
Figure 1.2. Schematic view of α -decay mechanism [9].	5
Figure 1.3. Schematic view of the Geiger-Nuttall rule, where the α -emitters with larger disintegration energies generally have short half-lives than those with smaller Q_α -values [12].	6
Figure 1.4. β^- -energy spectrum from the decay of ^{210}Bi [28].	7
Figure 1.5. Schematic scheme of ^{137}Cs decay, showing two different decay modes [28].	8
Figure 1.6. An example of secular equilibrium is shown. The parent ^{230}Th ($t_{1/2} = 7.538 \times 10^5 \text{ y}$) and its daughter ^{226}Ra ($t_{1/2} = 1600 \text{ y}$) decay to reach the point where their activity are equal [9].	12
Figure 1.7. Decay scheme of ^{40}K following the 10.72% decay branch of ^{40}K which undergoes decay by EC to stable ^{40}Ar and emits a characteristic photon with an energy of 1461 keV [28].	16
Figure 1.8. Schematic view of the ^{238}U decay chain and its decay products [72].	17
Figure 1.9. Schematic view of the ^{232}Th decay chain and its decay products [72].	17
Figure 1.10. Schematic view of the ^{235}U decay chain and its decay products [72].	17
Figure 2.1. Scanning Electron Microscope.	22
Figure 2.2. Example of a typical X-ray spectrum.	24
Figure 2.3. Schematic view of a gamma-ray spectrometer [72].	25
Figure 2.4. A coaxial hyper-pure germanium (HPGe) detector set up used at INMRI.	26
Figure 2.5. Electronic instrumentation used in the current study.	26

Figure 2.6. INMRI point-source S1 used for the calibration of the ND apparatus.	37
Figure 2.7. The observed relationship between the published gamma-ray energies and their centroid channel number from the SP-308 source used for the energy calibration.	39
Figure 2.8. Gamma-ray spectrum of ^{152}Eu calibration source.	40
Figure 2.9. S8 container and H37 object (a). Dimension of S8H37 container [mm] (b).	42
Figure 2.10. Absolute full-energy peak efficiency as function of gamma-ray energy for the HPGe detector.	43
Figure 2.11. H30 spacer and S1 point-source geometry (a). Schematic view of H30 spacer (b). Characterization of the ND calibration apparatus (c).	44
Figure 2.12. Absolute full-energy peak efficiency as function of gamma-ray energy for the HPGe detector.	45
Figure 2.13. Schematic view of S47H0 (a). S47H0 container (b). Mold of S47H0 container used (c).	47
Figure 2.14. Geometrical characterization of the ^{235}U and ^{227}Ac sources.	48
Figure 2.15. Activity distribution of ^{235}U source.	49
Figure 2.16. Schematic view of the ND measurement apparatus.	49
Figure 2.17. GM40-80-5 characterization provide from Ortec.	51
Figure 2.18. Spectrum of a ^{133}Ba point source measured on the end cap of the p-type detector [54].	55
Figure 2.19. The first part of the spectrum of the ^{133}Ba source measured on the detector end cap (dashed line) and at 15 cm distance (full line) with the p-type detector. The spectra were normalized to give equal number of counts in the 356 keV peak [54].	56
Figure 2.20. Same spectra as in Figure 2.19 for the energy range 250–500 keV [54].	57
Figure 2.21. Diagram of possible uncertainties possibly arising in the determination of activity concentration of ^{235}U , ^{238}U and ^{232}Th using gamma spectroscopy.	62
Figure 2.22: Interpretation of a PomPlot [70].	71
Figure 3.1. A Tuff brick.	75
Figure 3.2. Grinder used in the Tuff preparation.	76
Figure 3.3. Oven used to dry the Tuff sample.	76
Figure 3.4. Device used to sift the Tuff powder.	77

Figure 3.5. Ionex before (right side) and after (left side) regeneration.	78
Figure 3.6. The process of water purification in waterworks.	78
Figure 3.7. Titanium Oxide material after it is dried in microwave oven.	79
Figure 3.8. Inversina 2 L mixer used to homogenized the powder.	80
Figure 3.9. Titanium Oxide material in 50 grams Azlon bottles.	80
Figure 3.10. Backscattered electron image of Tuff sample (volcanic ash) (a) and its EDX spectrum (b).	81
Figure 3.11. Backscattered electron image of Ionex resin sample.	83
Figure 3.12. Backscattered electron image of TiO ₂ sample (a) and its EDX spectrum (b).	84
Figure 3.13. Tuff sample used for homogeneity evaluation.	85
Figure 3.14. Seven identical containers filled with the same amount of Ionex resin.	86
Figure 3.15. CS correction factor in the Tuff sample.	89
Figure 3.16. Calibration curve of the MR calibration apparatus (blue) and calibration curve of the measurement apparatus (red).	89
Figure 3.17. Difference in percentage between the efficiency of the MR calibration apparatus versus the efficiency of the measurement apparatus.	90
Figure 3.18. Tuff gamma-ray spectrum.	91
Figure 3.19. CS correction factor in the TiO ₂ sample.	96
Figure 3.20. Calibration curve MR calibration apparatus (blue) and calibration curve of the measurement apparatus (red).	96
Figure 3.21. Difference in percentage between the efficiency of the reference apparatus versus the efficiency of the Actual apparatus.	97
Figure 3.22. Ionex resin gamma-ray spectrum.	98
Figure 3.23. CS correction factor in the TiO ₂ sample.	100
Figure 3.24. Calibration curve MR calibration apparatus (blue) and calibration curve of the measurement apparatus.	100
Figure 3.25. Difference in percentage between the efficiency of the MR calibration apparatus versus the efficiency of the measurement apparatus.	101
Figure 3.26. TiO ₂ gamma-ray spectrum.	102

Figure 3.27. Schematic view of the metallic container and its lid filled with Ionex resin.	105
Figure 3.28. The metallic container with Ionex resin sample inside.	105
Figure 3.29. The CMR Ionex resin filled in the seven identical containers.	106
Figure 3.30. MR apparatus calibration curve (blue) and measurement (metal container) apparatus calibration curve (red).	109
Figure 3.31. Difference in percentage between the efficiency of the MR calibration apparatus versus the efficiency of the measurement (metal container) apparatus.	109
Figure 3.32. Ionex resin metal container gamma-ray spectrum.	110
Figure 3.33. Ionex resin ^{235}U Activity concentration results.	112
Figure 3.34. PomPlot of the activity concentration of ^{235}U in Ionex resin. Green, blue, and red solid lines indicate ζ -scores = 1, 2 and 3, respectively.	113
Figure 3.35. Ionex resin ^{238}U Activity concentration results.	114
Figure 3.36. PomPlot of the activity concentration of ^{238}U in Ionex resin. Green, blue, and red solid lines indicate ζ -scores = 1, 2 and 3, respectively.	115
Figure 3.37. Comparison of the standardization result of the activity concentration of ^{238}U in Ionex resin. The power-moderated mean and the corresponding uncertainty are represented by the lines.	118
Figure 3.38. PomPlot of the activity concentration of ^{238}U in Ionex resin. Green, blue, and red solid lines indicate ζ -scores = 1, 2 and 3, respectively.	118
Figure 3.39. Comparison of the standardization result of the activity concentration of ^{235}U in Ionex resin. The power-moderated mean and the corresponding uncertainty are represented by the lines. The purple point is rejected from the calculation.	119
Figure 3.40. PomPlot of the activity concentration of ^{235}U in Ionex resin. Green, blue, and red solid lines indicate ζ -scores = 1, 2 and 3, respectively.	119
Figure 4.1. ^{235}U source provided by JRC.	133
Figure 4.2. Calibration curve of the DN calibration apparatus (blue) and calibration curve of the DN measurement apparatus (red).	135
Figure 4.3. Difference in percentage between the efficiency of the DN calibration apparatus versus the efficiency of the DN measurement apparatus.	135
Figure 4.4. Calibration curve DN calibration apparatus (blue) and calibration curve of the DN measurement apparatus (red).	137

Figure 4.5. Difference in percentage between the efficiency of the DN calibration apparatus versus the efficiency of the DN measurement apparatus.	137
Figure 4.6. Measured gamma-intensities represented as black points. Black line present the PMM and the red lines present the PPMM uncertainty.	147
Figure 4.7. Measured gamma-intensities represented as rectangular black points for $^{227}\text{Ac} \rightarrow ^{223}\text{Ra}$. Red lines present the uncertainty on the PMM (black line).	151
Figure 4.8. Measured gamma-intensities for $^{223}\text{Ra} \rightarrow ^{219}\text{Rn}$ represented as rectangular black points. Red lines present the uncertainty on the PMM (black line).	153
Figure 4.9. Measured gamma-intensities for $^{219}\text{Rn} \rightarrow ^{215}\text{Pb}$ represented as rectangular black points. Red lines present the uncertainty on the PMM (black line).	153
Figure 4.10. Measured gamma-intensities for $^{211}\text{Pb} \rightarrow ^{207}\text{Pb}$ represented as rectangular black points. Red lines present the uncertainty on the PMM (black line).	154

List of tables

Table 1.1. Cosmogenic radionuclides of natural origin [73].	13
Table 1.2. Primordial singly occurring radionuclides are reported [73].	14
Table 2.1. The specification of the INMRI Ortec Germanium detector and the electronic operating system.	27
Table 2.2. INMRI source used for the calibration of the RM apparatus.	29
Table 2.3. INMRI point-sources used for the calibration of the ND apparatus.	33
Table 2.4. Main gamma-ray lines of the ^{152}Eu point source called SP-308.	37
Table 2.5. Chemical composition of the glass used for the source preparation.	48
Table 2.6. Technical specifications of Ortec detector.	50
Table 3.1. Approximate composition of Tuff sample.	82
Table 3.2. Approximate composition of Ionex resin sample.	83
Table 3.3. Approximate composition of TiO_2 sample.	84
Table 3.4. The data collected in the table represents the Tuff homogeneity measurement.	85
Table 3.5. The data collected in the table represents the Ionex resin homogeneity measurement.	86
Table 3.6. The data collected in the table represents the TiO_2 homogeneity evaluation.	87
Table 3.7. ^{235}U gamma emission energy [73].	91
Table 3.8. ^{234}Th gamma emission energy [73].	92
Table 3.9. ^{234}Th gamma emission energy [73].	92
Table 3.10. ^{212}Bi gamma emission energy [73].	93

Table 3.11. ^{208}Tl gamma emission energy [73].	94
Table 3.12. Results of Tuff sample by gamma- ray spectrometry.	94
Table 3.13. ^{234}Th gamma emission energy [73].	98
Table 3.14. Results of Ionex resin sample by gamma- ray spectrometry.	99
Table 3.15. Results of TiO_2 sample by gamma- ray spectrometry.	102
Table 3.16. Results for assessment of Tuff by gamma-spectrometry.	103
Table 3.17. Results for assessment of Ionex resin by gamma-spectrometry.	103
Table 3.18. Results for assessment of TiO_2 by gamma-spectrometry.	103
Table 3.19. Elemental composition of the Ionex resin.	104
Table 3.20. Elemental composition of the CMI metallic container provided by the aluminium producer.	106
Table 3.21. ENEA homogeneity measurement results.	107
Table 3.22. CMI homogeneity measurement results.	107
Table 3.23. JRC homogeneity measurement results.	108
Table 3.24. Results of Ionex resin sample by gamma- ray spectrometry.	110
Table 3.25. Laboratory results for ^{235}U and ^{238}U of the Ionex CMR.	111
Table 3.26. Significant value carried out from the PMM reference value evaluation for the ^{235}U activity concentration of the Ionex resin sample.	113
Table 3.27. Activity concertation reference value of ^{235}U .	114
Table 3.28. Significant value carried out from the PMM reference value evaluation for the ^{235}U activity concentration of the Ionex resin sample	115
Table 3.29. Activity concertation reference value of ^{238}U .	116
Table 3.30. Planning of the shipment of the Ionex resin sample.	117
Table 3.31. Laboratory number and associated name used for the two comparisons presented in Figure 3.37 and Figure 3.39.	120
Table 4.1. Emission probability of ^{235}U [73].	123
Table 4.2. Emission probability of ^{227}Th [76].	125

Table 4.3. Emission probability of ^{223}Ra [73].	128
Table 4.4. Emission probability of ^{211}Pb [73].	130
Table 4.5. Emission probability of ^{207}Tl [73].	131
Table 4.6. Standardized activities of ^{235}U sources ($k=1$) at 24/07/2009 09:30:00 measured at JRC.	133
Table 4.7. Standardized activities of ^{227}Ac sources ($k=1$) at 24/07/2009 09:30:00 measured at JRC.	134
Table 4.8. Results of P_γ evaluated at ENEA INMRI through ^{235}U source.	136
Table 4.9. Results of P_γ measured at ENEA INMRI through ^{227}Ac source.	138
Table 4.10. Information on the partners measurement conditions.	139
Table 4.11. Measured ^{235}U P_γ emission probabilities.	140
Table 4.12. Measured ^{235}U P_γ emission probabilities.	141
Table 4.13. New gamma emission probabilities derived from this work.	148
Table 4.14. New gamma emission probabilities derived from this work.	155

Introduction

Naturally Occurring Radionuclides are present in many natural resources. Industrial activities that exploit these resources may lead to enhanced potential for exposure to Naturally Occurring Radioactive Materials (NORM) in products, by products, residues and wastes.

Several Industry sectors are focused on the measurement of ionizing radiation originating from artificial radionuclides and Naturally Occurring Radionuclides are often taken as part of the natural background, regardless of their concentrations. NORM industries produce large amounts of waste and when such materials are being handled or processed, it is clearly necessary to determine the amount of nuclides present and their activity concentrations as accurately as possible.

This creates the need to develop methods to enable accurate and reproducible measurement of the natural radionuclides.

The gamma-ray spectrometry technique is the most commonly employed technique to determine the radionuclides present in a sample and their respective activity concentrations. The accuracy of the results directly depends on the accuracy of the calibration of the spectrometer and intensities of gamma-ray emitted during the decay.

The aim of this thesis is to develop one Certified Reference Material (CRM) representative of one of the most prevalent NORM cycle production in Europe and to improve the emission intensities of ^{235}U natural series to improve the precision and the accuracy of the activity measurement.

This work has been carried out in the framework of a collaboration between eleven European Metrological Institutes under coordination of BEV¹. The Italian institution involved in the project is ENEA², INMRI³, located in the Casaccia Research Center and it is where this thesis has been developed.

This study is part of The European Research Project MetroNORM “Metrology for Processing Materials with High Natural Radioactivity”, contract identifier JRP IND57.

¹ The Bundesamt für Eich- und Vermessungswesen (Federal Office of Metrology and Surveying), Austria.

² Italian National Agency for New Technologies, Energy and Sustainable Economic Development.

³ The National Institute of Ionising Radiation Metrology.

This thesis is divided as follow:

- In **Chapter 1** the worker and population risk following exposure to NORM materials are presented in detail. With the aim to explain the difficulties encountered in the activity measurement of this kind of materials. The different ways of radioactivity decay are investigate and the main aims of MetroNORM project are also described.
- In **Chapter 2** the methods used in this work are presented. We will describe the experimental apparatus used to measure the quantities of interest and in particular, we will pay the spectrometer calibration used to make accurate measurements of the activity of the samples.
- From a metrological point of view reference materials are fundamental tools to obtain reproducible and accurate measurements. They are widely used for the calibration of measuring instruments as gamma-ray spectrometer. At the present moment, suitable calibration reference materials for laboratory measurement of natural radionuclide are not available. In **Chapter 3** the first part of the experimental work is shown. The preliminary characterization of the three candidate reference materials are analyzed from different point of view: first of all the preparation of the materials is described, than the chemical composition and the homogeneity measurement of the material are explained, and at the end the radiological characterization of the materials is presented. In the last section of this character for the material chosen to became a CMR the procedure of certification is explained.
- In the first part of **Chapter 4** the measurement of gamma emission intensities in the upper part of the decay of ^{235}U ($^{235}\text{U} - ^{231}\text{Pa}$) series is explained. The determination of the activity of a ^{235}U source with absolute method permits to measure the emission intensity through gamma-ray spectrometry. In the second part of the chapter the lower part of the chain ($^{227}\text{Ac} - ^{207}\text{Pb}$) is investigated. In fact this part of the decay chain exhibit serious inconsistence with a large number of various emission only approximately known. The accurate activity measurement of ^{235}U and ^{227}Ac sources are presented and more precise emission probability are proposed.

Chapter 1

NORM and MetroNORM project

1.1 Ionizing radiation and radioactivity

Ionizing radiation occurs from the phenomenon of radioactivity: a nucleus from a radiative atom is unstable due to an oversupply of energy in the form of neutrons or protons surplus. The excess of energy is released under the form of particles. Every radioactive decay releases energy under the form of ionizing radiation [1] [2] [3].

We shall first distinguish between directly and indirectly ionizing radiation. Alpha and beta particles are directly ionizing radiation and this is only possible with charged particles. Photons or uncharged particles, like neutrons, are indirectly ionizing radiation. In this case ionization occurs after one or more energetic charged particles are formed. In fact, ionizing radiations can be energetic enough to push one or more electron out of the atom. This characteristic of the radiation is exploited for detection. All the ionizing radiation can cause biological effect by damaging the DNA in the cell nucleus [3] [4].

The Becquerel [Bq] is the SI (International System) unit for activity of a radioactive compound and gives the amount of disintegration per second [s^{-1}] and its name comes from the discoverer Henry Becquerel [5].

1.2 The radioactive decay law

Radioactive atoms decay according to a random process. The probability of a nucleus to decay in a time interval is independent of time. It was noted, three years after the discovery of radioactivity (1896), that the decay rate of a pure radioactive substance decreases in time according to an exponential law, called the Radioactivity Decay Law [6]. This law predicts how many radioactive nuclei are present at the time t in a certain substance and it decreases with time. The number of decaying nuclei dN in a given time interval dt is proportional to N , leading to the relation:

$$\lambda = -\frac{(dN/dt)}{N} \quad (1.1)$$

where λ is the decay (disintegration) constant which equals the probability per unit time for the decay of an atom (the right side of Equation (1.1)) and N is the number of nuclei present at time t . The exponential law of radioactive decay shown below is the solution of the differential Equation (1.2):

$$N(t) = N_0 e^{-\lambda t} \quad (1.2)$$

where N_0 represents the number of nuclei present at $t = 0$.

The half-life is the time in which half of the original nuclei decay, denoted by $t_{1/2}$. Using $N = N_0/2$, it follows that:

$$t_{1/2} = \frac{\ln 2}{\lambda} = \frac{0.693}{\lambda} = \tau_0 \ln 2 \quad (1.3)$$

where the mean lifetime is defined as the average time that a nucleus survives before decaying, being equal to $1/\lambda$ [6]. The activity A is defined as the rate at which decays occur in a sample and can be obtained by differentiating Equation (1.2), if the time interval dt over which the decay takes place is much smaller than λ^{-1} ($t_{1/2}$):

$$A = \left| \frac{dN}{dt} \right| = \lambda N_0 e^{-\lambda t} \quad (1.4)$$

$$A(t) = \lambda N(t) = A_0 e^{-\lambda t} \quad (1.5)$$

where $A_0 = \lambda N_0$, is the initial activity at $t = 0$.

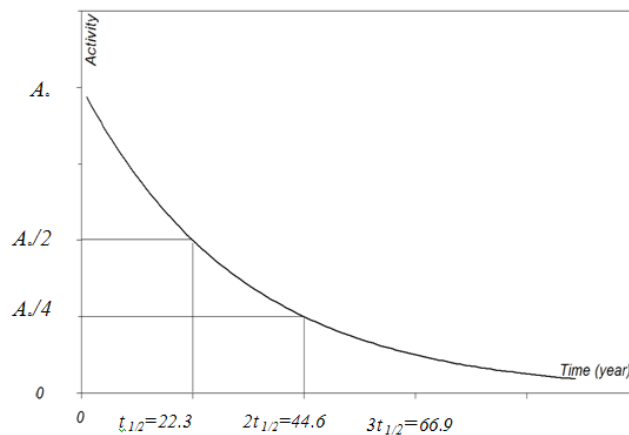


Figure 1.1. The activity is shown to decay exponentially with respect to time [9].

1.3 Types of decays

It is common terminology to call an unstable radioactive nucleus the parent and the more stable product nucleus daughter. In many cases, the daughter is also radioactive and undergoes further radioactive decay. Radioactive decay is spontaneous in the exact moment at which a given nucleus decay cannot be predicted, nor is it affected to any significant extent by events occurring outside the nucleus. Radioactive decay results in a conversion of mass into energy.

Radioactive decay is a process in which an unstable nucleus transforms into a more stable one by emitting particles and/or photons, with a consequent release of energy in the process. There are three primary decay types namely, α , β and γ decays [38].

Alpha decay

α -particles were first discovered by Ernest Rutherford in 1899, while he was running experiments with uranium [8]. In 1909 Rutherford showed that the α -particles are nuclei of helium, and consist of two protons and two neutrons [8]. Alpha emitting radionuclides can be natural or anthropogenic.

Alpha emission is a Coulomb repulsion effect which occurs predominantly in nature in heavy nuclei with a nuclear size $A \geq 210$. The repulsive Coulomb force between the nuclear protons increases with the nuclear size at a faster rate than the nuclear binding force [10]. α -particle emission decreases the Coulomb energy and increases the stability of heavy nuclei [6] [11]. α -particles exist within the potential well which is created by the daughter nucleus [9] (Figure 1.2). Before the emission, the α -particle is considered to be confined within the potential well. The probability that the α -particle reaches the surface and tunnels through the Coulomb barrier in order to be emitted is finite. Once the α -particle has penetrated the Coulomb barrier, it is repelled away and escapes from the daughter nucleus [9].

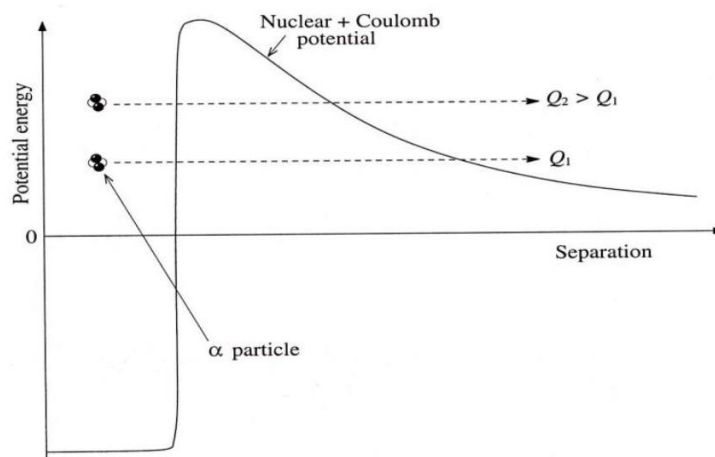


Figure 1.2. Schematic view of α -decay mechanism [9].

An α -decay occurs only if $Q > 0$ (Q is the amount of energy released by the reaction and it is the difference in masses between the parent and the daughter nuclei) [6], it is an exothermic reaction, where the energy of the nuclear reaction is released as a positive kinetic energy through the Q_α -value of this reaction. If Q_α is negative, it is not possible for the α -particle to tunnel through the barrier and escape [6]. The probability of escape from the nucleus is dependent on the Q -value. The following equation describes the energy conservation in α -emission [6] [9] [10]:

$$m_x c^2 = m_{x'} c^2 + T_{x'} + m_\alpha c^2 + T_\alpha \quad (1.6)$$

$$(m_x - m_{x'} - m_\alpha) c^2 = T_{x'} + T_\alpha \quad (1.7)$$

where T is the kinetic energy and m is the mass. The decay is possible only if the left hand side of Equation 1.7 has a positive value. In this case, the initial mass energy is greater than the final mass energy and Q_α -value is the difference in masses [6]. The Q -value typically ranges between 4 and 10 MeV of energy for NORM α -emitters. The inverse relationship between α -decay half-life [10] and the decay energy Q -value is called the Geiger-Nuttall rule, where the α -emitters with large disintegration energies have short-lives [10] (Figure 1.3).

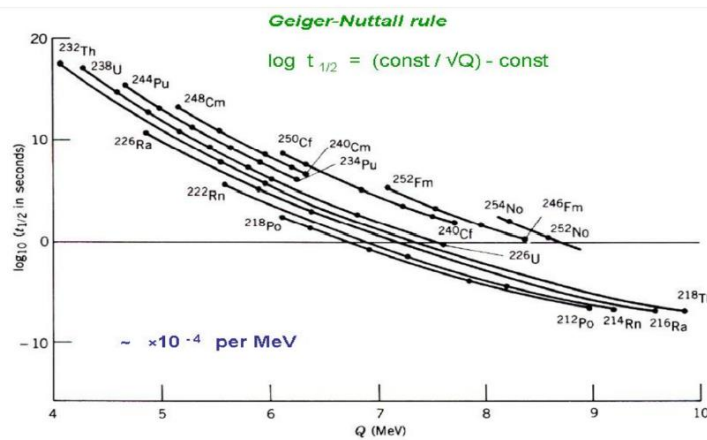


Figure 1.3. Schematic view of the Geiger-Nuttall rule, where the α -emitters with larger disintegration energies generally have short half-lives than those with smaller Q_α -values [12].

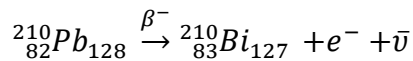
Beta decay

β -particles were discovered by Henri Becquerel in 1900 [13]. In the β -decay, both the atomic number (Z) and neutron number (N) of a nucleus change by one unit, but the total mass number, $A=N+Z$, remains constant [6]. Therefore, β -decay provides a convenient decay mode for an unstable nucleus to increment down a mass parabola of constant A to approach the stable isobar [6]. There are three processes by which nuclei may undergo radioactive

β -decay: β^- -decay, β^+ -decay and electron capture. A β -particle is much lighter than an α -particle which means that for a given energy, β -particles are much more penetrating [11].

Negative beta decay

The first process we hereby describe is the negative beta or β^- -decay. It can occur only if the daughter nucleus is more energetically stable than the parent nucleus: a neutron directly converts to a proton, electron and an anti-neutrino [10]. The formed proton remains in the nucleus and the electron is ejected as a β -particle. This process occurs when the ratio of neutrons to protons is larger than the stable ratio for that particular isobaric chain. This process leads to a decrease in the number of neutrons by one and to an increase in the number of protons by one [6]. The following example represents a β^- -decay process:



β -particles have a continuous distribution of energy, from 0 to an upper limit which is called the endpoint. This point is equal to the difference in energy between the initial and final states in the parent and daughter nucleus, respectively [6]. Since β -decay is a three body process (in contrast to α -decay which is a two-body process), in which the kinetic energy is shared between the β -particle and the antineutrino [6], emitted β^- -particles have a continuous distribution of kinetic energy, ranging from 0 to the maximum allowed by the Q_{β^-} -value (the beta “end point” energy). A continuous distribution of energy from 0 up to 1.16 MeV from β -particles emitted from ${}^{210}\text{Bi}$ [14] is shown in Figure 1.4.

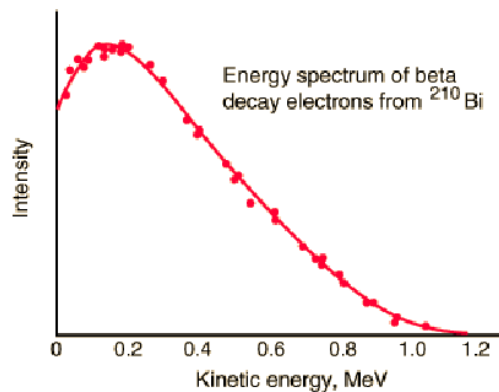


Figure 1.4. β -energy spectrum from the decay of ${}^{210}\text{Bi}$ [28].

In the β -decay, the Q -value can be defined as the difference between the initial and final nuclear mass energies [6]:

$$Q_{\beta^-} = [m(X^A) - m(X^{A'})]c^2 \quad (1.8)$$

where the masses are neutral atomic masses. The Q -value represents the energy shared by the electron and the neutrino:

$$Q_{\beta^-} = T_e + E_{\bar{\nu}} \quad (1.9)$$

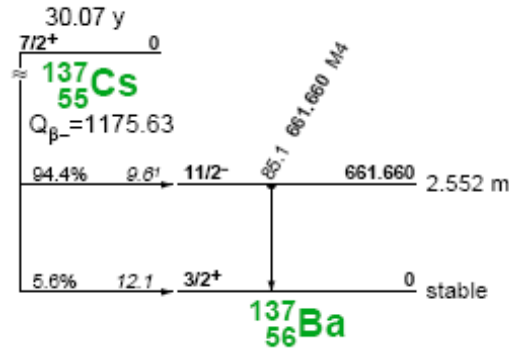
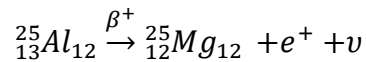


Figure 1.5. Schematic scheme of ^{137}Cs decay, showing two different decay modes [28].

Positive beta decay

The second weak interaction decay process is positive, β^+ -decay or “positron decay”. It occurs when the ratio of protons to neutrons is higher than the most stable isobar of that particular A chain (i.e. for “proton-rich” nuclei [11]). In this process, a proton is transformed into a neutron, a positron and a neutrino. As a result, the nuclear charge is decreased by one unit. As in β^- -decay, this decay is a three-body process and positrons are emitted with a continuous range of energies [14]. The following example represents a β^+ -decay process:



The Q -value must be greater than 0 for this process to occur [9]. The Q -value of β^+ -decay is given by [6]:

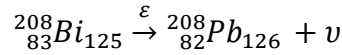
$$Q_{\beta^+} = [m(X^A) - m(X^{A'})]c^2 \quad (1.10)$$

Electron capture

In the electron capture (EC) process, an atomic electron orbiting close to the nucleus is captured. The electron combines with a proton and forms a neutron [6] with the emission of a

neutrino with a fixed energy. It is an alternative decay process to β^+ -decay and the proton is converted into a neutron. The parent nucleus absorbs an electron from the innermost orbit.

In EC, the mass of an atomic electron is converted into energy: differently from the β^+ -decay, fraction of the mass-energy is required to create a positron. This means that energy constraints on the occurring decay exist: for some particular isobaric cases, EC can occur while β^+ -decay cannot [9]. Since no particle is emitted in EC, the energy released escapes undetected. The following process is an example of EC:



Conservation of mass-energy defines the $Q_{\varepsilon c}$ -value as follow [6]:

$$Q_{\varepsilon c} = [m(X^A) - m(X^{A'})]c^2 - B_n \quad (1.11)$$

where B_n is the binding energy of the captured n-shell electron.

Gamma decay

Gamma-rays have energies typically in the range of 0.1 up to 10 MeV [6]. Gamma-ray photons originate from the nucleus, differently from alpha or β -particles. Gamma-ray photons have no mass and no charge. It is a quantum of electromagnetic energy that travels at the speed of light and can travel up to hundreds of meters in air before being attenuated [15]. Alpha and/or beta decays can often leave the daughter nucleus in an excited state, which may then de-excited in gamma-ray decays. This situation will lead the nucleus to emit one or more gamma-rays, characteristic to the energy difference between the intrinsic states of the nucleus [16]. For instance when the natural occurring radionuclide ${}^{226}\text{Rn}$ undergoes α -decay, ${}^{222}\text{Rn}$ is produced. This decay is often accompanied by a gamma-decay with a fixed energy of 186.21 keV.

There is another electromagnetic process that competes with gamma-decay called internal conversion. In this process, the excess of energy does not result in the emission of a photon but instead the electromagnetic multipole fields interact with the orbital electrons, leading to the ejection of one of the existing electrons from the atom. The amount of energy given to the bound, orbital electron must exceed its binding energy for this process to occur. This is a different process with respect to β^- -decay, in which the emitted electron is created in the decay process itself [6]. The tendency of this process can empirically be determined by the internal conversion coefficient which is defined by the Equation (1.12):

$$\alpha_{ic} = \frac{I_{ic}}{I_\gamma} \quad (1.12)$$

where α_{ic} is the internal conversion coefficient, I_{ic} is the intensity of de-excitation through the emission of conversion electron and I_γ is the intensity of the de-excited one through the competing gamma-ray emission branch only.

1.4 Radioactive decay

In nature, radionuclides are divided into three main radioactive decay series (i.e. headed by $^{235,8}\text{U}$ and ^{232}Th) which are still present on Earth in significant numbers, representing approximate states of the radiation equilibrium [6]. Radioactive equilibrium occurs in three general modes. The most common case is that of *secular equilibrium*, where the activities ($A_i = \lambda_i N_i$) of all radionuclides within each series are approximately equal.

Assuming that there are N_0 parent atoms at time $t=0$ with no other decay products present at $t=0$, then:

$$N_1(t = 0) = N_0 \quad (1.13)$$

$$N_2(t = 0) = N_3(t = 0) = \dots = 0 \quad (1.14)$$

The number of parent nuclei decreases with time due to radioactive decay. The nuclide concentrations following radioactive decay of an n-nuclide series in linear chain are found using *Bateman* equation [17]. For the decay of a parent nucleus, which decays into a subsequently radioactively unstable daughter nucleus, we can write:

$$\frac{dN_1}{dt} = -\lambda_1 N_1 \quad (1.15)$$

$$\frac{dN_i}{dt} = -\lambda_{i-1} N_{i-1} - \lambda_i N_i \quad (1.16)$$

This assumes that the nucleus n is the radioactively-stable final end product of the decay chain, and the decay constant of the initial daughter, granddaughter, great granddaughter decays are represented by $\lambda_1, \lambda_2, \lambda_3$ etc. and λ_i is the decay constant of i^{th} nuclide. As a result of the parent decay, the number of atoms of daughter nuclei increases, but due to its own decay this number also decreases with time, i.e.:

$$dN_2 = \lambda_1 N_1 dt - \lambda_2 N_2 dt \quad (1.17)$$

By integrating Equation (1.15) and Equation (1.17) and using the initial condition $N_2(0)=0$ the following results are obtained:

$$N_1(t) = N_0 e^{-\lambda t} \quad (1.18)$$

$$N_2(t) = N_0 \frac{\lambda_1}{\lambda_2 - \lambda_1} (e^{\lambda_1 t} - e^{\lambda_2 t}). \quad (1.19)$$

Then, the activity of the daughter nucleus can be expressed as:

$$A_2(t) \equiv \lambda_2 N_2(t) = N_0 \frac{\lambda_1 \lambda_2}{\lambda_2 - \lambda_1} (e^{\lambda_1 t} - e^{\lambda_2 t}) \quad (1.20)$$

Assuming zero concentrations of all daughters at time zero:

$$N_1(0) \neq 0 \text{ and } N_i(0) = 0 \text{ when } i > 1 \quad (1.21)$$

The concentration of n^{th} nuclide after time t was given by Bateman [17]:

$$N_n(t) = \frac{N_1(0)}{\lambda_n} \sum_{i=1}^n \lambda_i \alpha_i \exp[-\lambda_i t] \quad (1.22)$$

When α is a decay coefficient and α_i can be determined from the following equation:

$$\alpha_i = \prod_{j=1}^n \frac{\lambda_j}{(\lambda_j - \lambda_i)} \quad (1.23)$$

1.4.1 Secular equilibrium

If a system is closed for a time period significantly larger than the half-life of the daughter nuclide, the system will approach secular equilibrium, i.e. the activities (rates of decay) of the parent and the daughter will tend to equality.

Under secular equilibrium, the parent undergoes a very slow rate of decay with no appreciable change in its activity during many half-life of its decay products, while its daughter grow-in and then decay. Daughter nuclei can reach their parent activity in a closed system [18]. The concentration of the various daughter radionuclides that accompany the parents can be estimated using secular equilibrium for naturally occurring ones, i.e. ^{238}U with its six daughter to radium ^{226}Ra [19]. There are two conditions that are important to achieve this kind of equilibrium:

1. The parent radionuclide must have a half-life longer than it's progenies (e.g. ^{238}U , $t_{1/2} = 4.468 \times 10^9$ y).
2. A long period of time has to be taken into account, for instance five half-life of decay product having the longest half-life, to allow the in-growth of the decay products [18].

If half-life of the parent nucleus is much longer than the half-life of the daughter, (i.e. $\lambda_1 \ll \lambda_2$) the decay products emit radiation more quickly and the parents decay at an

essentially constant rate, for all practical times $e^{\lambda_1 t} \approx 1$. By substituting into Equation (1.19) we find:

$$N_2(t) \approx \frac{\lambda_1}{\lambda_2} (1 - e^{-\lambda_2 t}) \quad (1.24)$$

This is an example in which the daughter and the parent nuclei are decaying at the same rate $\lambda_2 N_2 = \lambda_1 N_1$, and as a result $A_2/A_1 \cong 1$ [6]. An example of approximate secular equilibrium is shown in Figure 1.6.

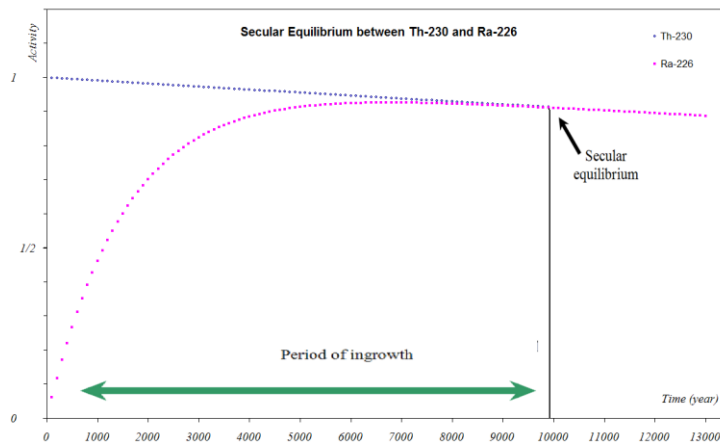


Figure 1.6. An example of secular equilibrium is shown. The parent ^{230}Th ($t_{1/2} = 7.538 \times 10^5 \text{ y}$) and its daughter ^{226}Ra ($t_{1/2} = 1600 \text{ y}$) decay to reach the point where their activity are equal [9].

For instance; the $^{230}\text{Th}/^{226}\text{Ra}$ ratio would be approximately 1 after 10000 years as shown in the Figure 1.6, which corresponds to approximately 6 times the half-life of ^{226}Ra . However sometimes, during geological processes, since Uranium decay chains are composed of different element, fraction can occur. This is known as radioactive disequilibrium [20]. Since Ra is generally more soluble than Th, it is usual to observe activity ratios ($^{226}\text{Ra}/^{230}\text{Th}$) of more than 1 in water and less than 1 in soils and sediment. This disequilibrium is time-dependent since it involves radioactive elements. Once a disequilibrium is produced, daughter-parent activity ratios will return towards secular equilibrium by radioactive decay over a timescale depending on the half-life of the daughter nucleus in the considered system [20].

1.5 Radioactivity in nature

Radioactive elements present in nature are divided into Cosmogenic and Terrestrial, depending on their origin.

Cosmogenic origin

Cosmic rays are composed mainly of high energetic, positively charged particles (mostly protons) and high energy photons [21]. The upper atmosphere protects the Earth and blocks most of the incoming cosmic rays however, a number of radionuclides are produced by the interaction of cosmic rays with Earth's upper atmosphere [22]. This nuclear interaction largely comes from secondary neutron capture and high-energy particle [23]. Spallation reactions are high energy interactions, typically with thresholds around 50 MeV , although in some cases the threshold can reach several hundreds of MeV [24]. Most of the cosmogenic radioactivity is produced from this process, when the bombardment reaction occurs between atoms in the atmosphere and cosmic rays [25]. Thermal neutrons (which are formed following initial cosmic rays spallation interactions) give rise to charge exchange and neutron capture reactions which are responsible for the production of ^{14}C by the (n,p) reaction on ^{14}N and ^{81}Kr following the (n,γ) reaction on ^{80}Kr respectively. The light radionuclide, ^7Be is also produced in the atmosphere following spallation on C, N and O nuclei. It is estimated that the 70% of the radioactive ^7Be is produced in the stratosphere, and 30% in the lower altitude troposphere.

A relatively small amount of radioactivity is also present in the environment from extraterrestrial dust and meteorites. Radioactive isotopes of Al, Be, Cl, I and Ne are formed following the spallation of extraterrestrial elements under cosmic ray bombardment. Earth is bombarded every year by approximately 10^7 kg of dust from the outer space which contains radioactivity at concentration of up to 27 Bq/kg , with a maximum limit of radioactivity from this source of $2.7 \times 10^8\text{ Bq}$, largely arising from nuclides such as ^7Be , ^{22}Na , ^{26}Al , ^{46}Sc , ^{48}V , ^{51}Cr , $^{53,54}\text{Mn}$, $^{56,57,58,60}\text{Co}$ and ^{59}Ni (Table 1.1). Other heavy radioactive elements such as thorium and uranium have also been detected in meteoritic materials [24] [26].

Table 1.1. Cosmogenic radionuclides of natural origin [73].

<i>Element</i>	<i>Nuclide</i>	<i>Half-life</i>	<i>Decade mode and gamma-line Energy [keV]</i>
Hydrogen	^3H	$12.3 \times 10^4\text{ y}$	β^- (100%)
Beryllium	^7Be	$5.33 \times 10^2\text{ d}$	EC (100%) and γ (477.612)
	^{10}Be	$1.51 \times 10^6\text{ y}$	β^- (100%)
Carbon	^{14}C	$5.73 \times 10^3\text{ y}$	β^- (100%)
Sodium	^{22}Na	$2.6 \times 10^0\text{ y}$	β^+ and γ (1279)
Aluminum	^{26}Al	$7.4 \times 10^5\text{ y}$	EC (100%)
Silicon	^{32}Si	$1.72 \times 10^2\text{ y}$	β^- (100%)
Phosphorus	^{32}P	$1.43 \times 10^1\text{ d}$	β^- (100%)
	^{33}P	$2.53 \times 10^1\text{ d}$	β^- (100%)

<i>Element</i>	<i>Nuclide</i>	<i>Half-life</i>	<i>Decade mode and gamma-line Energy [keV]</i>
Sulphur	³⁵ S	8.75 x 10 ¹ d	β ⁻ (100%)
Chlorine	³⁶ Cl	3.01 x 10 ⁵ y	EC (1.9%), β ⁻ (98.1%)
Argon	³⁷ Ar	3.50 x 10 ¹ d	EC (100%)
	³⁹ Ar	2.69 x 10 ² y	β ⁻ (100%)
Krypton	⁸¹ Kr	2.29 x 10 ⁵ y	EC (100%)

1.5.1 Terrestrial origin

Terrestrial radionuclides are common in the rocks, soil, water and ocean sand as well as in buildings materials [1]. These radionuclides were present when the planet Earth originated. Since some of these radionuclides have very long decay half-life (on the order of hundreds of millions of years or more), significant quantities of these radionuclides are still present on Earth today. These radionuclides can be categorized into two types:

- Singly Occurring Radionuclides.
- Decay chain [1].

Primordial Radionuclide

About 20 naturally occurring single primordial radionuclides have been identified so far. Most of them are radioactive nuclides with *half-life* > 10¹⁰ years and usually around 10¹⁵ years. The majority decay by beta emission, but some, such as ¹⁴⁷Sm and ¹⁵²Gd undergo (with a relatively low energy) *α-decay*.

Table 1.2. Primordial singly occurring radionuclides are reported [73].

<i>Radionuclide Parent</i>	<i>Decay product</i>	<i>Half-life [y]</i>	<i>Isotopic abundance [%]</i>	<i>Decay mode and Energy [keV]</i>	
⁴⁰ K	⁴⁰ Ac(EC) & ⁴⁰ Ca(β ⁻)	1.3 x 10 ⁹	0.010	Beta	1320
⁵⁰ V	⁵⁰ Ti(EC) & ⁵⁰ Cr(β ⁻)	6.0 x 10 ¹⁴	0.25	Beta	-
⁸⁷ Rb	⁸⁸ Sr(β ⁻)	4.7 x 10 ¹⁰	27.83	Beta	273
¹¹³ Cd	¹¹³ In(β ⁻)	9.0 x 10 ¹⁵	12.3	Beta	-

<i>Radionuclide Parent</i>	<i>Decay product</i>	<i>Half-life [y]</i>	<i>Isotopic abundance [%]</i>	<i>Decay mode and Energy [keV]</i>	
¹¹⁵ In	¹¹⁵ Sn(β^-)	5×10^{14}	95.70	Beta	490
¹²³ Te	¹²³ Sb(β^-)	1.2×10^{13}	0.87	EC	-
¹³⁸ La	¹³⁸ Ba(EC) & ¹³⁸ Ce(β^-)	1.1×10^{11}	0.09	Beta and Ec	270
¹⁴³ Ce	¹⁴³ Pr(β^-)	5×10^{16}	11.10	Alpha	1500
¹⁴⁴ Nd	¹⁴⁰ Ce(α)	2.1×10^{15}	23.90	Alpha	1830
¹⁴⁷ Sm	¹⁴³ Nd(α)	1.1×10^{11}	15.00	Alpha	2230
¹⁴⁸ Sm	¹⁴⁴ Nd(α)	8×10^{15}	11.20	Alpha	1950
¹⁴⁹ Sm	¹⁴⁵ Nd(α)	10^{16}	13.80	Alpha	< 2000
¹⁵² Gd	¹⁴⁸ Sm(α)	1.1×10^{14}	0.20	Alpha	2.14
¹⁵⁶ Dy	¹⁵⁷ Tb(α)	2×10^{14}	0.06	Alpha	3000
¹⁷⁶ Lu	¹⁷⁶ Yb(EC) & ¹⁷⁶ Hf(β^-)	2.7×10^{10}	2.60	Beta	570
¹⁷⁴ Hf		2×10^{15}	0.02	Alpha	2500
¹⁸⁰ Ta	¹⁸⁰ Hf(EC) & ⁴⁰ Ca(β^-)	1.6×10^{13}	0.01	Beta	-
¹⁸⁷ Re	¹⁸⁶ Os(β^-)	5×10^{10}	62.50	Beta	26
¹⁹⁰ Pt	¹⁸⁶ Os(α)	7×10^{11}	0.01	Alpha	3160
²⁰⁴ Pb	²⁰⁰ Hg	1.4×10^{17}	1.48	Alpha	2600

From Table 1.2, only two of the singly occurring primordial radionuclides are significant and important to be considered: ⁴⁰K and ⁸⁷Rb [1]. ⁴⁰K has a half-life at 1.277×10^9 y [27], an isotopic abundance of 0.0118% and a specific activity of 31.4 Bq/g of natural potassium. ⁴⁰K decay from β^- -decay to stable ⁴⁰Ca 89% of the time. The remaining 10.72% of ⁴⁰K undergoes decay by electron capture to stable ⁴⁰Ar. This latter decay branch also emits a characteristic gamma-ray at 1461 keV. This line is very useful to identify and quantify ⁴⁰K by gamma spectroscopy.

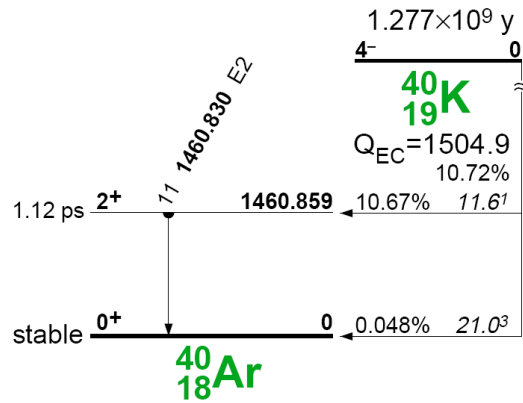


Figure 1.7. Decay scheme of ^{40}K following the 10.72% decay branch of ^{40}K which undergoes decay by EC to stable ^{40}Ar and emits a characteristic photon with an energy of 1461 keV [28].

Potassium is commonly distributed in Earth's crust. Its concentration is about 4% and its concentration in limestone is about 0.1% and may increase in some type of granite to about 4% [26] the mean activity concentration of ^{40}K found.

Decay chain

During the period of time from 10^{10} y ago until the condensation of the solar system, hydrogen and helium that resulted from the Big Bang almost 1.5×10^{10} y ago were fused into heavier elements into stellar interiors, nova and supernovae [10]. Earth was created from the recycled debris of these dead stars [6]. Most of these elements were initially radioactive. However, only a few of these radioactive elements have isotopes with long decay half-life compared to the age of the Earth, and the radioactive ones, which form the greatest fraction of our natural radiation, can still be observed. They can be categorized into three main decay series [29]. These are the natural decay chain headed by ^{238}U (4.5 billion years half-life), ^{232}Th (14.1 billion years half-life), and ^{235}U (700 million years half-life) respectively, as shown in Figure 1.8, Figure 1.9 and Figure 1.10. Each of them then decays through complex decay chains of alpha and beta decays and end at stable ^{206}Pb , ^{208}Pb and ^{207}Pb and nuclides respectively.

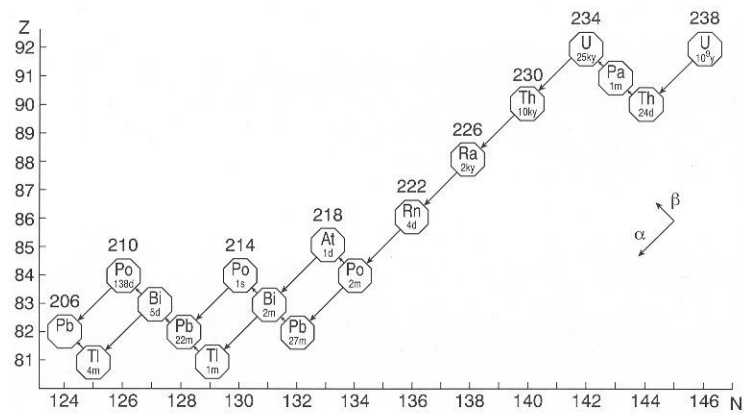


Figure 1.8. Schematic view of the ^{238}U decay chain and its decay products [72].

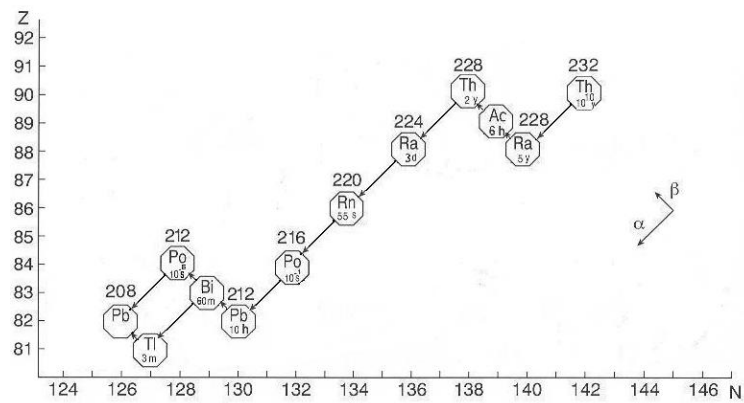


Figure 1.9. Schematic view of the ^{232}Th decay chain and its decay products [72].

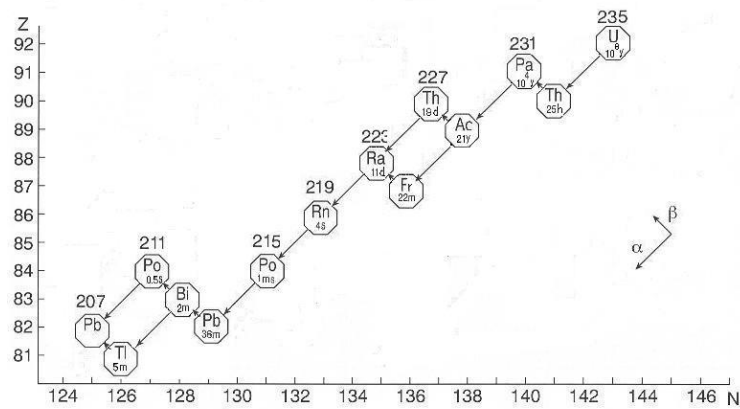


Figure 1.10. Schematic view of the ^{235}U decay chain and its decay products [72].

1.6 What is NORM

Radioactivity can be divided into artificial and natural. Artificial radionuclides are man-made, produced in a nuclear reactor or in a particle accelerator. A good example of artificial radioactivity is the nuclear waste produced in the production of electricity in a nuclear power plant and the radionuclides used in medical treatment.

Naturally Occurring Radioactive Material (NORM) indicates radioactive elements that can be found in the environment and in rocks that contain an increased level of radionuclides present in nature. Some of those radionuclides which are long-lived are present since the origin of Earth. There are three radioactive decay chains: Uranium series also called Radium series, Thorium series and Actinium series. Another important radionuclide is ^{40}K which is also present since the formation of Earth and thus is present in Earth's crust and it is also found in plants, human bones and animals. Those radionuclides are concentrated in some places, for example, uranium orebodies and phosphate ores. It is possible that radionuclides are accumulated in waste and by-product, via industrial processes. The level of NORM can vary from industry to industry. In common production processes NORM flows together with water, gas and oil mixtures and can build up in sludge, dust and waste materials [30] [31] [32] [33] [34].

Industries where NORM is mostly found are phosphate and metallurgic industries, zirconium sands, in the production of titanium oxides oil and gas industries and in buildings materials.

1.7 Hazards to human health and environment

Personnel working in industries that is in contact with NORM could have an increased risk to be exposed to NORM. This could originate from contamination where the worker has internal exposure due to ingestion and inhalation of radionuclides. For example, it is possible that the worker inhales dust and radon or ingests sludge. It is also possible that the worker is irradiated due to a source outside the body. Usually, the amount of gamma-radiation is not large enough to penetrate processing equipment and present a health risk for worker, but exceptions are found. The effect might vary with the time, depending on the total amount of energy that is absorbed and on which organ is exposed [35] [36].

When handling NORM contaminated products or waste, cautions have to be taken into account to prevent it to spread to nearby areas or to contaminate other product [34].

NORM are materials with high content of natural radioactivity. It is found in work activities as natural materials, or as a result from industrial processes. It is important to distinguish between this type of material, not used for the intrinsic radioactive properties, and the radioactive substances of natural origin which are used precisely for their radioactive properties. Italian legislation (Legislative Decree no. 230/95, as amended by Legislative Decree 241/00) regulates the exposure of workers and the population to work activities with the NORM. In particular, it identifies a set of activities with regulatory requirements:

- Industry using mineral phosphate and deposits for the fertilizers wholesale trade.
- Processing of minerals in the extraction of tin, iron-niobium and aluminum from bauxite.
- Processing of zircon sands and production of refractory materials.
- Processing of rare earth.
- Processing and use of thorium.
- Production of pigment from titanium dioxide.
- Material from oil and gas extraction.

The law provides an evaluation of the dose carried out for workers and members of the public. The action levels, expressed in terms of individual effective dose, it is equal to 1 mSv/year for workers and 0.3 mSv/year for members of the public.

For a proper evaluation of the dose of workers and the general public, a very accurate and precise measurement of the activity of natural radionuclides to which these individuals are exposed is needed. The use of CMRs for the calibration of the measuring instruments or validate activity measurement method or the accurate estimate of the probability of emission of radionuclides are essential for these purposes.

1.8 The MetroNORM project

This work of thesis fits in the project carried out with the European Metrology Research Program (EMRP) that is founded by the European Association of National Metrology Institutes (EURAMET). The EMRP allows European metrology institutes, industrial organizations and universities to collaborate on specific projects in several fields of research. The study performed in this thesis was included in “IND 57-MetroNORM, (Metrology for European NORM Industry)” where new measurement methods will be developed and adapted to the industry. For this project a collaboration between twelve countries of the European Union and the EC⁴-JRC⁵-IRMM⁶ has established. All of them have NORM or NORM industries in their countries [3].

Naturally occurring radionuclides are present in many natural resources. Industrial activities that exploit these resources may lead to enhanced potential for exposure to NORM in products, by-products, residues and wastes. Industries working with raw materials containing naturally occurring radioactive materials (NORM industries) produce large amounts of waste. These waste materials, generated from current and past activities, constitute a huge economic and ecological burden if they are not properly disposed of or re-used as input materials for the industry. The recycling and re-use of waste material support the use of “cleaner technologies”

⁴ European Community.

⁵ The European Commission’s Joint Research Center.

⁶ The Institute for Reference Materials and Measurement.

and result in cost savings. The radioactivity content of mineral feedstocks and process residues creates a need to control exposure to workers and members of the public in accordance with the IAEA Safety Standards: “In commercially exploited rare earths deposits, the level of thorium and uranium, depending on the type of mineral and its region of occurrence, generally exceed the worldwide median values for soil by up to 200 times of thorium and up to 30 times in the case of uranium”. When such minerals are being handled or processed, it is clearly necessary to determine the nuclides present and their activity concentrations as accurately as possible. Reference Materials will be needed to validate the radioanalytical procedures involved as well as methods for analysis and interpretation of the results.

1.9 Goal of the project

Within the JRP new methodologies will be developed for measurement of natural radionuclides, new CMR will be used for their calibration with traceability to national standards of partnering countries and nuclear data of natural radionuclides will be improved so that as many as possible descendants of uranium decay chain could be accurately measured. The expected results of this thesis are:

- CMR: development of a CMR traceable to national standards for natural radionuclides measurement adapted to the needs of the developed laboratory, adjusted to the typical composition of material and activity levels relevant for measured materials with total rel. uncertainties lower than 10%.
- A new validate activity concentration measurement method through gamma-ray spectrometry.
- Nuclear data improvement for ^{235}U series.

Chapter 2

Experimental methods

In this chapter we describe the operational principles and the setup of the devices adopted throughout this thesis. The experimental apparatus is composed of a scanning electron microscope coupled with an Energy Dispersive X-ray (EDX) Spectrometer for the chemical characterization of the samples and a gamma-ray spectrometer, used for the radiometric characterization.

2.1 Scanning electron microscopy

The scanning electron microscope is an instrument which allows to investigate the interaction between an electron beam, the probe, and the sample.

Through the Scanning Electron Microscope (SEM), it is possible to obtain morphological and structural information on the sample and, when coupled with an energy dispersion spectrometer, to obtain important chemical information.

The experimental apparatus is composed of three elements:

- An electronic column with an electron emitter on top (in this case a tungsten element) that generates the beam.
- A vacuum chamber where the samples are placed.
- A detection system connected to a computer for data processing.

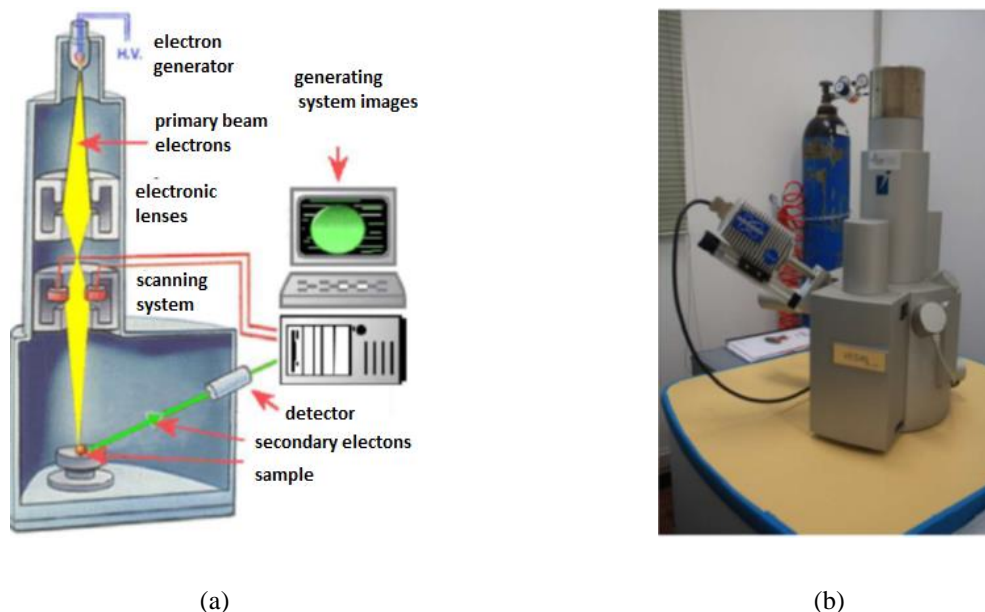


Figure 2.1. Scanning Electron Microscope.

The tungsten filament produces electrons by thermionic emission, and an electric field accelerates them in an energy range between $0.1 - 30 \text{ keV}$. The generated beam size is, however, too large to produce a sharp image. For this reason, an electronic lens system is placed inside the column, to focus the beam on the sample with an area of 10 nm . By changing this parameter (and the tube operational current) it is possible to have different magnifications and enlargements of the images. When the primary beam (that is generated by the tungsten filament) hits the sample, the movement along the Cartesian coordinates X, Y enables the scanning of a part of it, with the consequent image. Differently from an optical microscope, which provides a real image of the sample, the SEM, due to the electron beam scanning, returns a virtual image of the sample that comes from the signals emitted by the volume under investigation. The signal emitted from the exposure of the sample to the primary beam can be divided into two kinds, one formed by the secondary electrons and another one formed by the backscattered electrons:

- Secondary electrons are defined as those electrons whose energy is less than 50 keV . They originate from the interaction of the primary beam and the backscattered electrons with the valence electrons, the SE (Secondary Electrons) signal is formed by electrons belonging from the sample itself. They are expelled through inelastic processes from an extremely shallow and restricted region of the sample. The reason is that secondary electrons have a modest energy, so on their way to the surface they lose part of their energy from inelastic interaction and therefore only the closest electron to the "escape route" can escape from the sample surface. For this reason the secondary electrons detection provides morphological information.

- Backscattered electrons are electrons belonging to the primary beam that comes out from the sample as a result of elastic interaction. Their energy is close to the beam energy, and therefore higher than the secondary electrons energy. It can be concluded that BSE (BackScattered Electrons) origin region within the sample is bigger than the secondary electron region, with a consequent less accurate morphological location. The information provide from BSE signals is different from the topological information of the SE and it is related to the average atomic number of the interaction volume. The result of this signal is an image in which different shades of gray correspond to different Z numbers.

Microanalysis

The term microanalysis refers to the chemical investigation of a sample through the SEM scanning electron microscope. This investigation is carried out by measuring the energy and the intensity distribution of X-rays generated by the interaction of the electron beam with the sample, using an energy dispersive detector Energy Dispersive X-ray Spectrometer (EDS).

The EDS is a semiconductor detector and, to produce the signal, it exploits the photon electron-hole pair production in the semiconductor. The number of electron-hole pairs product in the detector is proportional to the incident photon energy. If each photon produces a certain number of charges within the device, these originate an induced charge at the electrodes. This variation of the electric charge produces a current flow in the device, that is proportional to the energy of the incident X-photon.

The signal is composed of the X-rays emitted from the sample due to interaction with the electron beam. This signal comes both from the surface and the deep layers of the sample.

An example of an EDX spectrum is shown in Figure 2.2. It can be observed that the spectrum is composed of two different signals: one continuous and two prominent peaks. The continuous curve of the background is due to bremsstrahlung, i.e. the braking radiation due to deceleration of the incident electrons within the material. Qualitatively, this emission is proportional to the atomic number of the target element, but the analysis of the continuous curve does not provide qualitative information about the sample composition. The important information comes from the sample characteristic X-ray that is on other type of signal. The signal formation takes place after the beam-shell interaction, which leads to an atomic electron ejection. The atom becomes a charged ion, it returns to ground state through a limited set of allowed transitions, bringing an external electron to fill the hole produced in the interaction. The excess energy can be released in two possible ways: with the emission of an Auger electron or the emission of an X-photon, the latter process is the one used by EDS detector. This signal is called characteristic radiation because the energies at which the photons are emitted (equal to the energy difference of the electronic shell) are specific to each element and transition. The spectrometric analysis of the signals allows us to find the chemical composition of the sample under investigation. This experimental apparatus is used to obtain the chemical characterization of the sample.

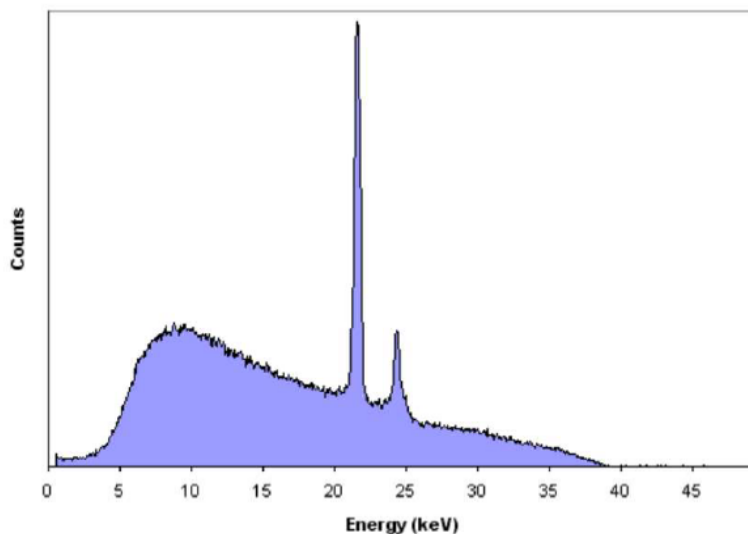


Figure 2.2. Example of a typical X-ray spectrum.

2.2 Gamma-ray spectrometry

A gamma-ray spectrometer is an instrument used for measuring the distribution of the gamma radiation intensity versus the photon energy [38].

The equipment used in gamma spectroscopy includes an energy-sensitive photon radiation detector, electronics to process detector signals produced by the detector, such as a pulse height analyzer (i.e., multichannel analyzer) with the associated amplifiers, and data readout devices to generate, display, and store the observed spectrum. Gamma spectroscopy detectors are based on passive materials that generate an electric pulse when a gamma interaction occurs in its sensitive volume. The interaction mechanisms are: photoelectric effect, Compton effect, and pair production. The photoelectric effect is the preferred interaction in the detector, because in this way all the energy of the incident gamma-ray is absorbed by the detector. Full energy absorption is also possible when a series of successive Compton or photoelectric interactions take place within the detector volume.

The voltage pulse produced by the detector, proportional to the energy released in the detector by the incident photon, is shaped into a Gaussian or trapezoidal pulse by spectroscopy amplifier and its amplitude measured by an analog-to-digital converter (ADC). The resulting digital amplitude is stored in a multichannel analyzer (MCA). ADCs have specific numbers of "bins" into which the pulses can be sorted; these bins represent the channels in the MCA spectrum. The information of interest (activity of the sample) is proportional to the height of the full energy peak recorded in the collected spectrum. The number of channels can be changed by modifying software or hardware settings. The number of channels is typically a power of two; common values include *512, 1024, 2048, 4096, 8192, or 16384 channels*. The choice of number of channels depends on the resolution of the system and the energy range

being studied. The multichannel analyzer output is sent to a computer, which stores, displays, and analyzes the data.

Individual radionuclides emit gamma-rays of specific energies that are characteristic for each specific nuclide. Spectrometers measure both the intensity and the energy of radiation, making it possible to study the source of the radiation. Indeed, gamma-ray spectrometry is a powerful device for monitoring the environment radiation.

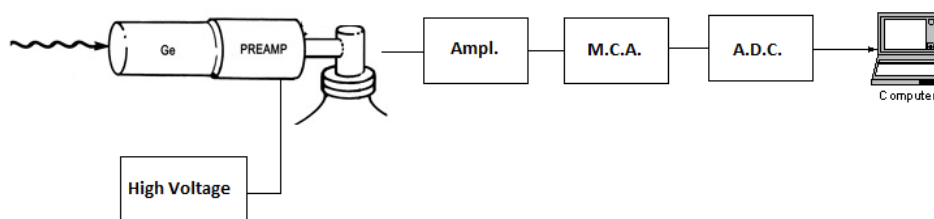


Figure 2.3. Schematic view of a gamma-ray spectrometer [72].

The usage of gamma spectrometry for the radiometric characterization of a material is a powerful and reliable tool but either the experimental apparatus and the sample under analysis need to be well characterized. In this work of thesis, gamma spectrometry was used for the evaluation of the physical quantity activities, i.e. the amount of radiation emitted by a material in the unit of time. To obtain an accurate and precise measurements of the activity of a sample, the measuring instrument has to be calibrated in an equally accurate and precise way. Throughout this chapter the tools used and the actions carried out for precisely setup of the experimental apparatus will be described [38].

2.3 Gamma-ray spectrometry at INMRI

The gamma-ray spectrometry system used at ENEA's INMRI laboratory is a high-resolution gamma-ray spectrometry system in a low background configuration and consists of a coaxial hyper-pure germanium (HPGe) (GEM40-80-5 by Ortec) detector with passive shielding, electronic signal processing instrumentation and digital data readout devices. The germanium detector was cooled with a liquid nitrogen cryostat (60 L) to reduce the leakage current present in the system at room temperature. The detector was embedded in a 10 cm thick lead shield to reduce background radiation from various natural radiation sources and to isolate it from other radiation sources used in nearby surroundings. The lead shielding was graded with an inner layer of 0.1 cm thick copper and cadmium to reduce the contribution from lead (Pb) X-ray fluorescence [38].



(a)



(b)

Figure 2.4. A coaxial hyper-pure germanium (HPGe) detector set up used at INMRI.

The detector was connected to an all in one electronic device (Ortec DSP 50) composed of a preamplifier, a shaping amplifier and a high voltage power supply which, used to convert the individual event energies into a pulse height spectrum. The pulse amplitude was converted to a discrete number using the 8192 channel multi-channel analyzer (MCA) contained in the all in one electronic. Data acquisition, display and analysis of gamma-ray spectra were performed using Gamma Vision software by Ortec [39]. Figure 2.4 illustrates a coaxial hyper-pure germanium HPGe detector enclosed by a set of lead shields graded with copper and cadmium. The all in one Ortec DSP 50 electronic and an interactive analysis feature of Gamma Vision software displaying on a computer screen are shown in Figure 2.5. The detector specifications are listed in Table 2.1.



(a)



(b)

Figure 2.5. Electronic instrumentation used in the current study.

Table 2.1. The specification of the INMRI Ortec Germanium detector and the electronic operating system.

<i>Detector</i>	Ortec
<i>Type</i>	HPGe (p-type)
<i>Energy Range</i>	15 keV – 3.3 MeV
<i>Diameter</i>	66 mm
<i>Length</i>	56 mm
<i>Absorbing Layers</i>	1.00 mm Al
<i>Inactive Ge</i>	700 μm
<i>Operating voltage</i>	+2500 V
<i>Relative Efficiency (1.33 MeV)</i>	40%
<i>Resolution (FWHM) at 122 keV</i>	900 eV
<i>Resolution (FWHM) at 1332 keV</i>	1.9 keV
<i>Peak to Compton Ratio</i>	64:1

2.4 Detector calibration

A digital gamma-ray spectrum is basically a list of number of pulses measured within small consecutive pulse height ranges [38]. Gamma-ray spectrometry allows the gamma-ray spectrum to be interpreted in terms of energy, rather than channels, amount of radionuclides and number of pulses. There are two main calibration tasks:

- Energy calibration: the relationship between channel and energy;
- Efficiency calibration: the relationship between the full energy peak count rate and the disintegration rate.

A number of factors can lead to an inaccurate calibration, resulting in an imprecise activity measurement. Ideally, the source used to calibrate the device and the sample to be measured should be the same, due to the identical geometry and chemical composition. The potential sources of uncertainty in the calibration process are:

- Energy shift caused by changing the source/detector orientation.
- Anomalous peak widths.
- Effect of source/detector distance.
- Effect of sample density.
- Pile up losses (random summing).
- True coincidence summing.

- Inaccurate decay corrections.
- Live time correction error.

The applications of the previous corrections to the efficiency curve of the spectrometer are of fundamental importance: the lack of even one of these aspects greatly contributes to increase the uncertainty associated to the sample activity measurement [38].

In this work we used two types of approaches for the calibration of the detector:

- The first configuration was called Reference Material (RM) calibration apparatus. This configuration was used for the gamma-ray spectroscopy measurement of the reference material. With the aim to made accurate measurement of the activity concentration of a non-point sample, the detector calibration has been carried out with extended sources (100 cm^3) and the measurements (RM measurement apparatus) were carried out with the source at contact with the detector.
- The second configuration was called Nuclear Data (ND) calibration apparatus. This configuration was used to evaluate the emission probability of the emission lines of the radionuclides belonging to the radioactive series of ^{235}U . With the purpose of making accurate measurements of these parameters, we chose a configuration of the calibration apparatus in order to minimize all possible sources of uncertainty associated with a gamma-ray spectrometry measurement. For this reason we chose point sources to perform the calibration measurements with the source to detector distance set at 10.05 cm in order to make coincidence summing effect negligible.

During this section we present the methodologies applied the calibration of the spectrometer in these two configurations and the techniques used to evaluate the most important sources of uncertainty encountered during the calibration process.

2.4.1 Standard source for detector calibration

Spectrometers are calibrated using appropriate gamma-ray spectrum. It is important to underline that the spectrum used in the calibration process should be of high quality and the reference activity value of the sources used should be traceable and accurate. For this reason, for the calibration of INMRI spectrometer we used standard certified sources.

Standard source used for reference material measurement

The INMRI sources used for the calibration of the RM calibration apparatus is composed of 17 multi-gamma sources containing different radionuclides with emission energies which cover the entire spectral band of interest for NORM measurement ($0\text{-}3\text{ MeV}$). The identification, the radionuclides, the chemical composition and the activity of the INMRI sources are shown in Table 2.2. All sources were composed of a solution of hydrochloric acid (HCl) with different normality in which the various radionuclides have been dissolved. The

sources have been inserted in a cylindrical container of 100 c^3 volume called S8H37, Figure 2.9.

Table 2.2. INMRI source used for the calibration of the RM apparatus.

<i>Source</i> [#]	<i>Radionuclide</i>	<i>Chemical</i> <i>Composition</i> [N]	<i>Activity</i> [Bq]
1949	^{133}Ba	HCl 1	3132.94
1950	^{133}Ba	HCl 1	3317.75
1951	^{133}Ba	HCl 1	4678.56
1971m	^{210}Pb	HCl 3.3	10821.46
1971m	^{241}Am	HCl 3.3	1094.50
1971m	^{109}Cd	HCl 3.3	9226.64
1971m	^{57}Co	HCl 3.3	319.49
1971m	^{57}Co	HCl 3.3	319.49
1971m	$^{123\text{m}}\text{Te}$	HCl 3.3	333.23
1971m	^{51}Cr	HCl 3.3	2127.48
1971m	^{113}Sn	HCl 3.3	1262.85
1971m	^{85}Sr	HCl 3.3	1122.95
1971m	^{137}Cs	HCl 3.3	1665.80
1971m	^{88}Y	HCl 3.3	2429.00
1971m	^{60}Co	HCl 3.3	1938.00
1971m	^{60}Co	HCl 3.3	1938.00
1971m	^{88}Y	HCl 3.3	2429.00
1979m	^{210}Pb	HCl 3.3	1683.53
1979m	^{241}Am	HCl 3.3	170.40
1979m	^{109}Cd	HCl 3.3	1417.23
1979m	^{57}Co	HCl 3.3	48.61
1979m	^{57}Co	HCl 3.3	48.61
1979m	$^{123\text{m}}\text{Te}$	HCl 3.3	49.24
1979m	^{51}Cr	HCl 3.3	264.44
1979m	^{113}Sn	HCl 3.3	186.24

<i>Source [#]</i>	<i>Radionuclide</i>	<i>Chemical Composition [N]</i>	<i>Activity [Bq]</i>
1979m	⁸⁵ Sr	HCl 3.3	158.80
1979m	¹³⁷ Cs	HCl 3.3	259.20
1979m	⁸⁸ Y	HCl 3.3	356.70
1979m	⁶⁰ Co	HCl 3.3	300.80
1979m	⁶⁰ Co	HCl 3.3	300.80
1979m	⁸⁸ Y	HCl 3.3	356.70
1989m	²¹⁰ Pb	HCl 2	2455.43
1989m	¹⁰⁹ Cd	HCl 2	1646.28
1989m	⁵⁷ Co	HCl 2	46.31
1989m	⁵⁷ Co	HCl 2	46.31
1989m	^{123m} Te	HCl 2	29.59
1989m	⁵¹ Cr	HCl 2	7.76
1989m	¹¹³ Sn	HCl 2	105.60
1989m	⁸⁵ Sr	HCl 2	42.10
1989m	¹³⁷ Cs	HCl 2	363.50
1989m	⁸⁸ Y	HCl 2	180.00
1989m	⁶⁰ Co	HCl 2	430.70
1989m	⁶⁰ Co	HCl 2	430.70
1989m	⁸⁸ Y	HCl 2	180.00
1997m	²⁴¹ Am	HCl 4	269.70
1997m	¹⁰⁹ Cd	HCl 4	1296.31
1997m	⁵⁷ Co	HCl 4	61.84
1997m	⁵⁷ Co	HCl 4	61.84
1997m	¹³⁹ Ce	HCl 4	57.70
1997m	⁵¹ Cr	HCl 4	1321.66
1997m	¹¹³ Sn	HCl 4	335.98
1997m	⁸⁵ Sr	HCl 4	198.96
1997m	¹³⁷ Cs	HCl 4	398.40
1997m	⁸⁸ Y	HCl 4	334.20

<i>Source</i> [#]	<i>Radionuclide</i>	<i>Chemical</i> <i>Composition</i> [N]	<i>Activity</i> [Bq]
1997m	⁶⁰ Co	HCl 4	395.10
1997m	⁶⁰ Co	HCl 4	395.10
1997m	⁸⁸ Y	HCl 4	334.20
2009m	²²⁶ Ra	HCl 0.5	2160.15
2023m	²¹⁰ Pb	HCl 2	44950.53
2023m	²⁴¹ Am	HCl 2	4469.10
2023m	¹⁰⁹ Cd	HCl 2	31091.94
2023m	⁵⁷ Co	HCl 2	895.07
2023m	⁵⁷ Co	HCl 2	895.07
2023m	^{123m} Te	HCl 2	614.44
2023m	⁵¹ Cr	HCl 2	245.84
2023m	¹¹³ Sn	HCl 2	2202.96
2023m	⁸⁵ Sr	HCl 2	973.25
2023m	¹³⁷ Cs	HCl 2	6651.70
2023m	⁸⁸ Y	HCl 2	3794.20
2023m	⁶⁰ Co	HCl 2	7931.70
2023m	⁶⁰ Co	HCl 2	7931.70
2023m	⁸⁸ Y	HCl 2	3794.20
2024m	²¹⁰ Pb	HCl 2	7387.02
2024m	²⁴¹ Am	HCl 2	734.60
2024m	¹⁰⁹ Cd	HCl 2	5088.99
2024m	⁵⁷ Co	HCl 2	146.07
2024m	⁵⁷ Co	HCl 2	146.07
2024m	^{123m} Te	HCl 2	99.34
2024m	⁵¹ Cr	HCl 2	37.63
2024m	¹¹³ Sn	HCl 2	355.97
2024m	⁸⁵ Sr	HCl 2	155.19
2024m	¹³⁷ Cs	HCl 2	1093.20
2024m	⁸⁸ Y	HCl 2	612.30

<i>Source [#]</i>	<i>Radionuclide</i>	<i>Chemical Composition [N]</i>	<i>Activity [Bq]</i>
2024m	⁶⁰ Co	HCl 2	1302.50
2024m	⁶⁰ Co	HCl 2	1302.50
2024m	⁸⁸ Y	HCl 2	612.30
2029m	²¹⁰ Pb	HCl 2	5776.30
2029m	¹⁰⁹ Cd	HCl 2	5194.77
2029m	⁵⁷ Co	HCl 2	188.31
2029m	⁵⁷ Co	HCl 2	188.31
2029m	^{123m} Te	HCl 2	203.65
2029m	⁵¹ Cr	HCl 2	1784.31
2029m	¹¹³ Sn	HCl 2	797.89
2029m	⁸⁵ Sr	HCl 2	730.54
2029m	¹³⁷ Cs	HCl 2	902.70
2029m	⁸⁸ Y	HCl 2	1447.70
2029m	⁶⁰ Co	HCl 2	1085.40
2029m	⁶⁰ Co	HCl 2	1085.40
2029m	⁸⁸ Y	HCl 2	1447.70
2035m	²¹⁰ Pb	HCl 2	67186.13
2035m	¹⁰⁹ Cd	HCl 2	43261.44
2035m	⁵⁷ Co	HCl 2	1181.18
2035m	⁵⁷ Co	HCl 2	1181.18
2035m	^{123m} Te	HCl 2	687.71
2035m	⁵¹ Cr	HCl 2	104.24
2035m	¹¹³ Sn	HCl 2	2439.31
2035m	⁸⁵ Sr	HCl 2	851.33
2035m	¹³⁷ Cs	HCl 2	9953.30
2035m	⁸⁸ Y	HCl 2	4101.10
2035m	⁶⁰ Co	HCl 2	11691.90
2035m	⁶⁰ Co	HCl 2	11691.90
2035m	⁸⁸ Y	HCl 2	4101.10

<i>Source</i> [#]	<i>Radionuclide</i>	<i>Chemical</i> <i>Composition</i> [N]	<i>Activity</i> [Bq]
CNT-152m	^{137}Cs	HCl 0.5	17.06
CNT-2041m	^{241}Am	HCl 0.5	4384.87
CNT-2049m	^{241}Am	HCl 1	46.75
CNT-2049m	^{137}Cs	HCl 1	170.00
CNT-2050	^{241}Am	HCl 1	8440.50
CNT-2050	^{137}Cs	HCl 1	30700.20
RICE-31	^{137}Cs	HCl 1	0.24
RICE-31	^{40}K	HCl 1	2.99

Standard source used for Nuclear Data measurement

The INMRI point-sources used for the calibration of the ND calibration apparatus was made of 89 point-sources containing many radionuclides with emissions energies which cover the entire spectrum of interest for NORM measurement (0-3 MeV). The identification, the radionuclides, and the activity of the INMRI point-sources are shown in Table 2.3. The geometry of each source is made of two polystyrene disc overlaid at the center of which is positioned the point source (Figure 2.6).

Table 2.3. INMRI point-sources used for the calibration of the ND apparatus.

<i>Source</i> [#]	<i>Radionuclide</i>	<i>Activity</i> [Bq]
138	^{137}Cs	1117.80
140	^{137}Cs	1254.00
780	^{210}Pb	10423.41
857	^{60}Co	134.40
900	^{152}Eu	624.30
1134	^{22}Na	1759.90
1190	^{210}Pb	1888.50
1298	^{133}Ba	5509.40
1366	^{241}Am	1743.40
1366	^{241}Am	1739.20

<i>Source [#]</i>	<i>Radionuclide</i>	<i>Activity [Bq]</i>
1366	¹³³ Ba	594.70
1366	¹³⁴ Cs	27.20
1366	⁶⁰ Co	144.60
1366	²² Na	38.20
1366	⁶⁰ Co	144.60
1458	²⁴¹ Am	14221.10
1458	⁶⁰ Co	1468.60
1511	²²⁶ Ra	430.86
1706	²⁴¹ Am	282.40
1706	¹³⁷ Cs	220.50
1706	⁶⁰ Co	89.20
1713	²¹⁰ Pb	2907.20
1731	¹⁰⁹ Cd	1075.37
1946	¹³³ Ba	784.66
1947	¹³³ Ba	330.87
1968	²⁴¹ Am	348.10
1968	¹⁰⁹ Cd	2873.69
1968	⁵⁷ Co	98.06
1968	^{123m} Te	97.73
1968	⁵¹ Cr	477.08
1968	¹¹³ Sn	369.26
1968	⁸⁵ Sr	307.63
1968	¹³⁷ Cs	529.34
1968	⁶⁰ Co	613.32
1968	⁶⁰ Co	613.32
1968	⁸⁸ Y	705.49
1969	²⁴¹ Am	481.30
1969	¹⁰⁹ Cd	4190.18
1969	⁵⁷ Co	148.39

<i>Source</i> [#]	<i>Radionuclide</i>	<i>Activity</i> [Bq]
1969	^{123m}Te	165.99
1969	^{51}Cr	1600.36
1969	^{113}Sn	631.93
1969	^{85}Sr	621.09
1969	^{137}Cs	733.48
1969	^{88}Y	1227.97
1969	^{88}Y	705.49
1969	^{60}Co	858.82
1969	^{88}Y	1227.97
2001	^{241}Am	18.40
2001	^{109}Cd	88.55
2001	^{57}Co	4.23
2001	^{139}Ce	3.96
2001	^{51}Cr	93.46
2001	^{113}Sn	23.10
2001	^{85}Sr	13.78
2001	^{137}Cs	27.16
2001	^{88}Y	23.00
2001	^{60}Co	26.94
2001	^{88}Y	23.00
2005	^{226}Ra	1183.95
2019	^{210}Pb	4938.02
2019	^{241}Am	490.80
2019	^{109}Cd	3434.56
2019	^{57}Co	99.28
2019	^{123m}Te	69.03
2019	^{51}Cr	29.77
2019	^{113}Sn	247.69
2019	^{85}Sr	111.44

<i>Source</i> [#]	<i>Radionuclide</i>	<i>Activity</i> [Bq]
2019	¹³⁷ Cs	730.66
2019	⁸⁸ Y	427.40
2019	⁶⁰ Co	872.27
2019	⁸⁸ Y	427.40
2032	²⁴¹ Am	647.90
2034	²⁴¹ Am	181.60
2051	¹³⁷ Cs	1358.93
2130	²¹⁰ Pb	452.71
Gold-Triga-4V1	¹⁹⁸ Au	650.69
Gold-Triga-4V2	¹⁹⁸ Au	48.32
IFO-16 BIS +Ag	¹³¹ I	55926.84
IFO-IRE-9 BIS +Ag	¹²⁴ I	2851.77
SIR III SP-1 mis-1	⁶⁴ Cu	166270.19
SIR III SP-1 mis-2	⁶⁴ Cu	121713.44
SIR III SP-1 mis-3	⁶⁴ Cu	89227.35
SP-19 INT	¹⁷⁷ Lu	57865.32
SP-20 INT	¹⁷⁷ Lu	59944.84
Test-1 SP-33	⁶⁴ Cu	9186.32
Test-2 SP-19	⁶⁴ Cu	23322.75
Test-2 SP-20	⁶⁴ Cu	28230.27
Test-2 SP-21	⁶⁴ Cu	16721.84

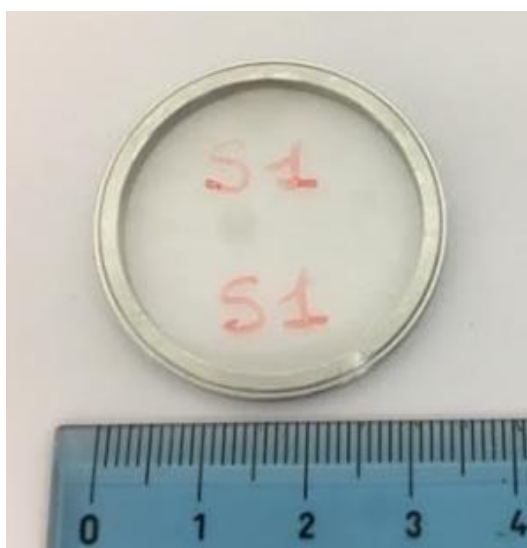


Figure 2.6. INMRI point-source S1 used for the calibration of the ND apparatus.

2.4.2 Energy calibration

The task of energy calibration is to derive a relationship between the peak position in the spectrum and the corresponding gamma-ray energy [38]. With energy calibration we indicate the procedure of measuring the spectrum of a source emitting gamma-rays with known energy and comparing the measured peak position with energy. The energy calibration of the spectrometry system was made with a ^{152}Eu point source called SP-308, the gamma-ray lines of the source and its decay details are shown in Table 2.4. The source is chosen to cover the spectral energy range used for NORM measurements ($0-3\text{ MeV}$). The calibration measurement was carried out for 500000 s (5.7 d), it is possible that some local non-linearity may exist in an amplifier-analyzer system. Discrete peaks were chosen along the entire range of measured energies to ensure an accurate energy calibration and to identify any potential non-linearities of the spectrometry system [41] [42]. As shown in Table 2.4, the channel numbers of the centroid positions for $24\ ^{152}\text{Eu}$ well known energy peaks were determined. Then, the numbers of the centroid channel were compared with the absolute gamma-ray energies derived from the reference data [42].

Table 2.4. Main gamma-ray lines of the ^{152}Eu point source called SP-308.

<i>Photon Energy</i> [keV]	<i>Channel</i> [#]	<i>Fit</i> [keV]	<i>Delta</i> [%]
46.54	115.22	44.69	-0.32
209.25	520.84	209.32	-0.04
238.63	594.00	238.66	-0.01

<i>Photon Energy</i> [keV]	<i>Channel</i> [#]	<i>Fit</i> [keV]	<i>Delta</i> [%]
295.22	735.05	295.20	0.01
338.28	842.46	338.27	< 0.001
351.93	876.37	351.86	0.02
409.46	1019.81	409.37	0.02
583.19	1453.25	583.13	0.01
609.31	1518.44	609.29	0.01
727.33	1812.79	727.25	0.01
755.31	1882.84	755.33	< 0.001
860.53	2145.26	860.52	< 0.001
911.20	2271.63	911.16	< 0.001
968.96	2415.75	968.93	< 0.001
1120.29	2793.38	1120.28	< 0.001
1238.11	3087.50	1238.15	< 0.001
1460.80	3643.26	1460.86	< 0.001
1620.74	4042.19	1620.71	< 0.001
1729.59	4314.18	1729.68	-0.01
1764.49	4401.33	1764.60	-0.01
1847.42	4608.34	1847.53	-0.01
2204.21	5498.48	2204.13	< 0.001
2442.86	6106.63	2447.72	0.001
2614.51	6523.18	2614.55	< 0.001

The linear relationship between the gamma-ray energies and channel numbers is clear from Figure 2.7 and can be parameterized by the following equation:

$$E = 2.4967(Ch[\#]) - 2.7079 \quad (2.1)$$

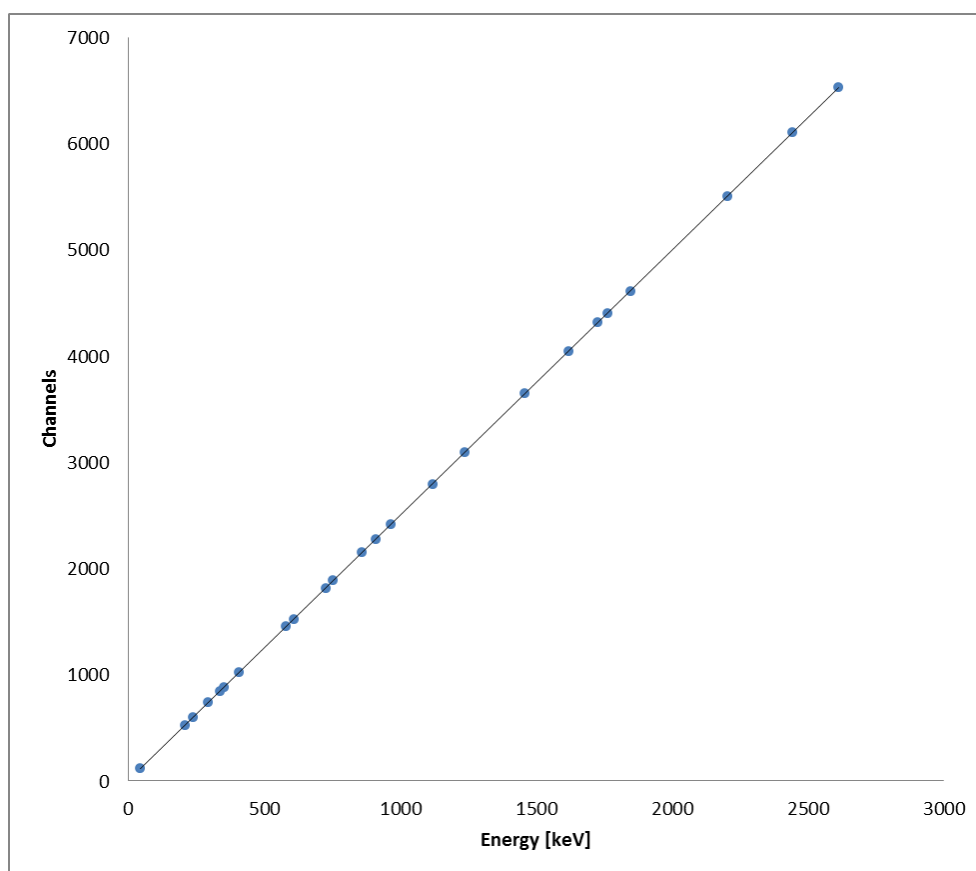


Figure 2.7. The observed relationship between the published gamma-ray energies and their centroid channel number from the SP-308 source used for the energy calibration.

The observed relationship between the gamma-ray energies and their channel numbers is shown in Figure 2.7.

The INRIM laboratory operational procedures provide a spectrometer energy calibration before each measurement.

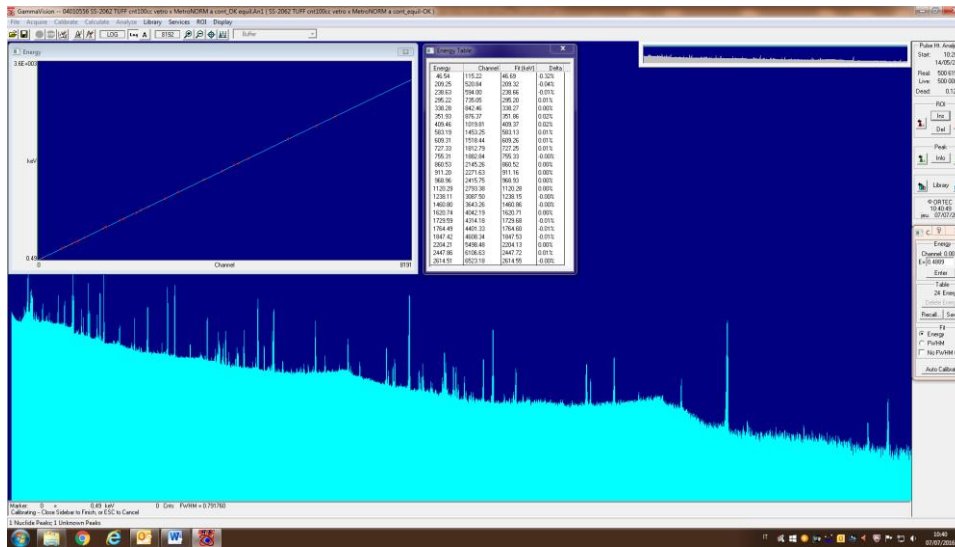


Figure 2.8. Gamma-ray spectrum of ^{152}Eu calibration source.

2.4.3 Experimental efficiency calibration

The full energy peak efficiency is one of the most important parameters in practical gamma-ray spectrometry. The calculation of full-energy peak efficiency is straightforward; it is the ratio between the number of counts detected in a peak and the number of photons emitted by the source [38]:

$$\varepsilon = \frac{N}{(S \times P_\gamma)} \quad (2.2)$$

where N is the full-energy peak count rate (in counts per second units), S is the source strength (in disintegration per second units, i.e. Becquerels) and P_γ is the probability of emission of the particular gamma-ray being measured. The source strength used in Equation (2.2) may need to be corrected for decay from the date of preparation and for decay during the measurement [38].

Experimentally an efficiency curve is constructed by measuring many gamma-rays and plotting efficiency against energy.

The efficiency calibration of the gamma-ray spectrometry set-up in the current work was performed in two steps. First of all the certificated INMRI sources were experimentally measured. After that, a Monte Carlo simulation was used to obtain correction factors used to modify the calibration curve and to adapt it to the measurement conditions.

Indeed, the calibration apparatus configurations used in this work were different from the configurations used for the samples activity measurements, from both a structural (chemical composition, density) and a geometrical point of view. If we do not consider these differences the uncertainty associated with the activity measurements will increase.

There are several reasons why the calibration apparatus should be different when compared to the measurement apparatus, as follow:

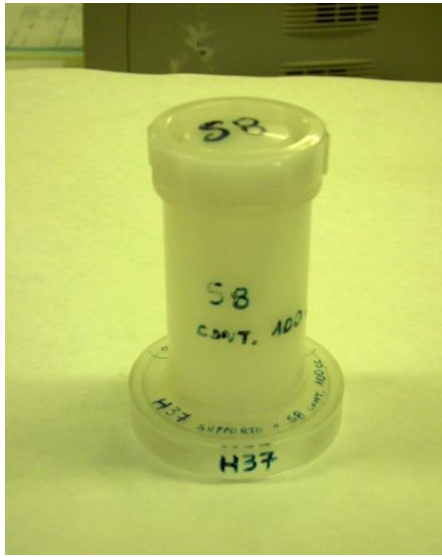
- Different shape of source.
- Absorption within the source.
- Random summing.
- True coincidence summing.
- Decay of the source during counting.

However, the predominant effects that could increase the uncertainty associated to the sample activity measurement are essentially three:

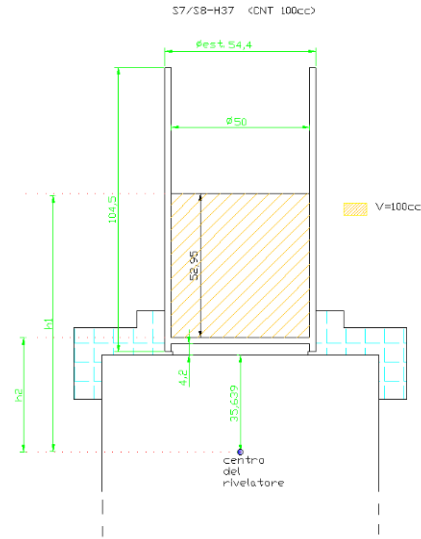
- A difference in the volume source measurement between the measurement geometry from the calibration geometry. We will then use the efficiency transfer technique to consider this difference [45].
- Self-attenuation due to the different capability of the sources in the two different configurations to reabsorb the photon emitted from itself. This parameter depends on the chemical composition and the density of the sample [45].
- Coincidence summing phenomenon, occurring when some nuclide emit multiple gamma-rays and X-rays when decaying to the ground state. If these gamma are emitted essentially at the same time, it is possible that multiple photons will be detected at the same time in the detector, giving rise to a single signal in the spectrum as if a single photon would have been detected [52].

Reference material calibration apparatus

To determine the detector efficiency curve in the RM calibration configuration we used the INMRI multi-gamma sources set, whose content is shown in Table 2.2. These standard sources were contained in cylindrical containers called S8H37 filled with 100 c^3 of radioactive solution. This container is an INMRI standard container that is shown in Figure 2.9 (a) and its dimensions are shown in Figure 2.9 (b). All the source under analysis have been placed at the center of the detector active volume throughs an object called H37 (Figure 2.9 (a)) with the aim of obtaining reproducible calibration measurements. This configuration has determined a distance between the container and the detector of 4.2 mm .



(a)



(b)

Figure 2.9. S8 container and H37 object (a). Dimension of S8H37 container [mm] (b).

The gamma-ray spectra of each source were accumulated for 50000 s and the net counts in the full-energy peaks determined. Only full-energy peaks which provide at least 20.000 net counts should be considered for the efficiency calibration [40]. The interference between multiple peaks must also be taken into account when choosing the individual peaks to be used for the efficiency calculation [41]. The efficiencies of each radionuclide contained in INMRI source at various energies were calculated using Equation 2.2. Once the efficiency calibration of the HPGe detector was carried out over the entire energy range of interest (0 – 3 MeV), using INMRI standard sources, all measured data were fitted to an efficiency function of the form like Equation 2.3:

$$\varepsilon_{\gamma} = \exp[P_1 + P_2(\ln E) + P_3(\ln E)^2 + P_4(\ln E)^3 + P_5(\ln E)^4 + P_6(\ln E)^5 + P_7(\ln E)^6] \quad (2.3)$$

where P_1, P_2, \dots, P_6 are parameters of the fitting function and ε_{γ} is the efficiency at energy E [keV].

The result of this fit is shown in the Equation (2.4) and the efficiency trend, as a function of energy, is shown in Figure 2.10:

$$\varepsilon_{\gamma} = \exp[-1555.44 + 1584.74(\ln E) - 672.82(\ln E)^2 + 152.04(\ln E)^3 - 19.27(\ln E)^4 + 1.30(\ln E)^5 - 0.04(\ln E)^6] \quad (2.4)$$

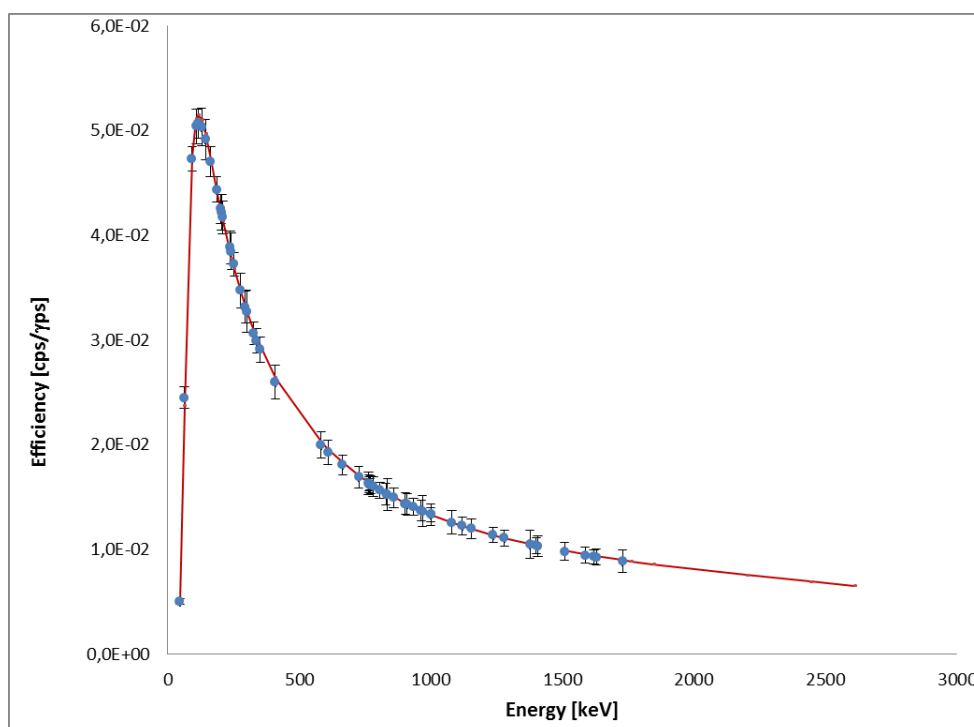


Figure 2.10. Absolute full-energy peak efficiency as function of gamma-ray energy for the HPGe detector.

The efficiency transfer can be used to calculate the correction factors for the detector efficiency curve under different experimental conditions [45]. The best method available to evaluate the correction factors is the Monte Carlo approach [48]. Throughout this work we used a dedicated software called GESPECOR to evaluate the corrections to the efficiency curve.

Nuclear data calibration apparatus

In this section we present the materials and the methodologies used for the calibration of the detector in the configuration used for nuclear data evaluation.

The evaluation of the detector efficiency curve in the ND calibration apparatus was carried out using the INMRI point-sources set, whose content is shown in Table 2.3. This configuration was developed to minimize all the possible uncertainty in the emission probability measurement. For this reason we decided to use point-sources for efficiency calibration of the detector. In fact the sample to be measured for the emission probability was geometrically very similar to a point source as we can see in chapter 4, in this configuration the correction factors due to efficiency transfer should be small.

Moreover all the sources used for the calibration were placed at the center of the detector active volume through the same object (H30, Figure 2.11) with the aim to obtain reproducible measurements for the calibration of the device.

The gamma-ray spectra of each source were accumulated for 50000 s and the net counts in the full-energy peaks determined. The efficiencies of each radionuclide contained in INMRI point-sources at various energies were calculated using Equation 2.2. Once the efficiency calibration of the HPGe detector was carried out over the entire energy range of interest (0 - 3 MeV), using INMRI standard point-sources, all measured data were fitted to an efficiency function of the form like Equation 2.3.

The result of this fit is shown in Equation (2.5):

$$\varepsilon_{\gamma} = \exp[819.38 + 807.98(\ln E) + 334.47(\ln E)^2 + 74.04(\ln E)^3 + 9.23(\ln E)^4 + 0.61(\ln E)^5 + 0.01(\ln E)^6] \quad (2.5)$$

The efficiency trend as a function of energy is shown in Figure 2.12:

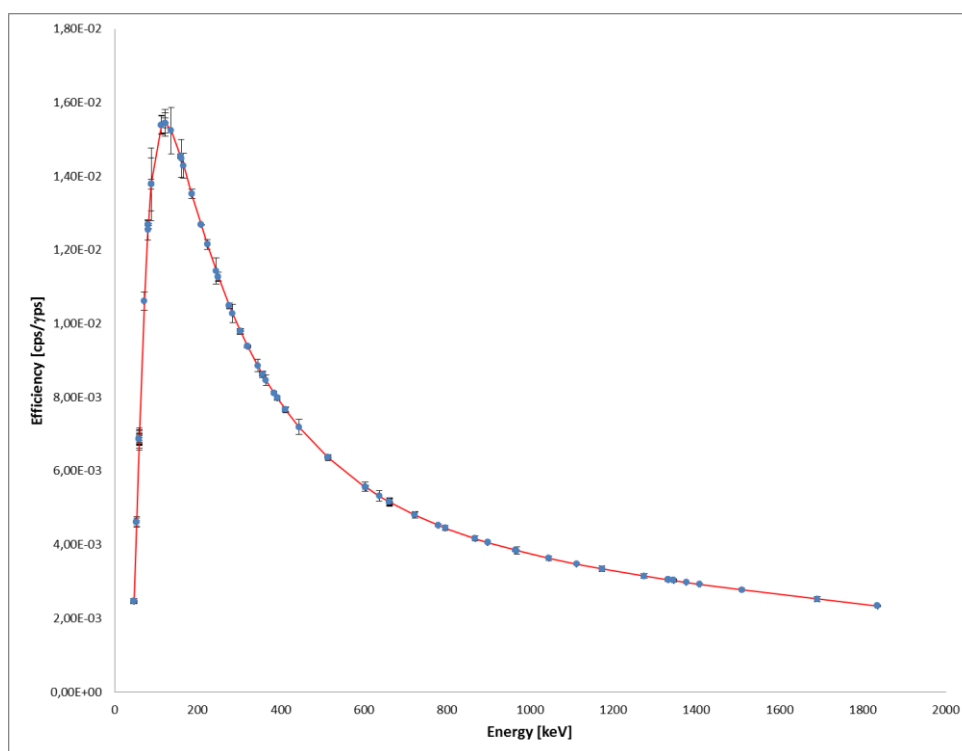


Figure 2.12. Absolute full-energy peak efficiency as function of gamma-ray energy for the HPGe detector.

The efficiency transfer can be used to calculate the correction factor to the detector efficiency under different measurement condition respect to the calibration configuration [44]. As

mentioned before in this work in order to evaluate all corrections to the efficiency curve we used a dedicated software called GESPECOR.

2.4.4 Measurement apparatus

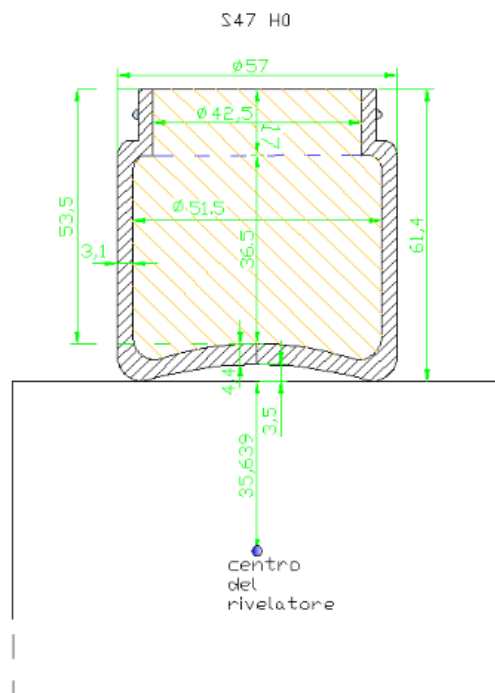
In this section we described the measurement apparatus used in the work in two different configurations.

Reference Material measurement apparatus

The experimental apparatus (measurement apparatus) used for samples measurement was different from the one used for the efficiency calibration of the device. The main differences between these two configurations were due to geometric effect (size and construction material of the container) and to the chemical composition of the samples. In fact, in the INMRI source radionuclides were dissolved in a water and hydrochloric acid (HCl) solution in different concentrations, while the measured matrices were solid, in detail: Tuff ($\rho = 0.96 \text{ g cm}^{-3}$), Ionex resin ($\rho = 0.79 \text{ g cm}^{-3}$) and TiO_2 ($\rho = 1.45 \text{ g cm}^{-3}$).

The container used for the RM measurements is shown in Figure 2.13, it is a glass container containing a sample volume of 100 cm^3 and called S47H0. The container internal dimensions have been obtained by filling the container with fast-setting plaster (the same type used by dentists to take teeth imprint). After the gypsum solidification, the glass container was broken and the internal dimension of the container was measured using a precision caliper (Mitutoyo CD-6'' ASX) taking care to report the thickness of glass, too. We show in Figure 2.13 the container internal dimensions (panel a), the container used for the measurement of the samples (panel b) and the plaster cast used to characterized S47H0 container (panel c).

We chose a glass container since it is a material capable of retaining radon. Having regard to the presence of radon gas in some of analyzed sample it is convenient to use a glass container to reach the secular equilibrium within the sample.



(a)



(b)



(c)

Figure 2.13. Schematic view of S47H0 (a). S47H0 container (b). Mold of S47H0 container used (c).

Nuclear data measurement apparatus

To measure the emission probability of the radionuclides belonging to the natural radioactive series of ^{235}U CIEMAT⁷ and JRC were prepared two sources: one made of absolute ^{235}U (SPE-2014) and the other of ^{227}Ac (SPE-2129). The geometrical characterization of the sources is shown in Figure 2.14.

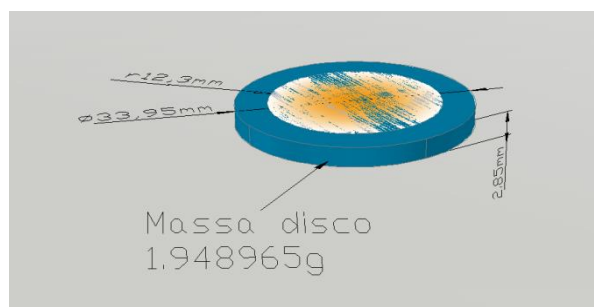


Figure 2.14. Geometrical characterization of the ^{235}U and ^{227}Ac sources.

The sources were deposited on a glass disk whose chemical composition is shown in Table 2.5.

Table 2.5. Chemical composition of the glass used for the source preparation.

<i>Elements</i>	<i>Abundance [mol%]</i>
SiO ₂	74.42
Al ₂ O ₃	0.75
MgO	0.30
CaO	11.27
Na ₂ O	12.90
K ₂ O	0.19
Fe ₂ O ₃	0.01
TiO ₂	0.01
SO ₃	0.16

⁷ Centro de Investigaciones Energéticas, Medioambientales y Tecnológicas.

During the deposition process it was evaluated of the spatial distribution of the activities of ^{235}U source on the glass disk. The result of this evaluation is shown in Figure 2.15.

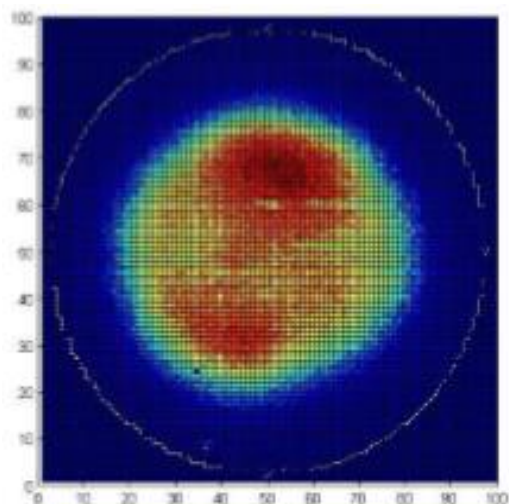


Figure 2.15. Activity distribution of ^{235}U source.

From Figure 2.15 it shows that the sources are not distributed over the entire disk, but on a circle of radius $r = 12.3\text{ cm}$. Note that the white circumference corresponds to the external surface of the source. We show in the Figure 2.15 the activity distribution of the ^{235}U source, it has a non-homogenous distribution. Red representing an activity distribution higher than that represented by yellow. However, in the evaluation of the corrections to the efficiency curve we considered both sources as uniform distributed on a circle of radius 12.3 mm . We show in Figure 2.16 a schematic view of the ND measurement apparatus, for this apparatus was used the same spacer shown in Figure 2.11 (H30).

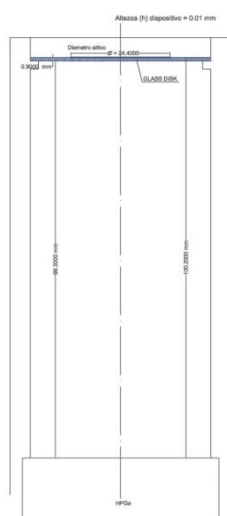


Figure 2.16. Schematic view of the ND measurement apparatus.

As can see from the Figure 2.16 the measurements of ^{235}U and ^{227}Ac sources were made at a 10.02 cm away from the detector. This geometric configuration has been chosen with the aim to minimize the coincidence summing effect. All this information has been used by GESPECOR for the evaluation of the corrections to the DN calibration apparatus efficiency curve.

2.4.5 Detector characterization

Throughout this work, the activity measurements were carried out with a coaxial detector GM40-80-5, it is produced by Ortec which has certified the low radioactivity content and technical specifications are listed in Table 2.6. The detector technical characteristics are shown in Figure 2.17, this information were used by GESPECOR to calculate all the efficiency curve correction factors.

Table 2.6. Technical specifications of Ortec detector.

<i>Cod.</i>	<i>Materials</i>		<i>Detector dimension [mm]</i>
A	5	Al	135
B	5	Al	41.28
C ₁	5	Al	1.5
C ₂	5	Al	1.5
D	1	Ge	55.5
E	1	Ge	32.95
F	6	Ge inactive	0.7
G	6	Ge inactive	0.7
H	6	Ge inactive	8
I ₁	4	empty	6
I ₂	4	empty	
L	1	Ge	41.6
M	3	Cu	4.4
N	6	Ge inactive	0.003
O	6	Ge inactive	
P	2	Al	
Q	2	Al	0.76

<i>Cod.</i>	<i>Materials</i>	<i>Detector dimension [mm]</i>
R	3/4 mix	
S	2 Al	3.2
T	2 Al	105
U	7 Mylar/Al- Mylar	0.03/0.03

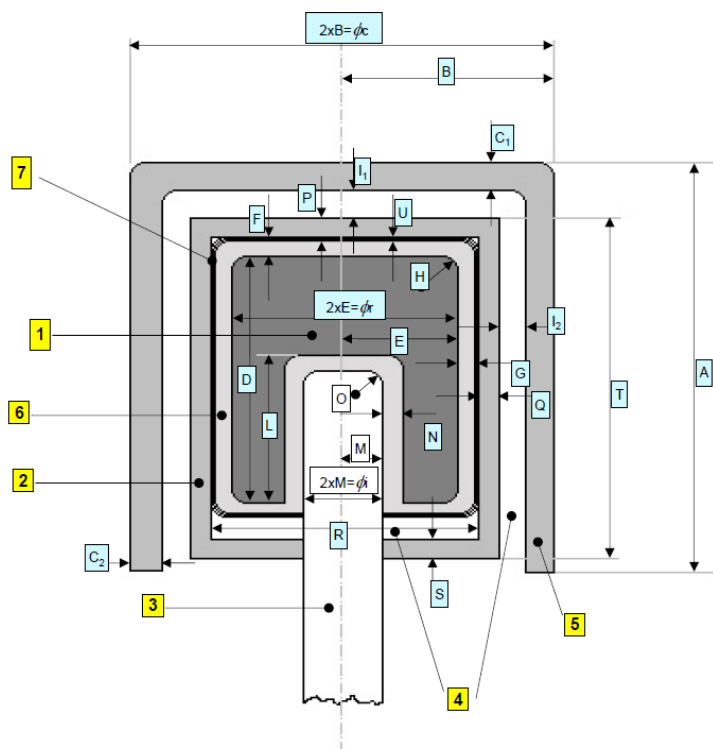


Figure 2.17. GM40-80-5 characterization provide from Ortec.

2.5 Efficiency transfer

Direct experimental calibration of the efficiency (ε) of Germanium gamma-ray spectrometers can be achieved only for a limited number of geometries and for specific sample matrices. Direct computation of ε by Monte Carlo method, for instance, can be carried out for any geometry and sample matrix, but has the drawback of being sensitive to the uncertainties associated to some detector parameters or to other issue, such as incomplete charge collection

in the crystal. On the other hand, the ratio between the efficiency for a particular geometry and the efficiency for a calibration measurement is much less sensitive to the model of detector and other input data required in the computation of the efficiency. This idea is the key point of the method of efficiency calibration using the efficiency transfer from a calibration measurement.

Formally, the method of efficiency transfer is based on equation:

$$\varepsilon_a^{(calc)} = k(a/ref)\varepsilon_{ref}^{(exp)} \quad (2.6)$$

where $k(a/ref)$ is the efficiency transfer factor from the calibration configuration (index ref) to the measurement configuration (index a); (calc) and (exp) indicate computed and measured values, respectively. All the quantities in Equation (2.6) are functions of E .

$k(a/ref)$ is defined by the ratio of the model efficiency computed in this work and the one with the Monte Carlo method:

$$k(a/ref) = \frac{\varepsilon_a^{(MC)}}{\varepsilon_{ref}^{(MC)}} \quad (2.7)$$

Substituting Equation 2.1 in Equation 2.6 we get:

$$\varepsilon_a^{(calc)} = \left[\frac{R}{(S \times P_\gamma)} \right] \times k(a/ref) = \left[\frac{R}{(S \times P_\gamma)} \right] \times k_{ET} \times k_{SA} \times k_{CS} \quad (2.8)$$

where k_{ET} is the correction due to efficiency transfer, k_{SA} is the correction due to self-attenuation and k_{CS} is the correction due to coincidence summing. Each of these correction factors is the ratio between the efficiency curve in which the correction is taken into account and the uncorrected one. In this work, the Monte Carlo method (based on the GESPECOR software [47]) was applied to evaluate this correction factors.

GESPECOR

GESPECOR is a Monte Carlo based code specifically developed for solving problems in efficiency calibration of Ge spectrometer. This program imagine a gamma-ray emitted from a position within the source, chosen at random and in a random direction, and follows it until it is totally adsorbed or otherwise lost to the system. The program will consider interactions as it passes through the sample, through the detector enclosure, through the dead layer of the detector and finally as it scatters through the detector, giving up its energy until it is completely absorbed or it escapes from the detector. Each simulated event provides a count

within the spectrum in a channel representing the amount of energy absorbed in the detector. At each stage, the program will consider the probability of interaction by various means. It will take into account gamma-rays that scatter within the detector and are then lost and those which would miss the detector but backscattered from the shielding into detector. It will also take consider those gamma-rays that are absorbed within the sample itself. Repeating this process several millions of times will generate a spectrum from which an efficiency curve can be derived [48].

Typical applications of this program are evaluating the matrix effect, the coincidence summing and the full peak efficiency.

In the following, we will present the physical nature of all corrections to the efficiency curve considered in this work. GESPECOR software needs the accurate characterization of the following parameters to run properly:

- Detector characterization.
- Calibration apparatus characterization.
- Measurement apparatus characterization.
- Chemical composition and density of the calibration source and the measurement sample.

It is very important to underline the fact that a very accurate characterization of these parameters will result in lower uncertainties associated with the measurement procedure [38].

Efficiency transfer in the case of volume source

In this work, the measurement geometry differs slightly from the one of the calibration source, from a volumetric point of view. We indicate as V_{ref} and V_a the volume of the calibration source and of the measurement source, respectively. A volume V is defined in such a way that V_{ref} and V_a are included in V . In the Monte Carlo simulation procedure, an emission point is randomly selected in V . If this point belongs both to V_{ref} and V_a then a photon is emitted towards the detector, the attenuation in V_{ref} and V_a is evaluated, then the photon is traced as in the usual procedure applied in GESPECOR; if at the end, the energy of the photon is completely absorbed in the detector, the full energy peak efficiency counter for both source are appropriately incremented with the weight associated to the photon. If the emission point belongs only to one of the two volumes, a photon is emitted and traced; if finally its energy is completely absorbed in the detector, the counter corresponding to that volume incremented. If the emission point does not belong to any of the two volumes, than a new emission point is randomly selected [45].

The output of the procedure is the efficiency for each of the volume source and transfer factor, together with their Monte Carlo statistical uncertainties. The statistical uncertainty of the transfer factor obtained in this way is much better than the value which would be derived from an independent evaluation of each efficiency at the same level of statistical uncertainty.

Self-attenuation

In ideal conditions, as mentioned earlier, the sample to be measured and the calibration source should have the same geometry, density and chemical composition. Under these conditions the self-attenuation in the two configurations (i.e. the photon attenuation within the sample), is the same [44]. In the case of real measurements, however, there will be differences which will require corrections in the evaluation of the activity of a sample to be taken into account. Each photon that passes through a material can have interactions inside it. The photons may lose part of their energy because of this interaction and could arrive to the detector with less energy with respect to its initial energy. In this way it will not contribute to the counts of the corresponding full energy peak (FEP). The total attenuation, i.e. the fraction of photons that interact within the source (regardless of the direction in which they are emitted by the source or nucleus), is usually of weak practical interest. On the contrary, the fraction of photons which are emitted in the solid angle subtended by the detector but attenuated within the source have to be taken into account and need some correction [44]. This coefficient depends on the chemical composition and on the density of the sample. If this information is not provided along with the sample, it becomes necessary for the operator to either measure the mass attenuation coefficient by the collimated beam method or estimate it by XCOM. In these work in order to use GESPECOR all the mass attenuation coefficients are estimated using XCOM through the knowledge of the chemical composition carried out through EDX measurement. XCOM is a web database that allows to calculate the linear attenuation coefficients for each element, compound or mixture for energies ranging from 1 keV to 100 GeV [51]. Throughout this thesis, the value of the correction factor due to self-absorption of the source is obtained through the use of the GESPECOR software.

Coincidence summing effect

Coincidence summing effects are of two origins. Random coincidences occur in the case when just by chance two photons emitted by different nuclei happen to interact with the detector so closely in time that the detector cannot resolve them into two different signals. Random coincidences are more and more important as the count rate increases, because the distribution of time intervals between two successive decays of different nuclides is displaced towards shorter time intervals in this case. True coincidence summing effects are produced when two or more than two photons emitted in the decay of the same nuclide happen to interact with the detector. Normally the time interval between the emissions of all the photons along the same decay path is much shorter than the resolving time of the detector system and consequently the detector will deliver a single signal, proportional with the summed energy deposited by all these photons together. True coincidence summing effects do not depend on source activity or count rate, but depend on the decay scheme of the nuclide. The evaluation of these effects requires a specific combination of decay data of the nuclide with the probability of photon interactions in the detector [50] [55].

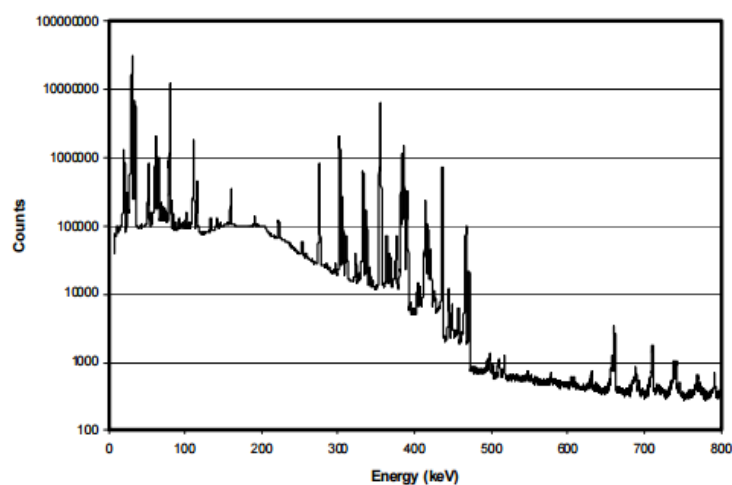


Figure 2.18. Spectrum of a ^{133}Ba point source measured on the end cap of the p-type detector [54].

As an exemplification of the magnitude of coincidence summing effects in Figure 2.18 the spectrum of a ^{133}Ba point source placed on the end cap of the p-type detector is displayed. In the decay of ^{133}Ba 9 gamma-rays with energies equal to 53, 79, 81, 160, 223, 276, 302, 356 and 383 keV are emitted. Correspondingly in the spectrum of ^{133}Ba measured in the absence of coincidence summing effects (e.g. with a low efficiency detector) only 9 peaks, with the energies given above, are expected. All the other peaks from the spectrum displayed in Figure 2.18 (except the 661 keV peak of ^{137}Cs) are the result of coincidence summing effects. For example the peaks from the higher energy part of the spectrum are due to random summing, e.g. the peak at the energy of 712 keV is the result of summing two 356 keV photons emitted by two different nuclides ($712=356+356$ keV). Note that although the count rate in the 356 keV peak is very high, the count rate in the 712 keV peak is low; from the count rate in this peak the order of magnitude of the random coincidences sum peaks can be inferred. It is clear that, even if random summing contributes also to the peaks that can be attributed to true coincidence summing, this contribution is much smaller than the contribution of true coincidence summing.

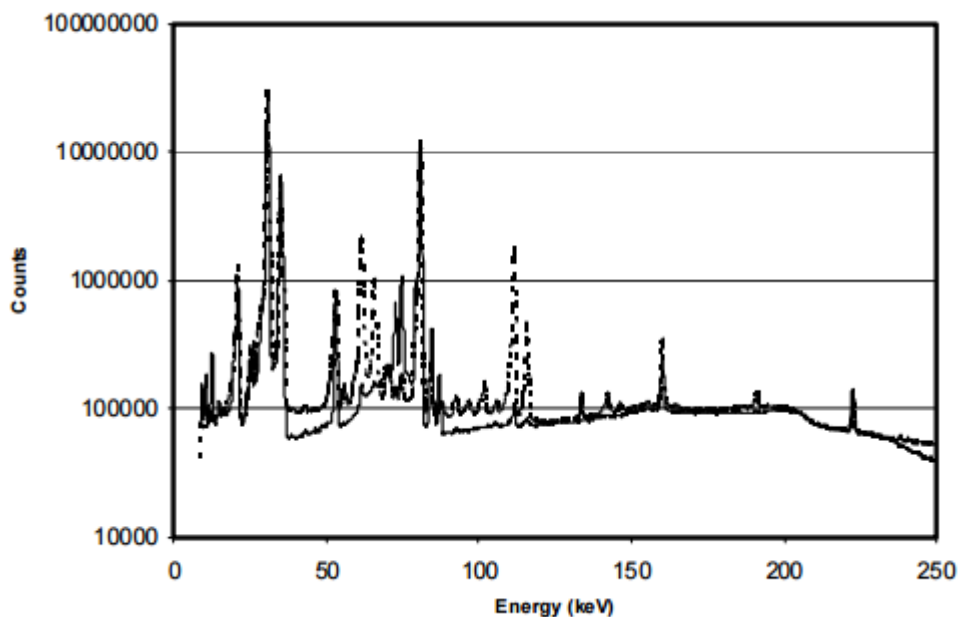


Figure 2.19. The first part of the spectrum of the ^{133}Ba source measured on the detector end cap (dashed line) and at 15 cm distance (full line) with the p-type detector. The spectra were normalized to give equal number of counts in the 356 keV peak [54].

A convenient way of evidencing the magnitude of the coincidence summing effects is to display the spectra of the same point source measured close to the detector and far from the detector. In the absence of coincidence summing effects the spectra should look similar, with the count rate in the peaks proportional with the solid angle. If a normalization factor is applied in such a way as to provide equal count rates in a selected peak in the two spectra, then the two normalized spectra should be practically identical (minor differences might be present due to background contribution). The deviation from this expectation is entirely the result of coincidence summing effects. In Figure 2.19 and Figure 2.20 two energy ranges from the spectra of the ^{133}Ba source located at 15 cm from the detector (full line) and directly on the end cap (dashed line) are displayed. The two spectra have been normalized at the 356 keV peak. The spectrum of the source measured close to the detector contains many peaks that are absent in the other spectrum (or have a much smaller count rate). Briefly speaking, the peaks at 132, 134, 304, 357 and 437 keV are due to sum peaks involving only gamma photons, while all the other pure sum peaks are due to summing. Due to the high efficiency of the detector, coincidence summing effects are not completely negligible even for the source located at 15 cm (note e.g. the presence of the 437 keV sum peak) [54].

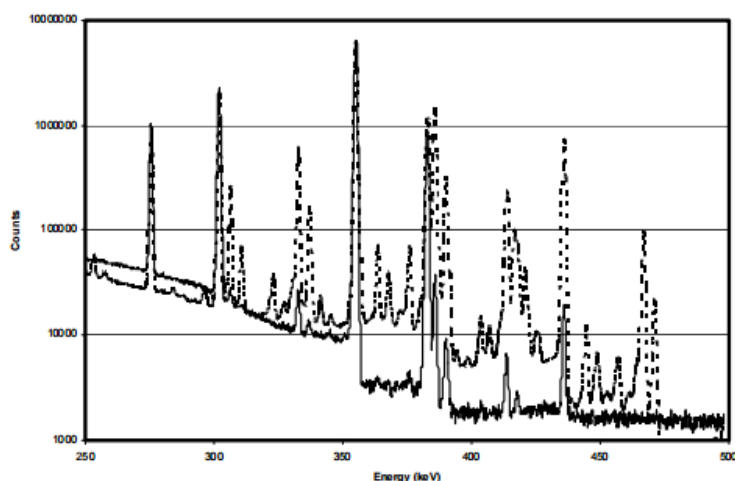


Figure 2.20. Same spectra as in Figure 2.19 for the energy range 250–500 keV [54].

In this work the corrections factor to the efficiency calibration curve of the measurement apparatus due to CS was carried out using GESPECOR software.

2.6 Calibration procedure

In this section we describe the procedure used to calibrate the INMRI detector in the two configurations used in this thesis.

Calibration procedure for reference material measurement

By using the values of the calibration efficiency (RM calibration apparatus) and the efficiency transfer computed by GESPECOR we obtained an accurate efficiency curves for all samples under investigation for the activity measurement of reference materials.

The procedure used to obtain all the corrections to the efficiency curve is the following:

- The set of source listed in Table 2.1 were measured on the INMRI HPGe detector in the MR calibration configuration.
- The set of 100 cm^3 sources called INMRI source, as can be seen from the Table 2.1, is composed of different radionuclides, dissolved in a solution composed of water and hydrochloric acid in different concentrations. We have used the technique of the efficiency transfer, through GESPECOR software for standardizing this set of sources to a solution composed of water and HCl at a concentration of 2 Normal ($\rho=1.001\text{ g cm}^{-3}$).

- Taking advantage of the above mentioned efficiency transfer technique, we performed a second GESPECOR run to evaluate the correction coefficient that takes into account the different geometries and chemical composition of the two container used for the calibration and for RM measurement.
- At this point we have evaluated the correction to the efficiency curve respect to the chemical composition and density of the material (self-attenuation). Each of these GESPECOR iterations produced the correction coefficients which have been subsequently multiplied to the experimental calibration curve (Equation 2.8).
- Finally, using the Monte Carlo simulations, we were evaluated the correction factors to the efficiency curve due to the phenomenon of coincidence summing.

The results of this procedure will be presented in the next chapter.

Calibration procedure for nuclear data measurement

By using the values of the measured calibration efficiency (ND calibration apparatus) and the efficiency transfer computed by GESPECOR we obtain an accurate efficiency curves of ^{235}U and ^{227}Ac .

The procedure used to obtain all the corrections to the efficiency curve is the following:

- The set of point-sources were measured on the INMRI HPGe detector in the ND calibration configuration.
- We used GESPECOR software to evaluate the geometrical difference between the ND calibration apparatus and the measurement apparatus.
- Through GESPECOR software we had evaluated the correction factor due to Coincidence summing and true coincidence summing effect. We obtained correction factors negligible because the source and the detector were at 10.05 cm of distance [45].

The results of this procedure will be presented in the Chapter 4.

2.7 Activity concentration determination

The number of counts under the full energy peak areas (corrected for background and blank peak areas), the counting time, the absolute full-energy peak efficiency for the energy of interest and the gamma-ray emission probability corresponding to the peak energy are used for the calculation of the activity concentration in the measured samples. The specific activity, in terms of the activity concentration, is defined as the activity per unit mass of the sample. The specific activity of individual radionuclides in samples is given by the following equation together with the legend explaining the meaning of the symbols [57]:

$$A = \frac{1}{\varepsilon I_{\gamma}} \left[\frac{N_{Nsa}}{LT_{sa}} - \frac{N_{Nb}}{LT_b} \right] \cdot e^{\frac{-\ln(2)[T_{ar} - T_{bsa}]}{t_{1/2}}} \cdot \frac{\ln(2)RT_{sa}}{86400 t_{1/2}} \cdot \frac{1}{\left[1 - e^{\frac{-\ln(2)RT_{sa}}{86400 t_{1/2}}} \right]} \cdot k_{SA} k_{ET} k_{CS} \quad (2.9)$$

- ε = Detector efficiency (experimentally measured).
- I_{γ} = Gamma emission intensity provide in DDEP database.
- N_{Nsa} = Source net area.
- N_{Nb} = Blank net area.
- LT_{sa} = Source live time.
- LT_b = Blank live Time.
- RT_{sa} = Source real time.
- T_{ar} = Date to which the activity has to be referred.
- T_{bsa} = Beginning date of the source measurement.
- $t_{1/2}$ = Half life.
- k_{SA} = Coefficient of self-attenuation.
- k_{ET} = Geometrical correction factor.
- k_{CS} = Coincidence summing coefficient.

In the above formula one recognizes two terms in which the half-life appears:

- The first one, $e^{\frac{-\ln(2)[T_{ar} - T_{bsa}]}{t_{1/2}}}$, brings back or forward in time the value of the activity referring it to the instant T_{ar} .
- The second term, $\frac{\ln(2)RT_{sa}}{86400 t_{1/2}} \cdot \frac{1}{\left[1 - e^{\frac{-\ln(2)RT_{sa}}{86400 t_{1/2}}} \right]}$, allows for the decay of the radionuclide during the measurement.

A warning has to be raised here: both of these terms are valid only if there is equilibrium between the parent nuclide and its daughters. On the contrary, if the radioactive processes are more complicated because the equilibrium has not been reached yet, more complicated terms have to be used, which, in general, will have to be calculated specifically for each case.

2.8 Emission probability determination

The method used in this work to evaluate the emission probability of a radionuclide involves the activity measurement of a source through a primary measurement method (i.e. mass spectrometry, gamma spectrometry). The knowledge of the source absolute activity allows us to use a relative measuring method, such as the gamma spectrometry, in order to assess the probability of emission of a radionuclide. Consider the Equation 2.12, if the object of our investigation is the I_γ we can write the relationship as follows:

$$I_\gamma = \frac{1}{\varepsilon A} \left[\frac{N_{Nsa}}{LT_{sa}} - \frac{N_{Nb}}{LT_b} \right] \cdot e^{\frac{-\ln(2)[T_{ar} - T_{bsa}]}{t_{1/2}}} \cdot \frac{\ln(2)RT_{sa}}{86400 t_{1/2}} \cdot \frac{1}{\left[1 - e^{\frac{-\ln(2)RT_{sa}}{86400 t_{1/2}}} \right]} \cdot k_{SA}k_{ET}k_{CS} \quad (2.10)$$

- ε = Detector efficiency (experimentally measured).
- A = A is the absolute activity of the source measured with a primary measurement method.
- N_{Nsa} = Source net area.
- N_{Nb} = Blank net area.
- LT_{sa} = Source live time.
- LT_b = Blank live time.
- RT_{sa} = Source real time.
- T_{ar} = Date to which the activity has to be referred.
- T_{bsa} = Beginning date of the source measurement.
- $t_{1/2}$ = Half life.
- k_{SA} = Coefficient of self-attenuation.
- k_{ET} = Geometrical correction factor.
- k_{CS} = Coincidence summing coefficient.

In the above formula one recognizes two terms in which the half-life appears:

- The first one, $e^{\frac{-\ln(2)[T_{ar} - T_{bsa}]}{t_{1/2}}}$, brings back or forward in time the value of the activity referring it to the instant T_{ar} .
- The second term, $\frac{\ln(2)RT_{sa}}{86400 t_{1/2}} \cdot \frac{1}{\left[1 - e^{\frac{-\ln(2)RT_{sa}}{86400 t_{1/2}}} \right]}$, allows for the decay of the radionuclide during the measurement.

A warning has to be raised here: both of these terms are valid only if there is equilibrium between the parent nuclide and its daughters. On the contrary, if the radioactive processes are more complicated because the equilibrium has not been reached yet, more complicated terms have to be used, which, in general, will have to be calculated specifically for each case.

In the efficiency evaluation we did not use the radionuclides that we wanted to calculate the emission probability, this operation was done to ensure that the activity term and efficiency term in the Equation 2.13 were independent.

2.9 Uncertainty evaluation

The main aim of the current study is to determine the value of the activity concentration for NORM radionuclide as ^{235}U , ^{238}U and ^{232}Th (and their decay progeny). These values will be indirectly inferred using Equation 2.12. The uncertainties of the parameters (input quantities in the measurement model) in this equation can be related to statistical (random) or systematic errors. The latter type of error occurs when the measurement itself promotes a consistent bias in all the results (i.e. from literature source). Systematic errors are corrected to the best knowledge, leaving an uncertainty characterized by a symmetrical distribution around the best estimate of the input quantity. Each uncertainty component generates a corresponding uncertainty on the measured output quantity. The various uncertainty components of the measurand are then combined in the final results giving the so called combined standard uncertainty of the results.

The uncertainty u characterizes the dispersion around the final value x where the unknown true value is expected to lie. A confidence interval is also usually quoted with the results of such a study called the expanded uncertainty. This can be obtained by multiplying the combined standard uncertainty by a suitable coverage factor k . In this case, the true value of activity concentration is covered by the interval between the limits $x - ku$ and $x + ku$ to give a $k\sigma$ confidence level [61].

This section discusses the source of uncertainty in the determination of the value of activity concentration of NORM radionuclide in the sample using the high-resolution gamma spectroscopy system.

Source of uncertainties

Identifying the source of uncertainty in gamma-ray spectroscopy is an essential step for determining high-quality results. The source of the standard uncertainties can be classified according to their origin into four categories [61]. These standard uncertainties are shown schematically in Figure 2.21.

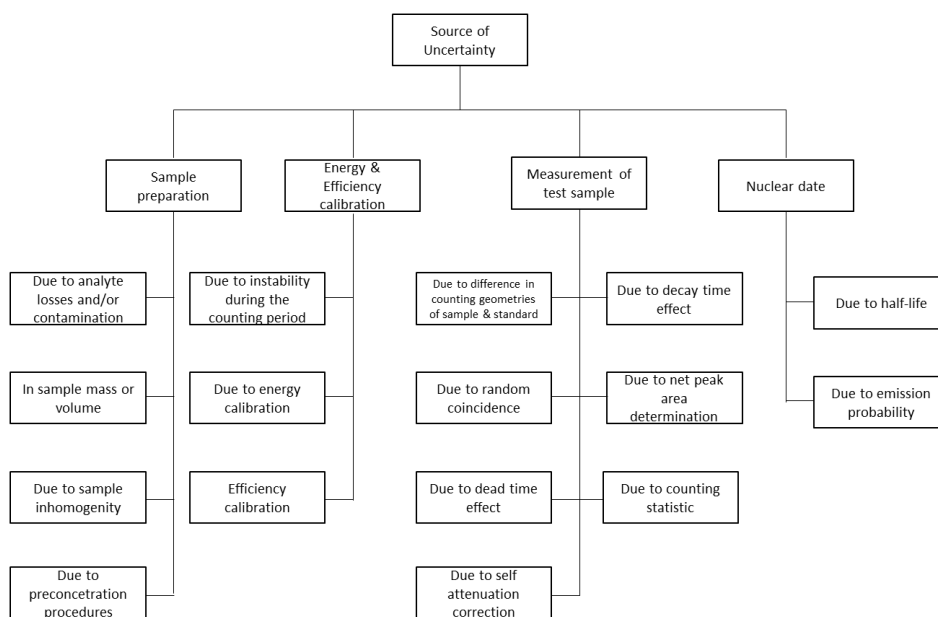


Figure 2.21. Diagram of possible uncertainties possibly arising in the determination of activity concentration of ^{235}U , ^{238}U and ^{232}Th using gamma spectroscopy.

Some of the uncertainties may be inferred before the start of measurement, such as uncertainties due to nuclear data and/or energy and efficiency calibrations. Other source of uncertainties, due to a variation of the sample and to the measurement of the test sample itself, are directly calculated from the measurement. Not all the mentioned uncertainties will significantly contribute to the combined uncertainties of the activity concentration. The most likely source of uncertainties in the current study are discussed in the following sections.

Energy and Efficiency Calibration

The purpose of the energy calibrations is to obtain a relationship between a peak position in the spectrum against the corresponding gamma-ray energy [61]. The energy calibration should cover the entire energy of interest ($0 - 3 \text{ MeV}$). The measured gamma-ray energies are only used to identify the nuclides in the spectrum. Any uncertainty in the measured gamma-ray energy does not affect the quantification of the final combined uncertainty associated with the number of counts in the peaks.

When a calibration source is prepared, it will be accompanied by a calibration measure. This will produce, for each nuclide, the activity per unit mass and the overall uncertainty on the activity: these uncertainties should then be taken into account when the efficiency calibration curve is created. In most of the cases, the calibration points will not exactly lie on the fitted calibration line. The degree of scatter of the calibration point around the line can be said to represent both the “goodness of fit” of the calibration data and the uncertainty of estimating the efficiency obtained by calculation from the calibration equation.

The other source of uncertainty in the calibration process is the usage of the Monte Carlo code to evaluate the correction to the efficiency curve due to the efficiency transfer, self-attenuation and true coincidence summing. The evaluation of this uncertainty is taken from GESPECOR software.

Uncertainty due to counting statistic

The most significant source of uncertainties in gamma-ray spectroscopy system is the statistical uncertainty due to counting statistic in a full energy peak at a given energy in the sample spectrum [61]. The counts of the radionuclide energies in the efficiency and sample spectrum were extracted using Gamma Vision the Canberra's software. The net peak count values were used to calculate the efficiency and activity concentrations of the sample.

Counting statistics are basically binomial. There are only two possible choices for each atom in the binomial distribution, i.e. to decay or not decay. Under most counting circumstances, this binomial distribution is assumed to become a Poisson distribution, if the number of nuclei is large and the observation time is short compared with the half-life of the radioactive species. If the mean value of the distribution is greater than ~ 20 , the Poisson distribution can be approximated by a normal or a "Gaussian" distribution. If the total number of possible events in binomial distribution is unknown, the Poisson distribution can be used in counting statistic.

It is important to derive a single parameter that can describe the degree of fluctuations predicted by a given statistical distribution. The overall uncertainty of the measurements is taken into consideration. The sum of the square of the difference in the measurement can be used to calculate the simple variance in the measurement [61], i.e.

$$var(x) = E(x) \tag{2.11}$$

where $E(x)$ is the expected value. A more convenient factor is the standard deviation, σ , which indicates the spread of the values about the $E(x)$:

$$\sigma = \sqrt{var(x)} \tag{2.12}$$

For a set of experimental, the predicted variance σ^2 , gives a measure of the scatter about the mean, predicted by a specific statistical model $P(x)$:

$$\sigma^2 = \sum_{x=0}^n (x - \bar{x})^2 P(x) \tag{2.13}$$

where $P(x)$ is the probability that an n count will be observed given the expected number of counts $E(x)$. The most likely number of decays is given by the Equation (2.17):

$$E(x) = pn = \bar{x} \quad (2.14)$$

where \bar{x} , in this case, is the mean value of the distribution. The Poisson distribution has similar properties to the binomial distribution, however the probability $p \ll 1$. This type of distribution can be calculated from the Equation (2.18):

$$P(x) = \frac{[E(x)]^x}{x!} e^{-E(x)} \quad (2.15)$$

Equation 2.18 can be written by using Equation 2.17 as follow:

$$P(x) = \frac{(\bar{x})^x}{x!} e^{-\bar{x}} \quad (2.16)$$

Then, the mean value of the distribution can be calculated from the Equation (2.20):

$$\sigma^2 = \sum_{x=0}^n x P(x) = pn \quad (2.17)$$

By using Equation 2.16, the predicted variance σ^2 of the distribution can be evaluated as follow:

$$\sigma^2 = \sum_{x=0}^n (x - \bar{x})^2 P(x) \quad (2.18)$$

$$\sigma^2 = \bar{x} \quad (2.19)$$

$$\sigma = \sqrt{\bar{x}} \quad (2.20)$$

Thus, the predicted standard deviation of any Poisson distribution is simply the square root of the mean value that characterizes that same distribution [61].

Nuclear data and decay half-life

Since the objects to analyze in gamma-ray spectrometry system are radionuclides, uncertainties in the evaluated nuclear data, such as the adopted decay half-life and absolute probabilities, contribute to the overall combined uncertainty of activity concentration. In most cases the uncertainty in the half-life is generally rather small compared to other source of uncertainty [61]. The data and the uncertainty on decay half-lives and gamma-ray transition branching ratios were taken for this study from DDEP database on the LHNB website.

Calculation of uncertainties for the reference material measurement

The estimated contribution from each component described in the previous section to the final uncertainty is a vital step in quantifying the uncertainty. As to the relative uncertainty related to the activity (Equation 2.12), it will contain several components due to the propagation of the relative uncertainty of all the quantities contained in the Equation (2.12). These components will be listed here:

- $u(A)|_{\varepsilon}$ = uncertainty of the activity due to the uncertainty of the efficiency ε .
- $u(A)|_{I_{\gamma}}$ = uncertainty of the activity due to the uncertainty of the gamma emission intensity (value provided by reference [73]).
- $u(A)|_{e^{-\frac{\ln(2)[T_{ar} - T_{bsa}]}{t_{1/2}}}}$ = $|T_{ar} - T_{bsa}| \ln(2) \frac{u(t_{1/2})}{t_{1/2}}$ uncertainty due to $t_{1/2}$.
- $u(A)|_{\frac{\ln(2)RT_{sa}}{86400 t_{1/2}} \cdot \frac{1}{\left[1 - e^{-\frac{\ln(2)RT_{sa}}{86400 t_{1/2}}}\right]}}$ = $\left[1 - e^{-\frac{\ln(2)RT_{sa}}{86400 t_{1/2}}}\right] \cdot \left[1 + \frac{\ln(2)RT_{sa}}{86400 t_{1/2}}\right] \cdot \left[\frac{u(t_{1/2})}{\left[1 - e^{-\frac{\ln(2)RT_{sa}}{86400 t_{1/2}}}\right]}\right]$.
- $u(A)|_{\left[\frac{N_{Nsa}}{LT_{sa}} - \frac{N_{Nb}}{LT_b}\right]}$ =
$$\begin{cases} N_{Nsa} \cdot \frac{u(LT_{sa})}{\left[\frac{N_{Nsa}}{LT_{sa}} - \frac{N_{Nb}}{LT_b}\right] \cdot LT_{sa}} \\ N_{Nb} \cdot \frac{u(LT_b)}{\left[\frac{N_{Nsa}}{LT_{sa}} - \frac{N_{Nb}}{LT_b}\right] \cdot LT_b} \\ N_{Nsa} \cdot \frac{u(N_{Nsa})}{\left[\frac{N_{Nsa}}{LT_{sa}} - \frac{N_{Nb}}{LT_b}\right] \cdot LT_{sa}} \\ N_{Nb} \cdot \frac{u(N_{Nb})}{\left[\frac{N_{Nsa}}{LT_{sa}} - \frac{N_{Nb}}{LT_b}\right] \cdot LT_b} \end{cases}$$
 uncertainty due to $LT_{sa}, LT_b, N_{Nsa}, N_{Nb}$.
- $u(A)|_{k_1}, u(A)|_{k_2}, u(A)|_{k_3}$ uncertainty due to the correction to the efficiency curve and provided by GESPECOR software.

The whole activity's relative uncertainty is just the square root of quadratic sum of the components of uncertainty:

$$\mathbf{u}(A) = \sqrt{\sum_j \mathbf{u}^2(A)|_j} \quad (2.21)$$

where the index j indicates the j^{th} component of the uncertainty.

The explicit form of the activity's uncertainty is:

$$\mathbf{u}(A) = \sqrt{\begin{aligned} & (\mathbf{u}(A)|_{\varepsilon})^2 + (\mathbf{u}(A)|_{I_{\gamma}})^2 + \left(\mathbf{u}(A) \left| \frac{\ln(2)[T_{ar} - T_{bsa}]}{t_{1/2}} \right. \right)^2 + \\ & + \left(\mathbf{u}(A) \left| \frac{\ln(2)RT_{sa}}{86400 t_{1/2}} \cdot \frac{1}{\left[1 - e^{-\frac{\ln(2)RT_{sa}}{86400 t_{1/2}}} \right]} \right. \right)^2 + \\ & + (\mathbf{u}(A)|_{LT_{sa}})^2 + (\mathbf{u}(A)|_{LT_b})^2 + (\mathbf{u}(A)|_{N_{Nsa}})^2 + (\mathbf{u}(A)|_{N_{Nb}})^2 + \\ & + (\mathbf{u}(A)|_{k_1})^2 + (\mathbf{u}(A)|_{k_2})^2 + (\mathbf{u}(A)|_{k_3})^2 \end{aligned}} \quad (2.22)$$

Calculation of uncertainties for the nuclear data measurement

The estimated contribution from each component described in the section on the nuclear data determination to the final uncertainty is a vital step in quantifying the uncertainty. As to the relative uncertainty related to the gamma emission intensity (Equation 2.13), it will contain several components due to the propagation of the relative uncertainty of all the quantities contained in the Equation 2.13. These components will be listed here:

- $\mathbf{u}(I_{\gamma})|_{\varepsilon}$ = uncertainty of the gamma emission intensity due to the uncertainty of the efficiency ε .
- $\mathbf{u}(I_{\gamma})|_A$ = uncertainty of the gamma emission intensity due activity measurement carried out through primary measurement method.

- $u(I_\gamma) \Big|_{e^{-\frac{\ln(2)(T_{ar} - T_{bsa})}{t_{1/2}}}} = |T_{ar} - T_{bsa}| \ln(2) \frac{u(t_{1/2})}{t_{1/2}}$ uncertainty due to $t_{1/2}$.
- $u(I_\gamma) \Big|_{\frac{\ln(2)RT_{sa}}{86400 t_{1/2}} \cdot \frac{1}{\left[1 - e^{-\frac{\ln(2)RT_{sa}}{86400 t_{1/2}}}\right]}} = \left[1 - e^{-\frac{\ln(2)RT_{sa}}{86400 t_{1/2}}}\right] \cdot \left[1 + \frac{\ln(2)RT_{sa}}{86400 t_{1/2}}\right] \cdot \left[\frac{u(t_{1/2})}{\left[1 - e^{-\frac{\ln(2)RT_{sa}}{86400 t_{1/2}}}\right]}\right]$
- $u(I_\gamma) \Big|_{\left[\frac{N_{Nsa}}{LT_{sa}} - \frac{N_{Nb}}{LT_b}\right]} = \begin{cases} N_{Nsa} \cdot \frac{u(LT_{sa})}{\left[\frac{N_{Nsa}}{LT_{sa}} - \frac{N_{Nb}}{LT_b}\right] \cdot LT_{sa}} \\ N_{Nb} \cdot \frac{u(LT_b)}{\left[\frac{N_{Nsa}}{LT_{sa}} - \frac{N_{Nb}}{LT_b}\right] \cdot LT_b} \\ N_{Nsa} \cdot \frac{u(N_{Nsa})}{\left[\frac{N_{Nsa}}{LT_{sa}} - \frac{N_{Nb}}{LT_b}\right] \cdot LT_{sa}} \\ N_{Nb} \cdot \frac{u(N_{Nb})}{\left[\frac{N_{Nsa}}{LT_{sa}} - \frac{N_{Nb}}{LT_b}\right] \cdot LT_b} \end{cases}$ uncertainty due to LT_{sa} , LT_b , N_{Nsa} , N_{Nb} .
- $u(I_\gamma) \Big|_{k_1}$, $u(I_\gamma) \Big|_{k_2}$, $u(I_\gamma) \Big|_{k_3}$ uncertainty due to the correction to the efficiency curve and provided by GESPECOR software.

The whole gamma emission intensity's relative uncertainty is just the square root of quadratic sum of the components of uncertainty:

$$u(I_\gamma) = \sqrt{\sum_j u^2(I_\gamma) \Big|_j} \quad (2.23)$$

where the index j indicates the j^{th} component of the uncertainty.

The explicit form of the gamma emission intensity's uncertainty is:

$$\begin{aligned}
 & u(I_\gamma) \\
 = & \sqrt{ \left(u(I_\gamma)|_\epsilon \right)^2 + \left(u(I_\gamma)|_A \right)^2 + \left(u(I_\gamma)|_{e^{-\frac{\ln(2)[T_{ar} - T_{bsa}]}{t_{1/2}}}} \right)^2 + \\
 & + \left(u(I_\gamma)|_{\frac{\ln(2)RT_{sa}}{86400 t_{1/2}} \cdot \frac{1}{\left[1 - e^{-\frac{\ln(2)RT_{sa}}{86400 t_{1/2}}} \right]}} \right)^2 + \\
 & + \left(u(I_\gamma)|_{LT_{sa}} \right)^2 + \left(u(I_\gamma)|_{LT_b} \right)^2 + \left(u(I_\gamma)|_{N_{Nsa}} \right)^2 + \left(u(I_\gamma)|_{N_{Nb}} \right)^2 + \\
 & + \left(u(I_\gamma)|_{k_1} \right)^2 + \left(u(I_\gamma)|_{k_2} \right)^2 + \left(u(I_\gamma)|_{k_3} \right)^2
 \end{aligned}
 \tag{2.24}$$

2.10 Determination of characteristic limits

The detection capabilities associated with measuring and analyzing radioactivity levels vary according to the instrumentation and analytic techniques used. For a low-level counting system, it is necessary to determine the ‘decision threshold’ above which counts can be considered statistically significant. The concept of a decision threshold (or critical level) and detection limit was established by Currie in 1968 [43]. The critical level, L_C , can be defined as a decision level above which the net counts represent some detected activity, with a certain degree of confidence. However, the decision limit is usually not significant for the activity measurement. A second limit, which is the detection limit can be introduced. The Detection Limit, L_D , can be defined as the number indicating the true net counts which will be detected above the acceptable level (L_C) with a given probability when real activity is present.

Mathematically, the decision threshold can be given by the following approximate relation [43] [57]:

$$L_C = 2.326 \frac{\sqrt{N_{sa} - bkg}}{LT_a \epsilon m I_\gamma} \tag{2.25}$$

And the detection limit by the following equation:

$$L_D = 4.65 \frac{\sqrt{N_{sa} - bkg}}{LT_a \epsilon m I_\gamma} \tag{2.26}$$

where N_{sa-bkg} are the background counts of the source and LT_a is the live time of the background measurement. These two limits are derived under the assumption that the only source of blank variability is due to statistical fluctuations and are expressed at the 95% confidence level.

The values of the decision threshold and detection limit of the gamma-ray spectrometry system were determined from the background measurement by counting an inactive blank container with the same geometry of the sample measurements, filled with de-ionized water.

2.11 Power moderate mean

The activity value of the CMR was obtained through the activity measurement carried out by three metrology institutes participating in the MetroNORM project. The power moderate mean (PMM) is based on a concept by Mandel-Paule [69] (M-P) mean. Its results are generally intermediate between arithmetic and weighted mean.

The power moderate mean can calculate an efficient and robust mean from any data set. For mutually consistent data, the method approaches a weights mean, the weights being the reciprocal of the variance (squared standard uncertainties) associated with the measured values. For data sets which might be inconsistent, the weighted mean is moderated by increasing the laboratory variance by a common amount and/or decreasing the power of the weighting factor. The task of this part of the work is to derive the best possible estimate of the object to measure (activity value of the CMRs) from a set of N measurement data x_i and associated standard uncertainty u_i . The method applies to data, which are mutually independent and normally distributed around the same value.

In the next part of the section the mathematical steps are shown in order of execution:

Calculate the M-P mean:

$$x_{mp} = \frac{\sum_{i=1}^N \frac{x_i}{x_i^2 + s^2}}{\sum_{i=1}^N \frac{1}{x_i^2 + s^2}} \quad (2.27)$$

where:

- x is the activity value;
- u is the uncertainty related to x value;
- s^2 is the variance;

using $s^2 = 0$ as initial value, which conforms to weighted mean.

Calculate the modified reduced observed X^2 value

$$\tilde{X}_{obs}^2 = \frac{1}{N-1} \sum_{i=1}^N \frac{(x_i - x_{mp})^2}{u_i^2 + s^2} \quad (2.28)$$

if $\tilde{X}_{obs}^2 > 1$ increase the variance s^2 and repeat step 1 and 2 until $\tilde{X}_{obs}^2 = 1$ is obtained, then assess the reliability of the uncertainties provided. After that calculate a characteristic uncertainty per datum, based on the variance associated with the arithmetic mean, \bar{x} or the M-P mean x_{mp} , whichever is larger.

$$S = \sqrt{N \cdot \max(u^2(\bar{x}), u^2(x_{mp}))} \quad (2.29)$$

in which

- $u^2(\bar{x}) = \sum_{i=1}^N \frac{(x_i - \bar{x})^2}{N(N-1)}$, $\bar{x} = \sum_{i=1}^N x_i$;
- and $u^2(x_{mp}) = \left(\sum_{i=1}^N \frac{1}{u_i^2 + s^2} \right)^{-1}$.

Calculate the reference value and uncertainty from a power-moderated weighted mean

$$x_{ref} = \sum_{i=1}^N x_i w_i \quad \frac{1}{u^2(x_{ref})} = \sum_{i=1}^N \left[\left(\sqrt{u_i^2 + s^2} \right)^\alpha S^{2-\alpha} \right]^{-1} \quad (2.30)$$

in which the normalized weighting factor is:

$$w_i = u^2(x_{ref}) \left[\left(\sqrt{u_i^2 + s^2} \right)^\alpha S^{2-\alpha} \right]^{-1} \quad (2.31)$$

where the power α is the reliability of uncertainty and can assume the following value: $\alpha = 2 - \frac{3}{N}$ where N is the number of value used to evaluate the PMM.

Statistical tools may be used to indicate data that are extreme. An extreme datum is such that the magnitude of the difference e_i between a measured value x_i and a candidate Key Comparison Reference Value (KCRV) x_{ref} exceeds a multiple of the standard uncertainty $u(e_i)$ associated with e_i :

$$|e_i| > k u(e_i), e_i = x_i - x_{ref} \quad (2.32)$$

where k is a coverage factor, typically between two and four, corresponding a specific level of confidence.

Applying the same Equation (2.33) and (2.34) to the PMM provides an elegant way to use the modified uncertainty:

$$u^2(e_i) = u^2(x_{ref}) \left(\frac{1}{w_i} - 1 \right) \quad (2.33)$$

$$u^2(e_i) = u^2(x_{ref}) \left(\frac{1}{w_i} + 1 \right) \quad (2.34)$$

The approach of using the modified uncertainties limits the number of values for which the inequity in Equation (2.32) holds.

After exclusion of any data, a new KCRV and its associated uncertainty are calculated, and on the basis of test (Equation (2.32)) possibly further extreme values are identified. The process is repeated until there are no further extreme values to be excluded [69].

Visualization of inter-laboratory comparison results in PomPlot

The PomPlot, an intuitive graphical method, is used for producing a summary overview of the participant' results of a common measurand. The PomPlot display (relative) deviations of individual results from the reference value on the horizontal axis and (relative) uncertainty on the vertical axis.

The PomPlot displays the relative deviations (D/MAD) of the individual results (x_{lab}) from reference value on the horizontal axis and relative uncertainties (u/MAD) on the vertical axis (Figure 2.20).

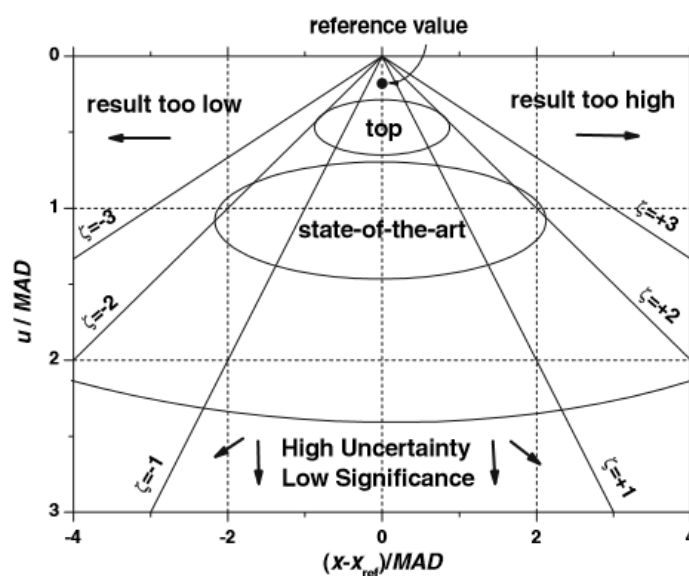


Figure 2.22: Interpretation of a PomPlot [70].

For both axes, the variables are expressed as multiples of MAD , which is defined as the median absolute deviation from the reference value (x_{ref}):

$$MAD = Median|D_i|, \quad (i = 1, \dots, n) \quad (2.35)$$

where D_i is the difference between the reported and reference activity:

$$D_i = x_{lab,i} - x_{ref} \quad (2.36)$$

The MAD was used because of its robustness. For every data point the uncertainties on $x_{lab,i}$ and x_{ref} :

$$u_i^2 = u^2(x_{lab,i}) + u^2(x_{ref}) \quad (2.37)$$

The ζ -score, $|\zeta| = |D/u| = 1, 2 \text{ and } 3$, are represented by diagonal solid lines, creating the aspect of a pyramidal structure (Figure 2.22). The ζ -score is a measure for the deviation between laboratory result and reference value relative to the total uncertainty, in conformity to with its definition. Dots on the right-hand side of the graph correspond to the results that are higher than the reference value while lower values are situated on the left. When the claimed uncertainty is low, the corresponding point is situated high in the graph. The most accurate results should be situated close to the top of the pyramid. Points outside of the $|\zeta| = \pm 3$ lines are probably inconsistent with the reference value [70].

Chapter 3

Reference Materials

Reference Materials are used for validation, quality assurance, calibration and development of new methods in many scientific disciplines. Therefore they form a benchmark for measurements.

In the ISO/Guide 30:2015 [64] a Reference Material (RM) is defined as a “material, sufficiently homogeneous and stable with respect to one or more specified properties, which has been established to be fit for its intended use in a measurement process”.

Instead a CRM is defined as a “Reference material accompanied by a certificate, one or more of whose property values are certified by a procedure which establishes traceability to an accurate realization to the unit in which the property values are expressed, and for which each certified value is accompanied by an uncertainty at a stated level of confidence” [64].

Aim of this part of the work is to realize and characterize a CRM for activity of natural radionuclides measurement with uncertainty up to 10% ($k=1$).

Three candidates CRMs were considered and evaluated:

- Tuff.
- Ionex resin.
- Titanium dioxide waste (TiO_2).

After a preliminary evaluation of the characteristics of those materials, we chose the Ionex resin to be elected as CRM through a characterization procedure. These materials, prepared by CMI⁸, were sealed in a metallic container. The standardization was carried out using a secondary measurement method, gamma-ray spectrometry with High purity Germanium (HPGe) detector. The reference value for the massic activity of ^{235}U and ^{238}U with the associated uncertainty was then carried out through a collaboration between three metrological institutes (CMI, ENEA, NPL⁹).

⁸ Czech Metrology Institute.

⁹ National Physical Laboratory.

Other task of this work is to use the CMR to develop a spectrometry activity measurement method for NORM sample: this procedure was provided by ENEA INMRI. At the end of this chapter the procedure used to validate the measurement method will be presented.

3.1 Preliminary evaluation of the candidate reference materials

In this part of the work, we present the preliminary evaluation of the candidate reference materials. These materials were prepared and found by three different institutes participating in the MetroNORM project, in particular the Tuff has been found and prepared by ENEA, Ionex resin by CMI and TiO_2 by NPL. Together with the procedure used for the preparation of the samples, in this section, we present the chemical characterizations, the homogeneity measurements and the preliminary activity measurements of the candidate reference materials.

3.1.1 Sample preparations

In this section we describe preparations, origins and main uses of all the samples under investigation.

Tuff

One of the materials chosen as a candidate reference material was Tuff. We chose this material for two main reasons: first of all because it has an enough amounts of natural radioactivity to be used as a calibration source for the spectrometer, the second reason is because it is widely used as a building material for homes and workplaces in the central-Italian regions. Tuff (from the Italian tufo) is a type of rock made of volcanic ash ejected from a vent during a volcanic eruption. Following ejection and deposition, the ash is compacted into a solid rock in a process called consolidation [65]. Tuff is widely used in Italy as a building material and it is extracted and processed by many industries. One of them is located in the Sabatini mountains in Rome's northern district.

These Tuff is called "bianco a scaglie nere" and it is typical of Sabatini Mountains: its name comes from the contamination of the Tuff by the pumice. The sample was purchased from an industry specialized in construction materials, located in the area of Anguillara (RM), the small town near ENEA Casaccia research center. In order to use it as reference material and to measure it with gamma spectrometry, the Tuff brick was crushed and the obtained powder was then sieved and dried.



Figure 3.1. A Tuff brick.

The grinding procedure took place in three distinct phases:

- The brick (*10 kg*) was coarsely crushed with an hammer, to obtain pieces small enough to be inserted into a grinder.
- We then coarsely ground the sample by setting the movable jaws of the grinder (Figure 3.2) at a distance of *10 mm*. This allowed us to make a Tuff dust, preventing the aggregation due to moisture present in the sample. The powder Tuff thus obtained was inserted into an oven at a temperature of *120 °C* for about *24 h* to delete all the moisture present in the sample (Figure 3.3). The optimum drying time was estimated by weighting the sample every three hours until the weighting has remained constant for at least three cycles of measurement.



Figure 3.2. Grinder used in the Tuff preparation.



Figure 3.3. Oven used to dry the Tuff sample.

- As a final step, we ground the Tuff for the second time by setting the jaws of the grinder to the shortest distance possible.

The drying of the sample carried out during the grinding process allowed us to calculate the coefficient fresh/dry (*1.13*) necessary during the analysis of the activity of the radioactive sample.

The sample, after the grinding procedure, was sifted (Figure 3.4). We selected the dust Tuff of magnitude less than the *100 mesh (150 μm)* to make the sample as compact as possible. The Tuff density is: *0.96 g cm⁻³*.



Figure 3.4. Device used to sift the Tuff powder.

Ionex resin

Ionex is a material from water purification filters used for removing uranium from water, one of the advantages of this material is that it can be regenerated. The uranium obtained from the regeneration can be then recycled in other industry sectors. Concerning water composition, there are two types of Ionex: weakly basic annex and strongly basic annex. The sample in Figure 3.5 is a strongly basic annex. It is a styren-divinylbenzene copolymer with trialkyl-amin-groups. The insoluble matrix in the form of small beads provides a high surface area. Mean bead size is *0.64 mm*.



Figure 3.5. Ionex before (right side) and after (left side) regeneration.

The Ionex technology (Figure 3.6) is beneficial because it is highly selective for uranium, does not change the taste or properties of drinking water and it is easy to operate.



Figure 3.6. The process of water purification in waterworks.

Radioactive Ionex was obtained from waterworks in the Czech Republic from an industry which is the producer of Ionex technology.

The sample analyzed contains a large amount of carbonates (sediments from water, approx. 250 g per 1 kg of Ionex), which caused inhomogeneity of the sample and had to be removed from the sample before gamma-ray spectrometry measurement.

The sample immersed in distilled water was placed into the ultrasonic bath. Then, the sample was washed with distilled water on a sieve (0.3 mm). Most of carbonates were removed. No significant amount of uranium was detected in the waste water nor in the removed carbonates. A sample of the treated Ionex was finally air dried in a desiccator with P₂O₅ and mixed up.

Bulk density of the active Ionex samples was about 0.79 g cm⁻³. The samples were dried in a desiccator with P₂O₅ and the content of water in Ionex resin sample was determined as 10%.

TiO₂

The titanium dioxide is a chemical compound that occurs in the form of colourless crystalline powder, tending to white; its chemical formula is TiO₂. The titanium dioxide, due to its high refractive index, is mainly used as white pigment in paints, plastics and building cement, and as a matting agent for coloured paints; for this reason, it is also commonly called "titanium white" [66] [68]. With the aim of making it a sample for gamma-ray spectrometry the following operation were operated: raw material was inserted into several large containers for drying in a microwave to get rid of all moisture content (Figure 3.7). After the drying process, the material was transferred into a mortar and carefully crushed.

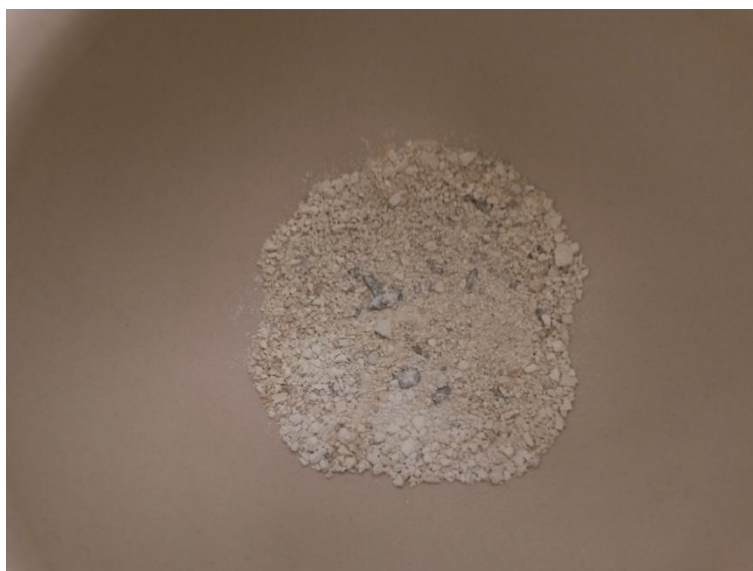


Figure 3.7. Titanium Oxide material after it is dried in microwave oven.

After that, content was ground into powder form using a gyro-mill, and the content was then sieved to 100 mesh (150 μm). The TiO₂ material was then transferred into an Inversina 2 L

mixer (Figure 3.8), to produce a perfectly homogenized powder, using a special three-dimension inversion kinematic.



Figure 3.8. Inversina 2 L mixer used to homogenized the powder.

At the end the material was bottled in 50 g Azlon bottles (Figure 3.9).

The density of this material is 1.45 g cm^{-3} .

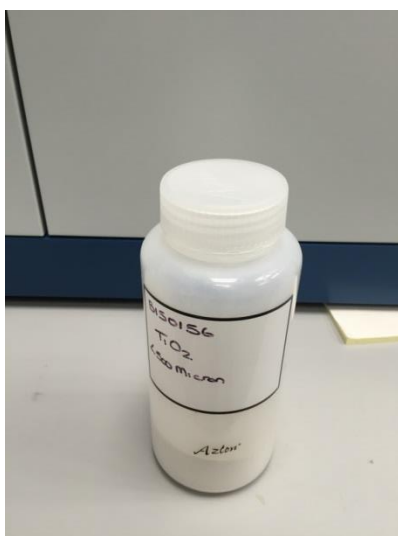


Figure 3.9. Titanium Oxide material in 50 grams Azlon bottles.

3.1.2 Chemical characterization

All NORM samples were examined in a Camscan MX2500 scanning electron microscope that is fitted with an Oxford Instruments Ltd. “INCA Energy” X-Max 80 Silicon drift detector for acquiring energy-dispersive X-ray (EDX) spectrum. Backscattered electron images, which show atomic number contrast, were examined for the presence of impurity phases within the sampled materials. The SEM was operated at an accelerating voltage of $30kV$, and EDX spectra were measured over a time period of 300 s to allow the detection of elements present in low concentrations i.e. $\approx 0.1wt\%$. The NORM samples were attached to SEM stubs using double-sided conductive carbon disks. A thin layer of carbon was deposited onto the samples by a thermal evaporation process to make them electrically conductive for electron microscopy and EDX analysis. The EDX spectra are processed using a matrix-correction program (ZAF-correction factors, where Z = atomic number, A = absorption and F = fluorescence) to quantify the chemical composition. However, it is not possible to quantify light elements such as carbon, oxygen and nitrogen accurately due to poorly known ZAF correction factors. NORM samples: Tuff (volcanic ash), Ionex Resin and TiO_2 were examined in the SEM and analyzed using EDX spectroscopy. Approximate sample compositions were determined from the EDX data. Carbon (apart from in the measurement of Ionex Resin) was excluded from the analysis as it was applied as a conductive layer on the samples.

Tuff

Through an EDX measurement, we have obtained the chemical composition of the sample. In Figure 3.10 (a) the image of Tuff sample obtained through the detection of backscattered electrons is shown, and in Figure 3.10 (b) the spectrum obtained with the EDX is shown. By using this information we have obtained the chemical composition of the material.

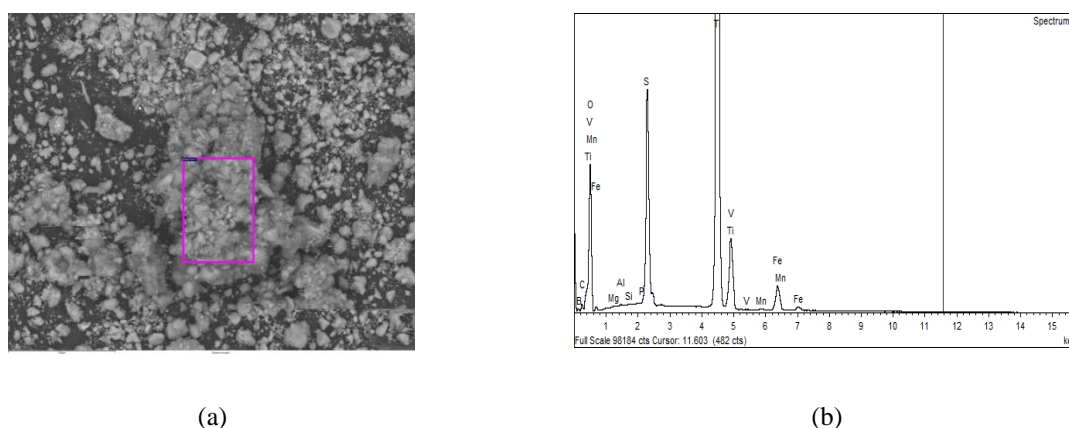


Figure 3.10. Backscattered electron image of Tuff sample (volcanic ash) (a) and its EDX spectrum (b).

The isotopic composition of the Tuff sample is shown in Table 3.1:

Table 3.1. Approximate composition of Tuff sample.

<i>Elements</i>	<i>Abundance [%]</i>
Si	34.44
K	19.64
Ca	17.66
Al	12.38
Fe	10.71
Ti	1.47
Ba	0.81
S	0.78
Sr	0.76
P	0.42
Mn	0.40
Zr	0.23
Pb	0.06
Th	0.02
Y	0.02
Nb	0.02

Ionex Resin

Ionex resin was examined in the SEM and analyzed using EDX spectroscopy. Approximate sample composition was determined from the EDX data. Unfortunately in this case EDX spectrum was not possible due to sample matrix. The backscattered electron image is shown in Figure 3.11. The composition of the sample with Ionex resin created, as we see in the next chapter, was determined also by CHNS - Carbon, hydrogen, nitrogen, and sulfur (light element) analysis on the device Elementar vario EL III. The content of oxygen was calculated

from the content of water in the sample (drying at $105\text{ }^{\circ}\text{C}$) and from the content of HSO_4 groups in the sample (from the content of sulphur).

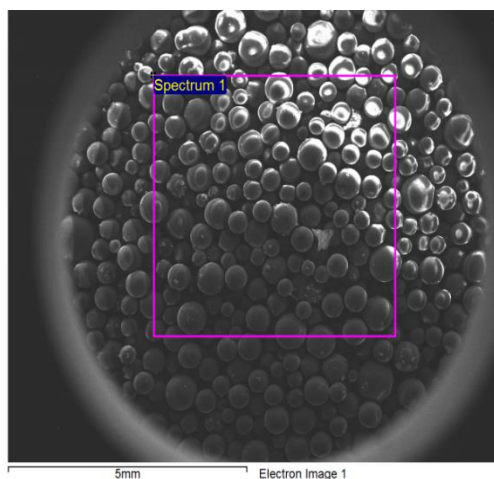


Figure 3.11. Backscattered electron image of Ionex resin sample.

The isotopic composition of the Ionex resin sample is shown in Table 3.2.

Table 3.2. Approximate composition of Ionex resin sample.

<i>Elements</i>	<i>Abundance [%]</i>
C	59.72
N	11.51
O	12.23
H	11.41
S	4.62
U	0.54

TiO₂

TiO_2 was examined in the SEM and analyzed using EDX spectroscopy. Approximate sample compositions were determined from the EDX data. The backscattered electron images and EDX spectrum are shown in Figure 3.12 and approximate chemical compositions are given in Table 3.3.

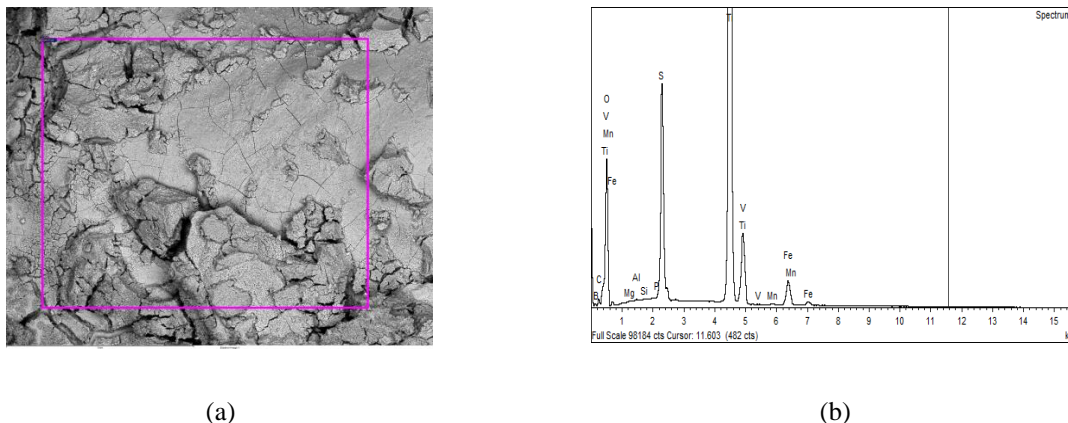


Figure 3.12. Backscattered electron image of TiO₂ sample (a) and its EDX spectrum (b).

Table 3.3. Approximate composition of TiO₂ sample.

<i>Elements</i>	<i>Abundance [%]</i>
O	44.11
Ti	41.69
S	9.21
Fe	2.84
H	2.15

3.1.3 Homogeneity measurements

A comparison of the net peak areas of the main energy gamma lines were made to evaluate the homogeneity for the three selected materials. CMI carried out evaluation data of homogeneity for the Ionex resin material, ENEA for the Tuff and NPL for TiO₂.

Tuff

The homogeneity of the Tuff is guaranteed because the entire sample was extrapolated from a single brick; the size of it is of most commonly used in the building industries.

The same amount of Tuff (100 g) was filled in six identical containers (Figure 3.13). Each of these containers was measured by gamma-ray spectroscopy for 84400 s.



Figure 3.13. Tuff sample used for homogeneity evaluation.

Then the spectra were analyzed and net peak counts for the most intense peaks were compared. The coefficient of variation for each nuclide is up to 1.04%. The results of radiation homogeneity for the Tuff sample using gamma-ray spectrometry are listed in Table 3.4.

Table 3.4. The data collected in the table represents the Tuff homogeneity measurement.

<i>Radionuclide</i>		^{208}Tl	^{214}Pb	^{212}Bi	^{228}Ac	^{40}K
<i>Photon Energy [keV]</i>		583.53	351.93	609.30	911.19	1460.80
Sample [#]	1	16751	25074	18135	11241	17093
	2	16804	24937	18132	11362	16578
	3	16776	25439	18252	11371	16996
	4	16750	24801	18248	11345	16876
	5	16800	24803	18134	11234	16850
	6	16685	24965	18080	11153	16944
Average [#]		16763	24989	18169,20	11293	16848,80
<i>Standard Deviation</i>		43.80	259.49	68.43	88.18	175.78
<i>Coefficient of Variation [%]</i>		0.26	1.04	0.38	0.78	1.04

Ionex Resin

The same amount of Ionex resin (50 g) was filled in the seven identical containers. Each of these containers was measured 50000 s.



Figure 3.14. Seven identical containers filled with the same amount of Ionex resin.

Then the spectra were analyzed and net peak counts of the most intense peaks were compared. The coefficient of variation for each nuclide is up to 1%.

Table 3.5. The data collected in the table represents the Ionex resin homogeneity measurement.

<i>Radionuclide</i>		^{234}Th	^{234}Th	^{235}U	^{235}U	^{235}U
<i>Photon Energy [keV]</i>		63.30	92.38 and 92.80	143.77	163.36	185.72
<i>Sample [#]</i>	1	437749	813453	88022	40192	421784
	2	437325	812135	89513	40446	427504
	3	435186	803363	89264	40322	426861
	4	434702	811453	89753	40774	427172
	5	432327	806705	89402	40194	423955
	6	433224	815118	88954	41085	426467
<i>Average [#]</i>		434897.30	810574.48	89073.27	40584.55	426259.46
<i>Standard Deviation</i>		1883.35	3304.39	553.32	362.62	1279.99
<i>Coefficient of Variation [%]</i>		0.43	0.41	0.62	0.89	0.31

TiO₂

The same amount (50 g) of TiO₂ was then filled in six identical containers (Azlon bottles, Figure 3.9). Each of these containers was measured for 30000 s. Then the spectra were analyzed and net peak counts of the most intense peaks were compared. The coefficient of variation for each nuclide is up to 1%.

Table 3.6. The data collected in the table represents the TiO₂ homogeneity evaluation.

<i>Radionuclide</i>		²⁰⁸ Tl	²¹⁴ Pb	²¹² Bi	²²⁸ Ac	⁴⁰ K
<i>Photon Energy [keV]</i>		583.53	351.93	609.30	911.19	1460.80
Sample [#]	1	7682	9173	6775	5524	9732
	2	7689	9230	6801	5495	9801
	3	7701	9306	6828	5600	9768
	4	7790	9219	6789	5489	9820
	5	7648	9389	6801	5510	9662
	6	7592	9210	6793	5442	9782
Average [#]		7684	9255	6798	5510	9761
<i>Standard Deviation</i>		65.3	79.0	17.6	52.2	56.9
<i>Coefficient of Variation [%]</i>		0.85	0.85	0.26	0.95	0.58

3.1.4 INMRI activity measurements

In this section we present the strategy used for the preliminary activity measurement of the candidate reference materials. The determination of the activity of natural origin radionuclides are complex due to the large number of radionuclides present in the samples. Moreover, each radionuclide can decay through many different nuclear transitions and thus, it has a large number of emission lines. If a radionuclide has multiple gamma-rays then the weighted mean from the activity of several gamma lines was calculated after checking if they are consistent with each other. The gamma lines used for a radionuclide are those with a probability greater than 1%. When we are calculating the activity of a decay chain, activity of a long-lived radionuclides are present and several short-lived daughter nuclides may also have contributed to the final activity. So the final activity for long-lived nuclides can be calculated as the weighted mean of the daughter nuclides activities, if they are in secular equilibrium. Assuming a state of secular equilibrium, a wide range of relatively intense gamma-ray transitions were used and these could be combined to estimate the activity concentrations of

^{238}U and ^{232}Th in the samples. The activity concentration of ^{238}U was determined using the gamma-ray transitions associated with decays of ^{226}Ra (186.21 keV), ^{214}Pb (295.22 and 351.93 keV) and ^{214}Bi (609.31, 1120.28, 1238.11, 1764.49 and 2204.21 keV). The gamma-ray energy peaks associated with decays of ^{228}Ac (338.32, 911.19 and 968.96 keV), ^{212}Pb (238.63 and 300.08 keV), ^{212}Bi (727.33 and 1620.73 keV) and ^{208}Tl (583.18 and 2614.51 keV) were used to determine the activity concentration of ^{232}Th . Activity for ^{235}U is calculated from its own gamma-lines, but for 186.62 keV line it is calculated from ^{226}Ra , which interferes with this gamma-line. The activity of ^{226}Ra was calculated from its daughter nuclides and therefore it is possible to calculate the amount of counts at the energy of 186.62 keV, by subtracting the counts from that peak, the result in counts for ^{235}U can be given. Activity of ^{227}Ac is calculated from ^{227}Th . ^{40}K is calculated from their own gamma-line (1460.82 keV). The nuclear decay data are taken from the DDEP website. Equilibrium between ^{226}Ra and the ^{222}Rn daughters in all samples have been reached, this is due because there were 30 d between sample preparation and measurement. The net number of counts under each photo-peak of interest were then background subtracted using the time corrected background spectrum taken using the de-ionized water blank measurement. The absolute full-energy peak efficiency and the relative gamma-ray intensity were used to calculate the final activity concentrations of a particular nuclide.

In the next sections were discuss in details the strategy used to determine the activity concentration of candidate reference materials.

Tuff

The Tuff sample was measured for 500000 s, one month after its preparation. This amount of time allows to establish the secular equilibrium within the sample.

The experimental apparatus was the measurement apparatus explained in Chapter 2, the use of the glass container guarantees the establishment of secular equilibrium. In fact glass permit to keep the Radon gas inside the container. We used GESPECOR software to evaluate: the geometrical correction respect to RM calibration apparatus, the self-attenuation and the CS correction. GESPECOR, to do this operations needs to know the chemical composition of the measured samples, its density ($\rho=0.96 \text{ g cm}^{-3}$) and the materials that constitute the experimental apparatus both in the measurement configuration and in the calibration configuration.

In Figure 3.15 the magnitude of CS corrections, as function of energy, carried out from GESPECOR software is shown. We can observe at specific points the differences due to coincidence summing. In this case corrections have the maximum value (-20%) for ^{208}Tl at 252.6 keV.

In Figure 3.16 the result of the calibration procedure respect to MR calibration curve is shown as function of energy. The curve in Figure 3.17 shows the relationship between the efficiency of the MR calibration apparatus versus the efficiency of the measurement apparatus, this is

done to underline how large the correction between these two different configurations could be.

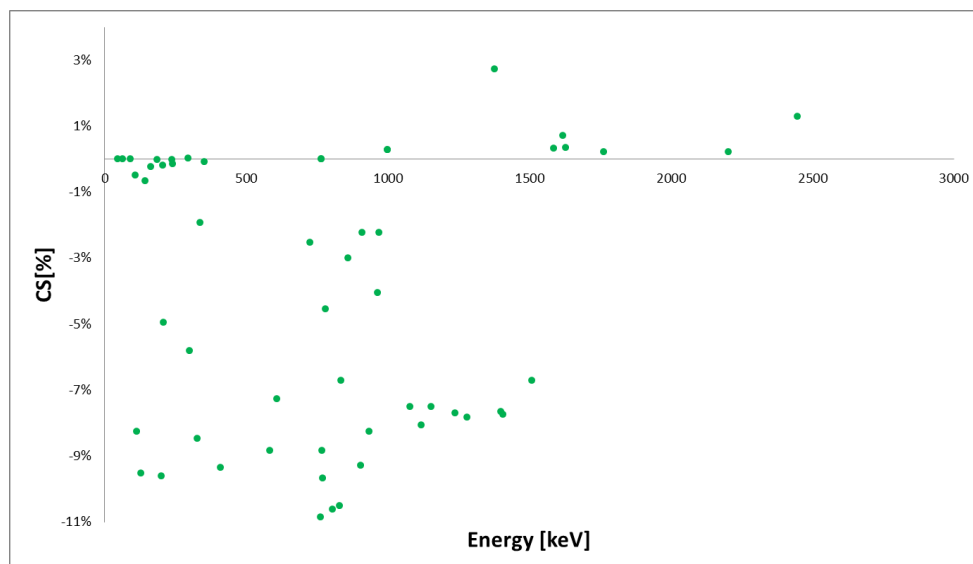


Figure 3.15. CS correction factor in the Tuff sample.

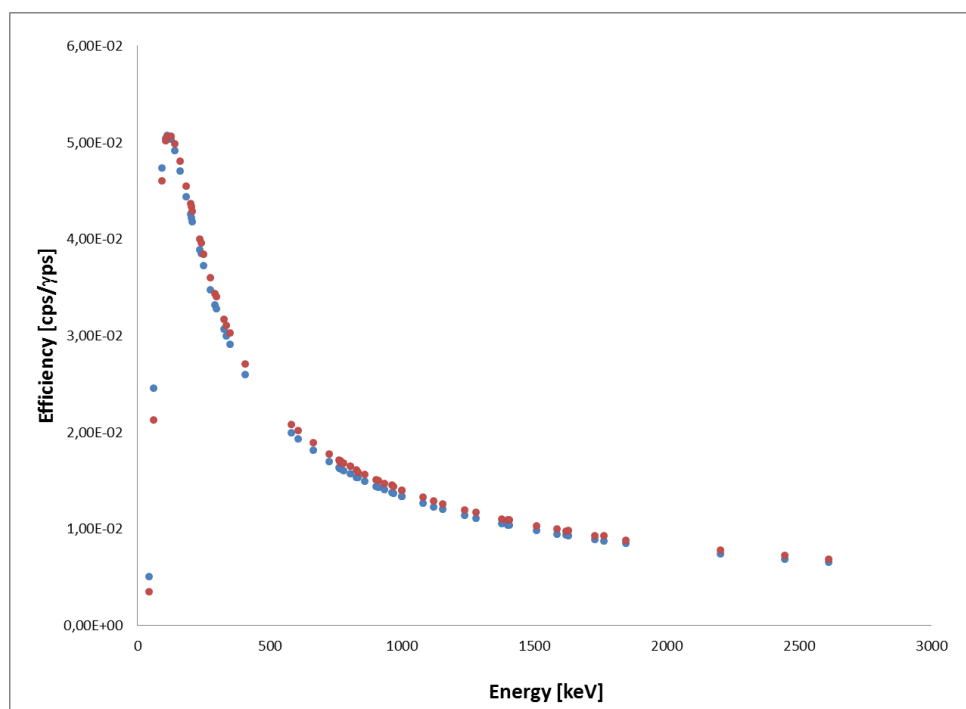


Figure 3.16. Calibration curve of the MR calibration apparatus (blue) and calibration curve of the measurement apparatus (red).

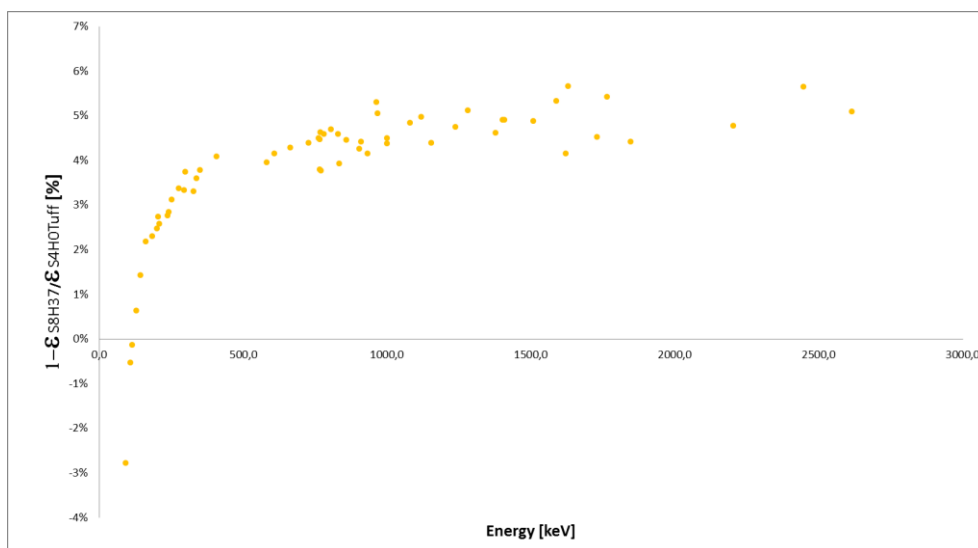


Figure 3.17. Difference in percentage between the efficiency of the MR calibration apparatus versus the efficiency of the measurement apparatus.

In Figure 3.16 we could observe that the percentage difference of the efficiency curve of the MR calibration apparatus compared to the efficiency curve of the measurement apparatus reaches a minimum of -2.8% at (^{214}Bi), at energies lower than 200 keV. In this part of the spectrum the dominant phenomenon that determines these differences between the two calibration curves is the CS [44]. On the other hand, for a 130 keV energy we observe a reversal of the trend described above. In fact, in this region of the spectrum the S4H0 configuration (Tuff) is more efficient than S8H37. The measurement configuration is geometrically more favourable than the MR calibration due to the shape of the container and due to the fact that it is positioned in contact with the detector since the disc-centering samples (H37) (Figure 2.9 (a)) in this configuration was not used. The correction factor due to the different geometrical configuration is more relevant respect to the CS correction for energies exceeding 200 keV. We can observe differences between the two configurations that are around 5%. The gamma-ray spectrometry spectrum of the Tuff sample is shown in Figure 3.18.

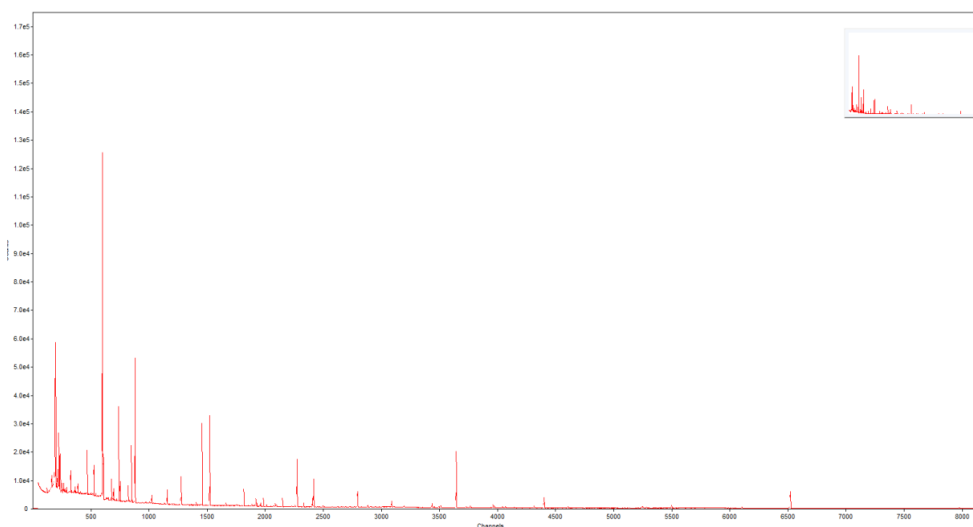


Figure 3.18. Tuff gamma-ray spectrum.

^{235}U disintegrates by alpha emission to the excited levels of ^{231}Th which in turn emits gamma-rays that can be detected to count the disintegrations of the parent nuclide (^{235}U). In Table 3.7, the most intense gamma energies emitted after the disintegration of one nuclide of ^{235}U are reported:

Table 3.7. ^{235}U gamma emission energy [73].

<i>^{235}U disintegrations counted by the gamma emission of ^{231}Th</i>			
<i>Photon Energy [keV]</i>	<i>Uncertainty – Energy [keV]</i>	<i>Photons per 100 disintegrations</i>	<i>Uncertainty - Photons per 100 disintegrations</i>
109.191	0.070	1.66	0.013
143.767	0.003	10.94	0.060
163.356	0.003	5.08	0.030
185.720	0.004	57.0	0.300
202.12	0.010	1.08	0.020
205.316	0.004	5.02	0.030

The most intense gamma emission takes place at 185.72 keV , however it is also known that ^{226}Ra (which belongs to the ^{238}U series) emits at 186.21 keV . Being these energies so close to each other, the relative counts would pile up in one single peak. Thus, first we have to evaluate the activity of ^{226}Ra from its daughter nuclides like ^{214}Pb and ^{214}Bi . Then subtract the ^{226}Ra contribution to 185.72 obtain the ^{235}U activity. ^{40}K decay in ^{40}Ar in an excited nuclear state through β^+ -decay afterwards it decays in its ground state through the emission of 1460.82 keV gamma-ray photon. ^{210}Pb activity measurement was carried out through the 46.53 keV emission line.

Table 3.8. ^{234}Th gamma emission energy [73].

<i>^{234}Th disintegrations counted by the gamma emission of ^{234m}Pa</i>			
<i>Photon Energy [keV]</i>	<i>Uncertainty – Energy [keV]</i>	<i>Photons per 100 disintegrations</i>	<i>Uncertainty - Photons per 100 disintegrations</i>
766.361	0.020	0.323	0.004
1001.026	0.018	0.847	0.008

^{228}Ra disintegrates with β^- -emission to ^{228}Ac , which possesses many gamma emissions. In Table 3.9 are listed the most probable emission lines of ^{228}Ac . This method produces the correct result only if the parent radionuclide (^{228}Ra) is in equilibrium with its daughter nuclides (^{228}Ac). Thanks to the short half-life of ^{228}Ac (6.13 h), one is justified to reckon that this condition will be fulfilled after waiting for a sufficiently long amount of time which is about 5 times this half-life. The most intense emission line of ^{228}Ac is those at 911.196 keV .

Table 3.9. ^{234}Th gamma emission energy [73].

<i>^{228}Ra disintegrations counted by the gamma emission of ^{228}Ac</i>			
<i>Photon Energy [keV]</i>	<i>Uncertainty – Energy [keV]</i>	<i>Photons per 100 disintegrations</i>	<i>Uncertainty - Photons per 100 disintegrations</i>
99.05	0.120	1.26	0.040
129.065	0.003	2.50	0.07
209.248	0.007	3.97	0.13

<i>²²⁸Ra disintegrations counted by the gamma emission of ²²⁸Ac</i>			
<i>Photon Energy [keV]</i>	<i>Uncertainty – Energy [keV]</i>	<i>Photons per 100 disintegrations</i>	<i>Uncertainty - Photons per 100 disintegrations</i>
270.245	0.007	3.55	0.10
328.004	0.007	3.04	0.11
409.460	0.013	2.02	0.06
911.196	0.006	26.2	0.08

²²⁸Th measurement was made through the measurement of ²¹²Bi and ²⁰⁸Tl which have emission lines of sufficiently intense to be measured by gamma-ray spectrometry. All the elements belonging to this radiative chain have a very short half-life, with the exception of ²²⁸Th which has a half-life of 1.91 years. Consequently, it will be sufficient to seal the sample and wait for a time greater than 5 times the longest half-life in the chain (²²⁴Ra 3.66 d) to determine the secular equilibrium within the sample. Once this condition is achieved it is possible to bring the activities of ²²⁸Th to that of ²¹²Bi and ²⁰⁸Tl. The most intense gamma emission lines used to measure ²¹²Bi and ²⁰⁸Tl are listed in Table 3.10 and Table 3.11. The 510.97 keV emission line of ²⁰⁸Tl was not included in the mean of ²⁰⁸Tl activity because that line has an interference with the single escape peak of the detector (511 keV). In fact, during the pair production, a possible phenomenon of interaction of radiation with matter, one of the two photons generated from the annihilation of the positron can escape from the detector. The other photon emitted at 180° respect to the first one can fully release its energy within the detector, creating a peak in the energy spectrum at 511 keV. In this condition there is an interference between the ²⁰⁸Tl peak and the single escape peak and since it is difficult to evaluate this interference we decided to eliminate these contributions from the evaluation of ²⁰⁸Tl the activity concentration.

Table 3.10. ²¹²Bi gamma emission energy [73].

<i>²²⁸Th disintegrations counted by the gamma emission of ²¹²Bi</i>			
<i>Photon Energy [keV]</i>	<i>Uncertainty – Energy [keV]</i>	<i>Photons per 100 disintegrations</i>	<i>Uncertainty - Photons per 100 disintegrations</i>
727.330	0.009	6.65	0.04

<i>²²⁸Th disintegrations counted by the gamma emission of ²¹²Bi</i>			
<i>Photon Energy [keV]</i>	<i>Uncertainty – Energy [keV]</i>	<i>Photons per 100 disintegrations</i>	<i>Uncertainty - Photons per 100 disintegrations</i>
785.37	0.090	1.11	0.01
1620.738	0.010	0.12	0.13

Table 3.11. ²⁰⁸Tl gamma emission energy [73].

<i>²²⁸Th disintegrations counted by the gamma emission of ²⁰⁸Tl</i>			
<i>Photon Energy [keV]</i>	<i>Uncertainty – Energy [keV]</i>	<i>Photons per 100 disintegrations</i>	<i>Uncertainty - Photons per 100 disintegrations</i>
510.723	0.020	22.5	0.2
583.187	0.002	85.0	0.3
860.531	0.020	12.4	0.4
2614.511	0.010	99.7	0.5

In Table 3.12 the activity concentrations of the more intense radionuclide present in the Tuff sample are reported.

Table 3.12. Results of Tuff sample by gamma- ray spectrometry.

<i>Radionuclide</i>	<i>$A_c \pm u(A_c)$ [Bq/g]</i>
²³⁵ U	19.1 ± 5.8
²²⁶ Ra	227.2 ± 36.1
²¹⁰ Pb	381.3 ± 76.2
²²⁸ Ra	344.29 ± 12.02

<i>Radionuclide</i>	$A_c \pm u(A_c)$ [Bq/g]
^{228}Th	347.81 ± 11.04
^{40}K	1765.2 ± 198.6

The chemical compositions of Tuff appear to be characterized by an exceptional enrichment in ^{238}U , ^{232}Th and ^{40}K , possibly due to a coupled effect of source composition and magma evolution at shallow levels. Lithification due to glass to zeolites conversion does not provide significant enrichment/depletion of ^{238}U and ^{232}Th , whereas volcanic rocks appear to undergo a remarkable enrichment during acid hydrothermal alteration. The characterization of the Tuff material showed that many radionuclides were present in the sample with enough activity to be measured on standard detector. The measured activities of this sample were in the same order than the one found in literature [67]. The activity of ^{235}U daughters may have been too low to be used easily for detector calibration.

Ionex resin

The Ionex resin sample was measured for 500000 s, one month after its creation. This time is necessary to establish the secular equilibrium in the radioactive chains. The density of this material is 0.79 g cm^{-3} .

The calibration apparatus used for this measurement was the MR calibration apparatus. For this measurement we used the INMRI standard container, S8H37. The activity concentration of ^{235}U was carried out through its most intense emission line and through the daughter of ^{238}U (^{234}Th and $^{234\text{m}}\text{Pa}$). We used GESPECOR software to evaluate the geometrical correction respect to MR calibration apparatus, the self-attenuation and the true coincidence summing correction in this configuration we had the same calibration and measurement apparatus the only difference were in the chemical composition between the calibration source and the sample under measurement.

The corrections due to the CS are shown in Figure 3.19, in Figure 3.20 is shown the result of the calibration procedure together with experimental calibration curve as function of energies (MR calibration apparatus). Instead in Figure 3.21 is shown the percentage difference between the MR calibration apparatus curve and the measurement configuration curve, to underline how large that correction might be.

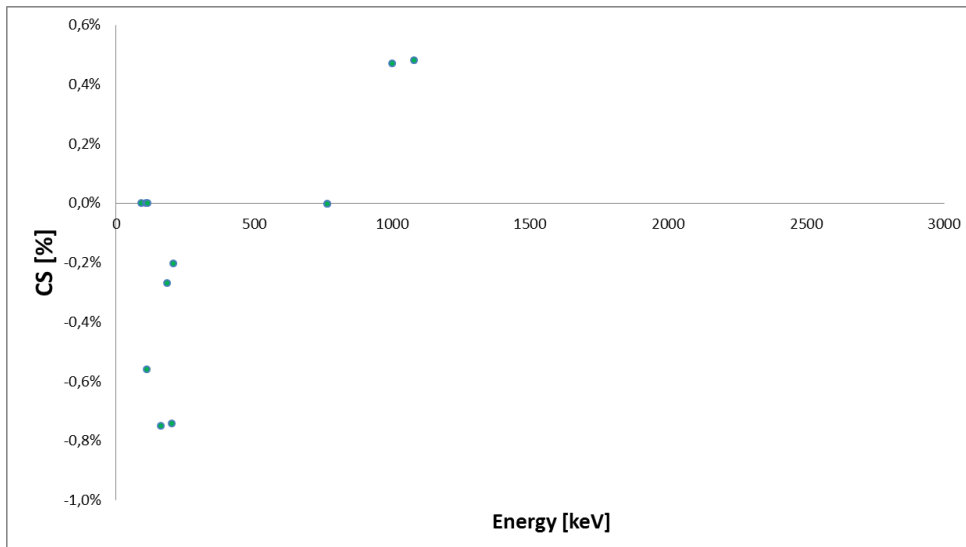


Figure 3.19. CS correction factor in the TiO_2 sample.

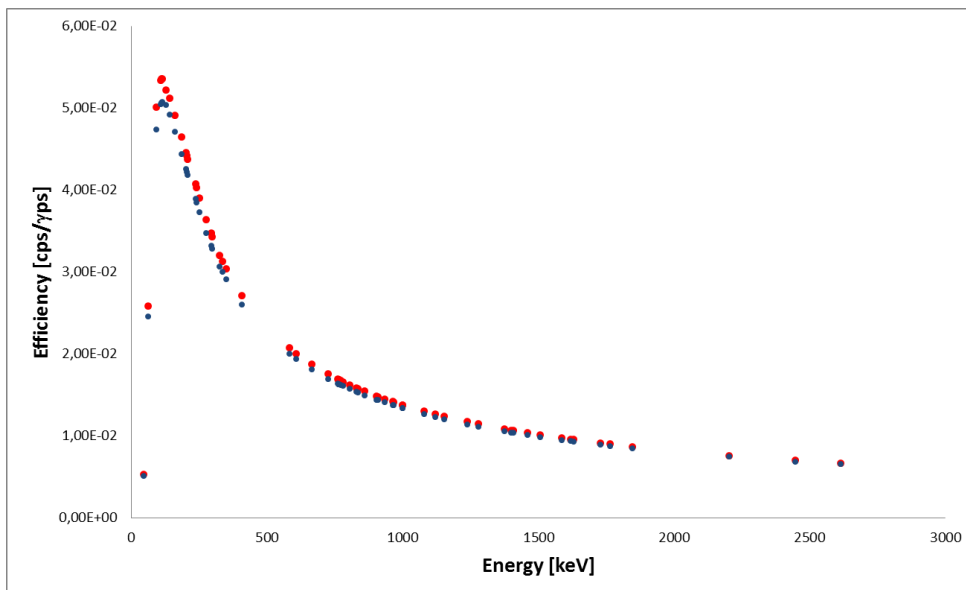


Figure 3.20. Calibration curve MR calibration apparatus (blue) and calibration curve of the measurement apparatus (red).

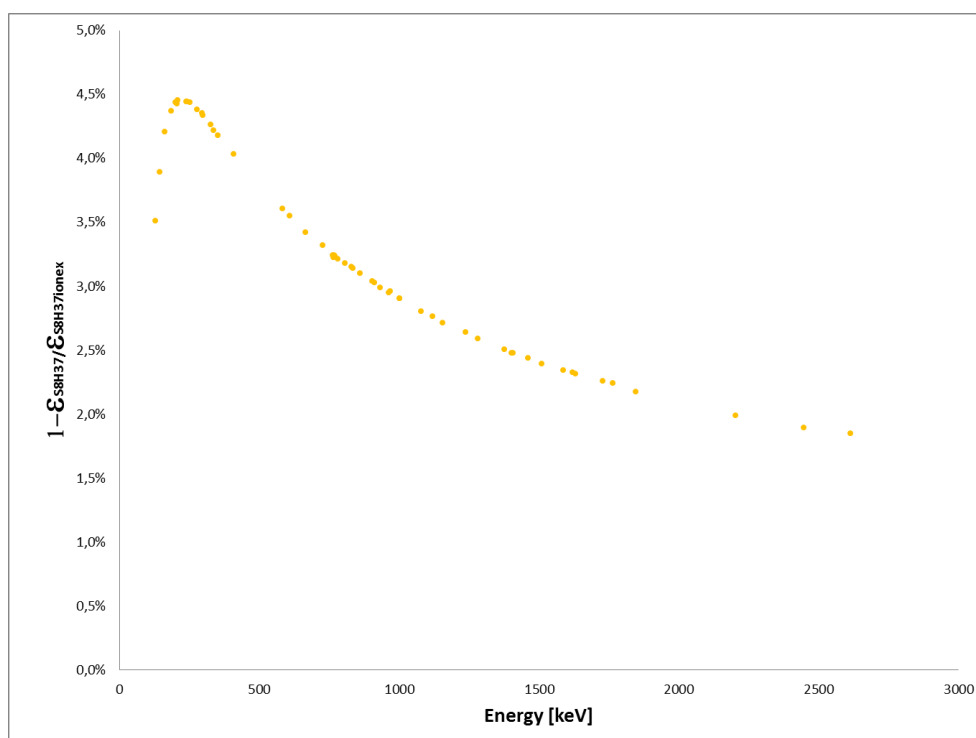


Figure 3.21. Difference in percentage between the efficiency of the reference apparatus versus the efficiency of the Actual apparatus.

In Figure 3.21 CS correction for those radionuclide used to evaluate the activity concentration of ^{235}U and ^{238}U (^{234}Th and $^{234\text{m}}\text{Pa}$ in secular equilibrium) are shown: these corrections are small and they are between -1% and 1% , throughout the whole energy spectrum. Looking at Figure 3.20 and Figure 3.21, we note that the corrections made to the MR calibration curves are small (2-5%), the maximum correction is of 4.5% at about 185 keV (^{235}U emission line). For energies above 200 keV the magnitudes of the corrections decrease with a minimum of 2% for energies higher to 2500 keV. We have this result because the experimental setup calibration and measurement configuration differ only in the chemical composition of the sample. In fact the calibration curve has been carried out with a solution of water and HCl ($\rho = 1.001 \text{ g cm}^{-3}$) while the measured sample was a resin ($\rho = 0.79 \text{ g cm}^{-3}$). The predominant phenomena on all the energetic spectrum are CS and self-absorption: this trend (Figure 3.20) is indeed consistent with the theoretical prediction.

The gamma-ray spectrometry spectrum of the Ionex resin sample is shown Figure 3.22.

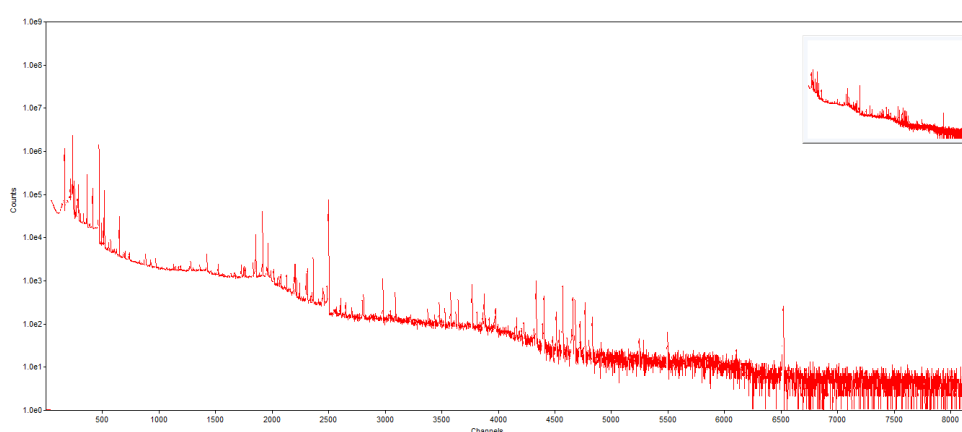


Figure 3.22. Ionex resin gamma-ray spectrum.

The ^{235}U and ^{238}U measurement was performed using the same strategy used for the Tuff sample measurement. ^{238}U disintegrates by alpha emission to ^{234}Th , which unfortunately possesses only two gamma emissions with a very low emission probability that, hence, cannot be used to count the disintegration of the parent nuclide. It follows that it is necessary to move down in the decay chain in order to find out a radionuclide by whose gamma emission one can extrapolate the disintegration of (^{238}U). This method produces the correct result only if the parent radionuclide (^{238}U) is in equilibrium with its daughter nuclides. However it is not necessary that ^{238}U be in equilibrium with all of its daughters, it is sufficient that the equilibrium is verified among three radionuclides: ^{238}U , ^{234}Th and ^{234}Pa . Thanks to the rather short half-life of ^{234}Th (24.1 d), one is justified to reckon that this condition will be fulfilled after waiting for a sufficiently long amount of time which is about 5 times this half-life. The radionuclide whose emissions will be measured to find out the activity of (^{238}U) is $^{234\text{m}}\text{Pa}$.

Table 3.13. ^{234}Th gamma emission energy [73].

<i>^{234}Th disintegrations counted by the gamma emission of $^{234\text{m}}\text{Pa}$</i>			
<i>Photon Energy [keV]</i>	<i>Uncertainty – Energy [keV]</i>	<i>Photons per 100 disintegrations</i>	<i>Uncertainty - Photons per 100 disintegrations</i>
766.361	0.020	0.323	0.004
1001.026	0.018	0.847	0.008

In Table 3.14 there are the INMRI Activity concentration results of the ^{235}U and ^{238}U of the Ionex resin sample.

Table 3.14. Results of Ionex resin sample by gamma- ray spectrometry.

<i>Radionuclide</i>	$A_c \pm u(A_c)$ [Bq/g]
^{238}U	163.7 ± 12.2
^{235}U	6.36 ± 0.31

The characterization of the Ionex resin material showed that many radionuclides were present in the sample with enough activity to be measured on the standard detector. We were interested only in the evaluation of ^{235}U and ^{238}U because Ionex resin is used as a filter for Uranium in water purification. The ratio between the ^{238}U and ^{235}U concentration is as expected and of the same order than the one found in literature [37].

TiO₂

The TiO_2 sample was measured for 500000 s , one month after sample creation. This time is necessary to establish the secular equilibrium within the sample.

The experimental apparatus was the measurement apparatus explained in Chapter 2. We use GESPECOR software to evaluate the geometrical correction respect to experimental reference calibration, the self-attenuation and the true coincidence summing correction. The parameter used by GESPECOR to evaluate these correction coefficients are the chemical composition of the measured samples and the materials that constitute the experimental apparatus both in the measurement configuration and in the calibration configuration.

The magnitude of the correction coefficients to the calibration curve due to CS is shown in Figure 3.23. As it is clear from the Figure 3.23 these corrections could reach a value of -20% in the case of ^{208}Tl (252.6 keV) and the value of 14% in the case of ^{224}Bi (665 keV).

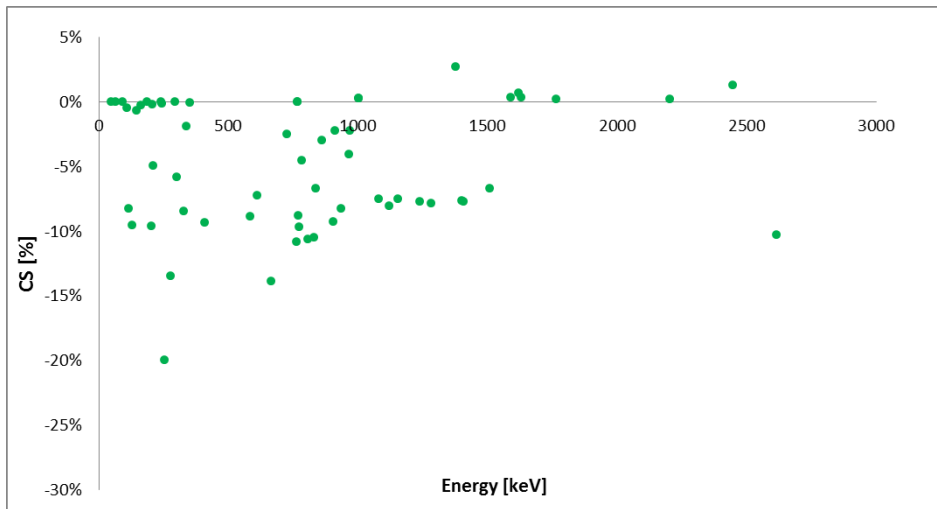


Figure 3.23. CS correction factor in the TiO_2 sample.

In Figure 3.24 we show the result of the calibration procedure (MR measurement apparatus) together with the calibration curve (MR calibration apparatus). Figure 3.25 then shows the perceptual difference between these two curves: this is done to underline how large this correction might be. This curve is obtained drawing the relationship between the efficiency of the reference apparatus versus the efficiency of the Actual apparatus.

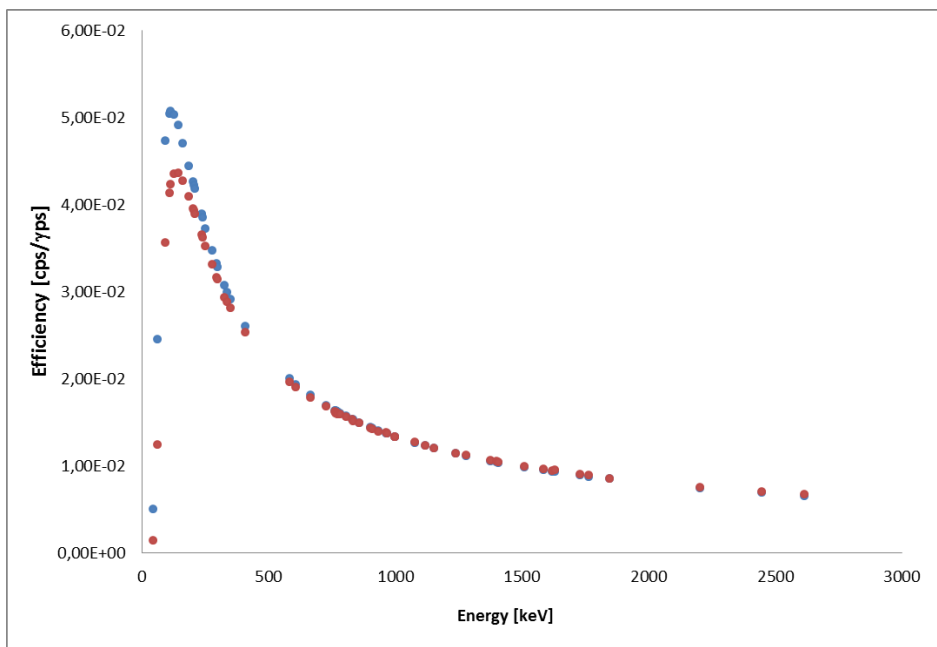


Figure 3.24. Calibration curve MR calibration apparatus (blue) and calibration curve of the measurement apparatus.

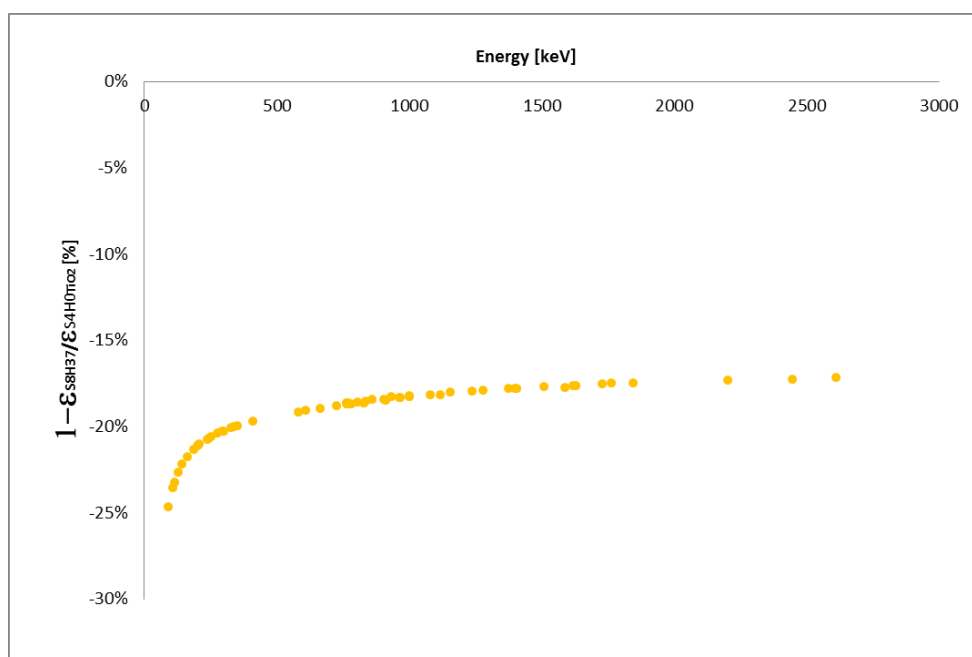


Figure 3.25. Difference in percentage between the efficiency of the MR calibration apparatus versus the efficiency of the measurement apparatus.

In the case of the TiO_2 sample the corrections to the efficiency curve are due to the different configurations taken into account between the calibration apparatus and measurement apparatus. TiO_2 material has a $\rho = 1.45 \text{ g cm}^{-3}$ density: it is higher than the density of the sources used for detector calibration ($\rho = 1.001 \text{ g cm}^{-3}$). For this reason the MR calibration configuration is more efficient than the measurement configuration. The trend of these correction factors are dominated at low energies by self-attenuation which added to the geometric differences of the two apparatus and to CS produce difference between the two curves up to 28%. While for higher energies ($> 200 \text{ keV}$) the magnitude of this correction decreases, for energies above 200 keV the dominant corrective factor is due to the geometrical differences between the MR calibration apparatus and measurement apparatus. In fact as the Tuff case the S4H0 configuration is more efficient respect the S8H37 configuration. As we can see in Figure 3.23, CS contributes to this difference.

The gamma-ray spectrometry spectrum of the Ionex resin sample is shown in the Figure 3.26.

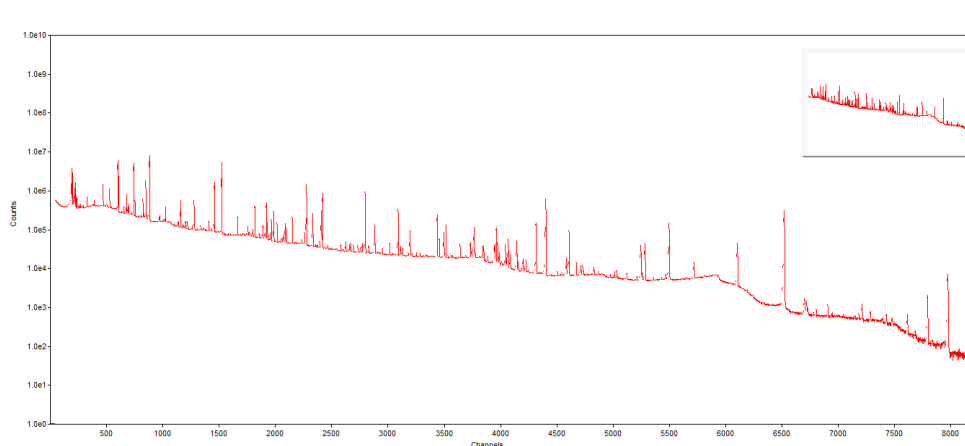


Figure 3.26. TiO₂ gamma-ray spectrum.

The activity concentration value of TiO₂ sample was carried out with the same strategy used for the Tuff and Ionex resin activity concentration measurement.

The results of TiO₂ activity concentration measurement are shown in Table 3.15.

Table 3.15. Results of TiO₂ sample by gamma- ray spectrometry.

<i>Radionuclide</i>	$A_c \pm u(A_c)$ [Bq/g]
²²⁶ Ra	30.74 ± 3.69
²¹⁰ Pb	4.88 ± 0.77
²²⁸ Ra	19.27 ± 0.43
²²⁸ Th	12.59 ± 0.68

The characterization of the Ionex resin material showed that many radionuclides were present in the sample with enough activity to be measured on the standard detector. It seems to be high enriched in ²²⁶Ra, ²²⁸Ra and ²²⁷Ac. The ratio between the ²³⁸U and ²³⁵U concentration is as expected.

3.1.5 Partner activity measurement

In this section the activity concentration measurements results obtained by the European MetroNORM partners on the candidate reference materials are presented, together with the results obtained by ENEA INMRI. We report in Table 3.16 the results of the Tuff sample, in

Table 3.17 the results obtained for the Ionex resin sample and Table 3.18 the results obtained for the TiO₂ sample.

Table 3.16. Results for assessment of Tuff by gamma-spectrometry.

<i>Laboratory</i>	<i>NRPA</i> ¹⁰	<i>NPL</i>	<i>IRMM</i>	<i>CMI</i>	<i>CIEMAT</i>	<i>CEA</i> ¹¹	<i>PTB</i>	<i>ENEA</i>
<i>Radionuclide</i>	$A_c \pm u(A_c)$ [Bq/g]							
²³⁸ U	419 ± 54	425 ± 45	417 ± 61	279 ± 90	No result	No result	No result	No result
²³⁵ U	19.8 ± 2.8	38 ± 6	22.8 ± 1.2	No Result	34 ± 8	No result	No result	19 ± 6
²²⁶ Ra	245 ± 49	210 ± 12	239 ± 13	260 ± 10	245 ± 49	242 ± 50	592 ± 67	227 ± 36
²¹⁰ Pb	195 ± 27	230 ± 45	325 ± 54	581 ± 111	195 ± 27	295 ± 25	287 ± 120	381 ± 76
²²⁸ Ra	378 ± 30	440 ± 20	409 ± 20	371 ± 15	No result	No result	No result	344.29 ± 12.02
²²⁸ Th	No result	415 ± 15	394 ± 36	366 ± 8	No result	No result	No result	347.80 ± 11.04
⁴⁰ K	2170 ± 220	2450 ± 45	2230 ± 12	1637 ± 166	2158 ± 379	2038 ± 10	No result	1765 ± 199

Table 3.17. Results for assessment of Ionex resin by gamma-spectrometry.

<i>Laboratory</i>	<i>NPL</i>	<i>CMI</i>	<i>ENEA</i>
<i>Radionuclide</i>	$A_c \pm u(A_c)$ [Bq/g]	$A_c \pm u(A_c)$ [Bq/g]	$A_c \pm u(A_c)$ [Bq/g]
²³⁸ U	230 ± 50	145 ± 4	163.7 ± 12.0
²³⁵ U	8 ± 2	6.5 ± 0.1	6.36 ± 0.31

Table 3.18. Results for assessment of TiO₂ by gamma-spectrometry.

<i>Laboratory</i>	<i>NPL</i>	<i>IRMM</i>	<i>CMI</i>	<i>CIEMAT</i>	<i>CEA</i>	<i>PTB</i>	<i>ENEA</i>
<i>Radionuclide</i>	$A_c \pm u(A_c)$ [Bq/g]						
²³⁸ U	No result	No result	0.44 ± 0.34	No result	No result	No result	No result
²³⁵ U	No result						
²²⁶ Ra	34.21 ± 1.21	31.71 ± 1.55	32.31 ± 0.70	No result	27 ± 1.4	51 ± 0.90	30.74 ± 3.69

¹⁰ Norwegian Radiation Protection Authority.

¹¹ Commissariat à l'énergie atomique et aux énergies alternatives.

<i>Laboratory</i>	<i>NPL</i>	<i>IRMM</i>	<i>CMI</i>	<i>CIEMAT</i>	<i>CEA</i>	<i>PTB</i>	<i>ENEA</i>
<i>Radionuclide</i>	$A_c \pm u(A_c)$ [Bq/g]						
²¹⁰ Pb	3 ± 1	5 ± 1	3.14 ± 0.84	5.71 ± 0.16	2.69 ± 0.93	2.24 ± 0.89	4.88 ± 0.77
²²⁸ Ra	20.82 ± 0.87	22.12 ± 1	21.22 ± 0.40	No result	No result	No result	19.27 ± 0.43
²²⁸ Th	13.35 ± 0.32	13.87 ± 1.03	12.07 ± 0.23	No result	No result	No result	12.59 ± 0.68
⁴⁰ K	No result	No result	0.017 ± 0.005	1.58 ± 0.03	0.35 ± 0.8	No result	No result

As we can see from the Table 3.16, Table 3.17 and Table 3.18, there is poor agreement between the results obtained by the various institutes. This is not an issue because the purpose of these preliminary measurements was to identify a material to be chosen as a reference material and not to obtain an accurate characterization of the sample.

3.2 Final evaluation of the Ionex resin Certified Reference Material

Looking at the results from the preliminary measurements on the candidate reference materials, it was decided to choose the Ionex resin as CMR. This material was chosen as CMR both because of its availability and its activity concentration: it has a sufficiently high activity to be used as a calibration source for a gamma-ray spectrometer. In this part of the work ENEA, JRC, CMI and NPL performed an accurate characterization of the Ionex resin CMR.

3.2.1 Certified Reference Material preparation

In this section the characteristics of the Ionex resin CMR prepared by CMI are presented. The resin composition is given in Table 3.19. The material density is 0.79 g cm⁻³.

Table 3.19. Elemental composition of the Ionex resin.

<i>Ionex resin</i>	
<i>Element</i>	<i>Abundance</i> [%]
C	59.7
N	11.5
O	12.2
H	11.4
S	4.6
U	0.5

CMI filled completely the metallic container (85 ml) with the resin before sealing it. A drawing of the metallic container is presented in Figure 3.27 and the elemental composition, provided by the aluminum producer, is given in Table 3.20. The metallic container Ionex with Ionex resin CMR inside is shown in Figure 3.28. The density of the container is 2.62 g cm^{-3} .

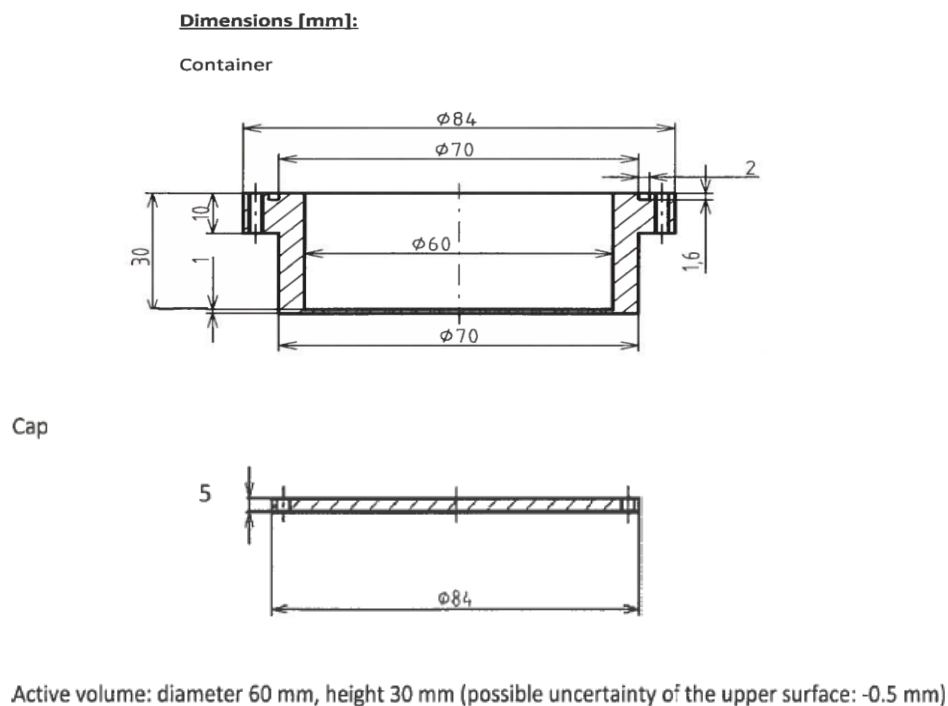


Figure 3.27. Schematic view of the metallic container and its lid filled with Ionex resin.



Figure 3.28. The metallic container with Ionex resin sample inside.

Table 3.20. Elemental composition of the CMI metallic container provided by the aluminium producer.

<i>Metal container</i>			
<i>Element</i>	<i>Abundance [%]</i>	<i>Element</i>	<i>Abundance [%]</i>
Si	1.1	Nn	0.05
Fe	0.24	Ti	0.02
Cu	0.03	Pb	0.01
Mn	0.53	Al	97.51
Mg	0.61	Cr	0.02

3.2.2 Homogeneity measurement

The results obtained on the homogeneity measurements of the CMR Ionex resin are presented in this section. The measurements were carried out by JRC, CMI and ENEA. The homogeneity measurements are fundamental for the characterization of a CMR. In fact, one of the most important characteristics of a CMR is its homogeneity [64]. The three institutions have carried out the homogeneity measurements on the same samples. For this purpose CMI have prepared seven identical containers (Figure 3.29) filled with the same amount of Ionex resin.



Figure 3.29. The CMR Ionex resin filled in the seven identical containers.

Each of these containers was measured for 50000 s. Then the spectra were analyzed and peak counts of the most intense peaks were compared. The coefficient of variation for all the measurement carried out from the three institute involved are up to 1%. The results of INMRI

measurement, the CMI measurement and the JRC results are reported in Table 3.21, Table 3.22 and Table 3.23, respectively.

Table 3.21. ENEA homogeneity measurement results.

Radionuclide		^{234}Th	^{234}Th	^{235}U	^{235}U	^{235}U	$^{234\text{m}}\text{Pa}$	$^{234\text{m}}\text{Pa}$
Photon Energy [keV]		63.30	92.38 and 92.80	143.77	163.36	185.72	766.361	1001.026
Sample [#]	1	328683	776129	102586	47141	497752	21097	46451
	2	333252	779938	102684	47671	502088	21489	46736
	3	331521	779471	103513	47274	499699	21152	46647
	4	333039	780446	102156	46654	499902	21724	46940
	5	330852	780453	103709	46953	500569	21319	47329
	6	329080	777329	103065	47113	499842	21407	46846
	7	331991	781106	103158	47041	500405	21708	46921
Average [#]		331203	779267	102982	47121	500037	21412	46839
Standard Deviation		1792.2	1838.2	544.1	310.7	1292.1	245.0	275.4
Coefficient of Variation [%]		0.54	0.24	0.53	0.66	0.26	1.04	0.59

Table 3.22. CMI homogeneity measurement results.

Radionuclide		^{234}Th	^{234}Th	^{235}U	^{235}U	^{235}U	$^{234\text{m}}\text{Pa}$	$^{234\text{m}}\text{Pa}$
Photon Energy [keV]		63.30	92.38 and 92.80	143.77	163.36	185.72	766.361	1001.026
Sample [#]	1	437749	813453	88022	40192	421784	33774	17927
	2	437325	812135	89513	40446	427504	34558	17577
	3	435186	803363	89264	40322	426861	34130	17536
	4	434702	811453	89753	40774	427172	34354	17874
	5	432327	806705	89402	40194	423955	34071	17763
	6	433224	815118	88954	41085	426467	34045	17733
	7	433768	805194	88602	41074	424673	34351	17562
Average [#]		434897.3	810574.4	89073.2	40584.5	426259.4	34183.9	17710.8
Standard Deviation		1883.35	3304.39	553.32	362.62	1279.99	238.99	145.00
Coefficient of Variation [%]		0.43	0.41	0.62	0.89	0.31	0.75	0.82

Table 3.23. JRC homogeneity measurement results.

Radionuclide	²³⁴ Th	²³⁴ Th	²³⁵ U	²³⁵ U	²³⁵ U	²³⁵ U	^{234m} Pa	^{234m} Pa	
Photon Energy [keV]	63.30	92.38 and 92.80	143.77	163.36	185.72	205,31	766.36	1001.02	
Sample [#]	1	546995	1339265	155125	68450	712050	21265	546995	1339265
	2	551135	1340260	151200	69470	711135	21215	551135	1340260
	3	552550	1343295	155530	68910	713905	21200	552550	1343295
	4	551480	1340510	156035	69220	711500	20725	551480	1340510
	5	56770	1344750	155390	70280	711775	21345	567700	1344750
	6	557440	1323760	155330	69455	711115	21045	557440	1323760
	7	550015	1326335	156290	68990	710600	20870	550015	1326335
Average [#]	552375	1334740	155545	69255	711725	21090	552375	1334740	
Standard Deviation	3680	7890	450	575	1070	205	3680	7890	
Coefficient of Variation [%]	0.67	0.59	0.29	0.83	0.15	0.53	0.97	0.28	

The results of these measurements show that Ionex resin sample produced by the CMI is sufficiently homogeneous to become a CMR.

3.2.3 INMRI activity measurement

The Ionex resin sample was measured for 500000 s. The secular equilibrium is guaranteed due to the fact that the sample was prepared more than one month before the measurement. The density of this material is 0.79 g/cm³.

For the activity concentration measurement we use the detector used for the other measurement carried out in this work. The used geometry was the metal container developed by CMI, this container was characterized by CMI: the geometrical configuration is shown in Figure 3.27 and the chemical composition of the container is listed in Table 3.20. The correction factor for this configuration were carried out using GESPECOR software, MR calibration curve (Figure 2.10). Using this information together with the chemical composition of the material (Table 3.19) we evaluated: the geometrical correction, the self-attenuation correction and the coincidence summing correction.

In Figure 3.30 the result of the calibration procedure together with experimental calibration curve (MR calibration apparatus) are shown. Figure 3.31 then shows the percentage difference as function of energy between these two curves, to underline the magnitude of the corrections.

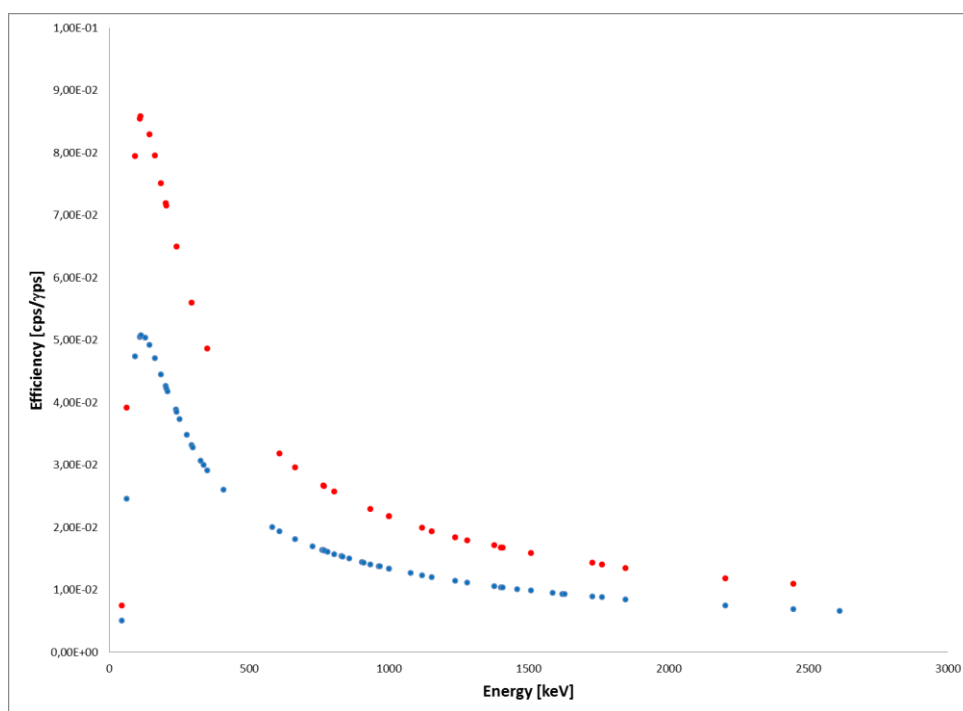


Figure 3.30. MR apparatus calibration curve (blue) and measurement (metal container) apparatus calibration curve (red).

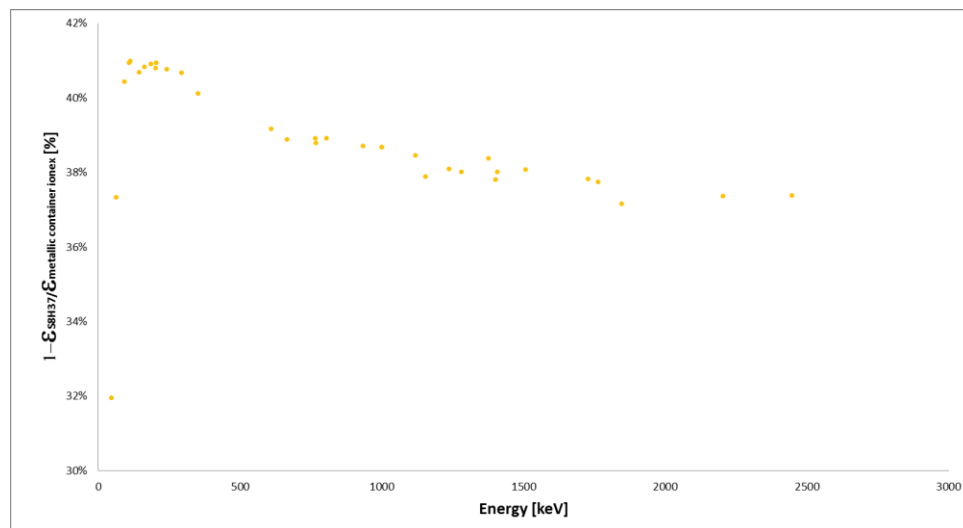


Figure 3.31. Difference in percentage between the efficiency of the MR calibration apparatus versus the efficiency of the measurement (metal container) apparatus.

From Figure 3.30 and Figure 3.31 we can observe that the corrections made to the MR calibration configuration curve respect to the measurement calibration curve are large (30-40%). The maximum corrections are about 41% in the energy range between 214.38 keV (^{235}U) up to 295.2 keV (^{214}Pd). For energies above 200 keV the magnitude of the corrections decreases slightly, they are around 38% over the entire energy spectrum. This large difference between the calibration curves is due to the fact that the calibration apparatus and the measurement apparatus differ both in the chemical nature of the sources and in the chemical composition of the containers. From Figure 3.31 we can observe the trend of the ratio between the MR calibration curve versus measurement configuration curve as a function of energies. The correction factors on the entire spectrum are dominated by the geometrical differences between the MR calibration apparatus and measurement apparatus. Especially due to the presence of the metal container in the measurement configuration that has a density $\rho = 2.62 \text{ g cm}^{-3}$.

The activity concentration value of Ionex resin in the metal container was carried out with the same strategy used for the other activity concentrations measurement.

The gamma-ray spectrometry spectrum of the Ionex resin sample is shown in Figure 3.32.

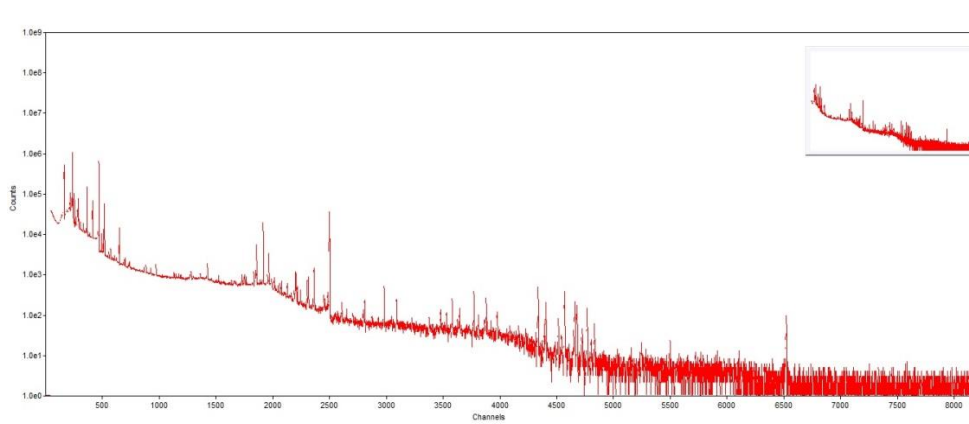


Figure 3.32. Ionex resin metal container gamma-ray spectrum.

In Table 3.24 activity concentration results of the ^{235}U and ^{238}U of the Ionex resin sample in the metal container.

Table 3.24. Results of Ionex resin sample by gamma- ray spectrometry.

<i>Radionuclide</i>	$A_c \pm u(A_c)$ [Bq/g]
^{238}U	167.8 ± 12
^{235}U	6.36 ± 0.3

3.2.4 Certified Reference Material activity characterization

The radiometric characterization of the Ionex resin CMR was jointly carried out by CMI, NPL and ENEA. This section contains the results of activity concentration measurements carried out by these institutes and the activity concentration value associated to the CMR obtained through the power moderate mean (PMM).

NPL measured all the sources by producing calibration sources of NORM radionuclides in matched geometry and direct like to like calibration to ensure no correction is needed for coincidence summing.

The Ionex resin was measured on the NPL low background HPGe detector called 'Galahad', which has a relative efficiency of 70% and which is a p-type coaxial detector with a thick outer dead layer, with low background Tudor Pb.

CMI use an HPGe detector with a relative efficiency of 40% the calibration curve was made using Monte Carlo code in order to determinate the total efficiencies and the CS correction factors.

Laboratory results for ^{235}U and ^{238}U of the Ionex CMR are listed in Table 3.25.

Table 3.25. Laboratory results for ^{235}U and ^{238}U of the Ionex CMR.

<i>Laboratory (#)</i>	<i>NPL (1)</i>	<i>CMI (2)</i>	<i>ENEA (3)</i>
<i>Radionuclide</i>	$A_c \pm u(A_c)$ [Bq/g]	$A_c \pm u(A_c)$ [Bq/g]	$A_c \pm u(A_c)$ [Bq/g]
^{235}U	8 ± 2	6.5 ± 0.1	6.36 ± 0.29
^{238}U	230 ± 50	145 ± 4	167.8 ± 12.1

In Figure 3.33 is shown the results of the three laboratories concerning the measure of the activity concentration of ^{235}U in the Ionex resin sample compared to the reference value (A_{ref}). Uncertainty bars represent the calculated combined standard uncertainties. The red dashed line, instead, represent the uncertainty associated with the reference value.

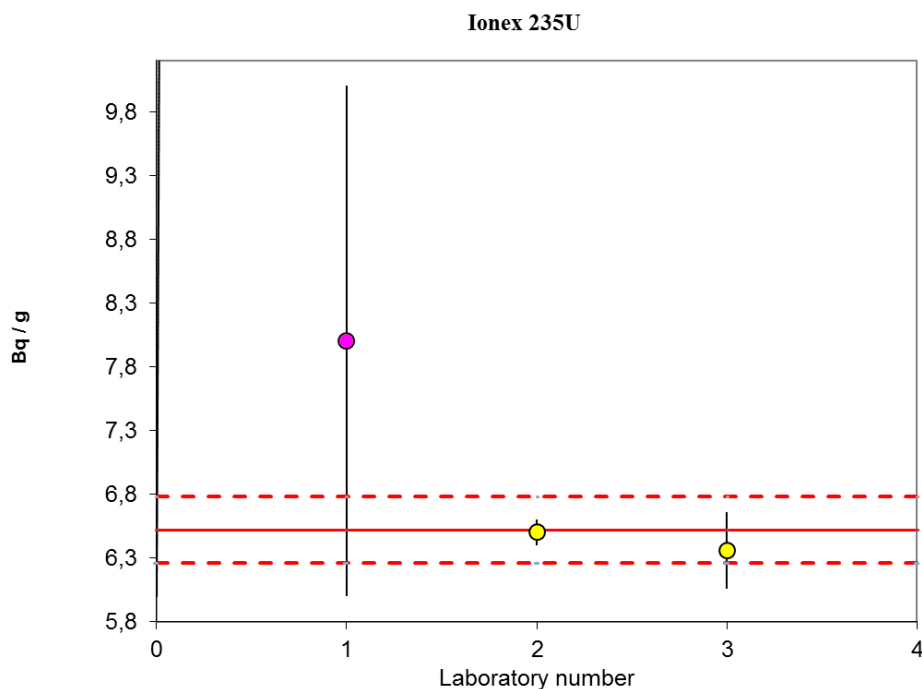


Figure 3.33. Ionex resin ^{235}U Activity concentration results.

In Figure 3.34 there is the comparison of the results in PomPlot, it displays (relative) deviations of individual results from the reference value on the horizontal axis (D/MAD section 2.11) and (relative) uncertainties on the vertical axis (u/MAD section 2.11). As we can see from the Figure 3.34 ENEA and CMI result have ζ -score < 1 . The ζ -score is a measure for the deviation between laboratory results and reference value relative to the total uncertainty (section 2.11). The JRC measurement is not consider with the others according to PMM criterion ($k=1$) and it has been rejected from the calculation.

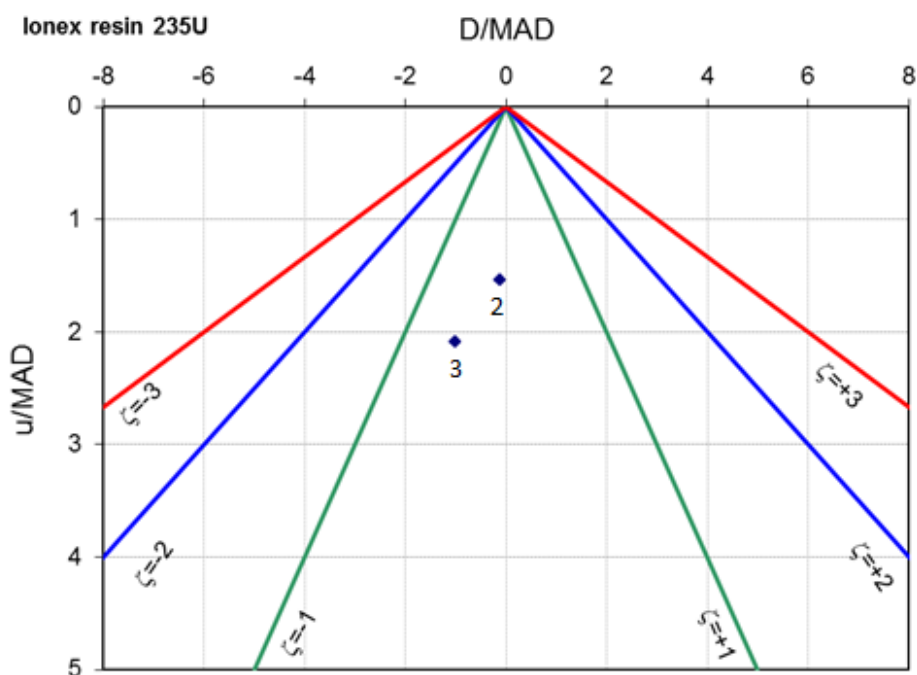


Figure 3.34. PomPlot of the activity concentration of ^{235}U in Ionex resin. Green, blue, and red solid lines indicate ζ -scores = 1, 2 and 3, respectively.

From Table 3.26 we can see some information carried out from the PMM reference value evaluation, i.e. the weight factor used in the PMM or the ζ -score of each laboratory. As we can observe from the Table 3.26 the CMI values is the weightiest value in the PMM (63.4%), instead the JRC weighted factor is zero, this is because the JRC value is according to PMM mean criterion ($k=1$).

Table 3.26. Significant value carried out from the PMM reference value evaluation for the ^{235}U activity concentration of the Ionex resin sample.

Laboratory [#]	A_c [Bq/g]	$u(A_c)$ [Bq/g]	Weight [%]	$x - x_{ref}$ [Bq/g]	u_{tot} [Bq/g]	ζ
1	8.0	2.0	0	1.6	2.0	0.8
2	6.5	0.1	63.4	0.1	0.1	0.6
3	6.4	0.3	36.6	-0.1	0.2	-0.5

In Table 3.27 we can see the ^{235}U reference value evaluated through the PMM and its associated uncertainty.

Table 3.27. Activity concentration reference value of ^{235}U .

A_{ref} [Bq/g]	$u(A_{ref})$ [Bq/g]
6.4	0.1

In Figure 3.34 is shown the results of the three laboratories concerning the measure of the activity concentration of ^{238}U in the Ionex resin sample. Reference value was calculated as power moderate mean of all obtained values.

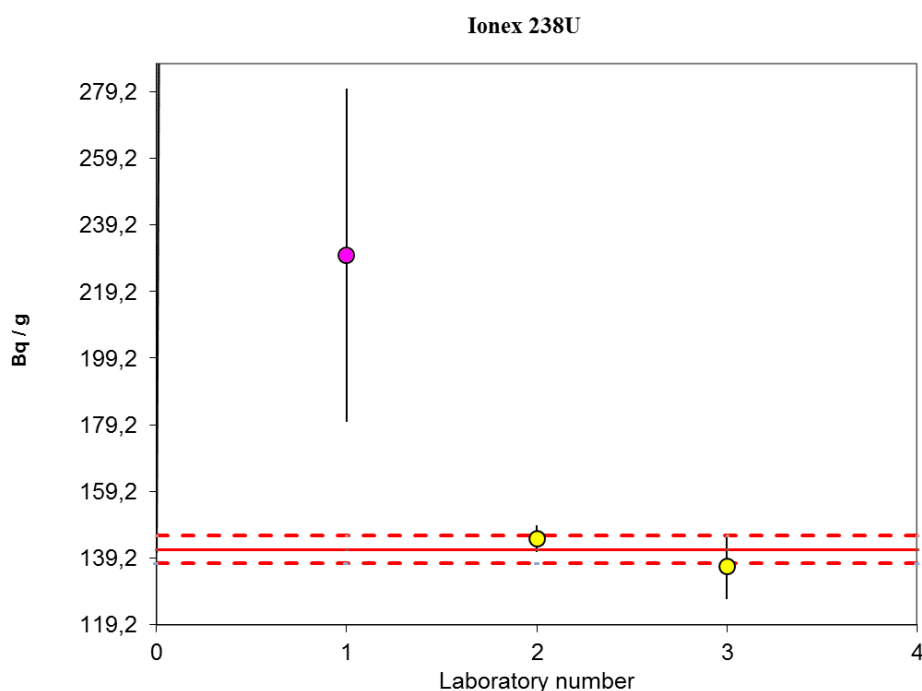


Figure 3.35. Ionex resin ^{238}U Activity concentration results.

In Figure 3.35 there is the comparison of the results in PomPlot, ENEA and CMI result have ζ -score < 1 . The JRC measurement is not consider with the others according to PMM criterion ($k=1$) and it has been rejected from the calculation.

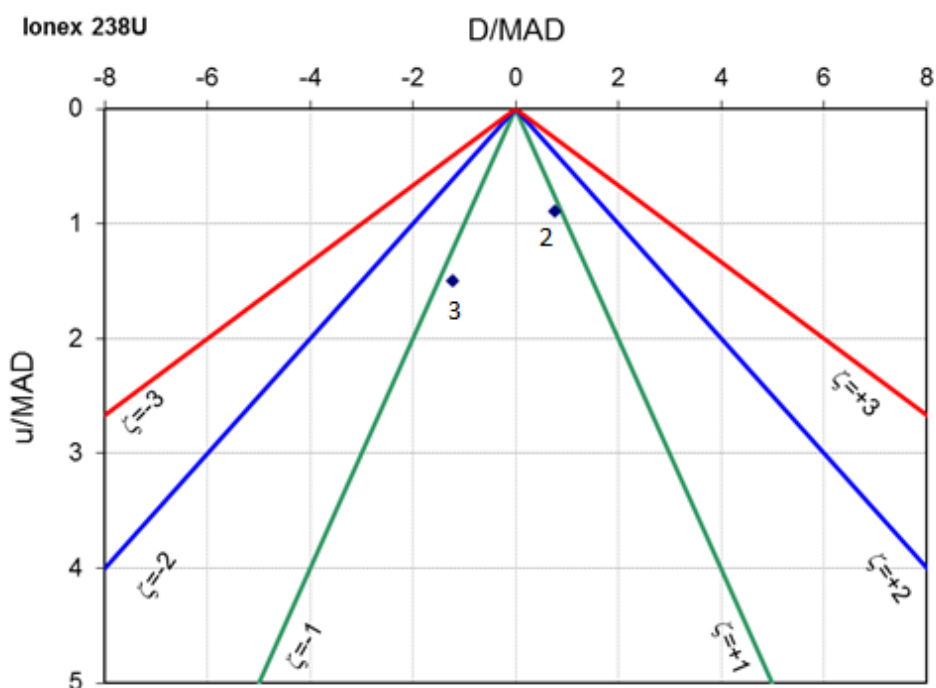


Figure 3.36. PomPlot of the activity concentration of ^{238}U in Ionex resin. Green, blue, and red solid lines indicate ζ -scores = 1, 2 and 3, respectively.

From Table 3.28 we can see some information carried out from the PMM evaluation of the ^{238}U reference value.

Table 3.28. Significant value carried out from the PMM reference value evaluation for the ^{235}U activity concentration of the Ionex resin sample

Laboratory [#]	A_c [Bq/g]	$u(A_c)$ [Bq/g]	Weight [%]	$x - x_{ref}$ [Bq/g]	u_{tot} [Bq/g]	ζ
1	230.0	50.0	0	88.2	50.2	1.8
2	145.0	4.0	61.1	3.2	3.7	0.9
3	136.7	9.8	38.9	-5.1	6.2	-0.8

In Table 3.29 are listed the ^{238}U reference value for the Ionex resin sample and its uncertainty.

Table 3.29. Activity concentration reference value of ^{238}U .

A_{ref} [Bq/g]	$u(A_{ref})$ [Bq/g]
141.8	4.2

The results obtained from the three laboratory involved in this characterization are used for the evaluation of the reference activity concentration through the PMM. From this evaluation we obtained a reference activity concentration values listed in Table 3.27 and Table 3.29 with an associated uncertainty of 1.56% for ^{235}U and 2.96% for ^{238}U .

3.3 Development and validation of a reference activity measurement method

The aim of this part of the work is to develop a procedure for measure radioactivity to be used in the European NORM industry. A traceable measurement for industrial NORM raw material, products, by-products, residues, and waste is defined by ENEA INMRI (Appendix). This procedure contains the recommendation of a new traceable method for the measurement of activity of natural radionuclides with an uncertainty up to 3%, and it has been validated through an inter-comparison between twelve institutes participating to MetroNORM project. The Twelve partners participated in the inter-laboratory comparison are: BEV, BOKU¹², CIEMAT, CMI, ENEA, GIG¹³, IJS¹⁴, IST¹⁵, JRC, MKEH¹⁶, NRPA and STUK¹⁷. The comparison was realized as a Round-Robin exercise where one sample was sent around to all participants.

The measurand was the activity concentration of ^{238}U and ^{235}U in Bq/g at the reference date of 01/12/2015, 00h00 UTC.

As only one sample of Ionex resin in the metal container was available, the container had been sent around to all the laboratories according to the schedule in Table 3.31.

¹² Universität für Bodenkultur Wien.

¹³ Główny Instytut Górnictwa, Śląskie Centrum Radiometrii Środowiskowej.

¹⁴ Institut Jožef Stefan.

¹⁵ Instituto Superior Técnico.

¹⁶ Magyar Kereskedelmi Engedelyezesi Hivatal.

¹⁷ Säteilyturvakeskus.

Table 3.30. Planning of the shipment of the Ionex resin sample.

MetroNORM WP1 D1.4.5 PLANNING		Measurement of the sample in the metal container																												
		2015												2016																
		Dec					Jan				Feb			Mar				Apr			May		30-May-16							
Laboratory	Country	30/11-06/12	7-13/12	14-20/12	21-27/12	28/12-03/01	4-10/01	11-17/01	18-24/01	25-31/01	1-7/02	8-14/02	15-21/02	22-28/02	29/02-6/03	7-13/03	14-20/03	21-27/03	28/03-3/04	4-10/04	11-17/04	18-24/04	25/04-1/05	2-8/05	9-15/05	16-22/05	23-29/05	Deadline for reporting the results		
ENEA	Italy																												send the sample to STUK	
STUK	Finland																													send the sample to IJS
IJS	Slovenia																													send the sample to REG(GIG)
REG(GIG)	Poland																													send the sample to JRC
JRC	Belgium																													send the sample to CIEMAT
CIEMAT	Spain																													send the sample to MKEH
MKEH	Hungary																													send the sample to BEV/PTP
BEV/PTP	Austria																													send the sample to REG(BOKU)
REG(BOKU)	Austria																													send the sample to IST
IST	Portugal																													send the sample to NRPA
NRPA	Norway																													return the sample to CMI
CMI	CZ																													measured in Feb. 2015

Two weeks had been allocated to each participant to measure the sample and to send it to the next participant.

As mentioned before, the activity concentration of ^{238}U and ^{235}U had to be reported. All the participants reported the activity concentration of ^{238}U and ^{235}U . The results of the inter-laboratory comparison were combined using the Power-Moderated Mean (PMM) with the default input parameters [69]. The reference activity concentration of ^{238}U and ^{235}U , calculated using the PMM, were respectively $(138.49 \pm 2.01) \text{ Bq/g}$ and $(6.34 \pm 0.08) \text{ Bq/g}$. The activity ratio based on these numbers is (21.8 ± 0.1) and the derived isotopic abundance of ^{235}U is $(0.71 \pm 0.05)\%$. Both values are compliant with known values [4].

Figure 3.37 and Figure 3.38 show, respectively, the reported activity concentration of ^{238}U and ^{235}U of the different participants compared to the PMM. The correspondence between the identifying number and the laboratory name is given in Table 3.31. In the case of ^{235}U activity, one measurement is not consistent with the others according to PMM default criterion and it has been rejected from the calculation. The PomPlots are presented in Figure 3.38 and Figure 3.40 [70]. In both cases, only 3 measurements are outside $|\zeta|=1$.

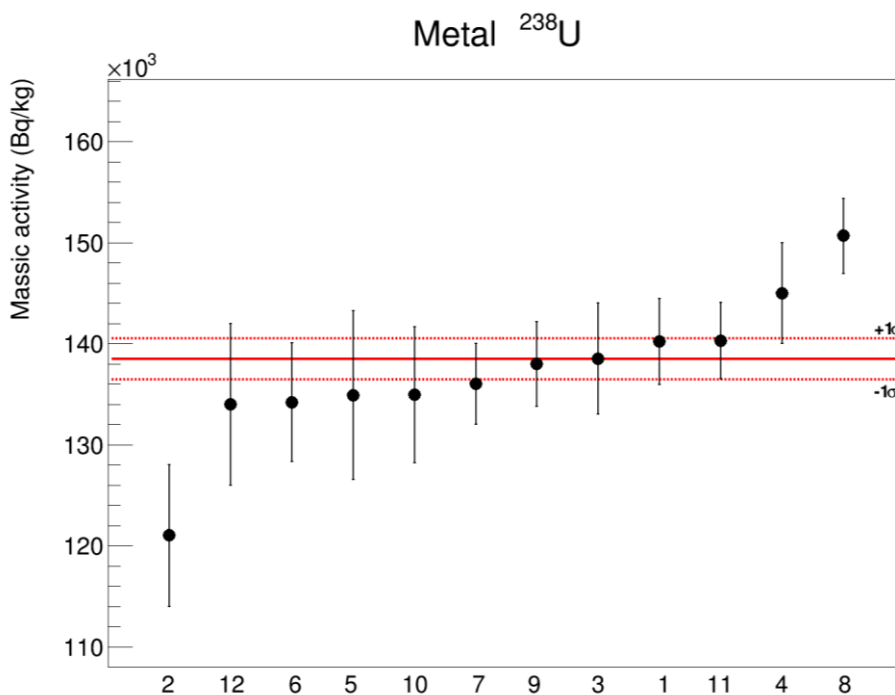


Figure 3.37. Comparison of the standardization result of the activity concentration of ^{238}U in Ionex resin. The power-moderated mean and the corresponding uncertainty are represented by the lines.

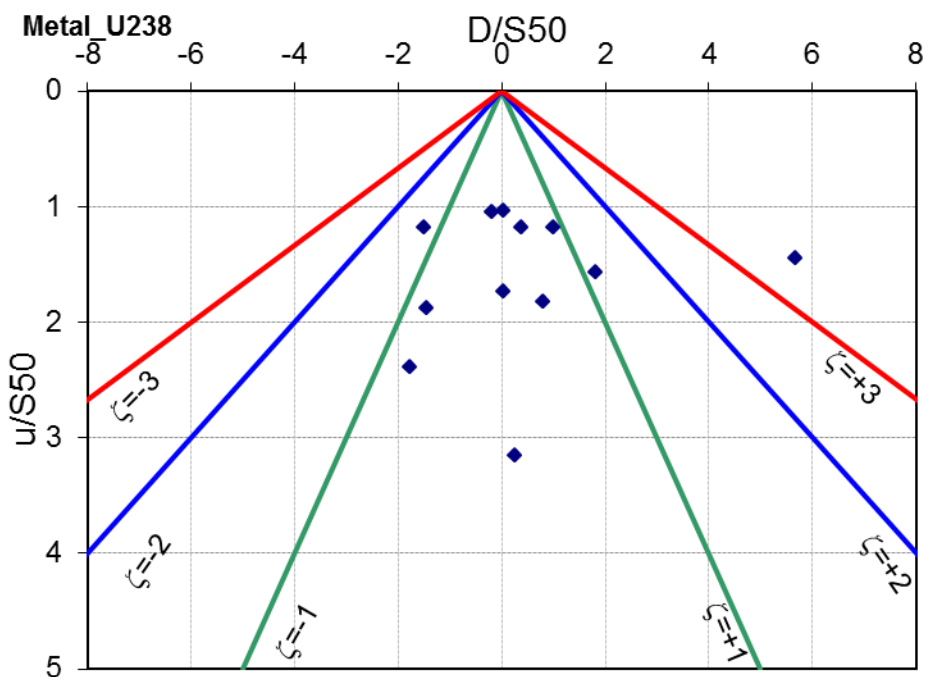


Figure 3.38. PomPlot of the activity concentration of ^{238}U in Ionex resin. Green, blue, and red solid lines indicate ζ -scores = 1, 2 and 3, respectively.

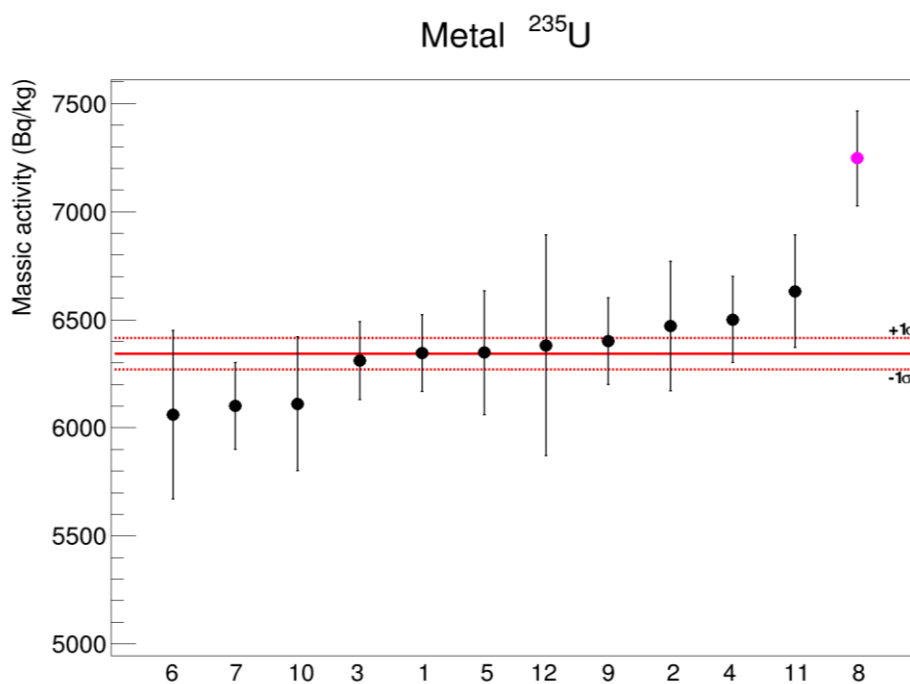


Figure 3.39. Comparison of the standardization result of the activity concentration of ²³⁵U in Ionex resin. The power-moderated mean and the corresponding uncertainty are represented by the lines. The purple point is rejected from the calculation.

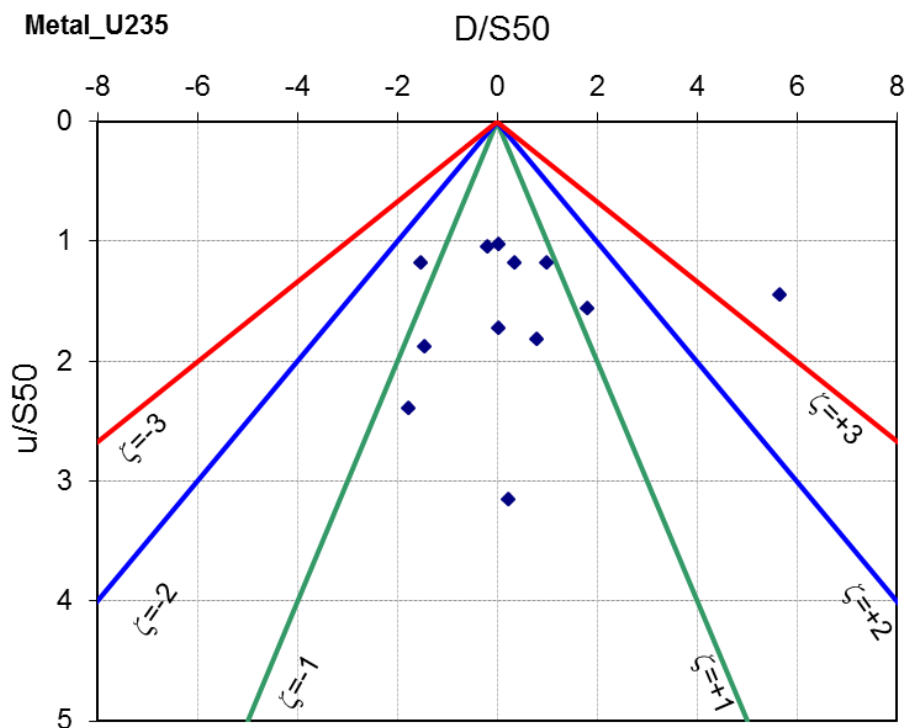


Figure 3.40. PomPlot of the activity concentration of ²³⁵U in Ionex resin. Green, blue, and red solid lines indicate ζ -scores = 1, 2 and 3, respectively.

Table 3.31. Laboratory number and associated name used for the two comparisons presented in Figure 3.37 and Figure 3.39.

<i>Laboratory</i>	<i> [#]</i>
BEV	1
BOKU	2
CIEMAT	3
CMI	4
ENEA	5
GIG	6
IJS	7
IST	8
JRC	9
MKEH	10
NRPA	11
STUK	12

All the foreseen participants could measure the Ionex resin in the metallic container produced by CMI and all of them reported their results. The standardized results of the activity of ^{238}U and ^{235}U are respectively $(138.49 \pm 2.01) \text{ Bq/g}$ and $(6.34 \pm 0.08) \text{ Bq/g}$ with an uncertainty coverage factor $k=1$ and at the reference date of 01/12/2015, 00h00 UTC. All the results, except one for ^{235}U , are consistent and the activity of ^{238}U and ^{235}U are standardized with uncertainties better than 1.5% ($k=1$).

Chapter 4

Determination of nuclear data

Naturally Occurring Radioactive Materials contain primordial radionuclides present in natural resources. When processed by industry these may lead to enhanced radiation levels and increased human exposure. Accurate activity measurements of the radionuclides present in NORM residue depend on the quality of available decay data. ^{235}U and its decay products are present in NORM residue. Improving our knowledge of their characteristic gamma-ray emission intensities would facilitate a more accurate quantification of the activity of these nuclides through gamma-ray spectrometry measurements. Of particular concern with regards to health risks are the α -decaying radionuclides from the lower part of the ^{235}U decay chain, ^{227}Ac and its decay products, which through inhalation can cause a high internal dose to the human body. On the other hand, some radionuclides can be used successfully in alpha immunotherapy to fight against cancer. This is also another important reason for study the decay scheme of ^{235}U , as inconsistencies still persist in spite of numerous studies on the subject.

The aim of this part of the work is to evaluate the emission intensities of the radionuclide in the ^{235}U decay series.

4.1 International contest of nuclear data

High quality evaluated nuclear and atomic data are needed in applied research and for detector calibration. Using inaccurate gamma-ray emission probabilities may results in serious miscalculation. For example, for radionuclides used in nuclear medicine a wrong radiation dose could have detrimental consequence on patient's health. For detector calibrations, the effect of inaccurate standard may be propagated to the measurements, thus producing incorrect results that are often difficult to identify. For this reason nuclear data are essential to the development, implementation and maintenance of all nuclear technologies. In gamma-ray spectrometry they are fundamental for the evaluation of the activity concentration of a radionuclide and to determinate its uncertainty. Consider the equation which expresses the activity of a radionuclide as a function of time (Equation 2.9), this expression suggests that

the activity of a radionuclide depends on: the half-life, decay scheme, (emission probability, energetic levels, transition probabilities between the various nuclear levels) internal conversion coefficients and many others. For this reason the accurate knowledge of these parameters are important for the quality of measurement. Because of the importance of nuclear data, the scientific community is constantly engaged in more accurate assessment of these coefficients.

The international network of Nuclear Structure and Decay Data (NSDD) Evaluators is sponsored by the IAEA, and consists of evaluation groups and data service centers in several countries. This network has the objective of providing up-to-date nuclear structure and decay data for all known nuclides by evaluating all existing experimental data.

Data resulting from this international evaluation collaboration is included in the Evaluated Nuclear Structure Data File (ENSDF) and published in the journals Nuclear Physics A and Nuclear Data Sheets. Until the end of the of eighties this results represented the recommended "best values" for the various nuclear structure and decay data parameters. The ENSDF master database is maintained by the US National Nuclear Data Center at the Brookhaven National Laboratory, these data are also available from other distribution centers including the IAEA Nuclear Data Section.

In the first half of the nineties it was founded the Decay Data Evaluation Project (DDEP) this group have the task to developed a critical method for evaluate recommended nuclear data. This project was born from the collaboration between some European Metrology Institute as the PTB and LNH and others. The first meeting of the new DDEP was held in Paris in 1995. In its initial meeting, this collaboration addressed the questions of objectives, working procedure and goals. Since that time, as part of this project, they were established several working groups that have had the aim to periodically collect the nuclear data available in the scientific community and to evaluate the recommended data. Recommended values are made available to users by means of various media, such as the World Wide Web, CD-ROMs, wall charts of the nuclides, handbooks, nuclear wallet cards and others.

In 2004 BIPM (Bureau International des Poids et Mesure) has recommended the use of DDEP evaluated decay data.

In the frame of the European Metrology Research Program (EMRP) 'MetroNORM', research is performed on the decay characteristics of the ^{235}U decay series, which is abundantly found in nature and at enhanced concentrations in NORM residue. There is need for reference decay data to improve the support the radio analytical procedures applied for the identification and quantification of radionuclides present in NORM material. In this context, the decay characteristics (gamma-ray emission intensities) of potentially harmful α -emitters in the ^{235}U decay series, i.e. ^{227}Ac and daughter nuclides, are investigated by the MetroNORM partner institutes. JRC produced ^{235}U and ^{227}Ac sources and accurately measured their activities by a primary method. The ^{227}Ac and the ^{235}U sources were standardized at JRC-IRMM in terms of activity and distributed among the partners to determine the gamma-ray emission probability.

4.2 Actual nuclear data available

The DDEP via an international working groups, periodically, evaluate the radionuclide emission intensity through a critical analysis of the measurements carried out by the scientific community and collected in ENSDF database. In the rest of this section the currently recommended DDEP values are shown. The following tables contain those radionuclides for which we measure the emission probability in this work. In particular we present all the probabilities emission of radionuclides considered in this study and belonging to the ^{235}U radioactive chain. Together with the values recommended by the DEEP we also present the measurement carried out over the years and which have led to the recommended emission probability value.

In the following tables, each line represents the evaluation of the emission intensities (I_γ) of a radionuclide performed over the years. While each column shows the results of the emission intensity measurements for the considered radionuclide conducted in a specific reference. The first box of each column shows the reference name as recorded in the ENSDF database together with the year in which it was published. In the following tables the last significant digit of the uncertainty values associated with the emission intensity are expressed in parentheses. The absolute gamma-ray emission probability (P_γ) can be deduced from the evaluated relative gamma-ray emission intensity using the derived normalization factor: $0.14230 (15)$.

- ^{235}U

Table 4.1. Emission probability of ^{235}U [73].

$E_\gamma(\text{keV})$	1966Ga03*	1971Cl03*	1971KrZlH*	1974Te03*	1975Va11*	1977Ba72*	1982Va04	1983BaZZ	1983O01	1984He12	1986LoZT	1992La05	1996Ru11*	LWM	Adopted*
182.1															
182.62		0.43 (3)	0.42 (4)	0.42 (14)	0.44 (10)	0.312		0.339 (17)			0.34 (2)	0.803 (103)	0.43 (5)	0.39 (5)	0.39 (5)
185.720							57.5 (9)	57.3 (6)	56.1 (8)	57.2 (5)	57.2 (2)	56.8 (13)	57.1 (3)	57.1 (3)	57.1 (3)
194.940	4.7	0.69 (5)	0.69 (6)	0.61 (9)	0.62 (6)	0.67		0.626 (13)			0.63 (1)	0.618 (48)	0.61 (2)	0.626 (10)	0.63 (1)
198.894		0.032 (3)	0.032	0.046 (6)	0.033 (5)	0.097 ?		0.047 (6)			0.42 (6)			0.036 (2)	0.036 (2)
199.6*						0.097 ?									~ 0.06*
202.12		1.06 (8)	1.1 (5)	1.07 (11)	1.07 (11)	1.25		1.08 (2)			1.08 (2)	1.16 (7)	1.06 (4)	1.080 (17)	1.08 (2)
205.316		5.3 (4)	5.18 (32)	4.9 (4)	5.0 (5)	5.51	5.0 (2)	5.05 (5)	5.03 (9)	4.96 (5)	5.01 (5)	4.98 (14)	5.03 (5)	5.015 (26)	5.02 (3)
215.28			0.42	0.029 (6)	0.029 (3)	0.025								0.029 (3)	0.029 (3)
221.386		0.126 (9)	0.08	0.12 (3)	0.116 (11)	0.125		0.114 (6)			0.12 (1)			0.118 (5)	0.118 (5)
228.76			0.0085		0.0074	0.0011									0.0074
233.50		0.042 (3)	0.021	0.034 (11)	0.032			0.029 (5)			0.029 (5)			0.038 (4)	0.038 (4)
240.88		0.074 (6)	0.0032	0.063 (17)	0.085	0.089		0.076 (6)			0.075 (6)			0.074 (4)	0.074 (4)
246.83		0.063 (5)	0.021	0.046 (17)	0.085	0.067 ?		0.053 (3)			0.053 (3)			0.055 (3)	0.055 (3)
251.5*						0.067 ?									~ 0.012*
266.47		0.0080 (6)	0.0053	0.0063 (17)	0.0095									0.0078 (6)	0.0078 (6)
275.35				0.051 (6)											0.051 (6)
275.49			0.042		0.032	0.114									0.032
279.5*						0.264									0.264
281.42					0.0063										0.0063
282.94	0.001		0.0032		0.0063	0.004									0.0063
289.56					0.0074										0.0074
291.2															
291.65			0.021	0.040 (6)	0.032	0.095									0.040 (6)
294.3*						0.033									0.033
301.7					0.0053										0.0053
310.69			0.0017		0.0053										0.0053
317.10					0.0011										0.0011

E_{γ} (keV)	1966Ga03*	1971Cl03*	1971KrZH*	1974Te03*	1975Va11*	1977Ba72*	1982Va04	1983BaZZ	1983Ol01	1984He12	1986LoZT	1992L05	1996Ru11*	LWM	Adopted*
325.8						0.004									0.004
343.5					0.0032										0.0032
345.4*						0.072 ?									-0.03*
345.92			0.0017	0.040 (6)	0.074	0.072 ?									0.040 (6)
350	0.006														0.006
356.03					0.0053										0.0053
371.8*						0.069 ?									
387.84				0.040 (6)	0.0085	0.159									0.040 (6)
390.27				0.040 (1)											0.040 (1)
410.29					0.0032										0.0032
433.0	0.001					0.004									0.004
448.40					0.0011										0.0011
455.1*					0.0085										0.0085
517.9*					0.00042										0.00042
742.5*					0.00042										0.00042
794.7*					0.00063										0.00063

x: Not placed in level scheme.

#: From intensity balance.

&: From $P_{\gamma}(198.9 + 199.6) = 0.097\%$.

^: From $P_{\gamma}(246.8 + 251.5) = 0.067\%$.

+: From $P_{\gamma}(345.4 + 345.9) = 0.072\%$.

*: Deduced using the LWM statistical method, unless otherwise specified.

a: The P_{γ} values have been deduced from the measured relative intensities and normalized to $P_{\gamma} = (57.1 \pm 0.3)\%$ for the 185.7 keV reference line.

b: This value, which deviates by a factor of about 10 from the results of the other measurements, was not used in the calculation of the recommended value.

Looking at Table 4.1 it can be noted that there are just a few estimates of the emission intensity for most of the ^{235}U emission lines, moreover, many of these estimates are extremely old. Instead, for some emission lines the emission intensity has never been assessed in case of 291.2 keV or 182.1 keV [73].

- ^{227}Ac

The absolute emission probabilities of gamma-rays in ^{227}Th (37.9 keV) have been deduced from the absolute β^- -emission probabilities in the ^{227}Ac β^- -decay using the ratio $P(\gamma 37.9 \text{ keV})/P(\gamma 28.6 \text{ keV})$ (emission probability at 39.7 keV of ^{235}U versus emission probability at 28.6 keV) and the recommended value is $P(\gamma 37.9 \text{ keV}) = 0.049$ [73].

- ^{227}Th

In this case we used the ^{227}Th emission probability carried out from the NNDC (National Nuclear Data Center) database because these values were not present in the DDEP database. Unfortunately in the NNDC database the historical reference information about the ^{227}Th recommended values were not available. For this reason in Table 4.2 are listed only the gamma-emission line energies and the relative emission probabilities [76].

Table 4.2. Emission probability of ^{227}Th [76].

<i>Recommended</i> E_γ [keV]	P_γ [%]	$u(P_\gamma)$ [%]
31.58	0.068	0.010
40.2	0.0155	0.0004
49.82	0.426	0.090
50.13	8.39	0.39
61.44	0.090	0.010
62.45	0.203	0.026
79.69	1.948	0.065
85.431	1.34	0.05
88.471	2.18	0.08
113.11	0.54	
117.2	0.199	0.014
123.58	0.014	0.005
141.42	0.119	0.023
150.14	0.0111	0.0031
162.19	0.0077	0.0026
168.36	0.0148	0.0026
169.95	0.0055	0.0022
173.45	0.0174	0.0026
184.65	0.036	0.004
197.56	0.013	0.004
200.5	0.013	0.009
201.64	0.024	0.003
204.14	0.227	0.026
204.98	0.164	0.026
206.08	0.254	0.026

<i>Recommended</i> E_γ [keV]	P_γ [%]	$u(P_\gamma)$ [%]
210.62	1.25	0.09
212.7	0.079	0.009
212.7	0.019	0.005
218.9	0.110	0.010
234.76	0.45	0.05
235.96	12.90	0.26
246.12	0.012	0.001
250.27	0.45	0.04
252.5	0.11	0.02
254.63	0.71	0.13
256.23	7.00	0.13
262.87	0.107	0.008
272.91	0.508	0.008
279.8	0.054	0.013
281.42	0.178	0.012
284.24	0.040	0.013
286.09	1.74	0.15
292.41	0.066	0.008
296.5	0.44	0.04
299.98	2.21	0.06
304.5	1.15	0.13
308.4	0.017	0.003
312.69	0.516	0.039
314.85	0.49	0.04
329.85	2.94	0.15
334.37	1.14	0.08

<i>Recommended</i> E_γ [keV]	P_γ [%]	$u(P_\gamma)$ [%]
342.55	0.35	0.09
346.45	0.012	0.001
382.2	0.006	0.001
466.8	0.00049	0.00003
493.1	0.0005	0.0001
524.5	0.00019	0.00004
536.9	0.0011	0.0002
756.9	0.00019	0.00005
775.8	0.0015	0.0001
781	0.0003	0.0001
797.3	0.0009	0.0001
803.9	0.0006	0.0005
812.6	0.0017	0.0003
823.4	0.0026	0.0003
842.5	0.0009	0.0001
846.7	0.00015	0.00003
908.6	0.0024	0.0003

• ^{223}Ra

Table 4.3. Emission probability of ^{223}Ra [73].

	Recommended E_γ (keV)	1968Br17	1970Kr01	1970Da08	1972HeYM	1976Bl13	1998Sh02	Evaluated I_γ
$\gamma_{1,0}$	4.47 (1) ^a							
$\gamma_{2,1}$	9.90 (2) ^a							
$\gamma_{2,0}$	14.37 (1) ^a							
$\gamma_{4,3}$	31.87 (2) ^a		0.000 74 (15)				0.001	0.000 74 (15)
$\gamma_{9,7}$	34.5 (2) ^b							
$\gamma_{12,9}$	69.5 (1) ^b						0.05 (2)	0.05 (2)
$\gamma_{15,12}$	70.9 (2) ^b						0.025 (8)	0.025 (8)
$\gamma_{11,7}$	102.2 (2) ^b						0.006 (3)	0.006 (3)
$\gamma_{17,13}$	103.2 (2) ^b	0.100 (14) ^c			0.12 (7) ^c		0.04 (2)	0.04 (2)
$\gamma_{12,7}$	104.04 (4) ^a					0.134 (15)	0.14 (2)	0.136 (15)
$\gamma_{11,6}$	106.78 (3)	0.164 (29)	0.14 (3)	0.16 (4)	0.19 (6)	0.157 (15)	0.17 (1)	0.164 (10)
$\gamma_{12,6}$	108.5 (2) ^b						0.04 (2)	0.04 (2)
$\gamma_{5,4}$	110.856 (10)	0.40 (6)	0.331 (29) ^f	0.41 (4)	0.21 (9) ^f	0.40 (4)	0.42 (3)	0.41 (3)
$\gamma_{22,18}$	112.6 ^c							
$\gamma_{13,8}$	114.7 (2)				0.07 (4)		0.07 (3)	0.07 (3)
$\gamma_{3,1}$	122.319 (10)	8.2 (11)	8.75 (15)	9.8 (10)	8.7 (4)	7.5 (8)	8.7 (1)	8.70 (10)
$\gamma_{20,14}$	131.6 (2)				0.037 (22)		0.04 (2)	0.04 (2)
$\gamma_{14,8}$	138.3 (3) ^b						0.012 (5)	0.012 (5)
$\gamma_{3,2}$	144.27 (2) ^a	22.1 (21)	23.8 (5)	23.0 (24)	27.4 (18) ^f	21.6 (22)	23.5 (5)	23.6 (5)
$\gamma_{17,12}$	147.2 (2) ^b						0.04 (2)	0.04 (2)
$\gamma_{4,1}$	154.208 (10)	38.6 (29)	41.1 (8)	38 (4)	44.4 (26)	38 (4)	41 (1)	41.0 (8)
$\gamma_{3,0}$	158.635 (10)	5.0 (5)	5.02 (10)	5.6 (6)	5.3 (4)	4.6 (4)	5.0 (1)	5.01 (10)
$\gamma_{16,8}$	165.8 (2)				0.037 (22)		0.04 (2)	0.038 (20)
$\gamma_{11,5}$	175.65 (15)		0.10 (3)		0.15 (4)		0.14 (3)	0.12 (3)
$\gamma_{12,5}$	177.3 (1)	0.21 (7)	0.34 (3)		0.35 (6)		0.34 (3)	0.33 (3)
$\gamma_{6,4}$	179.54 (6)	1.07 (29)	1.07 (29)	1.10 (13)	1.16 (15)	1.01 (10)	1.1 (1)	1.08 (10)
$\gamma_{20,12}$	199.3 (3)				0.022 (15)		0.02 (1)	0.021 (10)
$\gamma_{18,9}$	221.32 (24)	0.25 (7)	0.22 (4)		0.25 (4)		0.26 (4)	0.25 (4)
$\gamma_{19,8}$	247.2 (5)				0.066 (22)		0.07 (2)	0.068 (20)
$\gamma_{8,3}$	249.49 (3) ^a	0.26 (7)			0.29 (13)		0.28 (7)	0.27 (7)
$\gamma_{17,7}$	251.6 (3)	0.49 (11)	0.27 (7)	0.42 (15)	0.49 (15)	0.47 (7)	0.3 (1)	0.39 (7)
$\gamma_{5,2}$	255.2 (2)	0.43 (11)		0.37 (15)	0.24 (7)	0.33 (7)	0.38 (5)	0.34 (5)
$\gamma_{17,6}$	255.7 (3)				0.037 (22)		0.04 (2)	0.039 (20)
$\gamma_{18,6}$	260.4 (3)				0.044 (22)		0.05 (2)	0.047 (20)
$\gamma_{5,0}$	269.463 (10)	100 (11)	100 (2)	100 (7)	100 (4)	100 (4)	100 (2)	100 (2)
$\gamma_{10,3}$	270.3 (4) ^b						0.005 (3)	0.005 (3)
$\gamma_{23,12}$	286.0 (4) ^b						0.008 (4)	0.008 (4)
$\gamma_{12,4}$	288.18 (3)	1.14 (14)	1.16 (5)	1.08 (12)	0.93 (13) ^f	1.07 (5)	1.15 (3)	1.13 (3)
$\gamma_{6,2}$	323.871 (10)	26.5 (29)	29.4 (6)	26.5 (26)	26.8 (11)	26.8 (13)	28.7 (5)	28.5 (5)
$\gamma_{7,2}$	328.38 (3) ^a	1.43 (14)	1.52 (7)	1.19 (24)	1.18 (18)	1.40 (8)	1.5 (5)	1.43 (7)
$\gamma_{6,1}$	334.01 (6)	0.61 (9)	0.76 (6)	0.91 (18)	0.69 (11)	0.54 (7)	0.73 (4)	0.70 (4)
$\gamma_{6,0}$	338.282 (10)	19.3 (18)	21 (5)	19.0 (20)	19.2 (7)	18.5 (9)	20.4 (4)	20.0 (4)
$\gamma_{7,0}$	342.78 (2) ^a	1.43 (14)	1.70 (9)	1.5 (4)	0.71 (16) ^f	1.49 (12)	1.6 (1)	1.59 (9)
$\gamma_{23,9}$	355.5 (2) ^b						0.03 (1)	0.03 (1)
$\gamma_{14,4}$	355.7 (2) ^b						0.02 (1)	0.02 (1)
$\gamma_{8,2}$	361.89 (2) ^a	0.29 (7)	0.34 (4)	0.37 (7)	0.24 (6)	0.298 (22)	0.20 (5)	0.20 (5) ^g
$\gamma_{9,2}$	362.9 (2) ^b						0.11 (5)	0.11 (5)
$\gamma_{22,7}$	368.56 (12)				0.06 (3)		0.06 (3)	0.06 (3)
$\gamma_{8,1}$	371.676 (15)	3.9 (4)	3.56 (7)	4.0 (6)	4.2 (4)	3.14 (16)	3.5 (1)	3.51 (7)

	Recommended E_{γ} (keV)	1968Br17	1970Kr01	1970Da08	1972HeYM	1976Bl13	1998Sh02	Evaluated I_{γ}
$\gamma_{9,1}$	372.86 (1) ^{a,b}	≈ 0.7				0.73 (8)	0.36	0.36 ⁱ
$\gamma_{8,0}$	376.26 (2) ^a			0.088 (29)			0.09 (3)	0.09 (3)
$\gamma_{16,4}$	383.35 (2) ^a	≈ 0.04		0.11 (4)	0.029 (22)		-	0.05 (3)
$\gamma_{14,3}$	387.7 (2)				0.10 (4)		0.11 (4)	0.11 (4)
$\gamma_{23,7}$	390.1 (2)	≈ 0.05			0.022 (15)		0.05 (2)	0.032 (15)
$\gamma_{11,2}$	430.6 (3)				0.14 (4)		0.14 (4)	0.14 (4)
$\gamma_{12,2}$	432.45 (3) ^a	0.24 (3)	0.26 (4)	≈ 0.22	0.24 (6)	0.186 (30) ^f	0.25 (2)	0.25 (2)
$\gamma_{11,0}$	445.033 (12)	8.7 (4)	11.0 (8) ^f	9.3 (10)	9.2 (7)	8.5 (4)	9.3 (3)	9.0 (3)
$\gamma_{20,4}$	487.5 (2)	0.071 (14)	0.10 (4)	≈ 0.11	0.08 (4)		0.08 (1)	0.08 (1)
$\gamma_{-1,1}$	490.8 (3) ^b						0.012 (5)	0.012 (5)
$\gamma_{14,2}$	500.0 (4) ^b						0.010 (4)	0.010 (4)
$\gamma_{14,1}$	510.0 (4) ^b						0.003 (2)	0.003 (2)
$\gamma_{-1,2}$	523.2 (4) ^b						0.010 (4)	0.010 (4)
$\gamma_{16,2}$	527.611 (13)	0.50 (5)	0.54 (5)	0.51 (10)	0.47 (11)	0.410 (22) ^f	0.51 (3)	0.51 (3)
$\gamma_{-1,3}$	532.9 (4) ^b						0.010 (4)	0.010 (4)
$\gamma_{16,1}$	537.6 (1) ^b						0.015 (5)	0.015 (5)
$\gamma_{16,0}$	541.99 (2) ^{a,b}						0.010 (4)	0.010 (4)
$\gamma_{21,3}$	545.8 (5) ^b						0.008 (4)	0.008 (4)
$\gamma_{23,4}$	574.1 (7) ^b						0.008 (4)	0.008 (4)
$\gamma_{17,2}$	579.6 (3) ^b						0.010 (4)	0.010 (4)
$\gamma_{18,2}$	584.3 (3) ^b						0.010 (4)	0.010 (4)
$\gamma_{17,0}$	594.0 (3) ^b						0.010 (4)	0.010 (4)
$\gamma_{18,0}$	598.721 (24)	0.57 (6)	0.76 (7)	0.68 (11)	0.66 (13)	0.626 (30)	0.68 (3)	0.65 (3)
$\gamma_{19,2}$	609.31 (4)	0.36 (4)	0.54 (7)	0.46 (7)	0.30 (11)	0.373 (22)	0.41 (2)	0.40 (2)
$\gamma_{19,1}$	619.1 (4) ^b						0.025 (8)	0.025 (8)
$\gamma_{19,0}$	623.68 (4) ^a	0.057 (29)					0.06 (3)	0.06 (3)
$\gamma_{20,2}$	631.7 (7)			0.22 (7)			0.003 (2)	0.003 (2)
$\gamma_{20,1}$	641.7 (4) ^b						0.012 (5)	0.012 (5)
$\gamma_{20,0}$	646.1 (5) ^b						0.003 (3)	0.003 (3)
$\gamma_{22,2}$	696.9 (7) ^b						0.005 (2)	0.005 (2)
$\gamma_{22,0}$	711.3 (2) ^b	0.025 (7)					0.026 (7)	0.026 (7)
$\gamma_{23,2}$	718.4 (4) ^b						0.010 (4)	0.010 (4)
$\gamma_{23,1}$	728.4 (8) ^b						0.002 (1)	0.002 (1)
$\gamma_{23,0}$	732.8 (6) ^b						0.004 (2)	0.004 (2)
$\gamma_{-1,4}$	737.2 (8) ^b						0.002 (1)	0.002 (1)

^a From the adopted ²¹⁵Rn level energies.

^b From 1998Sh02; new gamma-ray transition observed.

^c Reported only by 1998Sh02 without uncertainty in energy and without intensity value.

^d Not reported by 1998Sh02 but observed in 1968Br37, 1970Da08, 1972HeYM, 1976Bl13.

^e Reported γ -ray with energy of 103.7 keV that may be a sum of 103.2 keV and 104.0 keV γ -rays.

^f Omitted on Chauvenet's criterion.

^g Adopted from 1998Sh02 because of possible contribution of impurity Pb γ -rays in measurements of single γ -spectra.

^h Adopted from 1998Sh02 because of contribution of unplaced 373.3 keV γ -ray observed in measurements of single γ -spectra and not observed in α - γ coincidences.

Even in this case, the studies on which are based the DDEP recommended values of the emission intensities are very old, and in some cases completely absent [73].

- ²¹⁵Po

There is no available information on the gamma-ray emission probabilities, except for the gamma emission probability at 438.9 keV ($P(\gamma_{438.9 \text{ keV}}) = 0.048 (5)\%$ (1968Br17) and 0.064 (2)% (1970Da09). These discrepant values do not conflict with the recommended value of $P(\gamma_{438.9 \text{ keV}}) = 0.058 (19)\%$ deduced by DDEP evaluation group from the alpha transition probability $P(\alpha_{0,1}) = 0.06 (2)$ and total internal conversion coefficient $\alpha_T = 0.0405 (6)$ [73].

• ^{211}Pb

Table 4.4. Emission probability of ^{211}Pb [73].

Eq. keV	1988Hi14	1976Bl13	1971Da34	1968Br17	1968Go15	1968Ha21	1967Da20	1967Da10	1965Co06	1965Me07	1963Va05	1962Gi03	deduced, rel	adopted, %
65		0.57 (6)	0.60 (4)	0.58 (11)			0.10 (5) *	~0.35 *		0.5 (2)			0.59 (3)	0.077 (4)
95			0.14 (2)					~0.10					0.14 (2)	0.018 (3)
314		0.20 (3)	0.24 (3)	0.19 (4)	0.10 (5)		0.26 (5)	0.21 (7)	0.90 (21) *	~0.2 *			0.206 (16)	0.0268 (21)
343		1.63 (13) *	0.27 (4)		0.15 (5)					~0.3 *			0.22 (3)	0.029 (4)
362		0.326 (24)		0.30 (8)									0.324 (23)	0.042 (3)
405	29.3 (9)	30.2 (14)	30.0 (9)	30.8 (15)	29.6 (20)	28.6 (11)	28.0 (28)	29.9 (35)	30.6 (28)	27.4 (12)	26 (5)	34(4)	29.4 (4)	3.83 (6)
427	13.9 (4)	14.2 (7)	13.5 (6)	14.3 (8)	13.7 (10)	11.6 (7)	14.0 (14)	13.9 (17)	21.5 (21) *	14.5 (14)	12.5 (25)	22 (3) *	13.9 (3)	1.81 (4)
429					0.065 (25)								0.065 (25)	0.008 (3)
504	0.045 (6)		0.12 (2) *		~ 0.006 *								0.045 (6)	0.0059 (8)
610		0.407 (24) *	0.18 (3)	0.38 (4)	0.25 (5)		0.30 (6)	0.21 (7)		0.9 (2) *		0.76 (13) *	0.25 (7)	0.033 (9)
676		0.130 (8)		0.173 (15)	0.10 (5)				1.3 (3) *				0.139 (7)	0.0181 (9)
705	3.6 (1)	3.6 (3)	3.77 (19)	3.68 (23)	3.7 (3)	2.9 (1) *	3.0 (3)	3.3 (4)	5.3 (6) *	3.7 (2)	3.8 (11)	5.5 (4) *	3.61 (7)	0.47 (1)
767	4.94 (16)	5.1 (4)	5.55 (28)	5.04 (30)	4.9 (3)	4.5 (1)	4.0 (4)	5.1 (6)	6.3 (6)	5.2 (2)		6.1 (4)	4.8 (3)	0.62 (4)
832	26.7 (8)	25.4 (20)	29.8 (7) *	25.6 (23)	24.1 (17)	27.4 (4)	23.0 (23)	26.4 (35)	26.4 (28)	27.4 (12)	24.8 (25)	34.2 (13) *	26.9 (3)	3.50 (5)
866	0.042 (6)	0.033 (4)	0.050 (8)	0.053 (15)	0.07 (2)		0.03 (1)	0.0347 (14)		0.04 (2)			0.0354 (13)	0.0046 (2)
1014	0.129 (8)	0.122 (8)	0.14 (1)	0.128 (15)	0.15 (1)		0.13 (2)	0.125 (21)		0.14 (2)			0.133 (4)	0.0173 (5)
1081	0.095 (6)	0.090 (7)	0.120 (12)	0.083 (10)	0.08 (1)	0.0025 (1) *	0.08 (2)	0.104 (14)	0.49 (7) *	0.13 (12) *			0.093 (4)	0.0121 (5)
1104	0.033 (4)	0.049 (5)	0.040 (6)	0.023 (5)									0.036 (5)	0.0047 (7)
1110	0.90 (3)	0.82 (6)	1.15 (8)	0.79 (8)	0.81 (6)	0.0105 (7) *	0.70 (15)	0.87 (10)	0.83 (14)	1.03 (10)	1.07 (16)	1.46 (19) *	0.891 (21)	0.116 (3)
1196	0.072 (5)	0.081 (6)	0.10 (1)	0.079 (15)	0.08 (1)		0.08 (2)	0.076 (14)		0.11 (3)			0.079 (3)	0.0103 (4)
1234			0.010 (2)	0.0053 (15)									0.0070 (23)	0.0009 (3)
1271	0.043 (4)	0.057 (5)	0.070 (7)	0.048 (8)	0.08 (1)	0.0006 (1) *	0.05 (1)	0.042 (7)		0.06 (2)			0.052 (9)	0.0068 (12)

• ^{211}Bi

There is a single line gamma-ray transition following the ^{211}Be decay. The adopted value by DDEP is $P(\gamma 351 \text{ keV}) = 13 (2)$ and it is carry out from five references (1968Br17, 1973UrZX, 1975VaYT, 1976Bl13, 1982Mo30 and 1988Hi14) [73].

• ^{207}Tl

The DDEP value of $P(\gamma 897.77 \text{ keV}) = 0.263 (9)\%$ was deduced from the intensity ratio of $I(\gamma 898g)/I(\gamma 351g) = 0.0202 (7)$ (1988Hi14) and $P(\gamma 351 \text{ keV in } ^{211}\text{Bi a decay}) = 13.02 (12)\%$. The absolute emission probability for the 569.698 g of 0.00185 (19)% was deduced from the intensity balance at the 569 keV level and by neglecting the small β^- -decay feeding contribution of $< 8 \times 10^{-5}$ reported in 1988Hi14 [73].

Table 4.5. Emission probability of ^{207}Tl [73].

	Recommended E_γ (keV)	1968Br17	1970Kr01	1970Da08	1972HeYM	1976BII3	1998Sh02	Evaluated I_γ
$\gamma_{1,0}$	4.47 (1) ^a							
$\gamma_{2,1}$	9.90 (2) ^a							
$\gamma_{2,0}$	14.37 (1) ^a							
$\gamma_{4,3}$	31.87 (2) ^a		0.000 74 (15)				0.001	0.000 74 (15)
$\gamma_{9,7}$	34.5 (2) ^b							
$\gamma_{12,9}$	69.5 (1) ^b						0.05 (2)	0.05 (2)
$\gamma_{15,12}$	70.9 (2) ^b						0.025 (8)	0.025 (8)
$\gamma_{11,7}$	102.2 (2) ^b						0.006 (3)	0.006 (3)
$\gamma_{17,13}$	103.2 (2) ^b	0.100 (14) ^c			0.12 (7) ^e		0.04 (2)	0.04 (2)
$\gamma_{12,7}$	104.04 (4) ^a					0.134 (15)	0.14 (2)	0.136 (15)
$\gamma_{11,6}$	106.78 (3)	0.164 (29)	0.14 (3)	0.16 (4)	0.19 (6)	0.157 (15)	0.17 (1)	0.164 (10)
$\gamma_{12,6}$	108.5 (2) ^b						0.04 (2)	0.04 (2)
$\gamma_{5,4}$	110.856 (10)	0.40 (6)	0.331 (29) ^f	0.41 (4)	0.21 (9) ^f	0.40 (4)	0.42 (3)	0.41 (3)
$\gamma_{22,18}$	112.6 ^c							
$\gamma_{13,8}$	114.7 (2)				0.07 (4)		0.07 (3)	0.07 (3)
$\gamma_{3,1}$	122.319 (10)	8.2 (11)	8.75 (15)	9.8 (10)	8.7 (4)	7.5 (8)	8.7 (1)	8.70 (10)
$\gamma_{20,14}$	131.6 (2)				0.037 (22)		0.04 (2)	0.04 (2)
$\gamma_{14,8}$	138.3 (3) ^b						0.012 (5)	0.012 (5)
$\gamma_{4,2}$	144.27 (2) ^a	22.1 (21)	23.8 (5)	23.0 (24)	27.4 (18) ^f	21.6 (22)	23.5 (5)	23.6 (5)
$\gamma_{17,12}$	147.2 (2) ^b						0.04 (2)	0.04 (2)
$\gamma_{4,1}$	154.208 (10)	38.6 (29)	41.1 (8)	38 (4)	44.4 (26)	38 (4)	41 (1)	41.0 (8)
$\gamma_{4,0}$	158.635 (10)	5.0 (5)	5.02 (10)	5.6 (6)	5.3 (4)	4.6 (4)	5.0 (1)	5.01 (10)
$\gamma_{16,8}$	165.8 (2)				0.037 (22)		0.04 (2)	0.038 (20)
$\gamma_{11,5}$	175.65 (15)		0.10 (3)		0.15 (4)		0.14 (3)	0.12 (3)
$\gamma_{12,5}$	177.3 (1)	0.21 (7)	0.34 (3)		0.35 (6)		0.34 (3)	0.33 (3)
$\gamma_{6,4}$	179.54 (6)	1.07 (29)	1.07 (29)	1.10 (13)	1.16 (15)	1.01 (10)	1.1 (1)	1.08 (10)
$\gamma_{20,12}$	199.3 (3)				0.022 (15)		0.02 (1)	0.021 (10)
$\gamma_{18,9}$	221.32 (24)	0.25 (7)	0.22 (4)		0.25 (4)		0.26 (4)	0.25 (4)
$\gamma_{19,8}$	247.2 (5)				0.066 (22)		0.07 (2)	0.068 (20)
$\gamma_{8,3}$	249.49 (3) ^a	0.26 (7)			0.29 (13)		0.28 (7)	0.27 (7)
$\gamma_{17,7}$	251.6 (3)	0.49 (11)	0.27 (7)	0.42 (15)	0.49 (15)	0.47 (7)	0.3 (1)	0.39 (7)
$\gamma_{5,2}$	255.2 (2)	0.43 (11)		0.37 (15)	0.24 (7)	0.33 (7)	0.38 (5)	0.34 (5)
$\gamma_{17,6}$	255.7 (3)				0.037 (22)		0.04 (2)	0.039 (20)
$\gamma_{18,6}$	260.4 (3)				0.044 (22)		0.05 (2)	0.047 (20)
$\gamma_{5,0}$	269.463 (10)	100 (11)	100 (2)	100 (7)	100 (4)	100 (4)	100 (2)	100 (2)
$\gamma_{10,3}$	270.3 (4) ^b						0.005 (3)	0.005 (3)
$\gamma_{23,12}$	286.0 (4) ^b						0.008 (4)	0.008 (4)
$\gamma_{12,4}$	288.18 (3)	1.14 (14)	1.16 (5)	1.08 (12)	0.93 (13) ^f	1.07 (5)	1.15 (3)	1.13 (3)
$\gamma_{6,2}$	323.871 (10)	26.5 (29)	29.4 (6)	26.5 (26)	26.8 (11)	26.8 (13)	28.7 (5)	28.5 (5)
$\gamma_{7,2}$	328.38 (3) ^a	1.43 (14)	1.52 (7)	1.19 (24)	1.18 (18)	1.40 (8)	1.5 (5)	1.43 (7)
$\gamma_{6,1}$	334.01 (6)	0.61 (9)	0.76 (6)	0.91 (18)	0.69 (11)	0.54 (7)	0.73 (4)	0.70 (4)
$\gamma_{6,0}$	338.282 (10)	19.3 (18)	21 (5)	19.0 (20)	19.2 (7)	18.5 (9)	20.4 (4)	20.0 (4)
$\gamma_{7,0}$	342.78 (2) ^a	1.43 (14)	1.70 (9)	1.5 (4)	0.71 (16) ^f	1.49 (12)	1.6 (1)	1.59 (9)
$\gamma_{23,9}$	355.5 (2) ^b						0.03 (1)	0.03 (1)
$\gamma_{14,4}$	355.7 (2) ^b						0.02 (1)	0.02 (1)
$\gamma_{8,2}$	361.89 (2) ^a	0.29 (7)	0.34 (4)	0.37 (7)	0.24 (6)	0.298 (22)	0.20 (5)	0.20 (5) ^g
$\gamma_{9,2}$	362.9 (2) ^b						0.11 (5)	0.11 (5)
$\gamma_{22,7}$	368.56 (12)				0.06 (3)		0.06 (3)	0.06 (3)
$\gamma_{8,1}$	371.676 (15)	3.9 (4)	3.56 (7)	4.0 (6)	4.2 (4)	3.14 (16)	3.5 (1)	3.51 (7)

	Recommended E_{γ} (keV)	1968Br17	1970Kr01	1970Da08	1972HeYM	1976Bl13	1998Sh02	Evaluated I_{γ}
$\gamma_{9,1}$	372.86 (1) ^{a,b}	= 0.7				0.73 (8)	0.36	0.36 ^c
$\gamma_{9,0}$	376.26 (2) ^a			0.088 (29)			0.09 (3)	0.09 (3)
$\gamma_{16,6}$	383.35 (2) ^a	= 0.04		0.11 (4)	0.029 (22)		-	0.05 (3)
$\gamma_{14,3}$	387.7 (2)				0.10 (4)		0.11 (4)	0.11 (4)
$\gamma_{23,7}$	390.1 (2)	= 0.05			0.022 (15)		0.05 (2)	0.032 (15)
$\gamma_{11,2}$	430.6 (3)				0.14 (4)		0.14 (4)	0.14 (4)
$\gamma_{12,2}$	432.45 (3) ^a	0.24 (3)	0.26 (4)	=0.22	0.24 (6)	0.186 (30) ^f	0.25 (2)	0.25 (2)
$\gamma_{11,0}$	445.033 (12)	8.7 (4)	11.0 (8) ^f	9.3 (10)	9.2 (7)	8.5 (4)	9.3 (3)	9.0 (3)
$\gamma_{20,6}$	487.5 (2)	0.071 (14)	0.10 (4)	=0.11	0.08 (4)		0.08 (1)	0.08 (1)
$\gamma_{-1,1}$	490.8 (3) ^b						0.012 (5)	0.012 (5)
$\gamma_{14,2}$	500.0 (4) ^b						0.010 (4)	0.010 (4)
$\gamma_{14,1}$	510.0 (4) ^b						0.003 (2)	0.003 (2)
$\gamma_{-1,2}$	523.2 (4) ^b						0.010 (4)	0.010 (4)
$\gamma_{16,2}$	527.611 (13)	0.50 (5)	0.54 (5)	0.51 (10)	0.47 (11)	0.410 (22) ^f	0.51 (3)	0.51 (3)
$\gamma_{-1,3}$	532.9 (4) ^b						0.010 (4)	0.010 (4)
$\gamma_{16,1}$	537.6 (1) ^b						0.015 (5)	0.015 (5)
$\gamma_{16,0}$	541.99 (2) ^{a,b}						0.010 (4)	0.010 (4)
$\gamma_{21,3}$	545.8 (5) ^b						0.008 (4)	0.008 (4)
$\gamma_{23,4}$	574.1 (7) ^b						0.008 (4)	0.008 (4)
$\gamma_{17,2}$	579.6 (3) ^b						0.010 (4)	0.010 (4)
$\gamma_{18,2}$	584.3 (3) ^b						0.010 (4)	0.010 (4)
$\gamma_{17,0}$	594.0 (3) ^b						0.010 (4)	0.010 (4)
$\gamma_{18,0}$	598.721 (24)	0.57 (6)	0.76 (7)	0.68 (11)	0.66 (13)	0.626 (30)	0.68 (3)	0.65 (3)
$\gamma_{19,2}$	609.31 (4)	0.36 (4)	0.54 (7)	0.46 (7)	0.30 (11)	0.373 (22)	0.41 (2)	0.40 (2)
$\gamma_{19,1}$	619.1 (4) ^b						0.025 (8)	0.025 (8)
$\gamma_{18,0}$	623.68 (4) ^a	0.057 (29)					0.06 (3)	0.06 (3)
$\gamma_{20,2}$	631.7 (7)			0.22 (7)			0.003 (2)	0.003 (2)
$\gamma_{20,1}$	641.7 (4) ^b						0.012 (5)	0.012 (5)
$\gamma_{20,0}$	646.1 (5) ^b						0.003 (3)	0.003 (3)
$\gamma_{22,2}$	696.9 (7) ^b						0.005 (2)	0.005 (2)
$\gamma_{22,0}$	711.3 (2) ^b	0.025 (7)					0.026 (7)	0.026 (7)
$\gamma_{23,2}$	718.4 (4) ^b						0.010 (4)	0.010 (4)
$\gamma_{23,1}$	728.4 (8) ^b						0.002 (1)	0.002 (1)
$\gamma_{23,0}$	732.8 (6) ^b						0.004 (2)	0.004 (2)
$\gamma_{-1,4}$	737.2 (8) ^b						0.002 (1)	0.002 (1)

^a From the adopted ²²⁹Rn level energies.

^b From 1998Sh02; new gamma-ray transition observed.

^c Reported only by 1998Sh02 without uncertainty in energy and without intensity value.

^d Not reported by 1998Sh02 but observed in 1968Br37, 1970Da08, 1972HeYM, 1976Bl13.

^e Reported γ -ray with energy of 103.7 keV that may be a sum of 103.2 keV and 104.0 keV γ -rays.

^f Omitted on Chauvenet's criterion.

^g Adopted from 1998Sh02 because of possible contribution of impurity Pb γ -rays in measurements of single γ -spectra.

^h Adopted from 1998Sh02 because of contribution of unplaced 373.3 keV γ -ray observed in measurements of single γ -spectra and not observed in α - γ coincidences.

4.3 Source preparation for nuclear data measurement

In this section we will describe the preparation and the activity concentration measurement of two radioactive sources (²³⁵U and ²²⁷Ac). The activity concentration was carried out by a primary measurement method in order to measure through a gamma-ray spectrometry the emission probability of the most important emission line of radionuclides belonging to the ²³⁵U radioactivity chain.

^{235}U source

The ^{235}U sources were produced from an initial solution of 0.5 ml containing 20 mg of Uranium in a 1 ml solution of $\text{HNO}_3\ 1.5\text{ M}$. The Source was prepared by drop deposition of approximately $60\ \mu\text{g}$ of the solution onto sprayed glass plates (outer diameter: 34 mm , inner diameter: 20 mm) [74].



Figure 4.1. ^{235}U source provided by JRC.

The measurement of the absolute activity was performed at JRC by using alpha spectrometry through a passivated implanted planar silicon detector. The detector has a real surface of 5000 mm^2 . The sources were placed at approximately at a distance of 5 cm from the detector, leading to a geometrical efficiency of $5.5\%-6.5\%$ of $4\pi\sigma$. The result is reported in Table 4.6.

The U235G0919 source was sent by the JRC to INMRI for the measurement of the uranium emission lines count rate for the evaluation of the emission probability.

Table 4.6. Standardized activities of ^{235}U sources ($k=1$) at 24/07/2009 09:30:00 measured at JRC.

Source	^{235}U activity [Bq]	Relative uncertainty [%]
U235G0919	38.5	0.2

²²⁷Ac source

The ²²⁷Ac solution was provided to JRC in a tip vial containing 0.5 ml (0.1 M HCl) solution with an activity of 4.5 MBq (ref. date: March 2015). The ²²⁷Ac is considered to be in secular equilibrium with its daughters.

The measure of absolute activity was carried out at JRC by using alpha spectrometry through a passivated implanted planar silicon detector. The detector has a real surface of 5000 mm². The sources were placed at a distance of approximately 5 cm from the detector, providing a geometrical efficiency of 5.5%-6.5% of 4πσ. The result is reported in Table 4.7.

The Ac227G157 source was sent by the JRC to INMRI for the measurement of the ²²⁷Ac and its daughters emission lines count rate for the measurement of the emission probability.

Table 4.7. Standardized activities of ²²⁷Ac sources ($k=1$) at 24/07/2009 09:30:00 measured at JRC.

Source	²²⁷ Ac activity [Bq]	Relative uncertainty [%]
Ac227G157	1077	0.65

4.4 Emission intensity measurement at INMRI

²³⁵U

In this section, we present the strategy used for the measurement of emission probability of the ²³⁵U. For this purpose, JRC has produced an absolute source of ²³⁵U as shown in the previous section. The count rates of the ²³⁵U emission lines used for the measurement of the emission probability were carried out with gamma-ray spectrometry. We measured the ²³⁵U source (U235G0919) at INMRI laboratory, via gamma-ray spectrometry, for 50000 s. Using Equation 2.4 we obtain, by interpolation, the efficiency values referred to the energy of the emission lines of interest. Then we used GESPECOR to evaluate the correction factors referred to these values of efficiency due to structural differences (geometry and chemical composition) between the ND calibration apparatus used for the calibration of the detector and the ND measurement apparatus used to measure the source provided by JRC. We used the following characterizations: the ND calibration apparatus, the ND measurement apparatus and the detector, explained in Chapter 2, to use the Monte Carlo software. We show in Figure 4.2 the efficiency curve as a function of energy of the ND measurement apparatus, together with the calibration curve (ND calibration apparatus). The curve in Figure 4.3 shows the difference in percentage between the efficiency values of the ND calibration apparatus versus the efficiency values of the ND measurement apparatus as a function of energy.

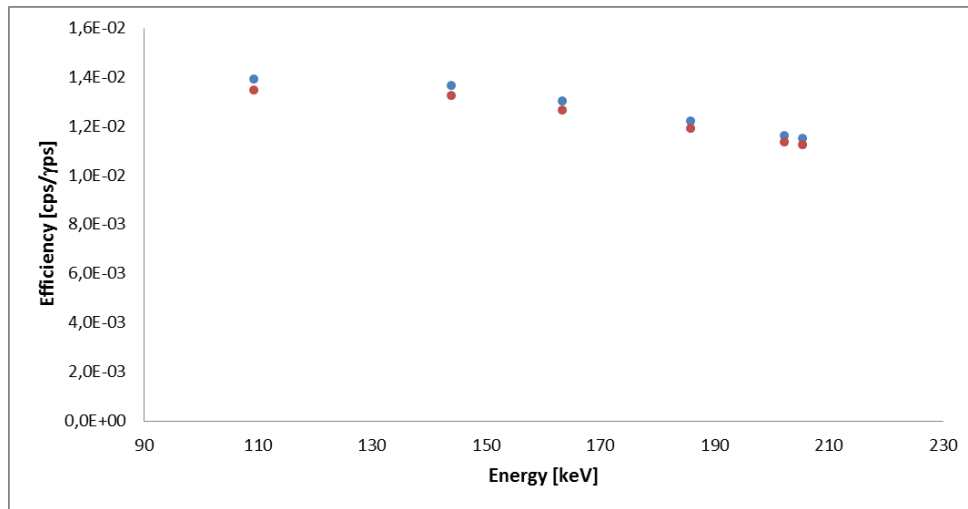


Figure 4.2. Calibration curve of the DN calibration apparatus (blue) and calibration curve of the DN measurement apparatus (red).

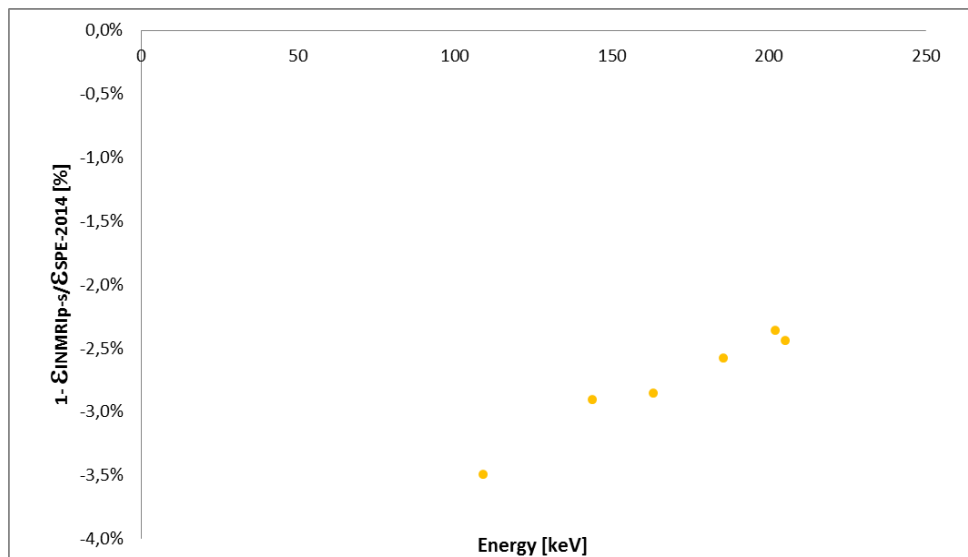


Figure 4.3. Difference in percentage between the efficiency of the DN calibration apparatus versus the efficiency of the DN measurement apparatus.

Figure 4.3 and Figure 4.4 show that the corrections applied to the calibration curve of the ND efficiency calibration apparatus to obtain the calibration curve of the ND measurement apparatus are small (i.e. 3.5% at 109.19 keV). The reason is that the two experimental configurations are very similar, especially from a geometrical point of view. Furthermore, the effects due to coincidence summing are negligible since the measurements have been carried out with the source at a distance of about 10 cm from the detector.

The results obtained from the P_γ measurement at the ENEA INMRI institute are shown in Table 4.8.

Table 4.8. Results of P_γ evaluated at ENEA INMRI through ^{235}U source.

<i>Photon Energy</i> [keV]	P_γ [%]	$u(P_\gamma)$ [%]
109.19	2.09	0.16
143.77	10.9	0.43
163.36	5.13	0.25
185.72	57.6	2.20
202.12	1.08	0.11
205.316	5.08	0.23

^{227}Ac

In this section, we present the strategy used for the measurement of the emission probability of the following radionuclide: ^{227}Th , ^{223}Ra , ^{319}Rn , ^{211}Pb , ^{211}Bi , ^{207}Tl . For this purpose, JRC has produced a source of ^{227}Ac containing all the radionuclides up to ^{207}Pb and belonging to the ^{235}U radioactive chain. The count rates of the emission lines used for the measurement of the emission probability were carried out using gamma-ray spectrometry. We measured at INMRI laboratory the ^{227}Ac source (Ac227G157) for 50000 s. Afterwards, we have used GESPECOR to evaluate the correction factors to the efficiency due to structural differences (geometry and chemical composition) between the ND calibration apparatus and the ND measurement apparatus. To use the Monte Carlo software, we considered the characterizations of: ND calibration apparatus, ND measurement apparatus and detector, explained in Chapter 2. In Figure 4.4 the calibration values obtained from the efficiency calibration in the ND calibration apparatus (Figure 2.12) are shown together with the results of the calibration procedure carried out through the use of GESPECOR software (ND measurement apparatus). The curve in Figure 4.5 shows the difference in percentage between the efficiency values of the ND calibration apparatus versus the efficiency values of the ND measurement apparatus.

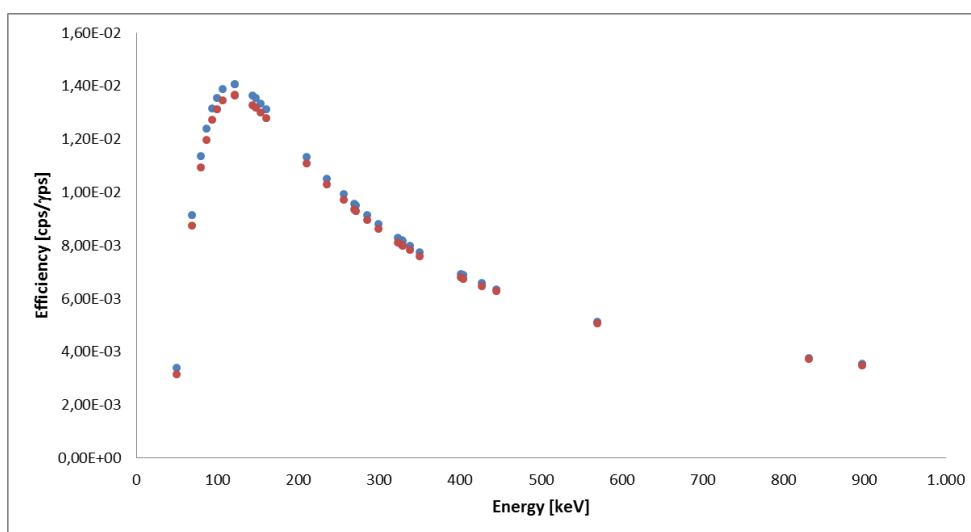


Figure 4.4. Calibration curve DN calibration apparatus (blue) and calibration curve of the DN measurement apparatus (red).

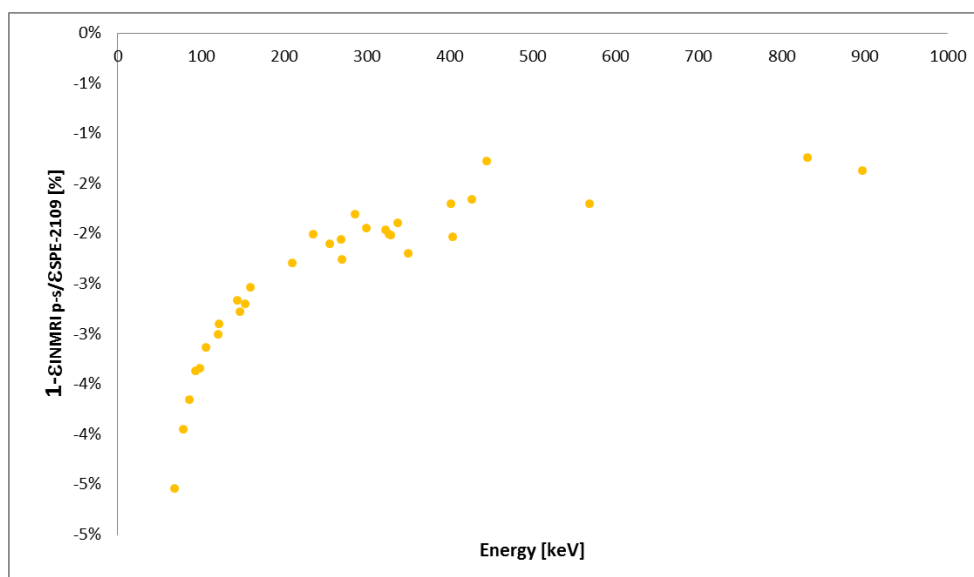


Figure 4.5. Difference in percentage between the efficiency of the DN calibration apparatus versus the efficiency of the DN measurement apparatus.

The results obtained from the P_γ measurement at ENEA INMRI institute are shown in Table 4.9.

Table 4.9. Results of P_γ measured at ENEA INMRI through ^{227}Ac source.

<i>Radionuclide</i>	<i>Photon Energy [keV]</i>	<i>P_γ [%]</i>	<i>$u(P_\gamma)$ [%]</i>
^{227}Th	79.69	0.01961	0.00214
^{227}Th	117.20	0.00208	0.00012
^{227}Th	210.62	0.01253	0.00054
^{227}Th	235.96	0.13317	0.00573
^{227}Th	256.23	0.07573	0.00326
^{227}Th	286.09	0.01795	0.00077
^{227}Th	299.98	0.02265	0.00097
^{227}Th	304.50	0.01103	0.00047
^{227}Th	312.69	0.00555	0.00024
^{227}Th	314.85	0.00493	0.00022
^{227}Th	329.85	0.03006	0.00129
^{223}Ra	122.32	0.01386	0.00061
^{223}Ra	154.21	0.06399	0.00275
^{223}Ra	158.63	0.00802	0.00035
^{223}Ra	179.54	0.00168	0.00009
^{223}Ra	269.46	0.14244	0.00612
^{223}Ra	338.28	0.02778	0.00119
^{223}Ra	445.03	0.01282	0.00056
^{219}Rn	271.23	0.11351	0.00488
^{219}Rn	401.81	0.06978	0.00300
^{211}Pb	404.83	0.04215	0.00181
^{211}Pb	427.15	0.01985	0.00085
^{211}Pb	704.67	0.00527	0.00024
^{211}Pb	831.98	0.03749	0.00161
^{211}Pb	1109.51	0.00129	0.00007
^{211}Bi	351.03	0.14156	0.00622
^{207}Tl	897.77	0.00295	0.00015

4.5 Emission intensity measurements from the international partners

The emission probability of the radionuclide belonging to the ^{235}U series was carried out through the gamma-ray spectrometry measurement of the ^{235}U and ^{227}Ac sources. The measurement apparatus used by MetroNORM partners are listed in Table 4.10.

Table 4.10. Information on the partners measurement conditions.

	<i>JRC</i>	<i>CIEMAT</i>	<i>CEA</i>	<i>CMI</i>
<i>Detector</i>	Low background HPGe Planar BEGe, Thin dead layer 50% relative efficiency	Extended range HPGe (p-type) Thin dead layer 40% relative efficiency	HPGe (p-type) 40% relative efficiency	HPGe 4018 Canberra (p-type)
<i>Exp. Conditions</i>	Underground lad (Hades), Nitrogen injected in measurement chamber to prevent radon accumulation			Laboratory used for any service
<i>Measurement [d]</i>	41	21	4	4
<i>Distance source detector [mm]</i>	120	150		30
<i>Full energy peak efficiency</i>	PTB point source	Point and volume source		MC

^{235}U

The five laboratories reported their values with the associated uncertainty budget, summarized in Table 4.11.

Table 4.11. Measured ^{235}U P_γ emission probabilities.

Photon Energy [keV]	JRC		CIEMAT		ENEA		CEA		CMI	
	P_γ [%]	$u(P_\gamma)$ [%]								
31.6	0.079	0.009								
42.01	0.070	0.009					0.063	0.004		
51.21	0.010	0.005								
54.25	0.016	0.005					0.034	0.003		
64.45							2.164	0.035		
72.7	0.275	0.020					0.373	0.021		
74.94	0.073	0.013					0.330	0.019		
96.09	0.648	0.036					0.645	0.014		
109.19	1.59	0.08			2.09	0.16	1.670	0.029		
120.35	0.022	0.009								
140.76	0.224	0.015					0.038	0.004		
143.77	11.02	0.52	10.64	0.10	10.92	0.43	10.87	0.16	10.92	0.13
150.94	0.076	0.009								
163.36	5.20	0.25	5.12	0.09	5.13	0.25	5.08	0.08	5.11	0.07
182.62	0.367	0.018	0.46	0.1			0.398	0.012		
185.72	58.27	2.74	57.2	0.3	57.6	2.2	57.8	0.8	56.60	0.65
194.94	0.635	0.031	0.77	0.09			0.77	0.02		
198.894	0.044	0.003					0.079	0.006		
202.12	1.069	0.051	1.080	0.090	1.081	0.111	1.274	0.026	1.051	0.024
205.316	5.08	0.24	5.03	0.11	5.08	0.23	5.06	0.09	5.00	0.06
215.28	0.0299	0.0020								
221.386	0.117	0.006							0.10	0.01

Photon Energy [keV]	JRC		CIEMAT		ENEA		CEA		CMI	
	P_γ [%]	$u(P_\gamma)$ [%]								
228.76	0.0067	0.0010								
233.5	0.032	0.002								
240.88	0.064	0.004					0.064	0.006		
246.83	0.0485	0.0029								
266.47	0.0067	0.0010								
275.35	0.032	0.02								
275.49										
289.56	0.0054	0.0010								
291.65	0.027	0.002								
345.92	0.038	0.003								
356.03	0.0024	0.0007								
387.84	0.026	0.002								
410.29	0.0023	0.0006								

²²⁷Ac

In Table 4.12 the results of the emission probability measurements are shown. They were carried out, through gamma-ray spectrometry, by the institutes involved in this project. All the gamma-rays reported in DDEP table of ²²⁷Ac, ²²³Ra, ²¹⁹Rn, ²¹⁵Po, ²¹¹Pb, ²¹¹Bi and ²⁰⁷Tl were considered in the spectrum analysis [73]. The ²²⁷Th decay data were coming from NNDC (National Nuclear Data Center) web page as the ²²⁷Th decay data are not reported in DDEP tables [73].

Table 4.12. Measured ²³⁵U P_γ emission probabilities.

Nuc.	Photon Energy [keV]	JRC		CIEMAT		ENEA		CEA		CMI	
		P_γ [%]	$u(P_\gamma)$ [%]								
²²⁷ Ac	37.9	0.0495	0.0031								
²²⁷ Th	31.58	0.0704	0.0056								

Development of a Reference Material
and determination of Nuclear Data for NORM analysis

Nuc.	Photon Energy [keV]	JRC		CIEMAT		ENEA		CEA		CMI	
		P_γ [%]	$u(P_\gamma)$ [%]								
²²⁷ Th	40.2	0.0663	0.0041								
²²⁷ Th	49.82									0.601	0.034
²²⁷ Th	50.13	9.386	0.54	9.204	0.182					9.908	0.543
²²⁷ Th	50.85										
²²⁷ Th	61.44	0.0628	0.0038								
²²⁷ Th	62.45	0.159	0.009								
²²⁷ Th	79.69	2.46	0.14			1.961	0.214				
²²⁷ Th	85.43	1.77	0.10								
²²⁷ Th	88.47	2.68	0.15								
²²⁷ Th	113.1	0.82	0.04							0.843	0.045
²²⁷ Th	117.2	0.198	0.010			0.208	0.012			0.200	0.013
²²⁷ Th	123.6	0.007	0.001								
²²⁷ Th	141.4									0.110	0.014
²²⁷ Th	141.4	0.122	0.005								
²²⁷ Th	150.1	0.017	0.002								
²²⁷ Th	162.2	0.017	0.002								
²²⁷ Th	168.4	0.012	0.001								
²²⁷ Th	169.9	0.008	0.001								
²²⁷ Th	173.4	0.014	0.002								
²²⁷ Th	184.6	0.041	0.002								
²²⁷ Th	197.6							0.010	0.000		
²²⁷ Th	200.5	0.016	0.001								
²²⁷ Th	201.6	0.019	0.001					0.020	0.001		
²²⁷ Th	204.1									0.200	0.017
²²⁷ Th	204.9	0.333	0.012							0.151	0.017
²²⁷ Th	206.1	0.286	0.010					0.252	0.007	0.256	0.011
²²⁷ Th	210.6	1.201	0.043	1.11	0.03	1.253	0.054	1.201	0.034	1.184	0.047
²²⁷ Th	212.7										
²²⁷ Th	212.7	0.096	0.004								
²²⁷ Th	218.9	0.102	0.004							0.097	0.015
²²⁷ Th	234.8	0.472	0.017							0.562	0.097
²²⁷ Th	236.0	12.698	0.450	12.58	0.25	13.317	0.573	12.896	0.364	13.083	0.410
²²⁷ Th	246.1	0.020	0.001								
²²⁷ Th	250.3	0.489	0.017							0.509	0.023

<i>Nuc.</i>	<i>Photon Energy [keV]</i>	<i>JRC</i>		<i>CIEMAT</i>		<i>ENEA</i>		<i>CEA</i>		<i>CMI</i>	
		P_γ [%]	$u(P_\gamma)$ [%]								
²²⁷ Th	252.5	0.092	0.003							0.140	0.008
²²⁷ Th	254.6	0.705	0.025							0.828	0.028
²²⁷ Th	256.2	6.771	0.240	6.79	0.14	7.573	0.326	6.980	0.197	7.038	0.222
²²⁷ Th	262.9	0.122	0.004							0.129	0.015
²²⁷ Th	272.9	0.529	0.019							0.513	0.018
²²⁷ Th	279.8	0.046	0.002							0.041	0.005
²²⁷ Th	281.4									0.174	0.008
²²⁷ Th	281.4	0.170	0.006								
²²⁷ Th	284.2	0.033	0.001								
²²⁷ Th	286.1	1.885	0.067	1.63	0.04	1.795	0.077	1.915	0.054	1.862	0.060
²²⁷ Th	292.4	0.059	0.002								
²²⁷ Th	296.5	0.432	0.015					0.470	0.013	0.455	0.015
²²⁷ Th	299.9			1.81	0.04			2.297	0.065		
²²⁷ Th	300.5	2.168	0.077			2.265	0.097				
²²⁷ Th	304.5	1.070	0.038			1.103	0.047	1.131	0.032	1.084	0.035
²²⁷ Th	308.4	0.020	0.001								
²²⁷ Th	312.7	0.539	0.019			0.555	0.024	0.557	0.016	0.563	0.019
²²⁷ Th	314.8	0.485	0.017			0.493	0.022			0.503	0.018
²²⁷ Th	329.8	2.733	0.097			3.006	0.129			2.852	0.092
²²⁷ Th	334.4	1.084	0.038	0.9795	0.0305			1.141	0.032	1.143	0.037
²²⁷ Th	342.5									0.635	0.022
²²⁷ Th	346.4	0.0095	0.0010								
²²⁷ Th	382.2	0.0063	0.0006								
²²⁷ Th	466.8	0.00135	0.00041								
²²⁷ Th	493.1	0.00134	0.00039								
²²⁷ Th	524.5	0.00128	0.00042								
²²⁷ Th	536.9	0.00170	0.00143								
²²⁷ Th	756.9	0.00097	0.00028								
²²⁷ Th	775.8	0.00801	0.00065								
²²⁷ Th	781	0.00101	0.00024								
²²⁷ Th	797.3	0.00174	0.00025								
²²⁷ Th	803.9	0.00211	0.00028								
²²⁷ Th	812.6	0.00342	0.00029								
²²⁷ Th	823.4	0.00337	0.00029								

Development of a Reference Material
and determination of Nuclear Data for NORM analysis

Nuc.	Photon Energy [keV]	JRC		CIEMAT		ENEA		CEA		CMI	
		P_γ [%]	$u(P_\gamma)$ [%]								
²²⁷ Th	842.5	0.00044	0.00014								
²²⁷ Th	846.7	0.00042	0.00014								
²²⁷ Th	908.6	0.00251	0.00021								
²²³ Fr	134.6									0.048	0.016
²²³ Ra	104.0	0.074	0.005								
²²³ Ra	106.8	0.016	0.003								
²²³ Ra	122.3	1.351	0.048	1.306	0.035	1.386	0.061			1.416	0.061
²²³ Ra	131.6	0.016	0.001								
²²³ Ra	144.3	3.623	0.128	3.439	0.058					3.763	0.155
²²³ Ra	147.2	0.006	0.001								
²²³ Ra	154.2	6.284	0.223	5.915	0.079	6.399	0.275			6.523	0.205
²²³ Ra	158.6	0.771	0.027	0.707	0.025	0.802	0.035			0.802	0.030
²²³ Ra	165.8	0.004	0.001							0.000	
²²³ Ra	175.6	0.020	0.002								
²²³ Ra	177.3	0.054	0.002								
²²³ Ra	179.5	0.184	0.007			0.168	0.009	0.151	0.004	0.133	0.015
²²³ Ra	221.3	0.030	0.002								
²²³ Ra	249.5	0.043	0.004								
²²³ Ra	251.6	0.017	0.002								
²²³ Ra	269.5	13.593	0.482			14.244	0.612			14.362	0.450
²²³ Ra	288.2	0.125	0.005								
²²³ Ra	323.9	3.704	0.131	3.54	0.08					3.964	0.126
²²³ Ra	328.2	0.190	0.007								
²²³ Ra	338.3	2.634	0.093	2.51	0.07	2.778	0.119			2.845	0.091
²²³ Ra	342.8									0.636	0.021
²²³ Ra	355.5	0.008	0.001								
²²³ Ra	361.9	0.034	0.001								
²²³ Ra	362.9	0.024	0.001								
²²³ Ra	368.6	0.015	0.001								
²²³ Ra	371.7	0.441	0.016							0.468	0.017
²²³ Ra	372.9									0.114	
²²³ Ra	376.3	0.009	0.001								
²²³ Ra	430.6	0.019	0.001					0.026	0.001		
²²³ Ra	432.4	0.035	0.001								

<i>Nuc.</i>	<i>Photon Energy [keV]</i>	<i>JRC</i>		<i>CIEMAT</i>		<i>ENEA</i>		<i>CEA</i>		<i>CMI</i>	
		P_γ [%]	$u(P_\gamma)$ [%]								
²²³ Ra	445.0	1.238	0.044	1.179	0.035	1.282	0.056			1.293	0.043
²²³ Ra	487.5	0.006	0.001								
²²³ Ra	500.0	0.001	0.001								
²²³ Ra	527.6	0.067	0.002							0.075	0.015
²²³ Ra	537.6	0.003	0.000								
²²³ Ra	542.0	0.001	0.001								
²²³ Ra	598.7	0.086	0.003							0.083	0.018
²²³ Ra	609.3	0.032	0.004								
²²³ Ra	619.1	0.002	0.001								
²²³ Ra	623.7	0.007	0.001								
²²³ Ra	711.3	0.003	0.000								
²²³ Ra	718.4	0.001	0.001								
²¹⁹ Rn	130.6	0.147	0.005							0.182	0.022
²¹⁹ Rn	271.2	10.971	0.389			11.351	0.488			11.512	0.361
²¹⁹ Rn	293.6	0.064	0.002								
²¹⁹ Rn	401.8	6.724	0.238			6.978	0.300			7.142	0.225
²¹⁹ Rn	517.6	0.046	0.002					0.047	0.001	0.047	0.015
²¹⁹ Rn	564.1	0.0048	0.0015								
²¹⁹ Rn	676.7	0.021	0.001								
²¹⁹ Rn	877.2	0.0007	0.0002								
²¹⁹ Rn	891.1	0.00047	0.00021								
²¹⁵ Po	438.9	0.0539	0.0020					0.057	0.002	0.0726	0.013
²¹¹ Pb	361.8	0.034	0.001								
²¹¹ Pb	404.8	4.027	0.143			4.215	0.181			4.305	0.142
²¹¹ Pb	427.1	1.888	0.067			1.985	0.085			1.986	0.076
²¹¹ Pb	429.6	0.004	0.001								
²¹¹ Pb	504.1	0.0021	0.0004								
²¹¹ Pb	609.5	0.025	0.003								
²¹¹ Pb	675.8	0.005	0.001								
²¹¹ Pb	704.7	0.508	0.018			0.527	0.024			0.530	0.028
²¹¹ Pb	766.7	0.299	0.077							0.781	0.026
²¹¹ Pb	832.0	3.635	0.129			3.749	0.161			3.764	0.120
²¹¹ Pb	865.9	0.006	0.000								
²¹¹ Pb	1014.3	0.012	0.005								

Nuc.	Photon Energy [keV]	JRC		CIEMAT		ENEA		CEA		CMI	
		P_γ [%]	$u(P_\gamma)$ [%]								
²¹¹ Pb	1080.6	0.013	0.001								
²¹¹ Pb	1103.5	0.004	0.000								
²¹¹ Pb	1109.5	0.119	0.004			0.129	0.007			0.161	0.059
²¹¹ Pb	1196.3	0.010	0.000								
²¹¹ Pb	1234.3	0.001	0.000								
²¹¹ Pb	1270.7	0.007	0.000					0.007	0.0001		
²¹¹ Bi	351.03	13.50	0.48			14.156	0.622			14.191	0.445
²⁰⁷ Tl	569.7	0.0063	0.0006								
²⁰⁷ Tl	897.8	0.2840	0.0102			0.295	0.015			0.349	0.013

4.6 Final measurements of the emission intensities

In the following, we describe the final measurement of the emission intensities of the radionuclide belonging to ²³⁵U chain.

The power moderated mean (PMM) was chosen to estimate the P_γ values for each gamma line [72]. The results are generally intermediate between arithmetic and weighted mean, depending on the reported uncertainties. A coverage factor of $k=2$ was selected to identify extreme data. Uncertainties are considered informative but imperfect with a tendency of being underestimated ($\alpha=2 - 3/N$). Below, PMM and measured values are illustrated for the cases in which the P_γ has been measured by three or more laboratories.

²³⁵U

In Figure 4.6 the measured gamma-intensities are shown, represented as black points, while red lines represent the uncertainty on the PMM (black line).

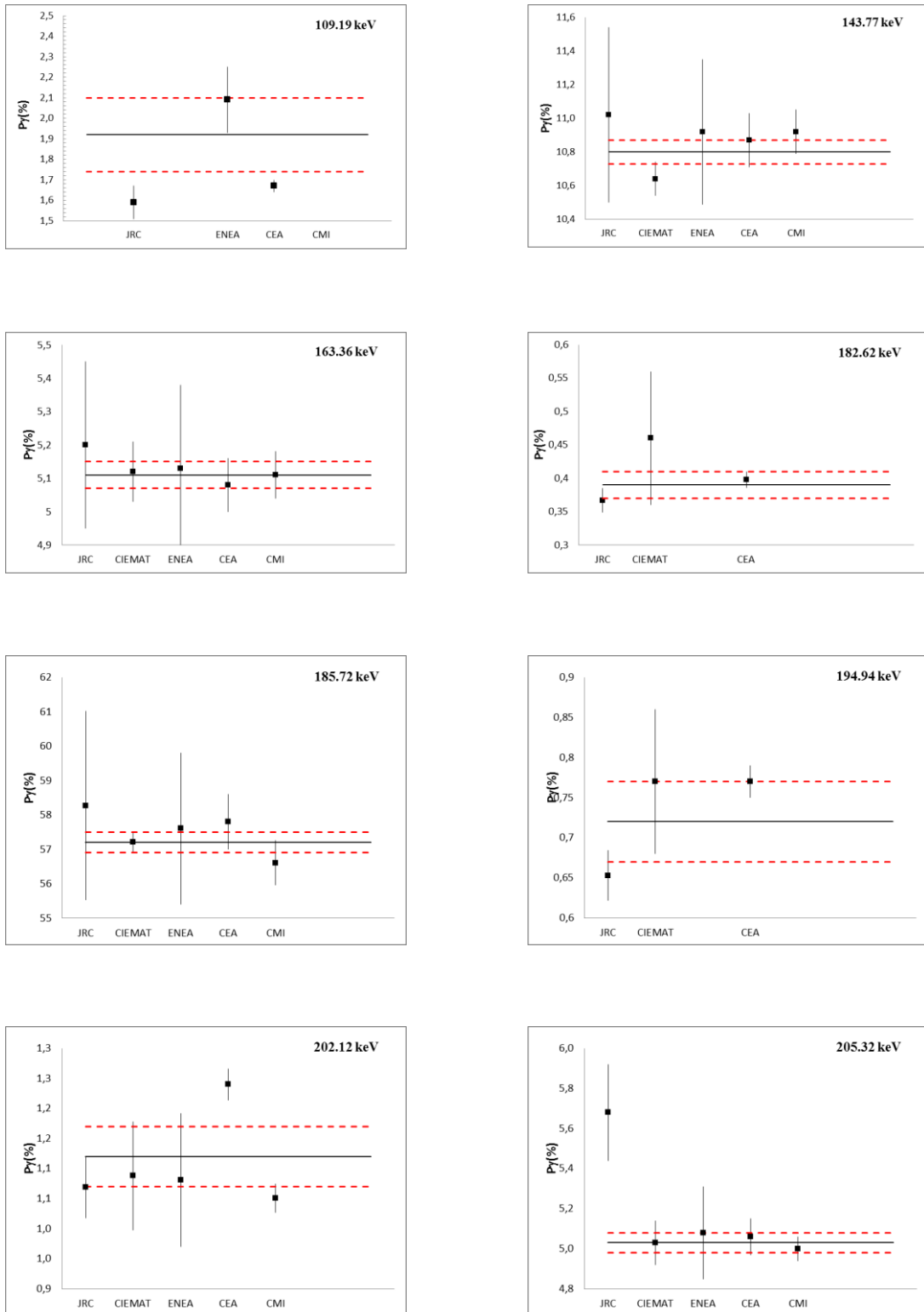


Figure 4.6. Measured gamma-intensities represented as black points. Black line present the PMM and the red lines present the PPM uncertainty.

In Table 4.13 the new gamma emission probabilities derived from this work are listed, together with the DDEP recommended value, the relative deviation of the calculated P_γ against the DDEP value is also reported in the last column.

Table 4.13. New gamma emission probabilities derived from this work.

<i>Photon Energy [keV]</i>	<i>DDEP</i>		<i>This work</i>		<i>Rel. dev. [%]</i>
	P_γ [%]	$u(P_\gamma)$ [%]	P_γ [%]	$u(P_\gamma)$ [%]	
31.6	0.017	0.006	0.079	0.009	365
42.01	0.056	0.009	0.066	0.004	18
51.21	0.034	0.007	0.010	0.00	-71
54.25	0.0285		0.025	0.009	-12
64.45	0.018		2.164	0.035	11922
72.7	0.116	0.02	0.324	0.049	179
74.94	0.051	0.006	0.20	0.13	292
96.09	0.091	0.011	0.646	0.015	610
109.19	1.66	0.13	1.92	0.18	16
120.35	0.026		0.022	0.010	-15
140.76	0.2	0.01	0.224	0.016	12
143.77	10.94	0.06	10.80	0.07	-1
150.94	0.09	0.03	0.076	0.009	-16
163.36	5.08	0.03	5.11	0.04	1
182.62	0.39	0.05	0.39	0.02	0
185.72	57.1	0.3	57.2	0.3	0.2
194.94	0.63	0.01	0.72	0.05	14
198.89	0.036	0.002	0.061	0.017	69
202.12	1.08	0.02	1.12	0.05	4
205.32	5.02	0.03	5.03	0.05	0.2

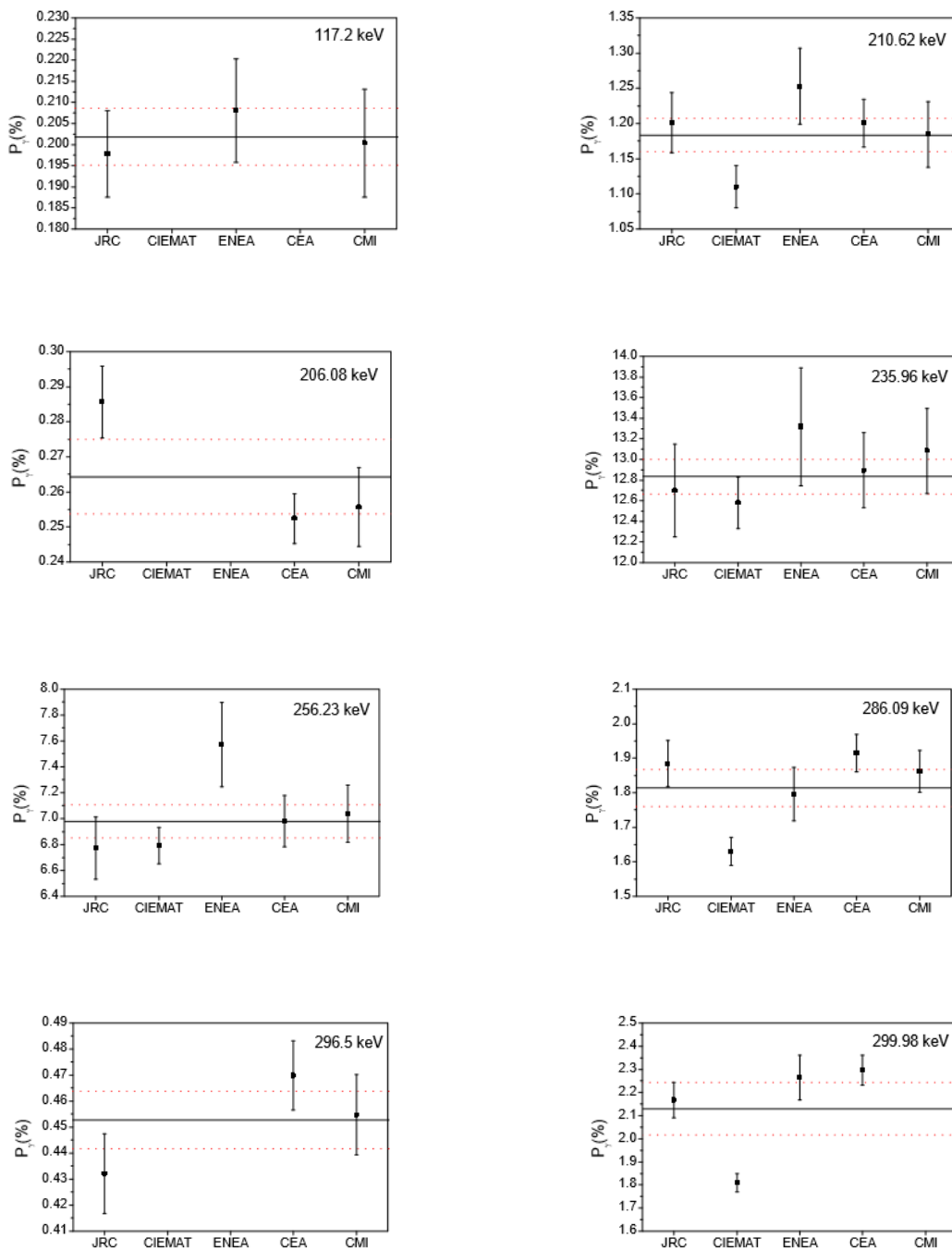
<i>Photon Energy</i> [keV]	<i>DDEP</i>		<i>This work</i>		<i>Rel. dev.</i> [%]
	P_γ [%]	$u(P_\gamma)$ [%]	P_γ [%]	$u(P_\gamma)$ [%]	
215.28	0.029	0.003	0.030	0.002	3
221.39	0.118	0.005	0.110	0.008	-7
228.76	0.0074	0.006	0.0067	0.0010	-9
233.5	0.038	0.004	0.032	0.002	-16
240.88	0.074	0.004	0.064	0.003	-14
246.83	0.055	0.003	0.049	0.003	-11
266.47	0.0078	0.0006	0.0067	0.0010	-14
275.35	0.051	0.006	0.032	0.002	-37
289.56	0.0074		0.0053	0.0010	-28
291.65	0.040	0.006	0.027	0.002	-33
345.92	0.040	0.006	0.038	0.003	-5
356.03	0.0053		0.0024	0.0007	-55
387.84	0.04	0.006	0.026	0.002	-35
410.29	0.0032		0.0023	0.0006	-28

There were P_γ values included in the DDEP library which were based in only one measurement more than 20 years ago and few of them did not report uncertainties. These include the 64.45 keV, 72.7 keV, 120.35 keV, 275.35 keV, 289.56 keV, 356.03 keV and the 410.29 keV gamma lines. In this work the P_γ for the above gamma-energies have been measured by at least one laboratory. In addition, for the main gamma-lines the laboratories agree within uncertainties on the measured P_γ . Special note should be given to the 96.09 keV gamma line. Although the measurements from the two laboratories agreed (relative difference less than 5%), the estimated value on the P_γ is almost 6 times higher than the DDEP. That should not exclude the validity of this measurement since the DDEP value is based in only one measurement in 1974 [73].

^{227}Ac

In Figure 4.7 the measured gamma-intensities for $^{227}\text{Ac} \rightarrow ^{223}\text{Ra}$ are shown, in

Figure 4.8 the measured gamma-intensities for $^{223}\text{Ra} \rightarrow ^{219}\text{Rn}$, and in Figure 4.9 the measured gamma-intensities for $^{219}\text{Rn} \rightarrow ^{215}\text{Po}$. The measurements are represented as rectangular black points instead red lines represent the uncertainty on the PMM (black line).



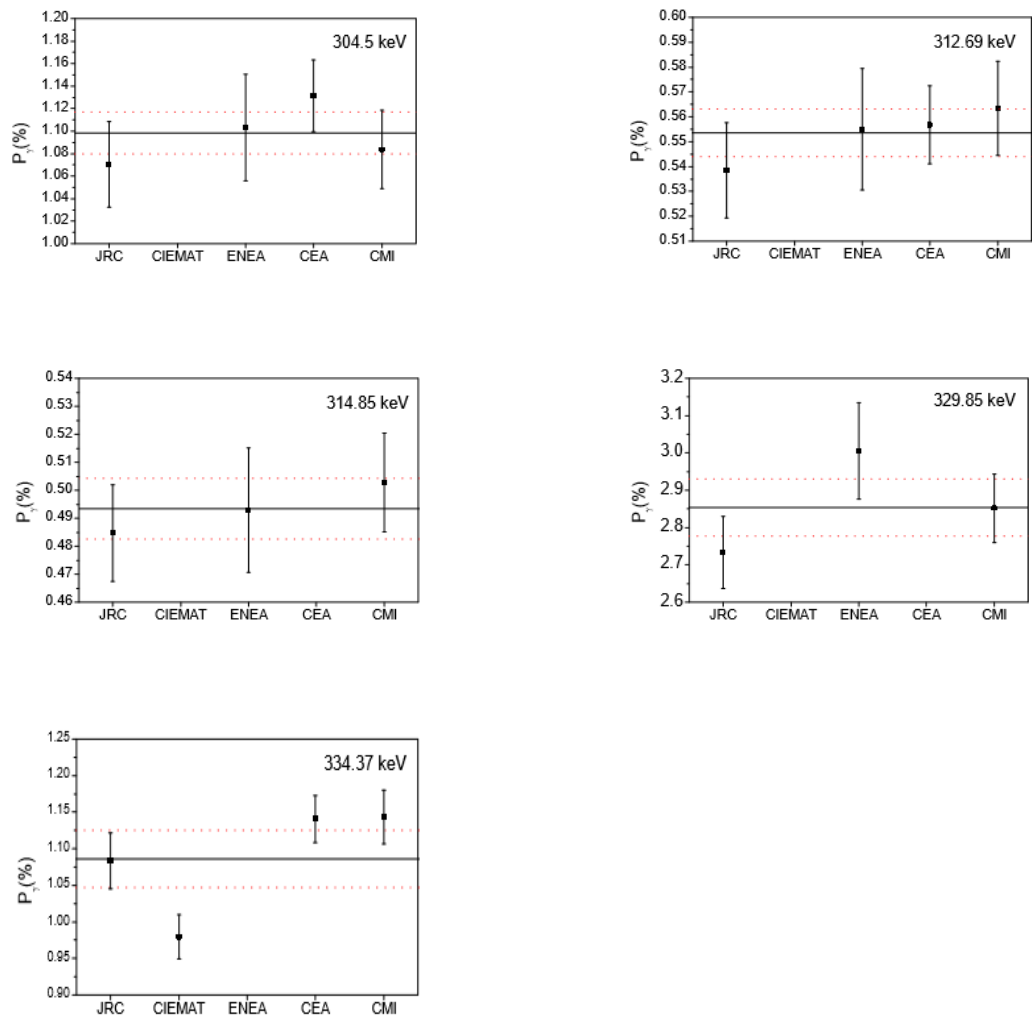
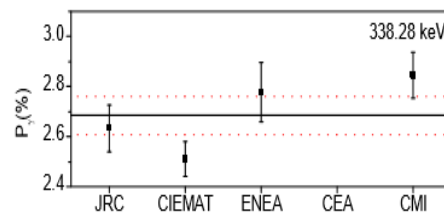
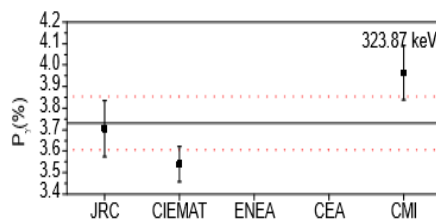
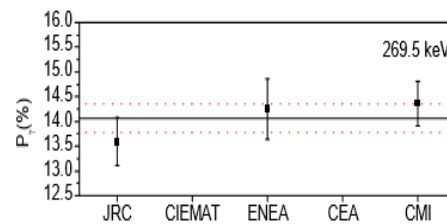
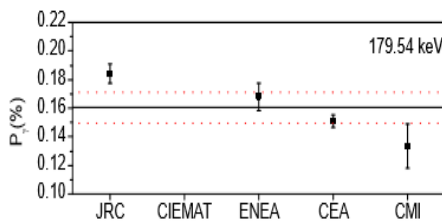
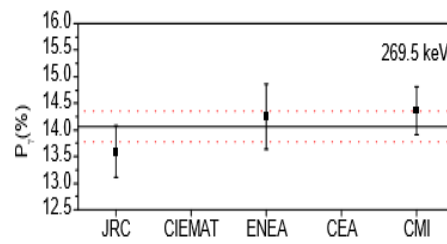
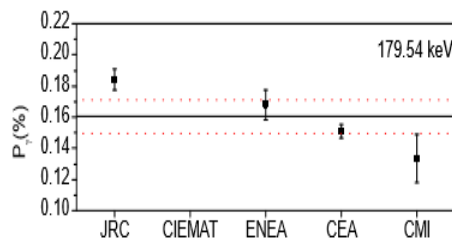
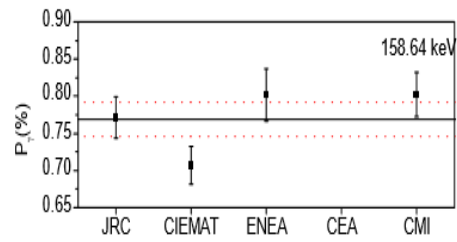
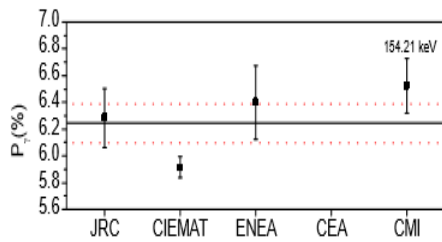
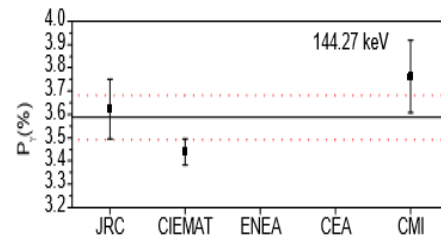
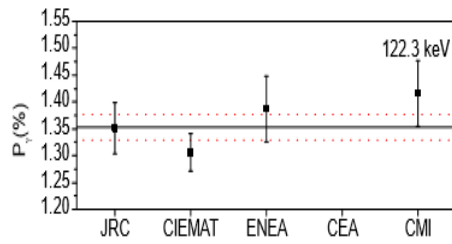


Figure 4.7. Measured gamma-intensities represented as rectangular black points for $^{227}\text{Ac} \rightarrow ^{223}\text{Ra}$. Red lines present the uncertainty on the PMM (black line).



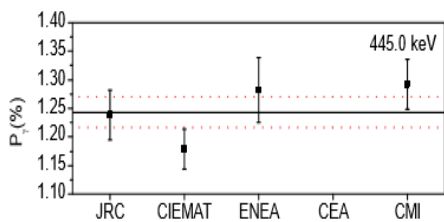


Figure 4.8. Measured gamma-intensities for $^{223}\text{Ra} \rightarrow ^{219}\text{Rn}$ represented as rectangular black points. Red lines present the uncertainty on the PMM (black line).

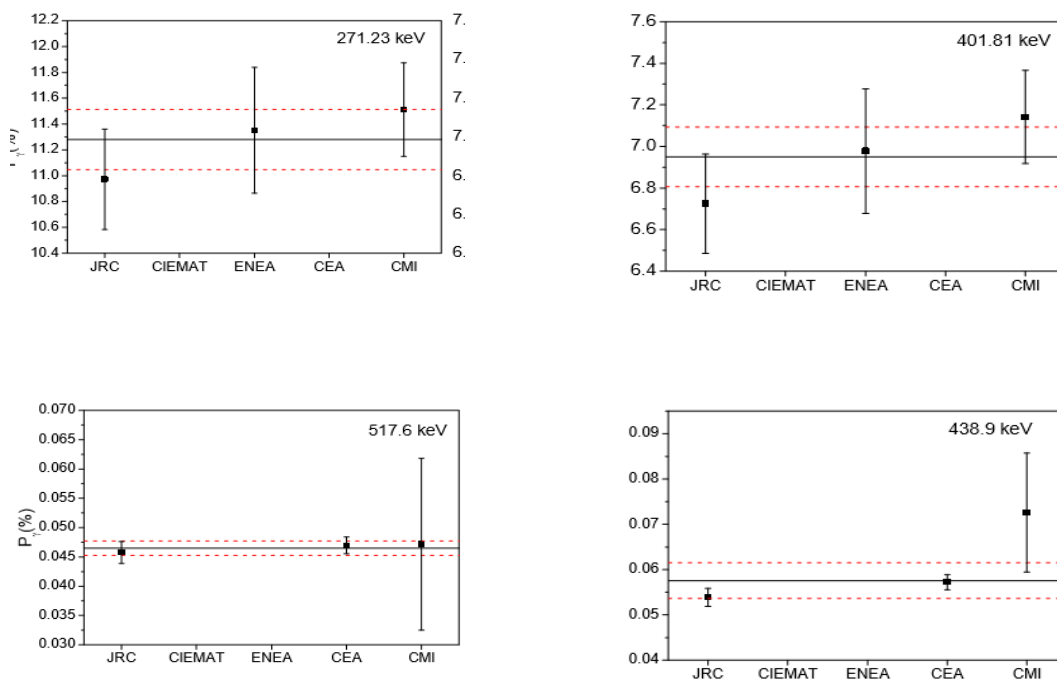


Figure 4.9. Measured gamma-intensities for $^{219}\text{Rn} \rightarrow ^{211}\text{Pb}$ represented as rectangular black points. Red lines present the uncertainty on the PMM (black line).

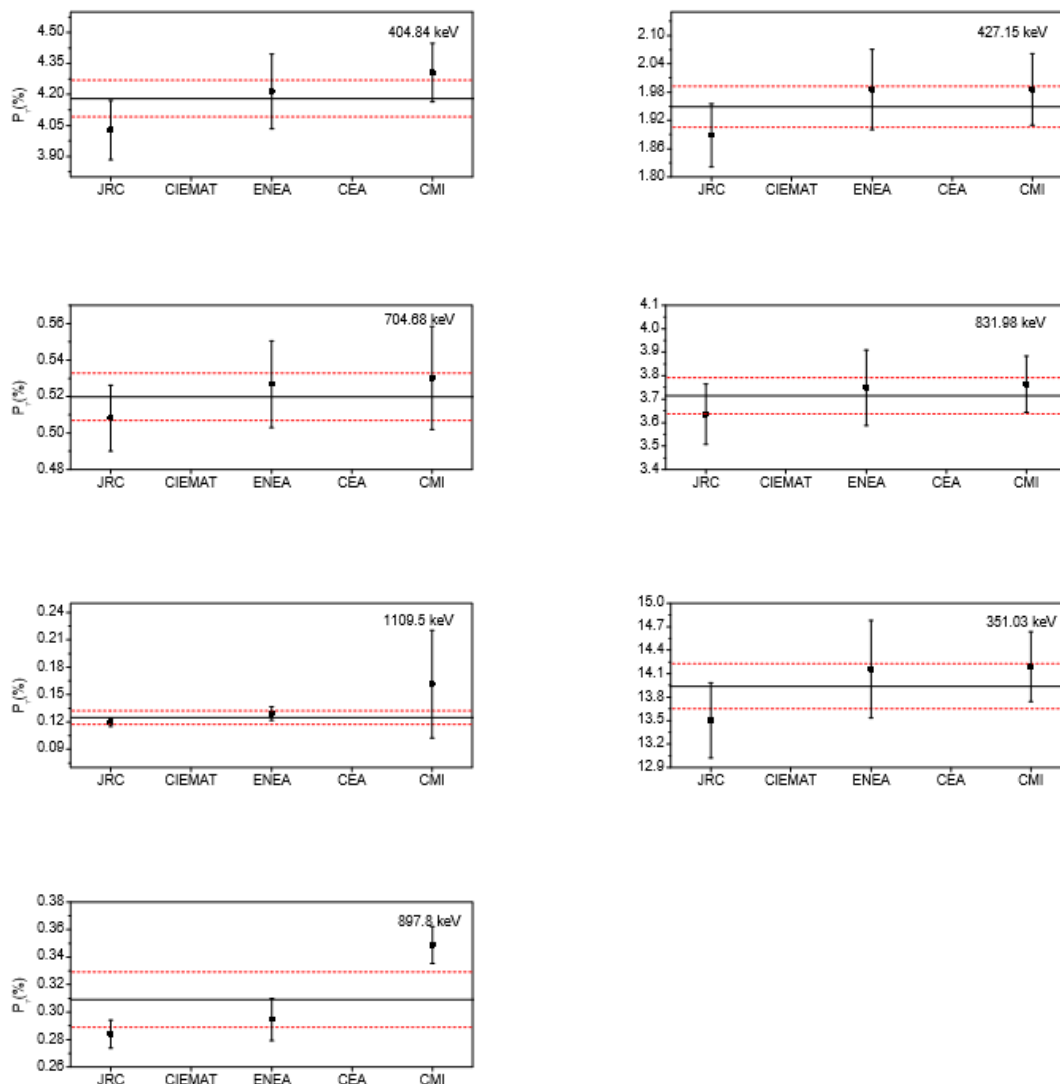


Figure 4.10. Measured gamma-intensities for $^{211}\text{Pb} \rightarrow ^{207}\text{Pb}$ represented as rectangular black points. Red lines present the uncertainty on the PMM (black line).

The Table 4.14 summarizes the gamma-emission probabilities, estimated with the PMM when measured by more than one laboratory. The relative deviation of the calculated P_γ against the DDEP/NNDC value is also calculated.

Table 4.14. New gamma emission probabilities derived from this work.

<i>Nuc.</i>	<i>Photon Energy [keV]</i>	<i>DDEP</i>		<i>This work</i>		<i>Rel. dev. [%]</i>
		P_γ [%]	$u(P_\gamma)$ [%]	P_γ [%]	$u(P_\gamma)$ [%]	
²²⁷ Ac	37.9	0.049		0.049	0.003	1
²²⁷ Th	31.58	0.068	0.010	0.070	0.006	3
²²⁷ Th	40.2	0.0155	0.0004	0.066	0.004	328
²²⁷ Th	49.82	0.426	0.090	0.601	0.034	41
²²⁷ Th	50.13	8.39	0.39	9.50	0.34	13
²²⁷ Th	61.44	0.090	0.010	0.063	0.004	-30
²²⁷ Th	62.45	0.203	0.026	0.159	0.009	-22
²²⁷ Th	79.69	1.948	0.065	2.22	0.25	14
²²⁷ Th	85.431	1.34	0.05	1.77	0.10	32
²²⁷ Th	88.471	2.18	0.08	2.68	0.15	23
²²⁷ Th	113.11	0.54		0.83	0.03	53
²²⁷ Th	117.2	0.199	0.014	0.202	0.007	2
²²⁷ Th	123.58	0.014	0.005	0.0067	0.0013	-53
²²⁷ Th	141.42	0.119	0.023	0.122	0.005	3
²²⁷ Th	150.14	0.0111	0.0031	0.017	0.002	56
²²⁷ Th	162.19	0.0077	0.0026	0.017	0.002	114
²²⁷ Th	168.36	0.0148	0.0026	0.012	0.001	-22
²²⁷ Th	169.95	0.0055	0.0022	0.008	0.001	45
²²⁷ Th	173.45	0.0174	0.0026	0.014	0.002	-20
²²⁷ Th	184.65	0.036	0.004	0.041	0.002	13
²²⁷ Th	197.56	0.013	0.004	0.010	0.000	-20
²²⁷ Th	200.5	0.013	0.009	0.016	0.001	26
²²⁷ Th	201.64	0.024	0.003	0.020	0.001	-17
²²⁷ Th	204.14	0.227	0.026	0.200	0.017	-12

<i>Nuc.</i>	<i>Photon Energy [keV]</i>	<i>DDEP</i>		<i>This work</i>		<i>Rel. dev. [%]</i>
		<i>P_γ [%]</i>	<i>u(P_γ) [%]</i>	<i>P_γ [%]</i>	<i>u(P_γ) [%]</i>	
²²⁷ Th	204.98	0.164	0.026	0.151	0.017	-8
²²⁷ Th	206.08	0.254	0.026	0.264	0.011	4
²²⁷ Th	210.62	1.25	0.09	1.18	0.02	-5
²²⁷ Th	212.7	0.079	0.009	0.0957	0.004	-2
²²⁷ Th	212.7	0.019	0.005			
²²⁷ Th	218.9	0.110	0.010	0.100	0.004	-8
²²⁷ Th	234.76	0.45	0.05	0.50	0.04	10
²²⁷ Th	235.96	12.90	0.26	12.83	0.17	-1
²²⁷ Th	246.12	0.012	0.001	0.020	0.001	67
²²⁷ Th	250.27	0.45	0.04	0.51	0.02	13
²²⁷ Th	252.5	0.11	0.02	0.12	0.02	5
²²⁷ Th	254.63	0.71	0.13	0.77	0.06	8
²²⁷ Th	256.23	7.00	0.13	6.98	0.13	0
²²⁷ Th	262.87	0.107	0.008	0.125	0.005	17
²²⁷ Th	272.91	0.508	0.008	0.521	0.013	2
²²⁷ Th	279.8	0.054	0.013	0.044	0.002	-18
²²⁷ Th	281.42	0.178	0.012	0.172	0.005	-4
²²⁷ Th	284.24	0.040	0.013	0.033	0.001	-16
²²⁷ Th	286.09	1.74	0.15	1.81	0.05	4
²²⁷ Th	292.41	0.066	0.008	0.059	0.002	-11
²²⁷ Th	296.5	0.44	0.04	0.45	0.01	3
²²⁷ Th	299.98	2.21	0.06	2.13	0.11	-3
²²⁷ Th	304.5	1.15	0.13	1.10	0.02	-4
²²⁷ Th	308.4	0.017	0.003	0.020	0.001	16
²²⁷ Th	312.69	0.516	0.039	0.554	0.009	7

<i>Nuc.</i>	<i>Photon Energy [keV]</i>	<i>DDEP</i>		<i>This work</i>		<i>Rel. dev. [%]</i>
		P_γ [%]	$u(P_\gamma)$ [%]	P_γ [%]	$u(P_\gamma)$ [%]	
²²⁷ Th	314.85	0.49	0.04	0.49	0.01	1
²²⁷ Th	329.85	2.94	0.15	2.85	0.08	-3
²²⁷ Th	334.37	1.14	0.08	1.09	0.04	-4
²²⁷ Th	342.55	0.35	0.09	0.63	0.02	82
²²⁷ Th	346.45	0.012	0.001	0.009	0.001	-21
²²⁷ Th	382.2	0.006	0.001	0.006	0.001	-2
²²⁷ Th	466.8	0.00049	0.00003	0.0013	0.0004	175
²²⁷ Th	493.1	0.0005	0.0001	0.0013	0.0004	147
²²⁷ Th	524.5	0.00019	0.00004	0.0013	0.0004	562
²²⁷ Th	536.9	0.0011	0.0002	0.0017	0.0014	55
²²⁷ Th	756.9	0.00019	0.00005	0.0010	0.0003	399
²²⁷ Th	775.8	0.0015	0.0001	0.0080	0.0007	418
²²⁷ Th	781	0.0003	0.0001	0.00101	0.00024	213
²²⁷ Th	797.3	0.0009	0.0001	0.00174	0.00025	90
²²⁷ Th	803.9	0.0006	0.0005	0.0021	0.0003	228
²²⁷ Th	812.6	0.0017	0.0003	0.0034	0.0003	104
²²⁷ Th	823.4	0.0026	0.0003	0.0034	0.0003	30
²²⁷ Th	842.5	0.0009	0.0001	0.0004	0.0001	-51
²²⁷ Th	846.7	0.00015	0.00003	0.0004	0.0001	182
²²⁷ Th	908.6	0.0024	0.0003	0.0025	0.0002	5
²²³ Fr	134.6	0.50	0.10	0.048	0.016	-90
²²³ Ra	104.04	0.019	0.002	0.074	0.005	284
²²³ Ra	106.78	0.023	0.001	0.016	0.003	-32
²²³ Ra	110.856	0.058	0.004	0.061	0.003	4
²²³ Ra	122.319	1.24	0.02	1.35	0.02	9

<i>Nuc.</i>	<i>Photon Energy [keV]</i>	<i>DDEP</i>		<i>This work</i>		<i>Rel. dev. [%]</i>
		<i>P_γ [%]</i>	<i>u(P_γ) [%]</i>	<i>P_γ [%]</i>	<i>u(P_γ) [%]</i>	
²²³ Ra	131.6	0.006	0.003	0.016	0.001	160
²²³ Ra	144.27	3.36	0.08	3.59	0.09	7
²²³ Ra	147.2	0.006	0.003	0.006	0.001	6
²²³ Ra	154.208	5.84	0.13	6.24	0.15	7
²²³ Ra	158.635	0.71	0.02	0.77	0.02	8
²²³ Ra	165.8	0.005	0.003	0.0036	0.0015	-33
²²³ Ra	175.65	0.017	0.004	0.020	0.002	16
²²³ Ra	177.3	0.047	0.004	0.054	0.002	15
²²³ Ra	179.54	0.154	0.014	0.160	0.011	4
²²³ Ra	221.32	0.036	0.006	0.030	0.002	-16
²²³ Ra	249.49	0.038	0.010	0.043	0.004	14
²²³ Ra	251.6	0.055	0.010	0.017	0.002	-69
²²³ Ra	269.463	14.23	0.32	14.06	0.29	-1
²²³ Ra	288.18	0.161	0.005	0.125	0.005	-22
²²³ Ra	323.871	4.06	0.08	3.73	0.12	-8
²²³ Ra	328.38	0.203	0.010	0.190	0.007	-6
²²³ Ra	338.282	2.85	0.06	2.68	0.08	-6
²²³ Ra	342.78	0.23	0.01	0.64	0.02	182
²²³ Ra	355.5	0.004	0.001	0.008	0.001	96
²²³ Ra	361.89	0.028	0.007	0.034	0.001	23
²²³ Ra	362.9	0.016	0.007	0.024	0.001	47
²²³ Ra	368.56	0.009	0.004	0.015	0.001	66
²²³ Ra	371.676	0.50	0.01	0.45	0.01	-9
²²³ Ra	376.26	0.013	0.004	0.0088	0.0006	-33
²²³ Ra	430.6	0.020	0.006	0.0226	0.0032	13

<i>Nuc.</i>	<i>Photon Energy [keV]</i>	<i>DDEP</i>		<i>This work</i>		<i>Rel. dev. [%]</i>
		P_γ [%]	$u(P_\gamma)$ [%]	P_γ [%]	$u(P_\gamma)$ [%]	
²²³ Ra	432.45	0.036	0.003	0.035	0.001	-2
²²³ Ra	445.033	1.28	0.04	1.24	0.03	-3
²²³ Ra	487.5	0.0110	0.0020	0.006	0.001	-42
²²³ Ra	500	0.0014	0.0006	0.001	0.001	-26
²²³ Ra	527.611	0.073	0.004	0.069	0.004	-5
²²³ Ra	537.6	0.0021	0.0007	0.003	0.000	56
²²³ Ra	541.99	0.0014	0.0006	0.001	0.001	-16
²²³ Ra	598.721	0.0920	0.0040	0.085	0.003	-7
²²³ Ra	609.31	0.057	0.003	0.032	0.004	-44
²²³ Ra	619.1	0.0036	0.0011	0.00209	0.00058	-42
²²³ Ra	623.68	0.009	0.004	0.00715	0.00071	-21
²²³ Ra	711.3	0.004	0.001	0.00297	0.00040	-20
²²³ Ra	718.4	0.0014	0.0006	0.00080	0.00062	-43
²¹⁹ Rn	130.58	0.133	0.011	0.163	0.017	23
²¹⁹ Rn	271.228	11.07	0.22	11.28	0.23	2
²¹⁹ Rn	293.56	0.075	0.003	0.064	0.002	-14
²¹⁹ Rn	401.81	6.75	0.22	6.95	0.14	3
²¹⁹ Rn	517.6	0.0430	0.0030	0.0465	0.0012	8
²¹⁹ Rn	564.1	0.0015	0.0003	0.0048	0.0015	223
²¹⁹ Rn	676.66	0.0180	0.0020	0.0207	0.0010	15
²¹⁹ Rn	877.2	0.00033	0.00011	0.0007	0.0002	100
²¹⁹ Rn	891.1	0.00090	0.00020	0.0005	0.0002	-48
²¹⁵ Po	438.9	0.058	0.019	0.0576	0.0039	-1
²¹¹ Pb	361.846	0.042	0.003	0.034	0.001	-19
²¹¹ Pb	404.834	3.83	0.06	4.180	0.088	9

<i>Nuc.</i>	<i>Photon Energy [keV]</i>	<i>DDEP</i>		<i>This work</i>		<i>Rel. dev. [%]</i>
		<i>P_γ [%]</i>	<i>u(P_γ) [%]</i>	<i>P_γ [%]</i>	<i>u(P_γ) [%]</i>	
²¹¹ Pb	427.15	1.81	0.04	1.95	0.04	8
²¹¹ Pb	429.65	0.008	0.003	0.004	0.001	-52
²¹¹ Pb	504.07	0.006	0.001	0.002	0.000	-64
²¹¹ Pb	609.55	0.033	0.009	0.025	0.003	-23
²¹¹ Pb	675.81	0.018	0.001	0.005	0.001	-74
²¹¹ Pb	704.675	0.470	0.010	0.520	0.013	11
²¹¹ Pb	766.68	0.62	0.04	0.78	0.03	26
²¹¹ Pb	831.984	3.50	0.05	3.71	0.08	6
²¹¹ Pb	865.92	0.0046	0.0002	0.0060	0.0003	31
²¹¹ Pb	1014.38	0.0173	0.0005	0.0120	0.0051	-30
²¹¹ Pb	1080.64	0.0121	0.0005	0.0130	0.0006	8
²¹¹ Pb	1103.52	0.0047	0.0007	0.0036	0.0002	24
²¹¹ Pb	1109.51	0.116	0.003	0.125	0.008	8
²¹¹ Pb	1196.33	0.0103	0.0004	0.0101	0.0005	-2
²¹¹ Pb	1234.3	0.0009	0.0003	0.0006	0.0002	-29
²¹¹ Pb	1270.75	0.0068	0.0012	0.0070	0.0004	3
²¹¹ Bi	351.03	13.00	0.19	13.94	0.29	7
²⁰⁷ Tl	569.698	0.0019	0.0002	0.0063	0.0006	241
²⁰⁷ Tl	897.77	0.263	0.009	0.309	0.020	17

In total, 145 P_γ are presented in Table 4.14 as an outcome of this part of the work. It is evident from Table 4.14 that for most of the gamma-lines studied, the new emission probabilities agree within uncertainties with most of DDEP/NNDC recommended values. In addition, the absolute uncertainties on the emission probabilities for the majority of the energies have been improved, as in the case of the 200.5 keV and 803.9 keV gamma-emission line of ²²⁷Th or in the case of the gamma emission line at 131.6 keV of ²²³Ra.

From Table 4.14 we can observe that there are some cases in which there are consistent improvements on the DDEP value of the emission probabilities of some radionuclide under investigation. However in all these cases the P_γ measured were carried out by one institute only.

Conclusion

Naturally occurring radionuclides are present in many natural resources. Industrial activities that exploit these resources may lead to enhanced potential for exposure to Naturally Occurring Radioactive Materials (NORM) in products, by products, residues and wastes.

Within this framework, the EC MetroNORM project has different purposes and aims: first of all new methodologies have been developed for measurements of natural radionuclides and new CMR have been used for their calibration with traceability to national standards of partnering countries. In addition, nuclear data of natural radionuclides have been improved, to accurately measure as many as possible descendants of the uranium decay chains.

Within the MetroNORM project, the main results of this thesis can be summarized as follows:

- A new CMR (Ionex resin) was characterized, through the measurement of activity concentration, with total relative uncertainties of about 1.6% ($k=1$).
- A standardized traceable measurement method for NORM industries was developed.
- Nuclear data for ^{235}U series radionuclides were improved and accuracies of its gamma-ray intensities were largely improved.

With the aim of identifying a representative material of the European production cycles, in which there is a high natural radioactive in products or residues in the waste, we carried out a preliminary evaluation of three candidate reference materials. Tuff was chosen as a material representative of industries producing construction materials, the Ionex resin as representative of the industries that are involved in the water purification and TiO_2 , widely used in industries producing paints.

These three matrices were subjected to a preliminary characterization process, carried out through the evaluation of the chemical composition, homogeneity and radiometric characterization of the samples. Based on the availability and on the amount of radioactivity present in the material, Ionex resin was chosen as the reference material to be certified. The new CMR was therefore considered for the calibration of the gamma-ray spectrometer used for the measurement of natural radioactivity.

The Ionex resin CMR has been certified through a characterization process carried out by three metrological institutes: CMI, JRC and ENEA. For this purpose, we carried out accurate

measurements of homogeneity and chemical composition of the material to obtain an activity measurement with an uncertainty less than 10%. We obtain an activity characterization of the CMR with an uncertainty of 1.56% for ^{235}U and 2.96% for ^{238}U . The evaluation of the activity of the CMR was performed through the use of power moderate mean that can calculate an efficient and robust mean from any data set. Moreover, ENEA has developed a measurement method to evaluate the activity of a sample with a high content of natural radioactivity. This measurement method has been validated through the use of CMR and through the organization of an inter-comparison that involved 12 participating institutions to the MetroNORM project. Hence, this part of the work was focused on providing to the end users of this project the necessary expertise for the evaluation of the natural radioactivity in the materials and the waste of their production cycles.

The second goal of this thesis was to measure the emission probability of the radionuclides belonging to the ^{235}U radioactive chain. For this purpose JRC prepared two radioactive sources, the first made of ^{235}U and the second composed of ^{227}Ac in equilibrium with its daughter. The activities of these two sources were first evaluated with a primary measurement method (α -spectrometry) and then the emission probability of the emission line of interest was carried out through gamma-ray spectrometry. We evaluated 180 emission lines of radionuclides belonging to the radioactive series of ^{235}U and we showed that, for most of the gamma-lines investigated, the new emission probabilities agree with most of DDEP/NNDC recommended values, within the uncertainties. In addition, the absolute uncertainties on the emission probabilities for the majority of the energies were largely improved. In some cases, such as the emission line at 96.09 keV of ^{235}U we found probability values different from the ones recommended by DDEP (the estimated value on the P_γ is almost 6 times higher than the DDEP). This result will be used by DDEP, over the next few years, for a critical analysis that could lead to a reassessment of the recommended values of emission probabilities.

In conclusion, this thesis and more generally the MetroNORM project provided methodologies for quantification of radioactivity in products and waste to industries using NORM materials. Moreover, the metrological institutions participating in the project have acquired the skills for the preparation of the CMR for industries who handle NORM in their national territory. This result is very important considering the increasing attention that the national authorities have in the protection of workers and the public from risks involving exposure to high concentrations of radionuclides of natural origin.

Acknowledgments

Desidero ringraziare sentitamente tutti coloro che hanno contribuito alla realizzazione della mia Tesi con suggerimenti, critiche ed osservazioni. Per il prezioso contributo scientifico ringrazio il Prof. Wolfango Plastino, ed il Dott. Pierino De Felice. Grazie per la loro guida sapiente, attenta e premurosa. Ringrazio tutti i dipendenti, dell'Istituto di Metrologia delle Radiazioni Ionizzanti e dell'Istituto di Radioprotezione in particolare: Aldo Fazio, il dott. Pierluigi Carconi e Francesca Zazzaron. Grazie per i loro preziosi consigli e per il tempo e le energie che hanno dedicato alla realizzazione del mio lavoro. Desidero ringraziare anche la dott.ssa Elena Fantuzi ed il dott. Enrico Maria Borra per avermi dato la possibilità di fare questa splendida esperienza. Un grazie speciale va a tutti i miei amici. Loro ci sono stati, ci sono e ci saranno sempre. Infine, questo traguardo è dedicato alla mia famiglia: grazie mamma, papà, F. e S.

Appendix



1st September 2013 – 31st August 2016

JRP EMRP IND57: MetroNORM

Metrology for processing materials with high natural
radioactivity

Report on deliverable D1.4.1

At least two measurement methods for absolute and spectrometry
activity measurement for the radionuclides selected in Task 1.1

Deliverable Number: **D1.4.1**
Deliverable Type: **Procedure**
Lead Participant: **ENEA**
Other Participants: **CEA, CIEMAT, CMI, NPL**
Delivery Date: **April 2015**



Table of Contents

1. SHORT REVIEW ON IONEX RESIN AND ITS PREPARATION WITH URANIUM	3
2. CONSIDERATIONS AND INITIAL CONTROLS	4
3. INFORMATION GATHERING (some information will be contained in <i>books</i> (B), nuclear data <i>web sites</i> (WS), in the <i>reports of the software</i> that controls the operation of the <i>hpge</i> (RS) or will have to be estimated by the operator from the <i>spectrum graph</i> (SPG); some other info may be either decided by the operator or contained in other available <i>documents</i> (OD); some other will have to be obtained by <i>monte carlo computer simulations</i> (MCS).....	5
4. HPGE COUNT RATE MEASUREMENT	7
5. ACTIVITY OR ACTIVITY CONCENTRATION CALCULATION	7



Introduction

In this document the steps of a relative measurement of the Activity of ^{238}U and ^{235}U contained in IONEX by HPGe will be listed and described with some details. For the sake of clarity, these steps can be arranged in four categories:

1. Short review on IONEX resin and its preparation with Uranium;
2. Considerations and initial controls;
3. Information gathering (some information will be contained in books (B), nuclear data web sites (WS), in the reports of the software that controls the operation of the HPGe (RS) or will have to be estimated by the operator from the spectrum graph (SPG); some other info may be either decided by the operator or contained in other available documents (OD); some other will have to be obtained by Monte Carlo computer simulations (MCS);
4. HPGe count rate measurement;
5. Activity or Activity concentration calculation.

1. Short review on IONEX resin and its preparation with Uranium

The IONEX technology is beneficial because it is highly selective for uranium, does not change the taste or properties of drinking water and is easy to operate. IONEX is a material from water purification filters used for removing uranium from water and can be regenerated.

IONEX is a styren-divinylbenzene copolymer with trialkyl-amin-groups. The insoluble matrix in the form of small beads provides a high surface area. Mean bead size is 0.64 mm. Radioactive IONEX for WP1 was obtained from Waterworks in the Czech Republic.

Preparation of the IONEX resin (material):

The sample of IONEX contained a large amount of carbonates (sediments from water, approx. 250 g per 1 kg of IONEX), which caused inhomogeneity of the sample and had to be removed from the sample before γ -spectrometry measurement. The sample immersed in distilled water was placed into the ultrasonic bath. Then, the sample was washed with distilled water on a sieve (0.3 mm). Most of carbonates were removed. No significant amount of uranium was detected in the waste water nor in the removed carbonates. The activity was measured with the liquid scintillation counter. The sediments were homogeneously distributed in the scintillation cocktail (Ready Gel) and waste water was measured as scintillation cocktail (Ultima Gold). A sample of the treated IONEX was finally air dried and mixed up.

SAMPLES:

Seven identical PVC containers were filled with equal amounts of the IONEX resin (94.58 (19) g). The sample of IONEX resin was kept in an 85-ml metal container of 6 cm diameter, 3-cm height and 1-mm thickness of the bottom. The chemical composition of the container is given in Table. Bulk density of the active IONEX sample was 0.79 g cm^{-3} . The content of water in IONEX resin



sample was determined as 10 %. The samples were dried in a desiccator with P₂O₅. The elemental composition of the IONEX is also given in the following Table.

IONEX resin		Metal container			
Element	Abundance %	Element	Abundance %	Element	Abundance %
C	59.7	Si	1.1	Nn	0.05
N	11.5	Fe	0.24	Ti	0.02
O	12.2	Cu	0.03	Pb	0.01
H	11.4	Mn	0.53	Al	97.51
S	4.6	Mg	0.61	Cr	0.02
U	0.5				

2. Considerations and initial controls

- 2.1. From what has been said about the IONEX resin and its capacity to wash out Uranium atoms from water, it is reasonable to hypothesise that Uranium contained in this resin is no more in equilibrium with its daughter nuclides. This consideration is important as it has repercussions on which gamma emissions and hence which radionuclides will be available in order to detect the disintegrations of ²³⁵U and ²³⁸U.
- 2.2. ²³⁵U disintegrates by alpha emission to the excited levels of ²³¹Th which in turn emits gamma rays that can be detected in order to count the disintegrations of the parent nuclide (²³⁵U). In Table 1, the most intense gamma energies emitted after the disintegration of one atom of ²³⁵U are reported:

Table 1

²³⁵ U disintegrations counted by the gamma emission of ²³¹ Th	
Energy (KeV)	Photons per 100 disintegrations
109.19 (7)	1.66 (13)
143.767 (3)	10.94 (6)
163.356 (3)	5.08 (3)
185.720 (4)	57.0 (3)
202.12 (1)	1.08 (2)
205.316 (4)	5.02 (3)

The most intense gamma emission takes place at 185.720 KeV, however it is also known that ²²⁶Ra (which belongs to the ²³⁸U series) emits at 186.211 KeV. Being these



energies so close to each other, the relative counts would pile up in one single peak. Thus, although one does not expect the presence of this radionuclide, it is appropriate to double-check its absence, once subtracted the blank, directly and by its daughter nuclides like ^{214}Pb and ^{214}Bi .

- 2.3. ^{238}U disintegrates by alpha emission to ^{234}Th , which unfortunately possesses only two gamma emissions with a very low emission probability that, hence, cannot be used to count the disintegration of the parent nuclide. It follows that it is necessary to move down in the decay chain in order to find out a radionuclide by whose gamma emission one can extrapolate the disintegration of (^{238}U). This method produces the correct result only if the parent radionuclide (^{238}U) is in equilibrium with its daughter nuclides. However it is not necessary that ^{238}U be in equilibrium with all of its daughters, it is sufficient that the equilibrium is verified among three radionuclides: ^{238}U , ^{234}Th and ^{234}Pa . Thanks to the rather short half-life of ^{234}Th (24.1 days), one is justified to reckon that this condition will be fulfilled after waiting for a sufficiently long amount of time which is about 5 times this half-life. The radionuclide whose emissions will be measured to find out the activity of (^{238}U) is $^{234\text{m}}\text{Pa}$.

Table 2
 ^{234}Th disintegrations
counted by the gamma emission of $^{234\text{m}}\text{Pa}$

Energy (KeV)	Photons per 100 disintegrations
766,361 (20)	0,323 (4)
1001,026 (18)	0,847 (8)

3. Information gathering

- 3.1. Beginning date and time of the count rate measurement T_{bsa} . Contained in (RS).
- 3.2. Date and Time to which the Activity or Activity concentration have to be referred T_{ar} (OD).
- 3.3. Real Time of the count rate measurement of the source RT_{sa} . Contained in (RS).
- 3.4. Live Time of the count rate measurement of the source LT_{sa} along with its uncertainty. Contained in (RS).
- 3.5. Background area of each of the significant¹ peaks of $^{234\text{m}}\text{Pa}$ (for ^{238}U) and for ^{231}Th (^{235}U). That is the counts of the gamma Compton background right under each peak. Contained in (RS).

¹ Significant is used to indicate a peak corresponding to a photon of $^{234\text{m}}\text{Pa}$ and ^{231}Th whose probability of emission γ is fairly large, so that the corresponding peak can be easily made out above the gamma background after a reasonable measurement duration (Live Time).



- 3.6. Source Net area N_{NSa} of each significant peak of ^{234m}Pa and ^{231}Th along with the related uncertainty. Net area being the gamma counts contained in each peak once subtracted of background area. Contained in (RS).
- 3.7. Live Time of the count rate measurement of the blank LT_b along with its uncertainty. Contained in (RS).
- 3.8. Background area of the blank corresponding to the peaks of ^{234m}Pa and ^{231}Th . That is the counts of the gamma Compton background right under each peak. Contained in (RS) since ^{234m}Pa and ^{231}Th are naturally occurring radionuclides or likelier in (SPG), if the peaks are too low to be identified by the software.
- 3.9. Blank net area N_{Nb} corresponding to the peaks of ^{234m}Pa and ^{231}Th along with the related uncertainty. Net area being the gamma counts contained in each peak once subtracted of background area. Contained in (RS), since ^{234m}Pa and ^{231}Th are naturally occurring radionuclides or likelier in (SPG), if the peaks are too low to be identified by the software.
- 3.10. Detection efficiency ϵ of the HPGe for a ^{234m}Pa and ^{231}Th standard source (i.e. arranged in a precise and reproducible geometry and contained in a matrix of known density and chemical composition) along with its uncertainty. If the HPGe is calibrated, i.e. possesses a single photon calibration curve, this information comes along with it. Conversely, were the HPGe spectrometer not calibrated, one may proceed along two different pathways: determine the efficiency by reading by the HPGe the count rate of a ^{234m}Pa and ^{231}Th source whose activity was previously assessed by an absolute measurement method; determine the efficiency curve in the energy range from 100 KeV up to 1100 KeV by available and easier to measure radionuclides whose emissions laid in this energy range, and disposed in a standard geometry and contained in a known matrix.
- 3.11. Gamma Emission Intensity or Photons per disintegration (I_γ) for each of the emission energy chosen for ^{234m}Pa and ^{231}Th , along with its uncertainty. Contained in (WS) [1].
- 3.12. Half life time $t_{1/2}$ for ^{234m}Pa and ^{231}Th along with its uncertainty. Contained in (WS) [1].
- 3.13. Mass m of the source along with its uncertainty. Either measured by the operator or provided with the sample.
- 3.14. Correction coefficient of self-attenuation k_1 along with its uncertainty for each of the emission energy chosen for ^{234m}Pa and ^{231}Th . Obtained by efficiency transfer simulations (ETNA, GESPECOR, GEANT or other Monte Carlo Codes) (MCS). This coefficient depends on the chemical composition and the density of the sample. If this information is not provided along with the sample, it becomes necessary for the operator to either measure the mass attenuation coefficient by the collimated beam method or estimate it by XCOM.
- 3.15. Geometrical correction factor k_2 , that is the coefficient due to possible differences of the reference geometry to that of the source, along with its uncertainty (ETNA, GESPECOR, GEANT or other Monte Carlo Codes) (MCS).
- 3.16. Correction coefficient of coincidence summing k_3 along with its uncertainty for each of the emission energy chosen for ^{234m}Pa and ^{231}Th . Obtained by Monte Carlo simulations (ETNA, GESPECOR, GEANT or other Monte Carlo Codes) (MCS).



4. Information gathering

- 4.1. As it was mentioned in the third section of this protocol, it is necessary to collect by HPGe measurements some information about the blank, that is a sample whose features are identical to those of the radioactive sample but for the absence of Uranium. Prepare the uncontaminated IONEX according to the standard geometry to which one will refer during all the protocol. Due to the possible presence in the IONEX of grains of different size and the possibility with time that they may sediment in the container according to their dimensions, it is advisable to homogenise the content by moving the container back and forth. Should the uncontaminated IONEX not be available, fill the standard geometry with bidistilled deionised water.
- 4.2. Place the blank in the detector according to a precise source-detector geometry, which will have to be replicated with the source.
- 4.3. Set the Live Time sufficiently long so that the uncertainty on the net Area of the peaks be not higher than 1%.
- 4.4. Start to count the gamma photons emitted by the blank.
- 4.5. Before placing the Uranium source (IONEX) in the standard geometry, homogenise its content.
- 4.6. Determine the mass of the source.
- 4.7. Place the source in the detector according to the precise source-detector geometry that was used during the blank measurement.
- 4.8. Set the Live Time sufficiently long so that the uncertainty on the net Area of the peaks be not higher than 1%.
- 4.9. Before starting the true counting of the gamma photons emitted by the source, it is necessary to perform several counting and compare them with each other in order to find out whether the equilibrium between ^{238}U and its daughter nuclide ^{234}Th has been reached. It is possible to compare the experimental curve with that obtained by the Bateman differential equations.
- 4.10. If the equilibrium between ^{238}U and ^{234}Th is established, start the counting of the gamma photons emitted by the source.

5. Information gathering

With the information gathered of section 3 and the count rate measurements of section 4, it is now possible to compute the activity and the activity concentration along with their uncertainty.

- 5.1. The formula for the Activity is reported here together with the legend explaining the meaning of the symbols:

$$A = \frac{1}{\varepsilon L_y} \left[\frac{N_{Noa}}{LT_{Noa}} - \frac{N_{Nb}}{LT_b} \right] \cdot F_1(T_{ar} - T_{Noa}, t_{1/2}) \cdot F_2(RT_{Noa}, t_{1/2}) \cdot k_1 k_2 k_3$$



- ε = Detector Efficiency
- I_γ = Gamma Emission Intensity
- N_{NSA} = Source Net Area
- N_{NB} = Blank Net Area
- LT_{SA} = Source Live Time
- LT_b = Blank Live Time
- RT_{SA} = Source Real Time
- T_{ar} = Date to which the Activity has to be referred
- T_{bsa} = Beginning Date of the Source Measurement
- $t_{1/2}$ = Half Life
- k_1 = Coefficient of self-attenuation
- k_2 = Geometrical correction factor
- k_3 = Coincidence summing coefficient
- F_1 = Coefficient that brings back or forward in time the value of the activity referring it to the instant T_{ar}
- F_2 = allows for the decay of the radionuclide during the measurement.

The explicit form of the two factors F_1 and F_2 depends in general on the evolution with time of the system of radionuclides and hence has to be evaluated case by case. Only if the evolution of the system is a simple exponential ($N(t)=N_0 \exp(-\lambda t)$ or $N(t)= N_0(1-$

$\exp(-\lambda t))$), the two factors F_1 and F_2 become $e^{\frac{-\ln(2)(T_{ar}-T_{bsa})}{t_{1/2}}}$ and $\frac{\ln(2)RT_{sa}}{86400 t_{1/2}} \cdot \frac{1}{1 - e^{\frac{-\ln(2)RT_{sa}}{86400 t_{1/2}}}}$

respectively.

We stress again that both of these terms are valid only if there is equilibrium between the parent nuclide and its daughter, i.e. if the evolution is a simple exponential. On the contrary, if the radioactive processes are more complicated because the equilibrium has not been reached yet, more complicated terms have to be used, which, in general, will have to be calculated specifically for each case.

5.2. As to the relative uncertainty related to the activity, it will contain several components due to the propagation of the relative uncertainty of all the quantities contained in the formula above. These components will be listed here:

$u(A)|_\varepsilon = u(\varepsilon)$ relative uncertainty of the activity due to the relative uncertainty of the efficiency ε

$u(A)|_{I_\gamma} = u(I_\gamma)$ relative uncertainty of the activity due to the relative uncertainty of the gamma emission intensity (value provided by reference [LNHB])



$$u(A)|_{F_1} = \frac{1}{F_1} \frac{\partial F_1}{\partial t_{1/2}} u(t_{1/2}) t_{1/2} \quad \text{relative uncertainty of the activity due to the relative uncertainty of } t_{1/2} \text{ contained in } F_1$$

$$u(A)|_{F_2} = \frac{1}{F_2} \frac{\partial F_2}{\partial t_{1/2}} u(t_{1/2}) t_{1/2} \quad \text{relative uncertainty of the activity due to the relative uncertainty of } t_{1/2} \text{ contained in } F_2$$

$$u(A)|_{\left[\frac{N_{Nsa}}{LT_{sa}} - \frac{N_{Nb}}{LT_b}\right]} = \begin{cases} N_{Nsa} \cdot \frac{u(LT_{sa})}{\left[\frac{N_{Nsa}}{LT_{sa}} - \frac{N_{Nb}}{LT_b}\right] \cdot LT_{sa}} \\ N_{Nb} \cdot \frac{u(LT_b)}{\left[\frac{N_{Nsa}}{LT_{sa}} - \frac{N_{Nb}}{LT_b}\right] \cdot LT_b} \\ N_{Nsa} \cdot \frac{u(N_{Nsa})}{\left[\frac{N_{Nsa}}{LT_{sa}} - \frac{N_{Nb}}{LT_b}\right] \cdot LT_{sa}} \\ N_{Nb} \cdot \frac{u(N_{Nb})}{\left[\frac{N_{Nsa}}{LT_{sa}} - \frac{N_{Nb}}{LT_b}\right] \cdot LT_b} \end{cases}$$

relative uncertainty of the activity due to the relative uncertainty of LT_{sa} , LT_b , N_{Nsa} , N_{Nb}

$$u(A)|_{k_1}, u(A)|_{k_2}, u(A)|_{k_3} = u(k_1), u(k_2), u(k_3) \quad \text{relative uncertainty of the activity due to the relative uncertainty of } K_1, K_2 \text{ and } K_3$$

The whole activity's relative uncertainty is just the square root of quadratic sum of the components of uncertainty:

$$u(A) = \sqrt{\sum_j u^2(A)|_j}$$

where the index j indicates the jth component of the uncertainty.
The explicit form of the activity's uncertainty is:

$$u(A) = \sqrt{\begin{aligned} & (u(A)|_{\epsilon})^2 + (u(A)|_{I_y})^2 + (u(A)|_{F_1})^2 + \\ & \quad + (u(A)|_{F_2})^2 + \\ & + (u(A)|_{LT_{sa}})^2 + (u(A)|_{LT_b})^2 + (u(A)|_{N_{Nsa}})^2 + (u(A)|_{N_{Nb}})^2 + \\ & \quad + (u(A)|_{k_1})^2 + (u(A)|_{k_2})^2 + (u(A)|_{k_3})^2 \end{aligned}}$$



5.3. Formulas to calculate the decision threshold and the Minimum Detectable Activity (Detection Limit).

$$\text{Decision Threshold : } L_c = 2.33 \cdot \frac{\sqrt{N_{sa-bkg}}}{LT_{sa} \epsilon m I_y}$$

$$\text{Detection Limit: } L_d = 4.65 \cdot \frac{\sqrt{N_{sa-bkg}}}{LT_{sa} \epsilon m I_y}$$

where N_{sa-bkg} are the background counts of the source.

Relative uncertainty of L_c

$$u(L_c) = \sqrt{(u(L_c)|_{LT_{sa}})^2 + (u(L_c)|_{\epsilon})^2 + (u(L_c)|_m)^2 + (u(L_c)|_{I_y})^2}$$

Relative uncertainty of L_d

$$u(L_d) = \sqrt{(u(L_d)|_{LT_{sa}})^2 + (u(L_d)|_{\epsilon})^2 + (u(L_d)|_{m_{sa}})^2 + (u(L_d)|_{I_y})^2}$$

where the components both for L_c and L_d are

$$u(L_c/d)|_{LT_{sa}} = \frac{u(LT_{sa})}{2 LT_{sa}}, \quad u(L_c/d)|_{\epsilon} = \frac{u(\epsilon)}{2 \epsilon}, \quad u(L_c/d)|_m = \frac{u(m_{sa})}{2 m_{sa}}, \quad u(L_c/d)|_{I_y} = \frac{u(I_y)}{2 I_y}$$

References

- [1] http://www.nucleide.org/DDEP_WG/DDEPdata.htm

BIBLIOGRAPHY

- [1] UNSCEAR, *Effects of Atomic Radiation to the General Assembly, in United Nations Scientific Committee on the Effect of Atomic Radiation*, 2000, United Nations, New York.
- [2] Chen S.B., Zhu Y.G., Hu Q.H., *Soil to plant transfer of ^{238}U , ^{226}Ra and ^{232}Th on a uranium mining-impacted soil from southeastern China*, *Journal of Environmental Radioactivity*, 2005, 82 (2), p. 223-236.
- [3] Van der Steen J., *Radiation protection in NORM industries*, NRG, Arnhem, The Nederland.
- [4] Brigido Flores O., Montalvan Estrada A., Rosa Suarez R., Tomas Zerquera J., et al., *Natural radionuclide content in building materials and gamma dose rate in dwellings in Cuba*, *Journal of Environmental Radioactivity*, 2008, 99 (12), p. 1834-1837.
- [5] Radford D.C., RadWare, in *Nucl. Instrum. Methods Phys*, 1995. 361, p. 297.
- [6] Krane K.S., et al., *Introductory nuclear physics*, John Wiley & Sons Ltd, 1988, New York, ISBN 047180553X.
- [7] Curie M., Debierne A., Eve A.S., Geiger H., Hahn O., Land S.C., Rutherford E., Schweidler E., *The Radioactive Constants as of 1930*, in *Review of Modern Physics*, 1931, The International Radium-Standards Commission.
- [8] Rutherford E., *The Scattering of Alpha and Beta Particles by Matter and the Structure of the Atom*, University of Manchester. Philos, 1911, 6 (21).
- [9] Nuclear Technology Education Consortium, *Radioactive Decay*, 2009, Available from: <http://www.ntec.ac.uk/Phys/pdfs/8- Radioactive%20Decay.pdf>.
- [10] Lilley J., *Nuclear Physics, Principles and Application*, 2001, West Sussex, England, UK, John Wiley & Sons Ltd.
- [11] Friedlander G., Miller J.M., *Nuclear and radiochemistry*, 3rd Ed. 1981, New York, John Wiley & Sons Ltd.

- [12] Butt D.K., Wilson A.R., *A Study of the Radioactive Decay Law*, J. Phys. London, 1972, A5, p. 1248.
- [13] Neary G.J., *The β -Ray Spectrum of Radium*, E. Proc. Roy. Soc., London, 1940, 175A, p. 71.
- [14] Hsue S.T., Langer L.M., Tang S.M., *Precise Determination of the Shape of the Twice Forbidden Beta Spectrum of ^{137}Cs* , Nucl. Phys., 1966, 86, p. 47-173.
- [15] Nelson G., Reilly D., *Gamma-Ray Interactions with Matter*, Available from http://www.sciencemadness.org/lan11_a/lib-www/lapubs/00326397.pdf.
- [16] Marilyn E., Noz G.Q., *Maguire Radiation Protection in the Health Sciences*, 2nd Ed., World Scientific Publishing Co. Pte. Ltd., 2007, USA.
- [17] Cetnar J., *General solution of Bateman equations for nuclear transmutations*, Annals of Nuclear Energy, 2006, 33 (7), p. 640-645, 174.
- [18] ANL, *Natural Decay Series, Uranium, Radium, and Thorium, in human health fact sheet*, 2005, Argonne National Laboratory.
- [19] Denagbe, S.J., *Radon-222 concentration in subsoils and its exhalation rate from a soil sample*, Radiation Measurements, 2000, 32 (1), p. 27-34.
- [20] Condomines M., Michaud V., *Magma dynamics at Mt Etna: Constraints from U-Th-Ra-Pb radioactive disequilibria and Sr isotopes in historical lavas*, Earth and Planetary Science Letters, 1995, 132 (1-4), p. 25-41.
- [21] UNSCEAR, *Effects of Atomic Radiation to the General Assembly, in United Nations Scientific Committee on the Effect of Atomic Radiation, 2000*, United Nations, 2000 New York.
- [22] Knoll, Gelman F., *Radiation Detection and Measurements*, 3rd Ed. 2000, New York: John Wiley & Sons Inc., ISBN 0-471-07338-5.
- [23] Szaflarski D. *Everyday Exposure to Radiation, Nuclear Chemistry*, Cruising Chemistry 1997, Available from http://www.chem.duke.edu/~jds/cruise_chem/nuclear/exposure.html.
- [24] Kathren R.L., *NORM sources and their origins*, Applied Radiation and Isotopes, 1998, 49 (3), p. 149-168.
- [25] Silberberg R., Tsao C.H., *Spallation processes and nuclear interaction products of cosmic rays*, Physics Reports, 1990, 191 (6), p. 351-408.
- [26] Klement Jr. A.W., *Natural Sources of Environmental Radiation*, In Handbook of Environmental Radiation, Ed. A.W. Klement Jr., 1982. p. 15-21, CRC Press, Boca Raton, Florida.

-
- [27] Browne E., Shirley V.S., *Table of Radioactive Isotopes*, John Wiley and Sons Inc., New York, 1986, 175.
- [28] Browne E., Firestone R.B., Shirley V.S., *Table of Radioactive Isotopes*, John Wiley and Sons Inc., New York, 1986.
- [29] Lilley J., *Nuclear Physics, Principles and Application*, 2001, West Sussex, England, UK, John Wiley & Sons Ltd.
- [30] IAEA, *Application of the Concepts of Exclusion, Exemption and Clearance*, in Safety Standards Series No. RS-G-1.7, 2004, IAEA, Vienna.
- [31] Wymer D.G., *Managing Exposure to NORM-Consensus or Chaos?*, in Proceedings of an international symposium, 2007, Seville, Spain, International Atomic Energy Agency (IAEA), Vienna.
- [32] Jobbagy V., Kovacs T., *Dependence of Radon Emanation from Red Mud on Heat Treatment*, in Proceedings of an international symposium, 2007, Seville, Spain, International Atomic Energy Agency (IAEA), Vienna.
- [33] Birky B.K., *Inhalation Doses and Regulatory Policy in Wet Acid Processing of Sedimentary Phosphate Rock*, in Proceedings of an international symposium, 2007, Seville, Spain, International Atomic Energy Agency (IAEA), Vienna.
- [34] Leopold K., *Chemical Types of Bonding natural Radionuclides in Technologically Enhanced Naturally Occurring Radioactive Materials (TENORM)*, in Proceedings of an international symposium, 2007, Seville, Spain, International Atomic Energy Agency (IAEA), Vienna.
- [35] Kevasan P.C., *Indian research on high levels of natural radiation*, In Proceedings of 4th International Conference on High Levels of Natural Radiation, Radiation Doses and Health Effects, Beijing, China, 1977, p. 111, 168.
- [36] Sunta C.M., *A review of the studies of the high background areas of the S-W coast of India In Proceedings of International Conference on High Level Natural Radiation Areas*, Ramsar, Iran, 3-7 November 1990, Ed. 1993, IAEA Publication Series, IAEA, Vienna, p. 71.
- [37] Vandenhove H., *Environmental contamination by the NORM industry: challenges for radioecology*, 2008, NRC 7, Budapest.
- [38] Gordon G., *Practical gamma-ray spectroscopy*, John Wiley & Sons Inc., 2007.
- [39] ORTEC GammaVision V7, *User Manual*, www.ortec-noline.com/Download/A.66-MNL.pdf.
- [40] ANSI, *American national standard for calibration and use of germanium spectrometers for the measurement of gamma-ray emission rates of radionuclide*, No. 42.14, 1999.

- [41] De Felice P., *Close-geometry efficiency calibration of p-type HPGe detectors with a ^{134}Cs point source*, Appl. Radiat. Isot., 2006, 64, p. 1303-1306.
- [42] Debertin K., Helmer R.G., *Gamma- and X-ray spectrometry with semiconductor detectors*, North-Holland, Amsterdam, 1988, p. 399, ISBN-13 978-0444871077, ISBN-10 0444871071.
- [43] *Calculating standard deviations and confidence intervals with a universally applicable spreadsheet technique*, Analyst 119, p. 2161-2165. DOI 10.1039/AN9941902161.
- [44] Sima O., *Matrix effects in the activity measurement of environmental samples - Implementation of specific corrections in a gamma-ray spectrometry analysis program*, Applied Radiation and Isotopes, Vol. 48, Issue 1, p. 59-69.
- [45] Sima O., *Transfer of the efficiency calibration of Germanium gamma-ray detectors using the GESPECOR software*, Applied Radiation and Isotopes, Vol. 56, Issue 1-2, p. 71-75, Published 2002.
- [46] Papachristodoulou C.A. and Ioannides K.G., J. Environ, Radioact., 64 (2-3), 2003, p. 195-203.
- [47] Yucel H. et al., Appl. Radiat. Isot., 67 (11), 2009, p. 2049-2056.
- [48] Sima O., *GESPECOR: a versatile tool in gamma-ray spectrometry*, Nucl. Chem., 248 (2), 2001, p. 359-364, DOI 10.1023/A:1010619806898.
- [49] Rujiwarodom R., *The Study of Equilibrium factor between Radon-222 and its Daughters in Bangkok Atmosphere by Gamma-ray Spectrometry*, EGU General Assembly, 2010, held 2-7 May, 2010 in Vienna, Austria, p. 249.
- [50] Suvaila R., *Complex gamma ray spectra analysis*, Romanian Report in physics, 2011, Vol. 63, No. 04, p. 975-987.
- [51] XCOM, <http://physics.nist.gov/PhysRefData/Xcom/html/xcom1.html>.
- [52] Sima O., *Accurate computation of coincidence summing corrections in low level gamma-ray spectrometry*, Applied Radiation and Isotopes, 2000, Vol. 53, Issue 1-2, p. 51-56.
- [53] Lepy M.C. et al., *Intercomparison of efficiency transfer software for gamma-ray spectrometry*, Applied Radiation and Isotopes, 2001, Vol. 55, Issue 4, p. 493-503.
- [54] Sima O., *Transfer of the efficiency calibration of Germanium gamma-ray detectors using the GESPECOR software*, Applied Radiation and Isotopes. 2002, Vol. 56, Issue 1-2, p. 71-75.

-
- [55] De Felice P., *Fast procedures for coincidence-summing correction in γ -ray spectrometry*, Appl. Radiat. Isot., 2002, Vol. 52, p. 745-752, DOI 10.1016/S0969-8043 (99) 00239-0.
- [56] De Geer L.E., *Currie detection limits in gamma-ray spectroscopy*, Applied radiation and Isotopes, 2004, Vol. 61, Issue 2-3, p. 151-160.
- [57] L'Annunziata M., *Handbook of radioactivity analysis*, Elsevier, 2012.
- [58] Vidmar T. et al., Appl. Radiat. Isot., 68 (12), 2010, p. 2352-2354.
- [59] Newman R.T., *Determination of soil, sand and ore primordial radionuclide concentrations by full-spectrum analysis of high-purity germanium detector spectra*, Applied Radiation and Isotopes, 2008, Vol. 66, Issue 6-7, p. 855-859.
- [60] Bruzzi L. et al., *Radioactivity in raw materials and end products in the Italian ceramics industry*, Journal of Environmental Radioactivity, 2000, 47, p. 171-181.
- [61] Bakr W.F., *Quantification of uncertainties in gamma-ray spectrometric measurement: a case study*, Journal of Nuclear and Radiation Physics, Vol. 6, No. 1-2, p. 55-67.
- [62] Kunze C. et al., *Assessment, handling and disposal of norm and tenorm: How Germany's radiation protection and waste management regulations work together to benefit the industry*, IRPA Regional Congress for Central and Eastern Europe, 2007, Brasov.
- [63] Condie K.C., *Chemical composition and evolution of the upper continental crust: Contrasting results from surface samples and shales*, 1993, Chem. Geol. 104, p. 1-3.
- [64] ISO Guide 30:2015, *Reference Materials - Selected term and Definitions*, International Organization for Standardization, Geneva, Switzerland.
- [65] Nuccetelli C., *New perspectives and issues arising from the introduction of (NORM) residues in building materials: A critical assessment on the radiological behavior*, Elsevier, Construction and Building Materials, 2015.
- [66] Gázquez ed al., *Characterization and valorization of norm wastes; application to the TiO₂ production industry*, 1st Spanish National Conference on Advances in Materials Recycling and Eco-Energy, 2009, Madrid.
- [67] Nuccetelli C. et al., *Natural radioactivity in buildings materials in the European Union: a database and an estimate of radiological significance*, Journal of environmental radioactivity, 2012, 105, p. 11-20.
- [68] *Production of titanium dioxide*, in Proc. Conf. Seville, Spain.

- [69] Pommé S. and Keightley J., *Determination of a reference value and its uncertainty through a power-moderated mean*, Metrologia, 2015, 52:S200-S212, DOI 10.1088/0026 - 1394/52/3/S200.
- [70] Spasova Y. and UWätjen U., *Visualisation of interlaboratory comparison results in PomPlots*, Accred. Qual. Assur., 2007, 12, p. 623-627.
- [71] Lépy M.C., *Uncertainty in gamma ray spectroscopy*, Metrologia, 2015, Vol. 52, No. 3.
- [72] Knoll G.F., *Radiation detection and measurement*, 4th Ed., John Wiley & Sons Inc., USA, 2010, p. 860, ISBN 978-0-470-13148-0.
- [73] DDEP values, http://www.nucleide.org/DDEP_WG/DDEPdata.htm, accessed on 29/06/2016.
- [74] Van Ammel R. et al., *Preparation of drop-deposited quantitative uranium sources with low self-absorption*, Nucl. Instr. Meth. A, 2011, 652, p. 76-78.
- [75] Monography, BIPM-5, *Table of Radionuclides*, Bureau International des Poids et Measure, 2004, Vol. 2, ISBN 92-822-2207-1.
- [76] NNDC values, <https://www.nndc.bnl.gov/>, accessed on 29/06/2016.